International Journal of Acoustics and Vibration

A quarterly publication of the International Institute of Acoustics and Vibration

Volume 21, Number 1, March 2016

EDITORIAL

ARTICLES

INFORMATION

Reduction of Machinery Noise by Controlling Vibration of Its Whole Casing

The concept of active noise control has been known for more than 80 years. However, although research has become more intense during last 20 years, very few practical applications have become available on the market. The main reason is that global noise reduction based on the phenomenon of destructive interference of the noise and the secondary sound generated by a control system is extremely difficult to achieve and is not economic. Therefore, real active control applications are mainly limited to active headsets or earplugs, headrests or similar systems generating local zones of quiet, like in cars and aircraft cabins or small workspaces. Active noise control has also been applied to ventilation systems with some commercial success. If the noise sources are separated from the user areas by windows or thin panels, these may be made to vibrate to reduce the noise passing through them. Such idea is known as active structural acoustic control. It has been found useful with aircraft cabin walls, for example. However, no good solutions exist so far to reduce the noise of industrial machinery or domestic appliances.

My research group, within a project sponsored by the National Science Centre, Poland, DEC-2012/07/B/ST7/01408, has addressed structural control to cope with the problem of machinery noise. The purpose of the control system is to generate vibration of all casing walls so as to acoustically isolate the machine ("block" the noise escaping through the casing). For some machines their own casings can be used, dependant on the structure, and for some others additional surrounding casings may be necessary. Without active control, the noise cannot be sufficiently reduced with passive isolation, because it may require thick layers of sound-absorbing materials, which increase the size and weight of the machinery and are an obstacle for heat dissipation.

Except from the general Fuller's idea we have not found any publications about control of the full machinery casings made of a number of connected walls in the literature. The problem is in fact very complicated. The vibration of each wall forced by actuators mounted to its surface excites the other walls through the sound field enclosed in the machine casing, the sound field outside the casing and the connected edges of neighbouring casing walls. Thus, in the first stage of our own research it was decided to consider casings walls with rigid frames in order to minimise the latter effect. Even then, the system is very multichannel. To effectively control noise over a given frequency range all relevant modes within it should be controllable and observable. Mathematical modelling and laboratory experiments revealed that as many as three actuators and three sensors may be needed for each wall, resulting in a system of fifteen inputs and fifteen outputs (the bottom wall naturally does not need to be controlled). The distribution of these sensors and actuators follows from an optimization process, which maximises measures of system controllability and observability. A reliable model of the structure was necessary for the optimization. The dynamic properties of the actuators and sensors - including their mass, size, and mounting - should be taken into account in this process, because their presence modifies the frequency response of the total structure significantly. The model accuracy was validated by laboratory experiments performed with a laser vibrometer. A memetic algorithm was employed to solve the complicated optimisation problem. Having correctly distributed sensors and actuators, different control strategies were applied. The response of vibrating plates, although well resistant to harsh environmental conditions, is significantly affected by changes in temperature. Therefore, after preliminary research it was decided to concentrate on adaptive controllers.

Due to very high coupling in the system, an individual single input – single output approach to control results in very poor performance and generally causes divergence of adaptive control filter tuning algorithms. Supervisory control used to manage the individual direct controllers in a higher layer is not efficient. However, the system becomes effective and robust if each plate is controlled individually with a multichannel system and the higher layer helps to compensate for their influence, i.e. decouples the system.

With the same actuators, different configurations and sensors were verified. Double-panel walls were tested, with one panel excited by actuators and the other sensed by accelerometers. This required an additional modelling and optimisation stage. A configuration with microphones located in the cavity between the panels was also concerned. Different types of actuators and sensors, and even the shunt technology were also examined in our research. However, the most efficient structure in terms of noise reduction was found to be with microphones located outside the machine casing, in front of the walls, which are used as error sensors. To improve the properties of such system, including its robustness, a round-robin technique was applied to select error signals for the multichannel subsystems operating for each wall. What is very remarkable, the system, if properly tuned, guarantees global control in the whole acoustical environment outside the machine casing. This has been confirmed with many observation microphones located in the exterior laboratory space and, additionally, by measurements made with a sound analyser.

Using the microphones outside the machine casing, however, is an academic solution, which rather cannot be commercially accepted. Therefore, our original virtual microphone control idea was applied. Thus, microphone measurements are only needed during the development stage, and appropriate auxiliary filters are designed. Then, during operation stage, only measurements with structural sensors are needed, and appropriate setpoints (which are zero for classic algorithms) are derived for the control systems. With this system, global noise control results were obtained, which are very similar to those obtained with the microphones. However, the total machinery system is compact, without any sensors located outside, and it is not very dependant on changing environmental conditions in the sound field.

Obtained results motivated my research group consideration of the problem of light-weight casings, in which the walls are connected directly, without a frame. The boundary conditions for the walls are thus elastically restrained against rotation. This complicates the problem further and requires more sophisticated modelling. Again, the optimisation was repeated to find the optimal number and distribution of sensors and actuators. Generally, in this case, more sensors and actuators are needed, if the same frequency range is concerned. Therefore, including also a much higher coupling in the system, additional challenges exist for designing the algorithms. Therefore, much effort was needed to reduce computational complexity without deteriorating performance and stability of the system. Control structures with the error sensors comprised of accelerometers attached to the casing walls, physical microphones located outside the casing and the virtual microphones were considered again. In the end, the effect was better than expected. Global noise reduction was obtained, reaching up to 15 dB for some frequency bands. It was even higher than for the machine casing with a rigid frame.

The proposed approach is applicable to any machine casings, inherited or additionally surrounding the device, which are made of a thin material with vibration control ability. Many examples exist in industry, but many machines used every day also meet this criterion such as washing machines, coffee makers, refrigerators, and more. We have decided to convince the scientific community, industrial partners and potential users by implementing the system for a real market-available washing machine. At this moment the experiments are being performed in our laboratory, and it is believed that in a few months this particular washing machine will be demonstrated to be much quieter.

In conjunction to developing the active solutions presented above, we have developed an original complete method for shaping frequency response of a vibrating plate for passive and active control applications by simultaneous optimization of the arrangement of additional masses and ribs. With this method, it is possible to move structural resonance peaks or valleys to desired frequencies, concentrate and widen them, enhance controllability and observability measures, etc. In several investigated examples, both academic and motivated by industrial needs, our approach resulted in appropriate solutions. The masses and ribs are thin, and the clue is in their shape and distribution. This method has a high potential for passively reducing noise passing through and improving features of the plate and whole machine casings, if used for noise control. The efficiency has been confirmed by laboratory experiments and measurements performed with a laser vibrometer. This solution is very low cost and, thus, particularly attractive.

It follows from all of the studies summarised in this editorial that appropriate solutions for successful machinery noise control will soon become apparent to users.

Marek Pawelczyk
IJAV Managing Editor

Frequency Capture Characteristics of Gearbox Bidirectional Rotary Vibration System

Ruqiang Mou, Li Hou, Zhijun Sun, Yongqiao Wei and Bo Li

School of Manufacturing Science and Engineering, Sichuan University (610065), Chengdu, China

(Received 25 September 2013; accepted 9 June 2014)

According to the characteristics of the gearbox and Lagrange mechanics, in this paper a bidirectional rotary vibration system dynamics model of the gearbox is established, using MATLAB to simulate the model, study the vibration characteristics of the system in both horizontal and vertical directions, and compare it to existing simplified models. Through the analysis of the model, the conditions of the system that produce frequency trapping are studied, and the frequency factors of the system are obtained. The results indicate that reducing eccentric mass, eccentricity, and rotary damping, and increasing damping movement, bearing stiffness, and input torque can improve system response speed and reduce the amplitude, which can avoid frequency trapping of the system. The study provides a theoretical basis for optimization and installation of the gearbox system.

1. INTRODUCTION

Due to the rapid development of modern industry, gears have become one of the key parts in the modern industry. The gear box has a fixed gear ratio, transmission torque, compact structure, etc., which is now widely used in various machines. But the gearbox forces are complex. Elastic and inertial forces needed to withstand the complex alternating load. The frequency of trapping will happen, allowing the system deformation or vibration, which affects the normal operation of the machine, or even damages it.

Frequency capture is a special nonlinear vibration phenomenon. During this phenomenon, when the external excitation frequency is close to the natural frequency of the system, the external excitation frequency will synchronize with the system's natural frequency, the frequency trapping.[5] It has been established that a class of non- ideal vertical vibration system vibration models, are being used to study the movement and rotary damping effect on the frequency capture, but it did not analyse other parameters on the frequency trapping effects.[1] A reverse rotation dual-drive vibration system model has been created to study the vibration frequency of the system model that achieves trapping conditions.[2] A vertical direction vibration model has been simplified to a general autonomy system, and the frequency of trapping phenomenon has been included, but it is not specific to the analysis of the physical parameters.[3] Research[4] on frequency capture simulation established the elastic support rotor system of the digital prototype model to study the torque and spring stiffness on the frequency of trapping effects. Researchers have studied the wind turbine blade fatigue loading frequency trapping.[5] Other research[6] studied the engineering nonlinear vibration problem, emphasizing the need to effectively take advantage of favourable nonlinear vibration and control of harmful nonlinear vibration.

This selection of a particular model of a gear transmission gearbox as the research object, which is based on the existing research,[7–14] regards the gearbox system as a nonlinear vibration system, takes into account the horizontal and vertical vibration of the gearbox, studies the frequency trapping conditions in the course of gearbox work, analyses the system parameters on frequency capture by a numerical simulation method, and achieves a frequency trapping gearbox digitization and visualization, which provides a theoretical basis for the dynamic optimization of the gearbox system.

2. MATHEMATICAL MODEL OF GEARBOX BIDIRECTIONAL ROTARY VIBRATION SYSTEM

A gearbox is mainly composed of the input shaft, output shaft, driving wheel, driven wheel, the motor (power source), the lid, and the support member. The gearbox is operated by driving the motor under the effect of the input operation, which leads to the driven wheel running. In the gearbox bidirectional rotary vibration system model shown in Fig. 1, m1 and m2, respectively, represent the driving wheel and the driven wheel produced by the eccentricity. When the motor rotates, the eccentric block generates two driven body vibration exciting forces. The vibration body from the horizontal, vertical, and torsional vibration in the direction, taking into account the torsional vibration little effect on the system,[2] thus ignoring the reverse direction vibrations.

In the simplified model, the body motion coordinates x, y, and two eccentric rotations of the rotor phase indicate the

$$\left\{\begin{array}{l} W=\frac{1}{2}M\left(\frac{dx}{dt}\right)^2+\frac{1}{2}M\left(\frac{dy}{dt}\right)^2+\frac{1}{2}J_1\left(\frac{d\theta_1}{dt}\right)^2+\frac{1}{2}J_2\left(\frac{d\theta_2}{dt}\right)^2 \\ +\frac{1}{2}m_1\left(\frac{dx}{dt}-r_1\frac{d\theta_1}{dt}\sin\theta_1\right)^2+\frac{1}{2}m_1\left(\frac{dy}{dt}+r_1\frac{d\theta_1}{dt}\cos\theta_1\right)^2 \\ +\frac{1}{2}m_2\left(\frac{dx}{dt}+r_2\frac{d\theta_2}{dt}\sin\frac{\theta_2}{2}\right)^2+\frac{1}{2}m_2\left(\frac{dy}{dt}+r_2\frac{d\theta_2}{dt}\cos\frac{\theta_2}{2}\right)^2 \\ U=\frac{1}{2}kx^2+\frac{1}{2}ky^2-(T_1\theta_1+T_2\theta_2) \\ D=\frac{1}{2}C\left(\frac{dx}{dt}\right)^2+\frac{1}{2}C\left(\frac{dy}{dt}\right)^2+\frac{1}{2}C_{\theta 1}\left(\frac{d\theta_1}{dt}\right)^2+\frac{1}{2}C_{\theta 2}\left(\frac{d\theta_2}{dt}\right)^2 \end{array}\right\}; \tag{1}$$

$$\left\{\begin{array}{l} W=\frac{1}{2}M\left(\frac{dx}{dt}\right)^2+\frac{1}{2}M\left(\frac{dy}{dt}\right)^2+\frac{3}{2}J_1\left(\frac{d\theta_1}{dt}\right)^2+ \\ \frac{1}{2}m_1\left(\frac{dx}{dt}-r_1\frac{d\theta_1}{dt}\sin\theta_1\right)^2+\frac{1}{2}m_1\left(\frac{dy}{dt}+r_1\frac{d\theta_1}{dt}\cos\theta_1\right)^2+ \\ 2m_1\left(\frac{dx}{dt}+r_1\frac{d\theta_1}{dt}\sin\frac{\theta_1}{2}\right)^2+2m_1\left(\frac{dy}{dt}+r_1\frac{d\theta_1}{dt}\cos\frac{\theta_1}{2}\right)^2 \\ U=\frac{1}{2}kx^2+\frac{1}{2}ky^2-2T_1\theta_1 \\ D=\frac{1}{2}C\left(\frac{dx}{dt}\right)^2+\frac{1}{2}C\left(\frac{dy}{dt}\right)^2+\frac{3}{4}C_{\theta 1}\left(\frac{d\theta_1}{dt}\right)^2 \end{array}\right\}; \tag{2}$$

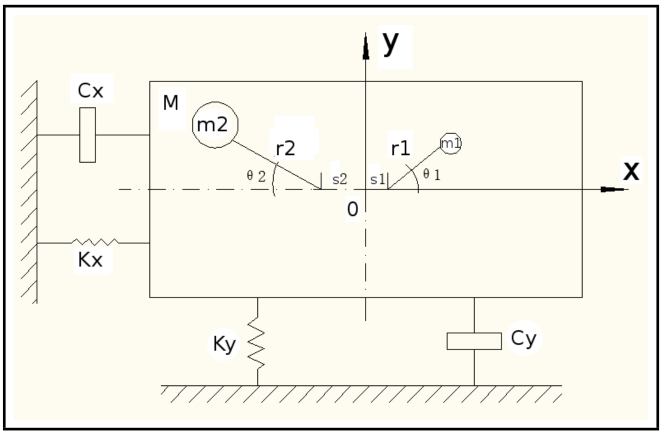

Figure 1. Integrated vibration model of the gearbox system.

generalized coordinates. According to the principle Lagrange equations of motion used to obtain the mathematical model, this is expressed as:

The system is a gear train. Using the system transmission ratio $i=2$, according to the transmission principle, the following relation can be deduced: $r_2=2r_1$; $\theta_2=2\theta_1$; $C_{\theta 2}=2C_{theta1}$; $m_2=4m_1$; $T_2=2T_1$; $J_2=8J_1$.

Taking the above relationship into Eq. (1), the Eq. (2) is obtained, where: W is the vibration system kinetic energy; U is the system potential energy; D is the energy dissipation function; x, y, θ_1, θ_2 are the vibration substrate horizontal displacement and the vertical displacement; eccentricity blocks 1 and 2 of the rotation angle; M, m_1, m_2, r_1, J_1, J_2 represent the vibration of the substrate mass, the drive gear, and driven gear eccentric mass, inertia quantitative and qualitative heart eccentricity; k, C, C_1, C_2 are the supporting stiffness coefficients, damping, and two rotary movement damping; and T is the input torque of the motor. By the Lagrange equation

$$\frac{\mathrm{d}}{\mathrm{d}t}\left(\frac{\partial W}{\partial \dot{q}_i}\right)-\frac{\partial W}{\partial q_i}+\frac{\partial U}{\partial q_i}+\frac{\partial D}{\partial \dot{q}_i}=Q_i\left(t\right); \tag{3}$$

the differential equations (4) and (5) can be obtained (see the top of the next page), where $m=m_1$; $r=r_1$; $J=J_1$; $\theta=\theta_1$; $T=T_1$; $C_1=C_{\theta 1}$.

3. RESPONSE CHARACTERISTICS OF THE VIBRATION SYSTEM FREQUENCY TRAPPING

According to the analysis, the following initial conditions were obtained: $r=4m$, $M=60000$ kg, $m=800$ kg, $k=2600$ N/m, $J=28000$ kgm^2, $c=62000$ Ns/m, $c_1=901.8$ Ns/m, $T=1406.46$ Nm.

Taking these conditions into Eq. (3), the numerical simulation software MATLAB was used to analyse the system, obtain the system horizontal and vertical displacement, and velocity and displacement response spectrum shown in Fig. 2.

As can be seen in Figs. 2(b)–(e), the horizontal and vertical directions of the vibration characteristics are similar, and the amplitude is approximately 5 mm. The difference lies in the amplitude of the horizontal symmetry about the x axis and the vertical symmetry slightly to the negative direction of the y-axis. According to the analysis, the two eccentric masses, eccentricity, rotating speed, and the direction of rotation are different. When the two eccentric masses rotate, the two eccentric blocks moves the system in the horizontal direction,

$$\left\{\begin{array}{l} (M+5m)\,\ddot{x}+kx+c\,\dot{x}=mr\left(\begin{array}{l}\dfrac{d^2\theta}{dt^2}\sin\theta+\left(\dfrac{d\theta}{dt}\right)^2\cos\theta\\ -4\dfrac{d^2\theta}{dt^2}\sin\dfrac{\theta}{2}-2\left(\dfrac{d\theta}{dt}\right)^2 cos\dfrac{\theta}{2}\end{array}\right)\\ (M+5m)\,\ddot{x}+kx+c\,\dot{x}=mr\left(\begin{array}{l}\dfrac{d^2\theta}{dt^2}\sin\theta+\left(\dfrac{d\theta}{dt}\right)^2\cos\theta\\ -4\dfrac{d^2\theta}{dt^2}\sin\dfrac{\theta}{2}-2\left(\dfrac{d\theta}{dt}\right)^2 cos\dfrac{\theta}{2}\end{array}\right)\\ \left\{\begin{array}{l}\left(3J+5mr^2\right)\dfrac{d^2\theta}{dt^2}-mr\,\ddot{x}\sin\theta+mr\,\ddot{y}\cos\theta+\\ 4mr(\ddot{x}\sin\dfrac{\theta}{2}+\ddot{y}\cos\dfrac{\theta}{2})+\dfrac{3}{2}c_1\dfrac{d\theta}{dt}\end{array}\right\}=2T \end{array}\right\}; \tag{4}$$

$$\left\{\begin{array}{l} (M+5m)\,\ddot{y}+ky+c\,\dot{y}=mr\left(\begin{array}{l}\left(\dfrac{d\theta}{dt}\right)^2 sin\theta-\dfrac{d^2\theta}{dt^2}cos\theta+\\ 2\left(\dfrac{d\theta}{dt}\right)^2 sin\dfrac{\theta}{2}-4\dfrac{d^2\theta}{dt^2}cos\dfrac{\theta}{2}\end{array}\right)\\ \left(\begin{array}{l}(3J+5mr^2)\dfrac{d^2\theta}{dt^2}+mr\,\ddot{y}\cos\theta+\\ 4mr\,\ddot{y}\,cos\dfrac{\theta}{2}+\dfrac{3}{2}C_1\dfrac{d\theta}{dt}\end{array}\right)=2T \end{array}\right\}; \tag{5}$$

respectively. One by one by shear displacement, horizontal displacement occurs on the final x-axis symmetry. However, when the two eccentric masses rotate in two eccentric vertical directions, respectively, the system increases with the displacement and with reduction; but due to the presence of two eccentric phases, this causes the vertical displacement not to remain symmetric about the x-axis, and moves the symmetry slightly in the negative direction on the y-axis.

From Figs. 2(c)–(e), it can be seen that the system vibration frequency is 0.122 Hz, which was captured by the system with the natural frequency 0.12 Hz. From Figs. 2(a)–(d) it can be seen that the input shaft speed is about 1.52 rad/s less than the rated speed, which indicates that, under the given parameters, the mechanical system will affect the rotation of the input shaft.

If only the vertical vibration is considered, then (3) can be simplified as in Eq. (5).[3]

The initial conditions remain constant, and by using MaATLAB's numerical simulation, the system vertical displacement, velocity, and displacement response spectrum were obtained, as shown in Fig. 3.

From Fig. 3 and 4, we can find that the system vertical vibration characteristics are similar in both the integrated model and the simplified model, and the frequency trapping phenomena have occurred, resulting in the input shaft speed being less than the rated speed, affecting the normal operation of the whole system. But the former model takes into account the horizontal and vertical vibrations in both directions, which is more in line with the actual working conditions.

If the parameters are taken as $M = 60000$ kg, $m = 800$ kg, $r = 4$ m, $J = 28000$ kgm^2, $k = 2600$ N/m, $c = 62000$ Ns/m, $c_1 = 901800$ Ns/m, $T = 1406460$ Nm, the vibration characteristic curve before the system is simplified can be obtained, as shown in Fig. 4, and the simplified system vibration characteristic curve can be obtained, as shown in Fig. 5.

Comparing Figs. 4 and 5, it can be seen that the frequencies of the systems are not trapping, and the input shaft has a stable speed in 2.21 rad/s, which has reached the rated speed. In the non-occurrence frequency capture, through the two model system response and frequency spectrum comparison, it was found that the former is more responsive than the latter. The former taking 20 s to stabilize the vertical vibration, while the latter requires 100 s to become stable. The former amplitude of the horizontal and vertical direction is not more than 15 mm, and the latter peak vibration is large, close to 30 mm, which can seriously devastate the supporting member. Thus, increasing the horizontal spring damping device helps to quickly reduce vibration.

4. EFFECT OF SYSTEM PARAMETERS ON THE VIBRATION SYSTEM FREQUENCY CAPTURE

From Eq. (3), it can be seen the system parameters such as eccentric mass, eccentricity, input torque, bearing stiffness, damping, and rotary movement damping will affect the vibrations of the gear box system. Therefore, it is important to anal-

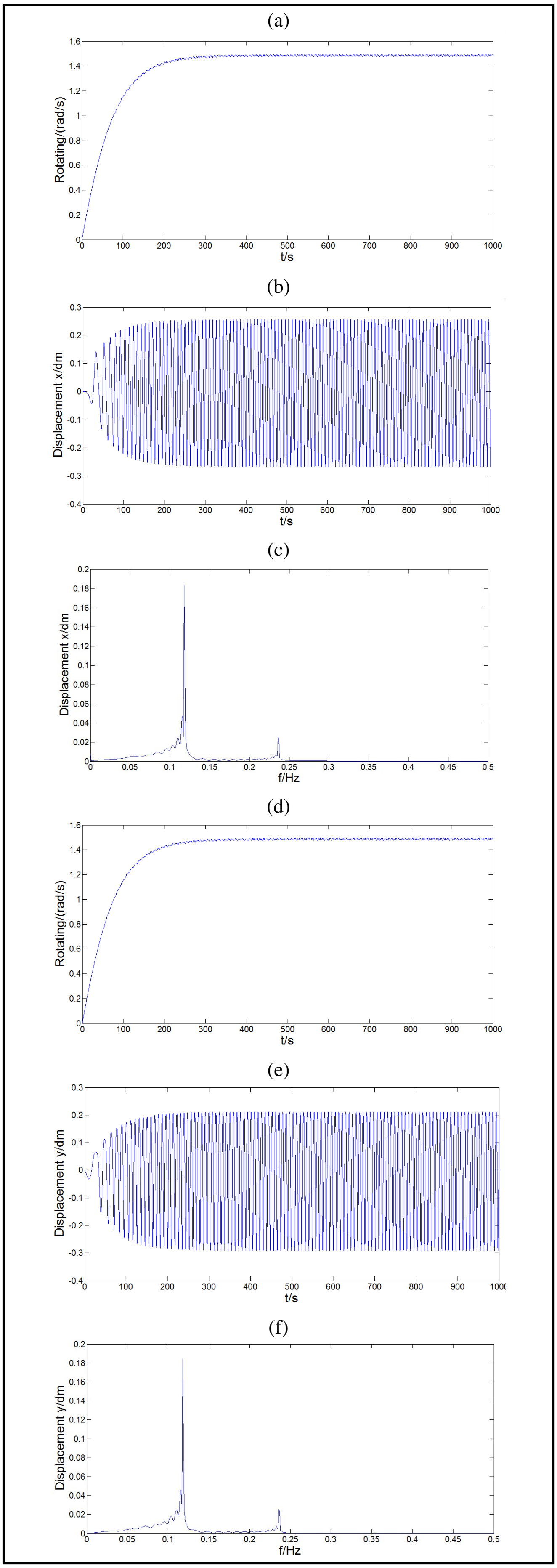

Figure 2. System horizontal and vertical displacement, velocity, and displacement response spectrum.

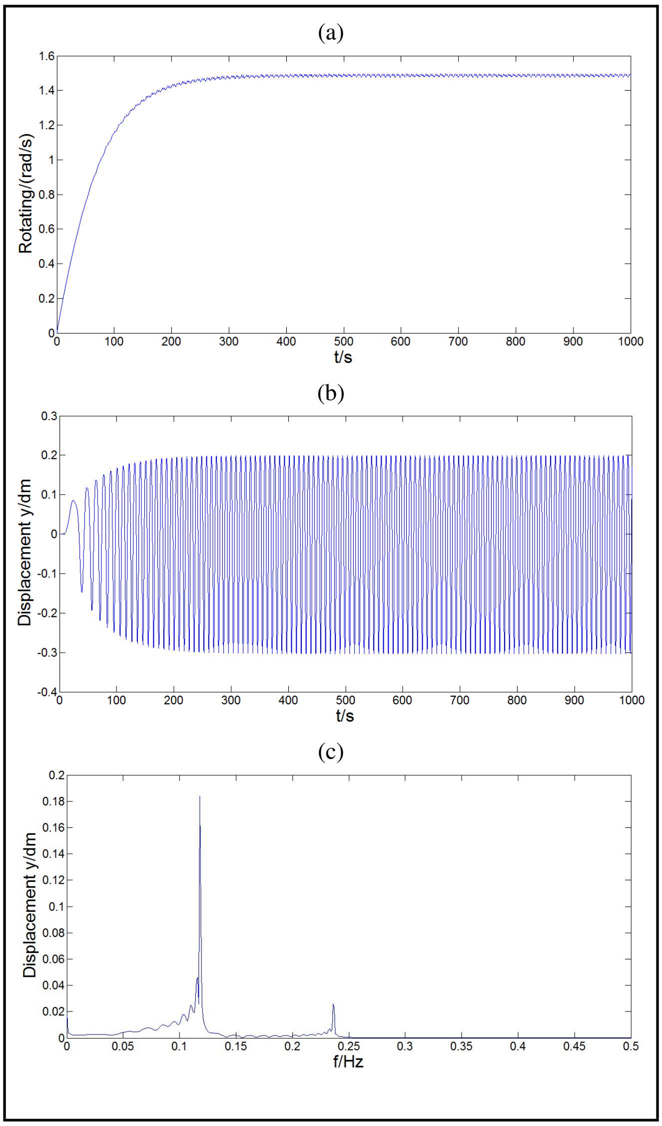

Figure 3. System vertical displacement, velocity, and displacement response spectrum.

yse the system parameters, which obtain the effect of the system parameters on the system trapping phenomenon.

The initial parameters are $M = 60000$ kg, $m = 800$ kg, $r = 4$ m, $J = 28000$ kgm^2, $k = 2600$ N/m, $c = 62000$ Ns/m, $c_1 = 901.8$ Ns/m, $T = 1406.46$ Nm.

Using the numerical simulation software MATLAB for Eq. (4), the system steady speed of the input shaft effect curve was obtained. In the case of the other parameters' constants, the eccentric mass effect on the input rotation speed is shown in Fig. 6.

Figure 6 shows the influence curve of the eccentric mass on the input speed, from which it can be seen that, as the eccentric mass m increases, the system response slows, and the stable speed of the input shaft decreases, the frequency of trapping system, meaning the system cannot reach the rated speed. While the vibration characteristics of the system diagram analysis found that the eccentric mass system will inevitably lead to an increase in amplitude, and that eccentric mass has a greater impact on the vibration system, it should be noted that during

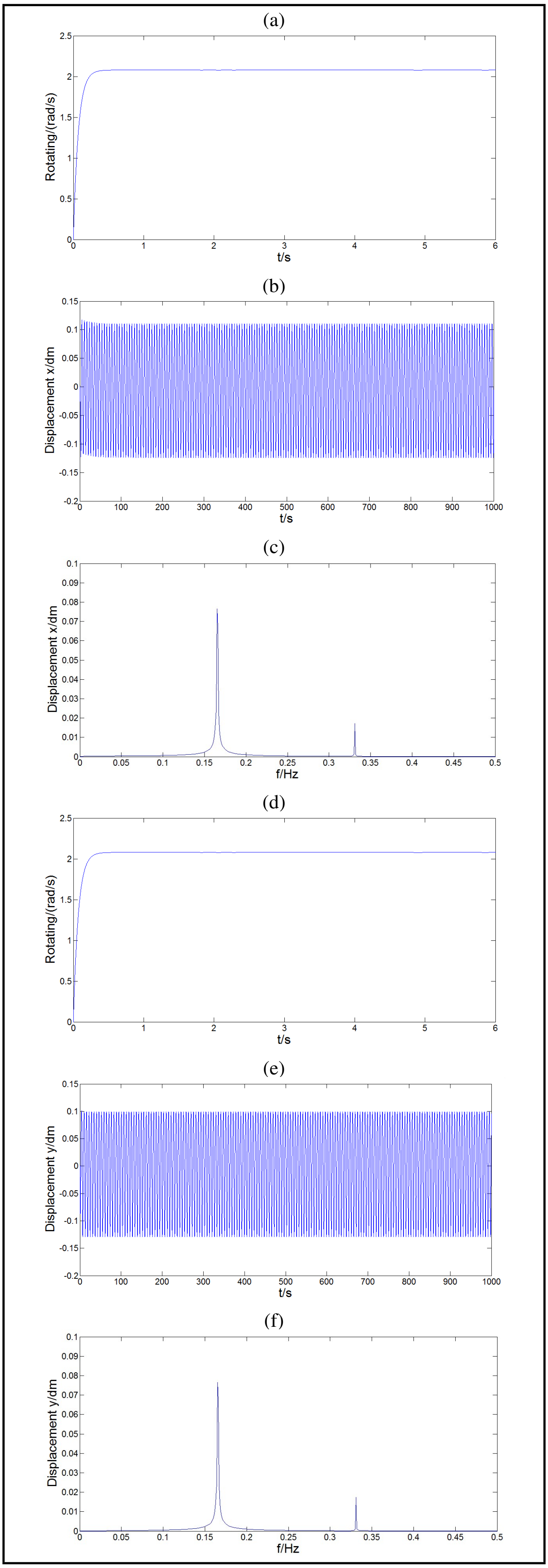

Figure 4. Simplified former system vibration characteristics curve.

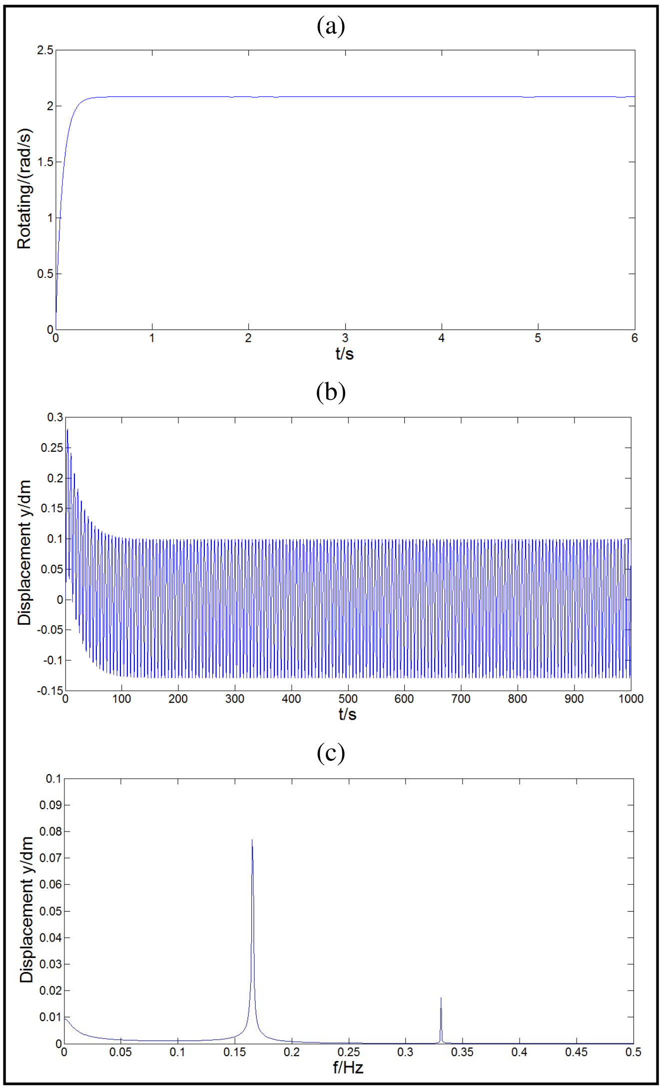

Figure 5. Simplified system vibration characteristic curve.

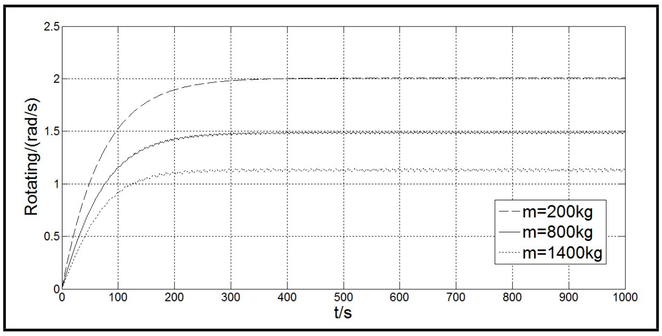

Figure 6. Eccentric mass effect on the input speed.

the design of the gearbox system, the eccentric mass must be strictly controlled.

Figure 7 show the movement damping effect on the input rotational speed curve, from which it can be seen that, as the mobile damping increases, the input shaft speed first decreases and then increases, so moving the damping can effectively avoid the natural frequency, which helps to avoid the trapping frequency. Depending on the system material properties, a generally larger movement damping factor, such as

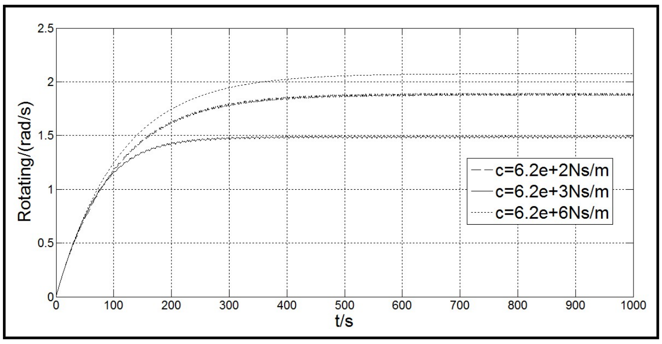

Figure 7. Mobile damping effect on the input speed.

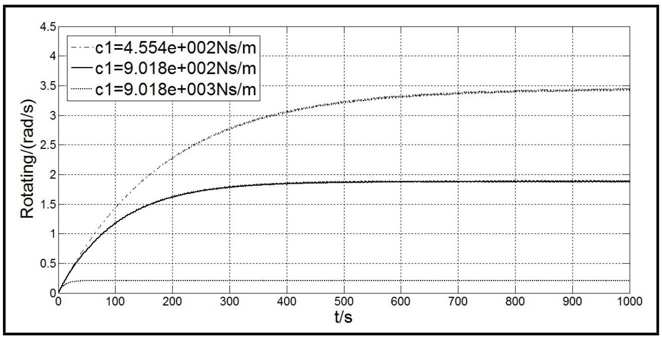

Figure 8. Rotary damping effect on the input speed.

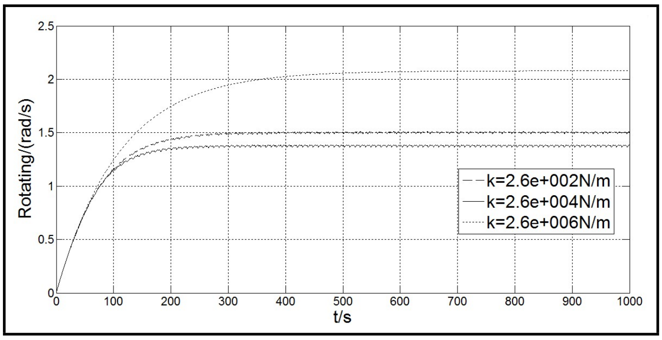

Figure 9. Bearing stiffness effect on the input speed.

$c = 6.5 \times 10^6$, can effectively reduce the amplitude,and avoid the frequency trapping conditions of the system, to ensure that the system works normally.

Figure 8 shows a rotary damping effect on the input rotational speed curve. From Fig. 8 it can be seen that, as the rotation damping increases, and the smaller the amplitude of the system, the input shaft speed decreases, resulting in the input shaft speed being less than the rated speed. Therefore, in order to avoid the system experiencing frequency trapping, ensure the amplitude of the system in the allowable range, and reduce the rotational damping as far as possible.

Figure 9 shows the bearing stiffness on the impact of input speed curve. As the bearing stiffness increases, the system response speed and input shaft speed first decreases, and then increases. When the stiffness is very low, the frequency of the system is easy to capture. When the stiffness is high, the natural frequency of the system has no influence on the frequency trapping. Therefore, in the design of the gearbox system, it

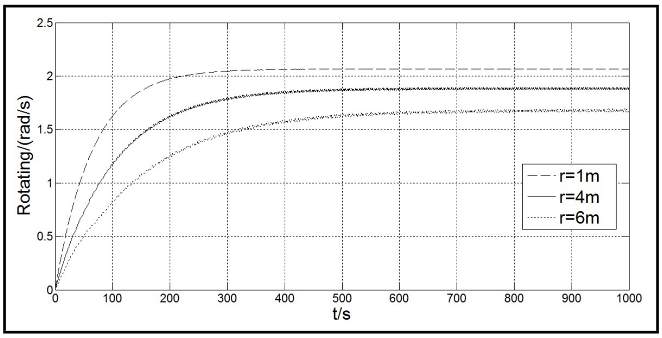

Figure 10. Eccentricity effect on the input speed.

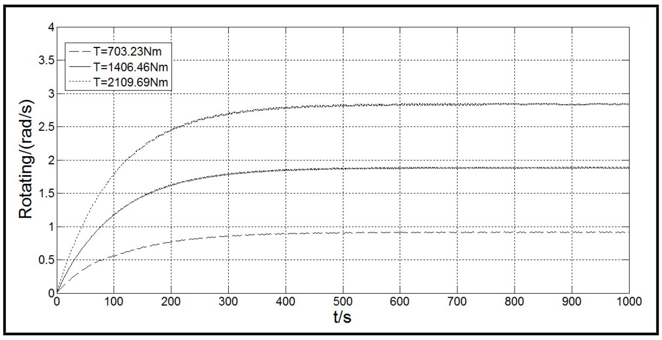

Figure 11. Input torque effect on the input speed.

is best to choose a larger bearing stiffness that can effectively avoid the system frequency trapping.

Figure 10 shows the eccentricity of the input rotational speed curve. It can be seen from the figure that as the eccentricity increases, the system response slows, the input shaft speed decreases, and the system experience frequency trapping, eventually causing the input shaft speed to be less than the rated speed. When the eccentricity is less than 1 m, the input shaft can reach the rated speed, and the system does not experience frequency capturing.

Figure 11 shows the input torque effect on the input speed curve, from which it can be seen that as the input torque increases, the system response speed becomes faster, the input shaft speed increases, the system does not experience frequency trapping, and the system can quickly reach the rated speed. Therefore, improving the system's input torque can effectively avoid the occurrence of frequency capturing.

5. CONCLUSION

According to the characteristics of the gearbox, a horizontally- and vertically- integrated dual rotary vibration model of the gearbox system was established, and the model frequency trapping was analysed. The simplified model exists only in the vertical direction vibration. By comparison, the integrated model is more realistic. In addition, this paper, using numerical simulation, analysed the system parameters' (such as the eccentric mass, eccentricity, input torque, bearing stiffness, damping, and rotary movement damping) effects on the system frequency capture. In summation, this study accomplishes and discusses the following:

1. According to the characteristics of the gearbox, establishes an integrated vibration model and recreates the system frequency trapping by numerical simulation.

2. When the system does not capture frequency compared with the simplified model, the integrated model has small amplitude and fast response speed; once the system frequency trapping is measured, the integrated vibration model can reflect the characteristics of both horizontal and vertical vibrations in both directions, which can more accurately describe the vibration characteristics of the system.

3. System parameters analysis showed that, for the integrated vibration model, reducing eccentric mass, eccentricity, and rotary damping, and increasing damping movement, bearing stiffness, and input torque can improve the response speed of the system. Also reducing the amplitude and preventing system frequency trapping, and reducing the vibration impact on the system, help the system to quickly reach the rated speed, which helps to ensure the normal operation of the system.

REFERENCES

[1] Xiong, W., Lu, M., and Wen, B. Characteristics of rotating frequency catching of non- ideal vibration systems, *J. Hunan U.: Nat. Sci.*, **30** (3), 44–48, (2003).

[2] Wang, D.-G., Zhao, C.-Y., Ren, Z.-H., and Wen, B.-C. Frequency-based capture control on revertible dual-motor-driven vibration system, *Chinese J. Constr. Mach.*, **6** (3), 282–286, (2008).

[3] Zhang, Nan, *et al.* Characteristics of frequency capture of nonlinear vibration systems, *J. Dongbei U.: Nat. Sci.*, **30** (8), 1170–1173, (2009).

[4] Han, Qingkai, *et al.* Frequency capture simulation and experiment of a rotor system with elastic supports, *J. Vib. Shock*, **27** (8), 63–66, (2008).

[5] Zhang, L. and Wu, J. Frequency capture characteristics in wind blade fatigue loading process, *J. Sichuan U.: Eng. Sci. Ed.*, **43** (6), 248–252, (2011).

[6] Wen, Bangchun, *et al. Engineering nonlinear vibration*, Science Press, Beijing, 2008.

[7] Qingkai, H., Wang, L., Yao, H., and Wen, B. Simulation and experiment analyses on resonance for a rotor system with elastic supports, *Proc. IDETC/CIE 2007*, Las Vegas, Nevada, USA, (2007). http://dx.doi.org/10.1115/detc2007-34420

[8] Zhu, Caichao, *et al.* Research of nonlinear dynamic characteristics of wind power gear box system, *J. Mech. Eng.*, **41** (8), 203–206, (2005).

[9] Xiong, Wanli, *et al.* Mechanism of electromechanical-coupling on self-synchronous vibration and vibratory synchronization transmission, *J. Vib. Eng.*, **13** (3), 325–331, (2000).

[10] Chunyu, Z., Degang, W., Hao, Z., Jie, L., and Bangchun, W. Frequency capture of vibration system with two-motor drives rotating in same direction, *Chinese J. Appl. Mech.*, **26** (2), 283–287, (2009).

[11] Liu, Z., Zhou, X., Ye, H., Xiang, W., and Yang, S. Design and realization of system software for vibration sources signal separation of gearbox, *Mach. Tool Hydr.*, **36** (5), 198–201, (2008).

[12] Liu, J., Yang, J., Yang, M., Zeng, J., and Yang, J. Vibration signal acquisition and analysis system of wind turbine gearbox based on MATLAB and VC, *Guangdong Elec. Power*, **26** (6), 70–74, (2013).

[13] Shen, Guoji, *et al.* The estimates of gearbox vibration signal phase based on Wigner distribution, *Chinese J. Mech. Eng.*, **40** (9), 186–188, (2004).

[14] Li, Hao, *et al.* The noise reduction of gearbox vibration signal processing based on Wavelet transform, *Mach. Des. Manu.*, **3**, 82–83, (2013).

Acceleration Sensor-based First Resonance Vibration Suppression of a Double-clamped Piezoelectric Beam

Zhi-cheng Qiu

School of Mechanical and Automotive Engineering, South China University of Technology, Guangzhou 510641, PR China

State Key Laboratory of Robotics, Shenyang Institute of Automation, Chinese Academy of Sciences, Shenyang 110016, PR China

Fan-kong Meng

School of Mechanical and Automotive Engineering, South China University of Technology, Guangzhou 510641, PR China

Jian-da Han and Jin-guo Liu

State Key Laboratory of Robotics, Shenyang Institute of Automation, Chinese Academy of Sciences, Shenyang 110016, PR China

(Received 13 November 2013; accepted 12 March 2014)

This paper investigates resonance vibration suppression under persistent excitation near the first structural resonant frequency of a clamped-clamped (doubly-clamped) piezoelectric flexible beam. In this study, an acceleration sensor is used to measure the resonant vibration. Firstly, the finite element method (FEM) is utilized to derive the dynamics model of the system, and modal analysis is carried out. Secondly, an acceleration feedback-based proportional-integral control algorithm and variable structure control algorithms are designed, and a numerical simulation is performed. Finally, a doubly-clamped piezoelectric flexible beam experimental setup is constructed. Experiments are conducted on resonant vibration suppression using the designed control algorithms. The numerical simulation and experimental results demonstrate that the resonant vibration can be suppressed by using the designed control methods, and the improved variable structure control method shows better control performance in suppressing the resonant vibration.

1. INTRODUCTION

Flexible beam structures are characterized by light weight, low structural damping, and low modal frequencies, and they are one of the main structure types used in the engineering field and aerospace structures.[1] Vibrations are easily caused when flexible beams are subjected to heavy loads or affected by a variety of unexpected external factors in the course of their work. Furthermore, these vibrations will last for a long time. If the vibrations are not suppressed effectively, the prolonged vibrations will reduce the working accuracy and working life of large and complex structures, such as space crafts and space robot manipulators. Moreover, if the structure is excited at its resonance frequencies, it will be seriously damaged.[2] Therefore, active vibration control of flexible structures is an important concern.

During the past few decades, a considerable amount of study in the area of active vibration control of flexible structures has been conducted by many researchers. In their investigations, piezoelectric materials (such as PZT, PVDF) are widely used in active vibration control for flexible structures. They provide inexpensive, reliable, and non-intrusive means of actuating and sensing vibrations in flexible structures.[4] Wang, et al.,[5] conducted a study on the vibration control of smart piezoelectric composite plates; they investigated the effect of the stretching-bending coupling of the piezoelectric sensor and actuator pairs on the system stability of smart composite plates. The classical negative velocity feedback control method was adopted for the active vibration control analysis of smart composite plates with bonded distributed piezoelectric sensors and actuators in their study. Sabatini, et al.,[6] studied active damping strategies and relevant devices that could be used to reduce the structural vibrations of a space manipulator with flexible links during its in orbit operations. They proposed an optimized adaptive vibration control via piezoelectric devices. Carlos, et al.,[7] conducted an experimental study into the control of a cantilever beam, which had a PZT patch bonded to it as an actuator and a collocated PVDF patch which was used as the sensor. Their experimental results demonstrated the effectiveness of the active vibration control method. Direct output feedback-based active vibration control has been implemented on a smart cantilever beam at its resonant frequency using PZT sensors and actuators by Parameswaran, et al.,[8] They compared the performance of the conventional PC-based control and a dedicated real-time control at resonance, and their experimental results demonstrated that the implementation of real-time control provides a much more controlled response of the system with an excellent transient response, as well as a highly reliable steady state response.

What's more, the acceleration sensor-based control strategy is an effective control method used in vibration suppression.[9–11] Its best feature is that acceleration is used as the feedback signal, which can be directly measured by accelerometers. In addition, acceleration is easier to measure than strain, displacement, or velocity.[9,12] Considerable works have been done using the acceleration sensor-based feedback control strategy, showing that acceleration feedback control is effective and robust in vibration measurement and active control.[12–17]

Mahmoodi, et al.,[9] used an active vibration control method called modified acceleration feedback for vibration control of plate structures as an extension of modified positive position feedback. PZT patches were utilized to suppress the vibration of the plate, and the method was successfully verified on a test plate in the laboratory. Preumont, et al.,[12] proposed a local control scheme using acceleration feedback and a collocated proof-mass actuator for active damping of beam-like structures. They conducted experimental investigations of vibration suppression under resonant excitations. Gatti, et al.,[13] conducted a theoretical and experimental study of the active vibration control of a simply supported beam using a piezoelectric patch actuator and a physically collocated accelerometer. Shin, et al.,[14] proposed an active vibration control method of clamped-clamped beams using acceleration feedback controllers with a non-collocated sensor and a moment pair actuator configuration. Qiu, et al.,[15,16] presented an acceleration sensor-based active vibration control for a cantilever beam and a cantilever plate with bonded piezoelectric patches. The phenomenon of phase hysteresis and time delay were considered in their work. The PD control method, a nonlinear control method and acceleration signal-based sliding mode control algorithm were utilized to suppress vibration. Chatterjee[17] presented a theoretical basis of time-delayed acceleration feedback control of linear and nonlinear vibrations of mechanical oscillators.

In this paper, active vibration control of a doubly-clamped flexible beam with bonded discrete PZT actuators and mounted accelerometer is investigated. The FEM method is utilized to model the system, and the acceleration feedback-based proportional-integral controller and the acceleration feedback-based variable structure controller are designed. Both theoretical and experimental studies were undertaken to verify the presented methods.

The original contributions of this paper are detailed as follows: (a) The model of a piezoelectric clamped-clamped beam with an accelerometer is obtained by FEM. The FEM model is used for simulations of acceleration feedback control algorithms. (b) Acceleration sensor-based proportional and integral control and variable structure control are designed. (c) Simulations and experiments are conducted to validate the effectiveness of the designed controllers in suppressing the resonant vibration of the clamped-clamped beam under persistent excitation.

This article is organized as follows: In Section 2, the dynamic model of a doubly-clamped piezoelectric beam bonded with piezoelectric actuators and an accelerometer is derived by using the finite element method. In Section 3, the acceleration feedback-based proportional-integral control algorithm and the acceleration feedback based variable structure control method are proposed, and a numerical simulation is carried out. In Section 4, a doubly-clamped piezoelectric flexible beam experimental system is constructed. Experiments are conducted by using the proposed control algorithms. Finally, the conclusion is drawn in Section 5.

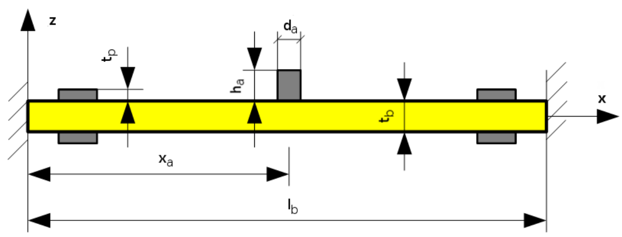

(a) The $x-z$ plane

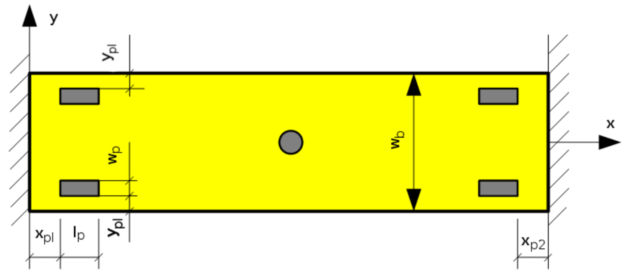

(b) The $x-y$ plane

Figure 1. Schematic diagram of a doubly-clamped piezoelectric flexible beam.

2. SYSTEM MODELLING

In this section, a mathematical model is derived for a doubly-clamped piezoelectric beam structure equipped with an acceleration sensor and PZT actuators. The finite element method is used to build the dynamics model. The four-node rectangle plate element is utilized. The state-space representation form of the dynamics model is obtained, including acceleration sensing and piezoelectric driving. Modal analyses are performed.

2.1. The Doubly-clamped Piezoelectric Flexible Beam

The doubly-clamped piezoelectric flexible beam is schematically depicted in Fig. 1. The flexible beam is bonded with PZT patches and an accelerometer. Eight PZT patches are bonded on both surfaces of the flexible beam. The patches are divided into two groups, and are used as the excited actuator and control actuator. Each group is composed of four piezoelectric patches, symmetrically bonded on both surfaces close to both clamped sides. Either group can be used as a one-channel actuator by parallel connection. The left group is used as the actuator to excite the vibration of the beam, and the right group is used to suppress the vibration of the beam.

As shown in Fig. 1, the accelerometer is located in the intermediate position of the flexible beam, used to detect the vibration of the beam. The length, width, and thickness of the flexible beam structure are $l_b = 600$ mm, $w_b = 120$ mm, and $t_b = 2$ mm, respectively. Those of the PZT patches are $l_p = 50$ mm, $w_p = 15$ mm, and $t_p = 1$ mm, respectively. The diameter and height of the accelerometer are $d_a = 18$ mm and $h_a = 22$ mm, respectively. The location of the piezoelec-

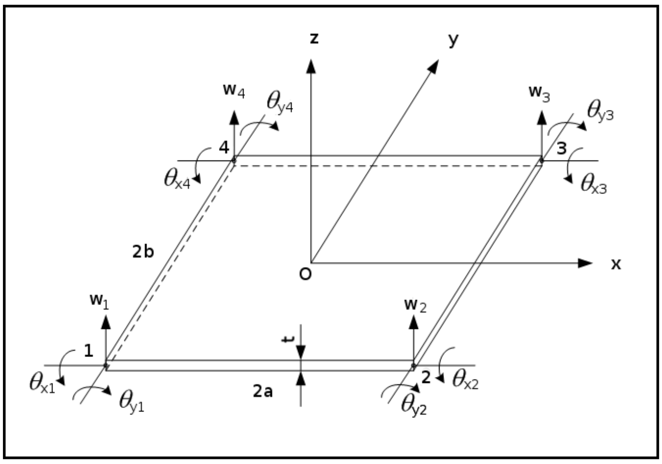

Figure 2. Four-node rectangle plate element.

tric actuators and the accelerometer are shown in Fig. 1, where $x_{p1} = x_{p2} = 50$ mm, $y_{p1} = y_{p2} = 15$ mm, and $x_a = 300$ mm.

2.2. The Element Dynamics Equation

The beam is discretized by using the four-node rectangle plate element, as shown in Fig. 2. There are three degrees of freedom at each node of the four-node rectangle plate element, described as w, θ_x, and θ_y, respectively. The element nodal displacement vector can be expressed as

$$\mathbf{d}^e = \begin{matrix} [w_1 & \theta_{x1} & \theta_{y1} & w_2 & \theta_{x2} & \theta_{y2} \\ w_3 & \theta_{x3} & \theta_{y3} & w_4 & \theta_{x4} & \theta_{y4}]^T. \end{matrix} \tag{1}$$

The transverse displacement of any point in the element can be expressed as[18]

$$w(x, y) = \mathbf{N}\mathbf{d}^e; \tag{2}$$

where $\mathbf{N} \in \mathbf{R}^{1\times 12}$ is the displacement shape function.

The element strain matrix can be expressed using the element nodal displacement vector[18,19]

$$\boldsymbol{\epsilon} = z\mathbf{B}\mathbf{d}^e; \tag{3}$$

where $\mathbf{B}$ is a matrix representing the relationship between the element strain matrix and element nodal displacement vector, and z is the variable in the thickness direction.

The dynamics equation of the four-node rectangle plate element can be written as[20]

$$\mathbf{m}_b^e\ddot{\mathbf{d}}^e + \mathbf{k}_b^e\mathbf{d}^e = \mathbf{f}_{ext}^e; \tag{4}$$

where $\mathbf{m}_b^e$ is the element mass matrix, $\mathbf{k}_b^e$ is the element stiffness matrix, $\ddot{\mathbf{d}}^e$ is the element nodal acceleration vector, $\mathbf{d}^e$ is the element nodal displacement vector, and $\mathbf{f}_{ext}^e$ is the element external force vector.

In Eq. (4), $\mathbf{m}_b^e = \int\limits_{V_b} \rho_b\mathbf{N}^T\mathbf{N}dV$, $\mathbf{k}_b^e = \int\limits_{V_b} z^2\mathbf{B}^T\mathbf{D}_b\mathbf{B}dV$, in which ρ_b represents the material densities of the flexible beam, V_b is the element volumes of the rectangle plate element, $\mathbf{D}_b$ is the elastic modulus matrix of the rectangle plate element, z represents the variable in the thickness direction, and its range is $[-t_b/2 \;\; t_b/2]$.

In this investigation, the piezoelectric element is regarded as an ordinary rectangle plate element, so the piezoelectric element mass matrix $\mathbf{m}_p^e = \int\limits_{V_p} \rho_p\mathbf{N}^T\mathbf{N}dV$, and the piezoelectric element stiffness matrix is $\mathbf{k}_p^e = \int\limits_{V_p} z^2\mathbf{B}^T\mathbf{D}_p\mathbf{B}dV$, in which ρ_p denotes the densities of the piezoelectric material, V_p is the element volumes of the piezoelectric element, $\mathbf{D}_p$ is the elastic modulus matrix of the piezoelectric material, z represent the variable in the thickness direction, and its range is $[-t_p/2 \;\; t_p/2]$.

As shown in Fig. 1, PZT patches are used as actuators to excite or suppress the vibration of the doubly-clamped piezoelectric beam. When a PZT patch is applied to a voltage only in the thickness direction, the stress matrix is[21]

$$\boldsymbol{\sigma} = -\mathbf{e}^T E_z; \tag{5}$$

where $\boldsymbol{\sigma}$ represents the stress matrix in the piezoelectric actuator caused by the electric field, $\mathbf{e}$ is the piezoelectric stress constant vector, and E_z is the strength of the electric field within the piezoelectric actuator.

When the input voltage of the piezoelectric actuator is V_a, the strength of the electric field within the piezoelectric actuator is[22]

$$E_z = \frac{V_a}{t_a}; \tag{6}$$

where t_a is the thickness of the piezoelectric actuator.

Substituting Eq. (6) into Eq. (5), the stress matrix in the piezoelectric actuator is obtained as

$$\boldsymbol{\sigma} = -\mathbf{e}^T\frac{V_a}{t_a}. \tag{7}$$

The driving force of PZT actuators demands that the stress within the piezoelectric element is uniformly distributed along the thickness direction of the piezoelectric patches. The torque generated by the stress is

$$\mathbf{M}_a = \int\limits_{t_b/2}^{t_a+t_b/2} \sigma z dz = -\int\limits_{t_b/2}^{t_a+t_b/2} \mathbf{e}^T E_z dz = \overline{z}_a\mathbf{e}^T V_a; \tag{8}$$

where $\mathbf{M}_a$ is the torque caused by the PZT actuator, and $\overline{z}_a = (t_b+t_a)/2$ denotes the distance the centreline of the PZT patch to the centreline of the beam.

When a voltage is applied, the work done by the PZT actuator is

$$\begin{aligned} \mathbf{F}_a^e\mathbf{d}^e &= \int\int \begin{bmatrix}\theta_x & \theta_y & \theta_{xy}\end{bmatrix} \mathbf{M}_a dxdy \\ &= \int\limits_{S_a} \mathbf{B}^T\overline{z}_a\mathbf{e}^T V_a\mathbf{d}^e dS = \mathbf{f}_{ctrl}^e \cdot V_a\mathbf{d}^e; \end{aligned} \tag{9}$$

where $\mathbf{F}_a^e$ is the equivalent nodal load generated by the PZT actuator, $\mathbf{f}_{ctrl}^e$ is the piezoelectric element driving force coefficient vector, θ_{xy} is the torsional angle corresponding to both the x- and y- axes, and $\mathbf{f}_{ctrl}^e = \int\int \mathbf{B}^T\overline{z}_a\mathbf{e}^T dxdy$.

2.3. State-space Form of the System Model

The element meshing and numbering of nodes and elements for the doubly-clamped beam is shown in Fig. 3. The number in parentheses indicates the element number, and the numbers near the element node indicate the node numbers. There are 24 elements along the length direction and 8 elements along

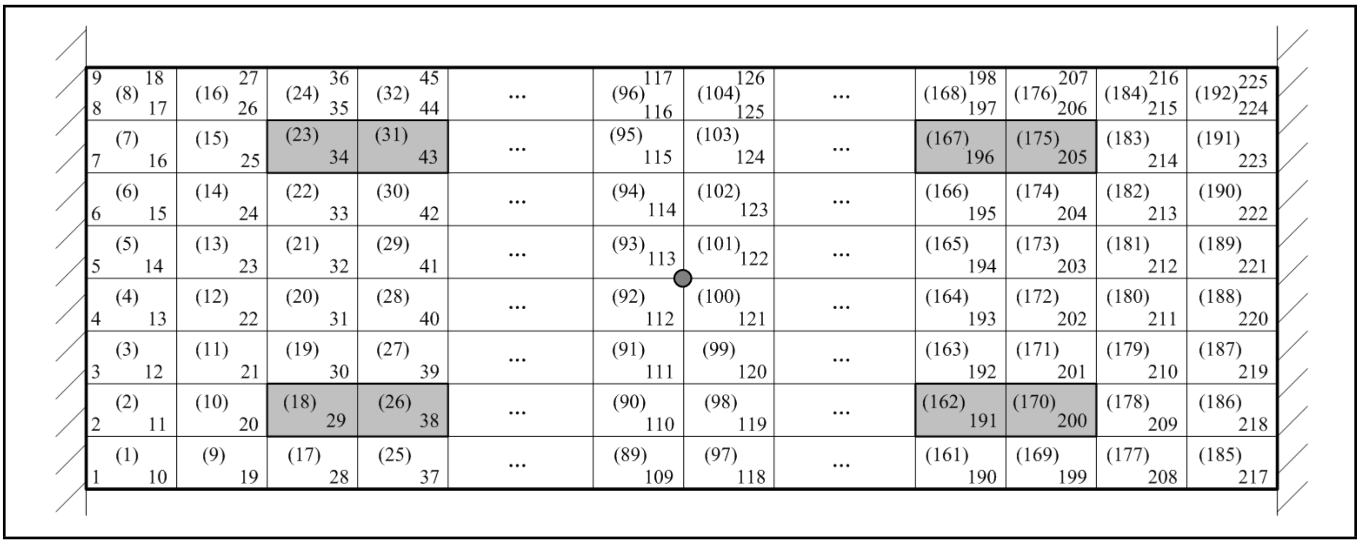

Figure 3. Meshing and numbering of the elements and nodes for the doubly-clamped piezoelectric beam.

the width direction, so the flexible beam is divided into 192 elements and the number of nodes is 225. The length of the element is 25 mm, and the width of the element is 15 mm. Each of the PZT patches is divided into two parts in the x direction, and one part in the y direction. After applying the boundary condition to the beam, the number of the free nodes of the beam is 207.

The accelerometer is mounted in the intermediate position of the flexible beam, *i.e.* the node in the middle position of the beam structure numbered 113 is regarded as the observation node of acceleration output. When the finite element method is used to model the dynamics model of the flexible beam system, the effect of the accelerometer on the structural characteristics should be considered. Here, the effect of the mounted acceleration sensor on the overall stiffness of the structure is ignored; while the mass of the accelerometer cannot be neglected. Its mass is evenly assigned to the four adjacent elements, so the element numbers are 92, 93, 100, and 101.

After assembling the element mass matrix, the element stiffness matrix and the exciting force coefficient vector of the piezoelectric element, one can obtain the global mass matrix, global stiffness matrix and global control force coefficient vector. The boundary conditions of the flexible beam are two clamped sides. Therefore, the corresponding rows and columns should be deleted in the global mass and stiffness matrices, and in the global exciting and control force vectors. Considering the Rayleigh damping effect, the dynamics equation of the piezoelectric flexible beam structure can be written as

$$\mathbf{M}\ddot{\mathbf{d}}(t) + \mathbf{C}\dot{\mathbf{d}}(t) + \mathbf{K}\mathbf{d}(t) = \mathbf{F}_a \cdot V_a(t) + \mathbf{F}_c \cdot V_c(t); \quad (10)$$

where $\mathbf{M} \in \mathbf{R}^{3m\times 3m}$ and $\mathbf{K} \in \mathbf{R}^{3m\times 3m}$ are the global mass matrix and global stiffness matrix, respectively; $\mathbf{C} = \alpha\mathbf{M} + \beta\mathbf{K}$ is the damping matrix, in which α and β are Rayleigh damping constants respectively; $\ddot{\mathbf{d}}(t) \in \mathbf{R}^{3m\times 1}$, $\dot{\mathbf{d}}(t) \in \mathbf{R}^{3m\times 1}$, and $\mathbf{d}(t) \in \mathbf{R}^{3m\times 1}$ are the global nodal acceleration vector, the global nodal velocity vector, and global nodal displacement vector, respectively; $\mathbf{F}_a \in \mathbf{R}^{3m\times 1}$ and $\mathbf{F}_c \in \mathbf{R}^{3m\times 1}$ are the global active force vector used to excite the vibration of the flexible beam and the global control force vector that suppresses the vibration of the beam, respectively; $V_a(t)$ is the excitation voltage applied on the vibration excitation piezoelectric actuators; $V_c(t)$ is the control voltage applied on the vibration suppression piezoelectric actuators; and m is the total number of nodes, where $m = 207$ after applying the boundary conditions.

The output vibration signal measured by the acceleration sensor is[12]

$$y_a(t) = \mathbf{T}\ddot{\mathbf{d}}(t); \quad (11)$$

where $y_a(t)$ is the measured output of the acceleration sensor; $\mathbf{T} \in \mathbf{R}^{1\times 3m}$ is the acceleration output matrix corresponding to the observation position; $\ddot{\mathbf{d}}(t)$ is the global nodal acceleration vector; and m is the total number of the nodes.

For the convenience of numerical simulation, Eqs. (10) and (11) should be converted into a state-space form. By using a modal transformation $\mathbf{d} = \mathbf{\Phi}\mathbf{g}$, the dynamics equations of the system can be written as[23]

$$\overline{\mathbf{M}}\ddot{\mathbf{g}}(t) + \overline{\mathbf{C}}\dot{\mathbf{g}}(t) + \overline{\mathbf{K}}\mathbf{g}(t) = \overline{\mathbf{F}}_a \cdot V_a(t) + \overline{\mathbf{F}}_c \cdot V_c(t); \quad (12)$$

and

$$y_a(t) = \mathbf{T}\mathbf{\Phi}\ddot{\mathbf{g}}(t); \quad (13)$$

where $\mathbf{\Phi}$ is the modal matrix; $\mathbf{g}$ is the modal coordinate vector, $\overline{\mathbf{M}} = \mathbf{\Phi}^T\mathbf{M}\mathbf{\Phi}$ is the generalized mass matrix; $\overline{\mathbf{C}} = \mathbf{\Phi}^T\mathbf{C}\mathbf{\Phi}$ is the generalized damping matrix; $\overline{\mathbf{K}} = \mathbf{\Phi}^T\mathbf{K}\mathbf{\Phi}$ is the generalized stiffness matrix; $\overline{\mathbf{F}}_a$ is the generalized vibration excitation force vector; and $\overline{\mathbf{F}}_c$ is the generalized vibration control force vector.

The state-space representation of $Eqs.$ (12) and (13) is expressed as

$$\begin{cases} \dot{\mathbf{X}}(t) = \mathbf{A}\mathbf{X}(t) + \mathbf{B}_a V_a(t) + \mathbf{B}_c V_c(t) \\ y_a(t) = \mathbf{C}\mathbf{X}(t) + \mathbf{D}_a V_a(t) + \mathbf{D}_c V_c(t) \end{cases}; \quad (14)$$

where $\mathbf{X} = [\mathbf{g}(t)\ \dot{\mathbf{g}}(t)]^T$ is the state vector; $\mathbf{A} = \begin{bmatrix} \mathbf{0} & \mathbf{I} \\ -\overline{\mathbf{M}}^{-1}\overline{\mathbf{K}} & -\overline{\mathbf{M}}^{-1}\overline{\mathbf{C}} \end{bmatrix}$ is the system matrix, $\mathbf{B}_a = \begin{bmatrix} \mathbf{0} \\ \overline{\mathbf{M}}^{-1}\mathbf{\Phi}^T\mathbf{F}_a \end{bmatrix}$ is the vibration excitation force matrix; $\mathbf{B}_c = \begin{bmatrix} \mathbf{0} \\ \overline{\mathbf{M}}^{-1}\mathbf{\Phi}^T\mathbf{F}_c \end{bmatrix}$ is the vibration control force matrix; $\mathbf{C} = -\mathbf{T}\mathbf{\Phi}\left[\overline{\mathbf{M}}^{-1}\overline{\mathbf{K}}\ \overline{\mathbf{M}}^{-1}\overline{\mathbf{C}}\right]$ is the acceleration output matrix; and $\mathbf{D}_a = \mathbf{T}\mathbf{\Phi}\overline{\mathbf{M}}^{-1}\mathbf{\Phi}^T\mathbf{F}_a$ and $\mathbf{D}_c = \mathbf{T}\mathbf{\Phi}\overline{\mathbf{M}}^{-1}\mathbf{\Phi}^T\mathbf{F}_c$ are direct transfer coefficients.

Table 1. The modal frequencies of the first four modes of the doubly-clamped beam.

Order	ANSYS software (Hz)	FEM model (Hz)	Relative error
1	21.453	21.8914	2.04%
2	67.212	66.7915	-0.65%
3	81.231	81.3994	0.21%
4	116.33	116.6680	0.32%

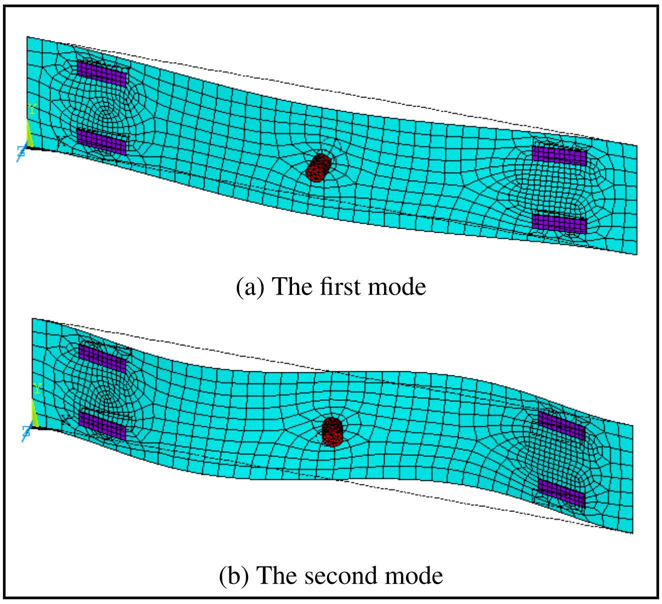

(a) The first mode

(b) The second mode

Figure 4. The first four vibration modes of the doubly-clamped beam obtained by employing ANSYS software.

2.4. Modal Analysis of the System

The geometrical size of the beam, the PZT patch, and the accelerometer can be seen in section 2.1. The flexible beam is made of epoxy resin. Young's modulus, Poisson's ratio, and the mass density of the beam structure are E_b = 34.64 Gpa, ν_b = 0.33 and ρ_b = 1865 Kg/m^3, respectively. Young's modulus, Poisson's ratio, and the mass density of the PZT patches are E_p = 63 Gpa, ν_p = 0.33, and ρ_p = 7650 Kg/m^3, respectively, and the piezoelectric strain constant is $d_{31} = 166\times10^{-12}$. The mass of the accelerometer is 38 g, and Young's modulus, Poisson's ratio, and the mass density are E_b = 210 Gpa, ν_b = 0.3 and ρ_b = 7850 Kg/m^3, respectively.

The model of the doubly-clamped beam system can be obtained by using the finite element modelling method, and one can also get modal frequencies and modal shapes of the system by using ANSYS software. When ANSYS software is employed to carry out modal analyses, the SHELL63 element is used to generate mesh of the beam, and the SOLID45 element is used to generate mesh of the PZT patches and the accelerometer. The modal frequencies of the flexible beam system are listed in Table 1, calculated by using the FEM method and ANSYS, respectively. The relative errors between the two methods are less than 3%. Comparison of the results demonstrates the correctness of the model built by using the FEM. Figures 4 (a) and (b) illustrate the mode shapes of the first two modes obtained by ANSYS.

3. CONTROL ALGORITHM AND NUMERICAL SIMULATION

3.1. Acceleration Feedback-based Proportional-Integral Control

In order to suppress the vibration under resonant excitation of a doubly-clamped beam effectively, active control algorithms need to be designed. During this investigation, the system output is the acceleration in the middle of the beam measured by the accelerometer. The measured signals of acceleration sensors generally comprise a large amount of noises, and the derivative of such signals will cause a much larger amount of noises. Since the integration of the measured acceleration signals will attenuate the measured noises, the acceleration sensor-based proportional-integral feedback control algorithm is utilized. To filter out the high frequency noises, a band-pass filter is applied to process the signals measured by the acceleration sensor before the controller design. The central frequency of the designed filter is 21.8914 Hz, and its bandwidth is 30 rad/s in the numerical simulation.

The acceleration sensor-based proportional-integral feedback control algorithm is

$$u(k) = -K_p y_{acc}(k) - K_I \sum_{j=1}^{k} y_{acc}(j); \tag{15}$$

where k is the serial number of the sampling time points; $y_{acc}(k)$ is the acceleration signal at the sampling instants; $u(k)$ is the control output; K_P is the proportional gain; and K_I is the integral gain.

3.2. Acceleration Feedback-based Variable Structure Control

The variable structure control (VSC) algorithm is easily implemented, including selecting the switching function and the control law.[24,25] When sliding mode variable structure control methods are designed to suppress the vibration of the doubly-clamped beam, the switching function of the VSC is composed of both the acceleration signal and its integration. The switching function is expressed as

$$s(k) = -c_1 y_{acc}(k) - c_2 \sum_{j=0}^{k} y_{acc}(j); \tag{16}$$

where $y_{acc}(k)$ is the acceleration signal at the sampling instants, and c_1 and c_2 are constants greater than 0.

When the switch variable structure control is designed, the switching function at the sampling interval is selected as a switch to determine the controller's output. Therefore, the acceleration-based switch variable structure control law $u_v(k)$ is written as

$$u_v(k) = Asgn[s(k)]; \tag{17}$$

where A is a positive constant, denoting the control amplitude; $sgn(\cdot)$ is the sign function; and it is

$$sgn\,[s(k)] = \begin{cases} 1, & s(k) \geq 0 \\ -1, & s(k) < 0 \end{cases}. \tag{18}$$

However, to realize the switch variable structure control, VSC requires high switching frequency associated with large

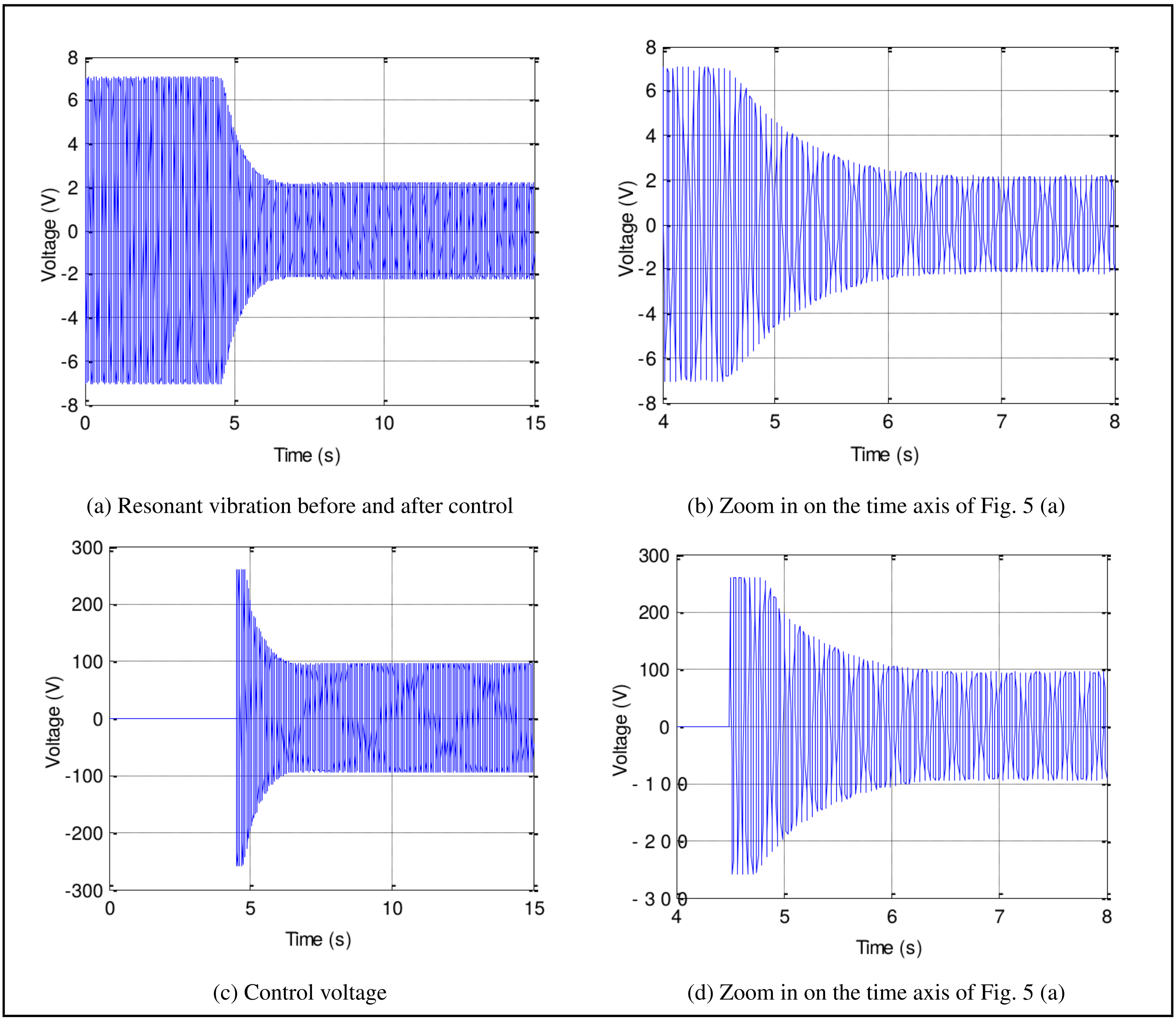

(a) Resonant vibration before and after control

(b) Zoom in on the time axis of Fig. 5 (a)

(c) Control voltage

(d) Zoom in on the time axis of Fig. 5 (a)

Figure 5. Simulation results of acceleration based proportional-integral control.

control gains, which in practice may cause chattering and excite the high frequency vibration of the system. To avoid the problem of this switching method, the switch surface $s_{law}(k)$ is selected as

$$s_{law}(k) = -\epsilon sgn\left[s(k)\right] - qs(k); \tag{19}$$

where $s(k)$ is the switching function mentioned above, and ϵ and q are positive constants.

Then, the control law of the improved VSC $u_r(k)$ is

$$u_r(k) = Asgn\left[s_{law}(k)\right]. \tag{20}$$

3.3. Numerical Simulation Results

In this section, numerical simulations are carried out to evaluate the effectiveness of the algorithms designed in section 3.1 and section 3.2. The structural size and mechanical properties of the flexible beam, the PZT patches and the accelerometer are described in the previous section. By using the FEM method, the matrices corresponding to the first two modes model are obtained as $\mathbf{A}$ =

$$\begin{bmatrix} 0 & 0 & 1 & 0 \\ 0 & 0 & 0 & 1 \\ -1.8919\times10^{4} & 1.1126\times10^{-6} & -1.2379 & 0 \\ 1.1726\times10^{-6} & -1.1612\times10^{5} & 0 & -2.5180 \end{bmatrix},$$

$\mathbf{B}_a = \begin{bmatrix} 0 \\ 0 \\ 0.0042 \\ 0.0012 \end{bmatrix}$, $\mathbf{B}_c = \begin{bmatrix} 0 \\ 0 \\ 0.0042 \\ -0.0012 \end{bmatrix}$, $\mathbf{C} = \begin{bmatrix} 4.99\times10^{4} & -8.91\times10^{-6} & 3.2715 & 0 \end{bmatrix}$, $D_a = -0.011$, $D_c = -0.011$.

In the simulation research, the sampling period is specified as $T_s = 3$ ms. By converting the continuous-time model to the discrete-time one, the coefficient matrices of the discrete-time system are obtained. The numerical simulation can be carried out by using the coefficient matrices of the discrete-time system. The excited signal actuated on the actuators is a sinusoidal signal, and the frequency of the excited signal is 21.8914 Hz, with an amplitude of 130 V.

The control gains of the acceleration sensor-based proportional-integral feedback control algorithm are chosen as $K_p = 1.0$, $K_I = 0.01$. The control action is applied at the

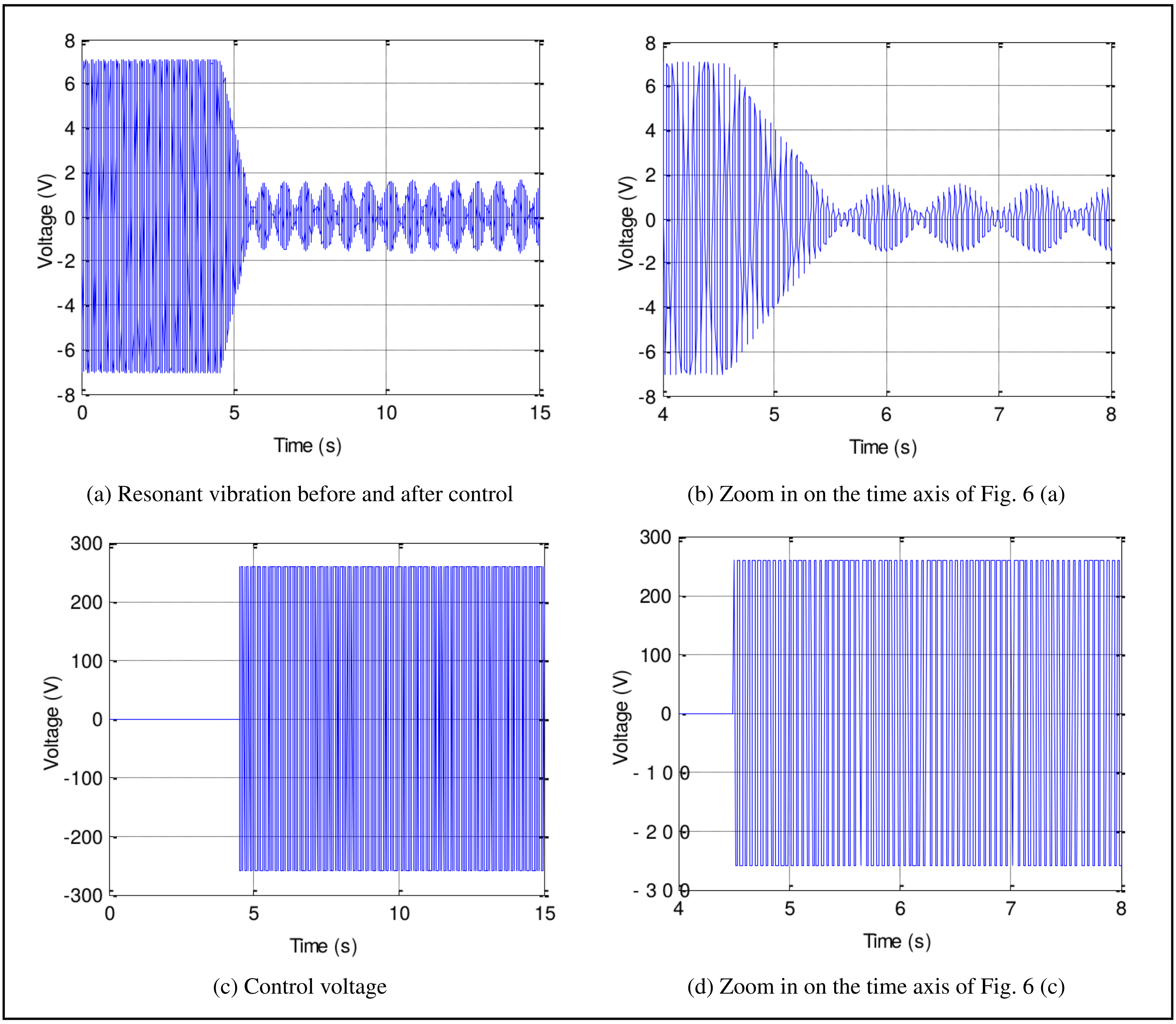

(a) Resonant vibration before and after control

(b) Zoom in on the time axis of Fig. 6 (a)

(c) Control voltage

(d) Zoom in on the time axis of Fig. 6 (c)

Figure 6. Simulation results of switch variable structure control.

moment of $t = 4.5$ s. The time-domain resonant vibration response before and after control is shown in Fig. 5 (a), and the control voltage applied on the PZT actuators is plotted in Fig. 5 (c). Figures 5 (b) and (d) are the enlarged view of Figs. 5 (a) and (c) from 4 seconds to 8 seconds, respectively. As depicted in Figs. 5 (a) and (b), when the control action is not applied, the vibration amplitude is about 7 V. After applying the active control, the vibration is suppressed, and the vibration amplitude will gradually become smaller. When the vibration response is stable, the vibration amplitude is about 2.2 V. As depicted in Fig. 5 (c), when the control action is not applied, the control voltage is 0 V. When the active control is applied, the control voltage reaches saturation in a short time, and then decreases in stable amplitude. From the simulation results, it can be seen that the amplitude of the control voltage and the controlled vibration response can stay at a constant level when applying the proportional plus integral control algorithm.

When using the switch variable structure control algorithm, the control gain is specified as $A = 5$, and the constants are selected as $c_1 = 0.65$, $c_2 = 0.01$. Figure 6 (a) shows the time-domain resonant vibration response before and after control. Figure 6 (c) shows the control voltage applied on the PZT actuators. Figures 6 (b) and (d) are the enlarged view of Figs. 6 (a) and (c) from 4 seconds to 8 seconds, respectively. When the control action is not applied, the vibration amplitude is about 7 V. When the active control is applied, the vibration is suppressed. When the vibration response is stable, the vibration amplitude increases and decreases periodically; the maximum vibration amplitude is about 1.5 V. As depicted in Figs. 6 (c) and (d), the control voltage is saturated continuously at a high frequency switching once the active control is applied.

When using the improved variable structure control algorithm, the parameters are chosen as $A = 5$, $c_1 = 0.7$, $c_2 = 0.02$, $\epsilon = 2.5$, and $q = 1.2$. Fig. 7 (a) shows the time-domain resonant vibration response before and after control. Figure 7 (c) shows the control voltage applied on the PZT actuators. Figures 7 (b) and (d) are the enlarged view of Figs. 7 (a) 7 (c) from 4 seconds to 8 seconds, respectively. When the active control is applied, the vibration is suppressed significantly. When the vibration is stable, the vibration amplitude increases and decreases periodically, and the maximum vibration amplitude is about 0.9 V. As depicted in Fig. 7 (c),

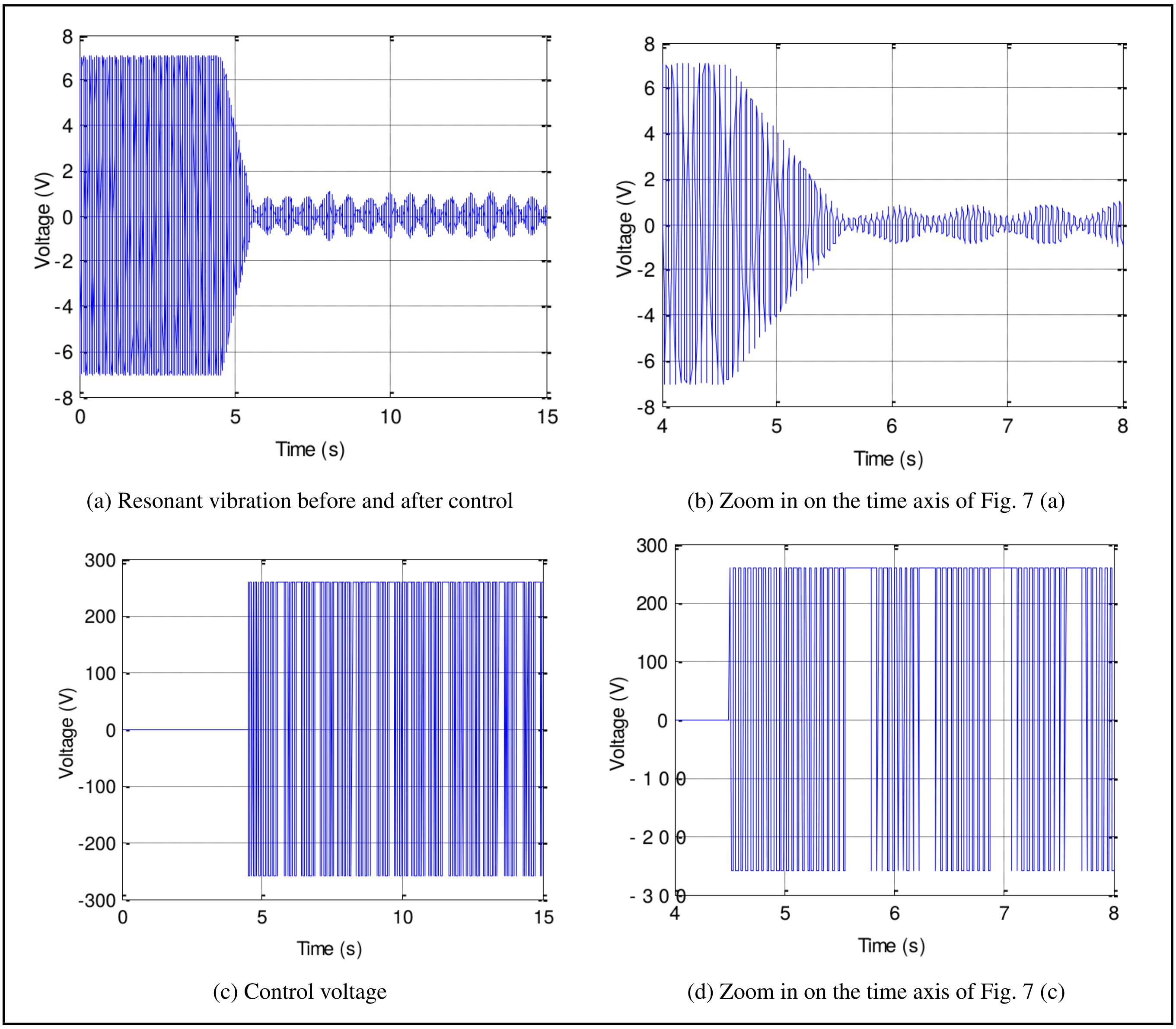

Figure 7. Simulation results of improved variable structure control.

once the active control is applied, the control voltage is saturated continuously. The reason that plots 7 (c) and (d) have several intervals is that a building time is needed; thus, the switch does not happen.

From Figs. 6 and 7, one can see that the control voltage amplitude of the variable structure control is the maximum value. This can provide the maximum control energy to suppress the periodical vibration. The vibration response amplitudes change periodically. This is because the following reasons: if the vibration amplitude is suppressed to become much smaller, the control value stays for a smaller time. Then the vibration amplitude will be increased. After the vibration becomes larger, the control effects are applied rapidly. Thus, the vibration amplitude will decrease.

From the simulation results, one can see that the acceleration feedback-based control algorithm can suppress the resonant vibration effectively. The amplitudes of resonant vibrations are reduced much better than with PI control, as compared to those of the designed variable control algorithms. Furthermore, the improved variable structure control algorithm shows the best control performance among the three methods.

4. EXPERIMENTS

In order to verify the effectiveness of the designed acceleration sensor based vibration control method, a doubly-clamped piezoelectric flexible beam experimental system was developed. Experiments on modal identification and resonant vibration suppression of the piezoelectric flexible beam were conducted.

4.1. Introduction of the Experimental Setup

The schematic diagram of the doubly-clamped piezoelectric beam experimental system is illustrated in Fig. 8. The experimental setup constitutes a doubly-clamped flexible beam structure bond with PZT patches bonded on both sides, and an accelerometer (type: CA-YD-127) is mounted in the intermediate position of the beam.

The photograph of the experimental setup is shown in Fig. 9. The practical locations of the PZT patches and the accelerometer sensor are schematically illustrated in Fig. 1. The dimensions and material properties of the beam, piezoelectric patches, and the accelerometer are given in Section 2.4. A

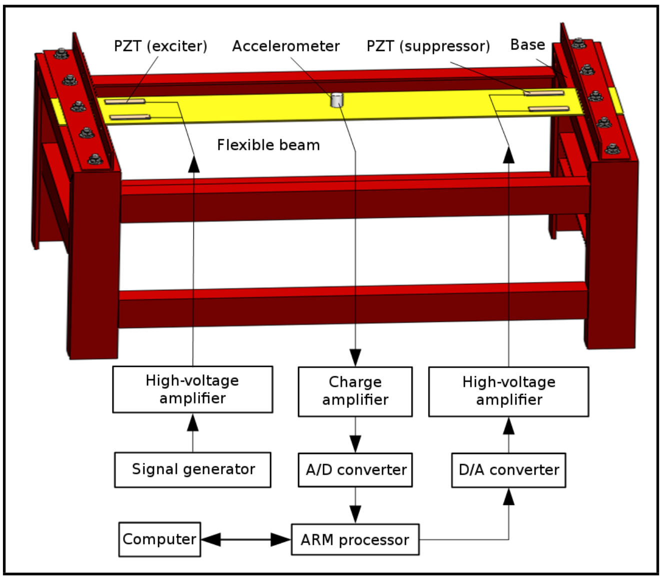

Figure 8. Schematic diagram of the doubly-clamped piezoelectric beam experiment system.

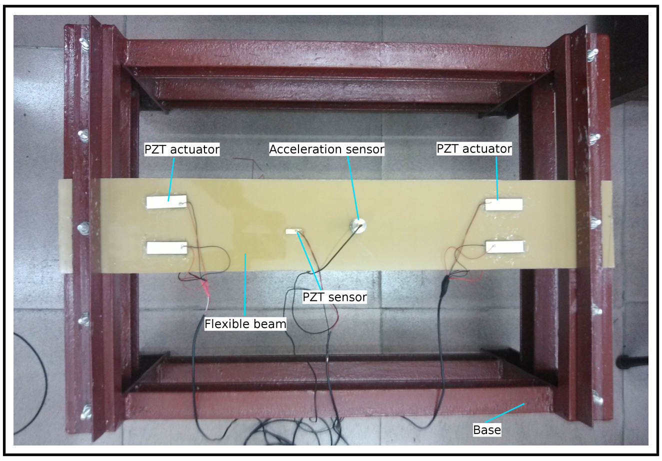

Figure 9. Experimental setup of the doubly-clamped beam.

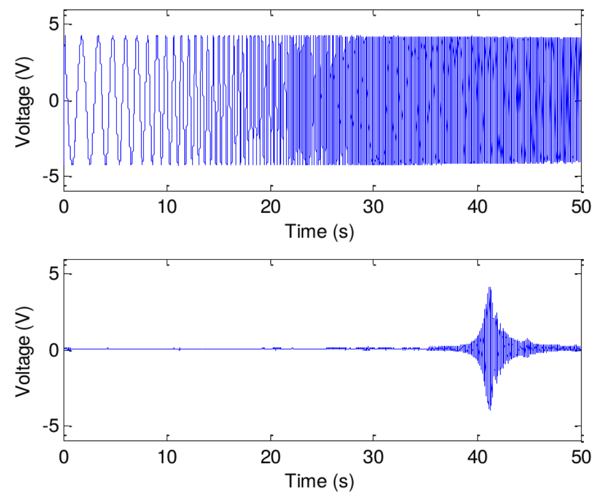

(a) The excited swept sine signal and time-domain response of the flexible beam.

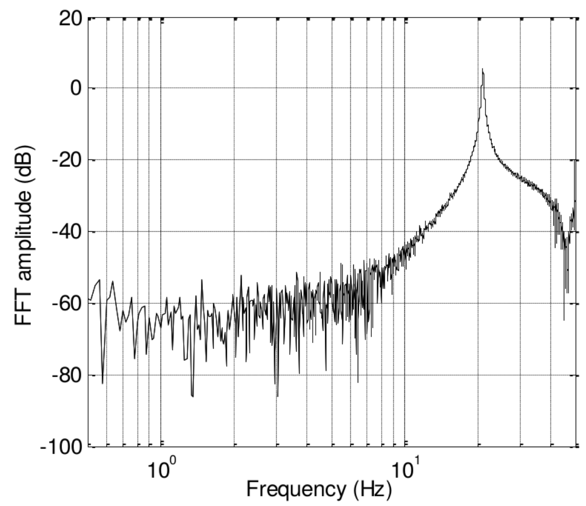

(b) Frequency response

Figure 10. Acceleration sensor measured swept sine vibration response excited by PZT actuators.

signal generator (type: SP-F05) is used to generate sinusoidal excitation signals. The generated excitation signal is amplified by a piezoelectric amplifier (APEX PA240CX) to excite the resonant vibration of the beam by using the excited piezoelectric actuator. The piezoelectric amplifier used for vibration excitation can amplify the excitation sinusoidal signal from a low voltage range, from -5 V to +5 V to a high voltage range, from -130 V to +130 V. The piezoelectric acceleration sensor's signal is amplified by charge amplifiers (YE5850) to the voltage range of -10 V to +10 V, and converted into digital data through an A/D (analog to digital) chip (AD7862, 4-channel, 12 Bit). The output of the controller is sent to the piezoelectric amplifier used for vibration suppression through a D/A (digital to analog) converter (AD7847, 2-channel 12-bit). The vibration suppression piezoelectric actuators are driven by a high-voltage amplifier APEX PA241DW, which amplifies the signal from a low voltage range, from -5 V to +5 V, to high voltage range, from -260 V to +260 V). An ARM board keeps communicating with a personal computer (PC), which is used as the signal processing and control system. The sampling period of the control experiments is selected as 3 ms.

4.2. Modal Frequency Identification of the Flexible Beam

To identify the practical modal frequencies of the doubly-clamped piezoelectric beam, excitation analyses are used. The swept sine signal is generated by a signal generator SP-F05, ranging from 0.5 Hz to 50 Hz, and the exciting time and amplitude is 50 s and 4 V, respectively. Then, it is amplified by a high-voltage amplifier APEX PA240CX and applied to the vibration excitation PZT actuators. Thus, the swept frequency response is obtained. Figure 10 (a) shows the excited swept sinusoidal signal and the time-domain response signal measured by the piezoelectric acceleration sensor. By employing fast Fourier transform (FFT), one can obtain the frequency response as shown in Fig. 10 (b). From Fig. 10 (b), it can be known that the first modal frequency of the doubly-clamped beam is 21.0 Hz.

In practice, the measured signals of acceleration sensors generally comprise a large amount of noises when the vibration of the first mode of the doubly-clamped beam is excited

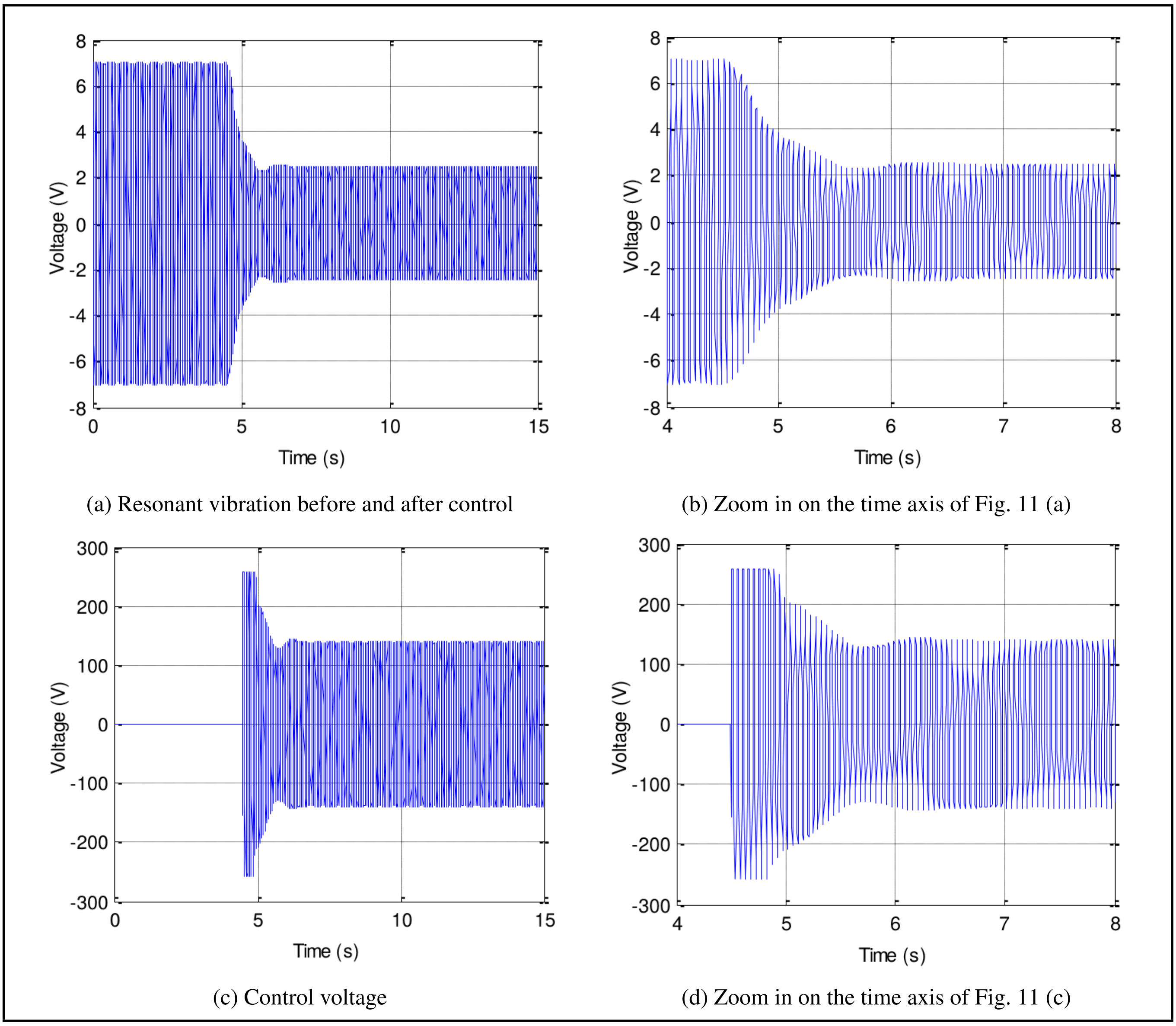

(a) Resonant vibration before and after control

(b) Zoom in on the time axis of Fig. 11 (a)

(c) Control voltage

(d) Zoom in on the time axis of Fig. 11 (c)

Figure 11. Experimental result of acceleration-based proportional-integral control.

by PZT actuators. To filter out the high frequency noises of the measured signal, a band-pass filter must be applied to controller design, and the central frequency of the filter is 21.0 Hz and its bandwidth is 30 rad/s in the experimental investigation.

4.3. Experiment Results on Resonant Vibration Suppression

For resonant vibration suppression of the first vibration mode, the sinusoidal excitation signal is generated by the signal generator SP-F05. The amplitude and frequency of the sinusoidal excitation signal are 4 V and 21.0 Hz, respectively. The frequency is the same as that of the first vibration mode. Firstly, the acceleration sensor-based proportional-integral feedback control method is used to suppress the vibration under resonant excitation.

The control gains of the acceleration sensor-based proportional-integral feedback control algorithms are specified as $K_p = 1.1$, $K_I = 0.02$. The control parameters between simulations and experiments are a little different. This is the reason why the parameters used in the simulation are not precisely consistent with those of the flexible physical beam, which was used perfectly in the experimental material. The physical parameters of the flexible plate, such as the material density, Young's modulus, uniformity, etc., cannot be precisely calculated. Moreover, the mass of the glue and the connected signal wires of the PZT patches are not considered in the model. These factors will affect the characteristics of the system. Therefore, the control parameters are inconsistently selected.

The control action is applied at the moment of $t = 4.5$ s. The time-domain resonant vibration responses before and after control and control voltage are applied on the PZT actuators are shown in Figs. 11 (a) and (c), respectively. Figures 11 (b) and (d) are the enlarged view of Figs. 11 (a) and (c) from 4 seconds to 8 seconds. As depicted in Fig. 11 (a), when the control action is not applied, the vibration amplitude is about 7 V. After the active control is applied, the control voltage reaches saturation abruptly. The beam's large amplitude vibration is suppressed to a small amplitude vibration quickly, and the control voltage is decreased accordingly. When the vibration is stable, the vibration amplitude is about 2.5 V, and the amplitude of the control voltage is almost unchanged.

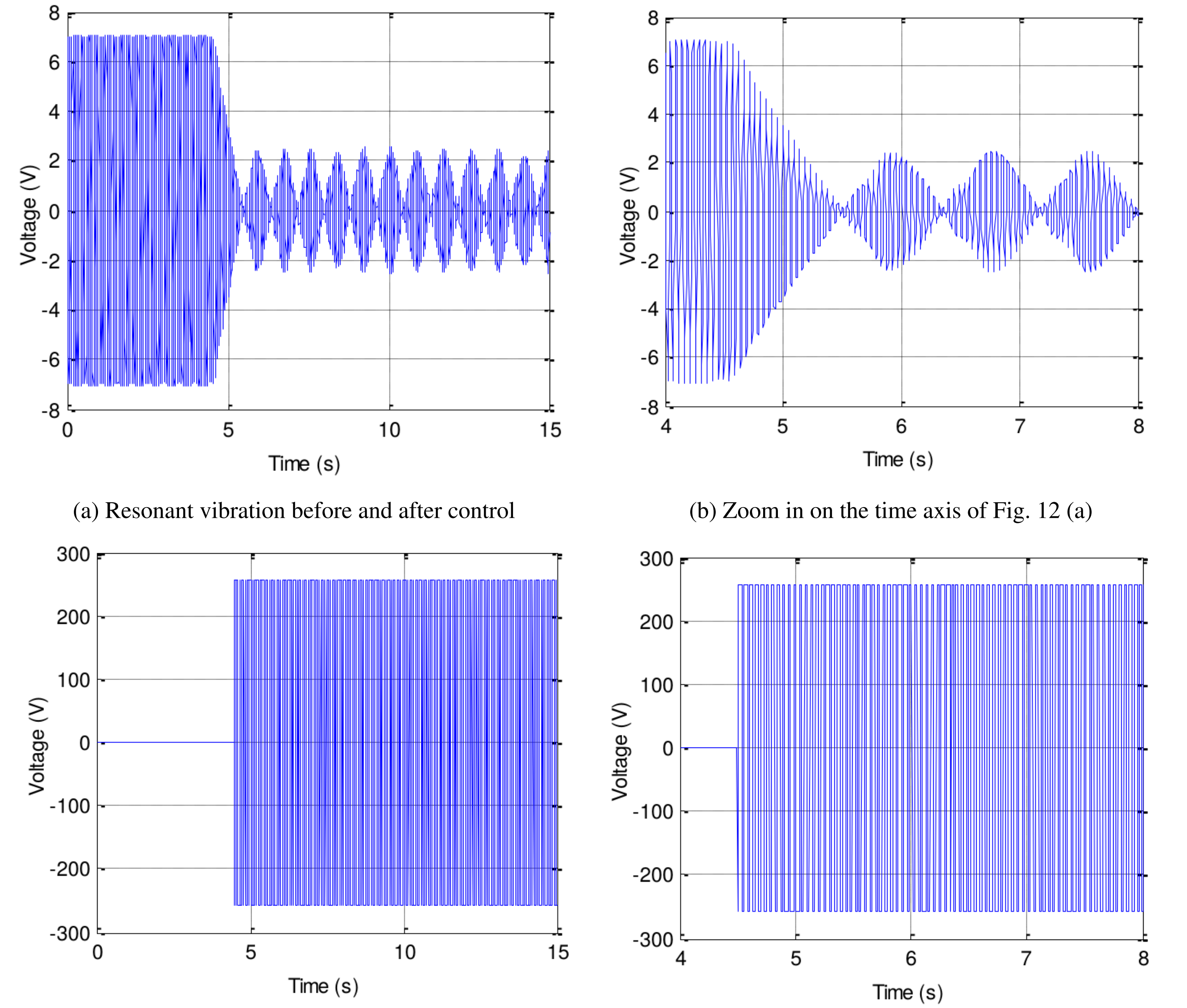

(a) Resonant vibration before and after control

(b) Zoom in on the time axis of Fig. 12 (a)

(c) Control voltage

(d) Zoom in on the time axis of Fig. 12 (c)

Figure 12. Experimental result of switch variable structure control.

This is the difference between the acceleration sensor-based proportional-integral feedback control algorithm and the subsequent variable structure control algorithm. The experimental results demonstrate the effectiveness of the acceleration sensor-based proportional-integral feedback control algorithm controller. Furthermore, the experimental results are in good accordance with the simulation results to some extent.

When using the switch variable structure control algorithm to suppress the resonant vibration, the constants are chosen as $c_1 = 0.8$, $c_2 = 0.02$. Figure 12 (a) shows the time-domain resonant vibration response before and after control. Figure 12 (c) shows the control voltage applied on the PZT actuators. Figures 12 (b) and (d) are the enlarged view of Figs. 12 (a) and (c) from 4 seconds to 8 seconds, respectively. When the control action is not applied, the vibration amplitude is about 7 V. After the active control is applied, the vibration is suppressed quickly. When the vibration is stable, the vibration amplitude increases and decreases periodically. The maximum vibration amplitude of the stable vibration response is about 2.5 V. As depicted in Fig. 12 (c), when the active control is applied, the control voltage is saturated continuously at a high frequency.

When using the improved variable structure control algorithm, the parameters are selected as $c_1 = 0.6$, $c_2 = 0.04$, $\epsilon = 2.5$, and $q = 1.8$. Figure 13 (a) shows the time-domain resonant vibration response before and after control. Figure 13 (c) shows the control voltage applied on the PZT actuators. Figures 13 (b) and 13 (d) are the enlarged view of Figs. 13 (a) and (c) from 4 seconds to 8 seconds, respectively. After the active control is applied, the vibration is suppressed. When the vibration is stable, the vibration amplitude increases and decreases periodically, and the maximum vibration amplitude is 1.6 V. As depicted in Fig. 13 (c), when the active control is applied, the control voltage is saturated continuously. This is why there is a building time where switch does not happen. The experimental results are in good accordance with the simulation results to some degree.

Remarks: The parameters of the designed controllers are provided by trial and error method in simulations and experiments. To guarantee the stability conditions of the controllers, control spill-over for higher-mode vibrations should be consid-

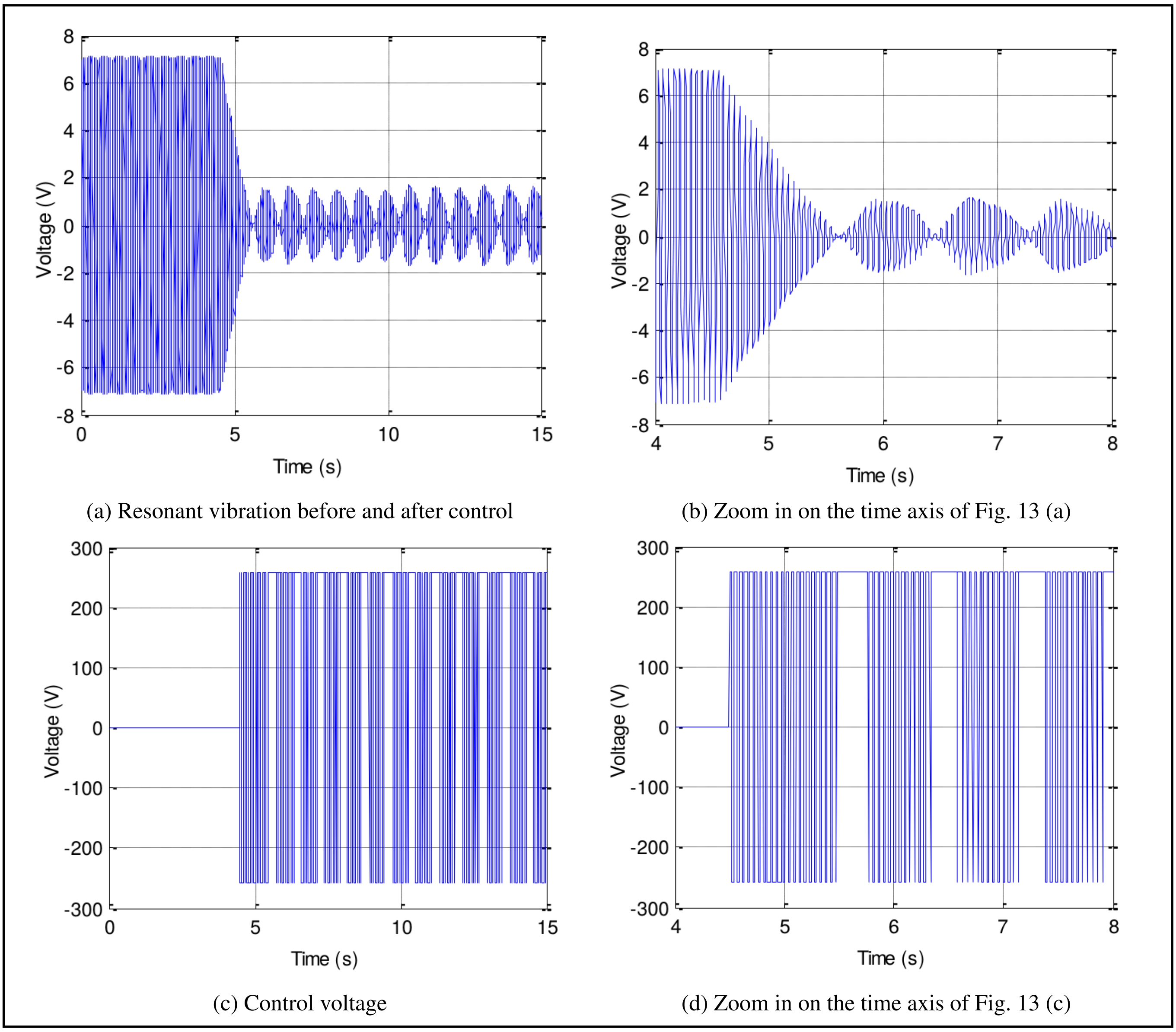

(a) Resonant vibration before and after control

(b) Zoom in on the time axis of Fig. 13 (a)

(c) Control voltage

(d) Zoom in on the time axis of Fig. 13 (c)

Figure 13. Experimental result of improved variable structure control.

ered. Here, low-pass filters are applied to prevent spill-over.

From the experimental results, it can be concluded that the acceleration feedback-based control algorithm can suppress the resonant vibration effectively. In addition, the improved variable structure control algorithm shows a better performance in these proposed methods.

5. CONCLUSIONS

This paper presents the theoretical analysis and experimental results of the first resonant vibration suppression of a doubly-clamped flexible beam with bonded discrete PZT actuators and a mounted accelerometer. The dynamics model of the flexible beam system is obtained by using the finite element method. Acceleration sensor-based proportional-integral control method and sliding mode variable structure control algorithms are used to suppress the resonant vibration of the beam excited by piezoelectric actuators. Numerical simulations and experiments are conducted to compare the results of the different control methods. The resonant vibration of the doubly-clamped beam is effectively suppressed by the proposed methods. The experimental results confirm the effectiveness and robustness of the presented acceleration sensor-based control strategies. What's more, the improved variable structure control method shows better control performance in suppressing the resonant vibration.

ACKNOWLEDGEMENTS

This work was partially supported by the National Natural Science Foundation of China under Grant 51175181, partially supported by the Fundamental Research Funds for the Central Universities SCUT, and in part by State Key Laboratory of Robotics Foundation. The authors gratefully acknowledge these support agencies.

REFERENCES

1 Dwivedy, S. K. and Eberhard, P. Dynamic analysis of flexible manipulators, a literature review, *Mech. Mach. Theory*, **41** (7), 749–777, (2006). http://dx.doi.org/10.1016/j.mechmachtheory.2006.01.014

[2] Lin, J. and Liu, W. Z. Experimental evaluation of a piezoelectric vibration absorber using a simplified fuzzy controller in a cantilever beam, *J. Sound Vib.*, **296** (3), 567–582, (2006). http://dx.doi.org/10.1016/j.jsv.2006.01.066

[3] Chang, W., Gopinathan, S. V., Varadan, V. V., and Varadan, V. K. Design of robust vibration controller for a smart panel using finite element model, *J. Vib. Acoust.*, **124** (2), 265–276, (2002). http://dx.doi.org/10.1115/1.1448319

[4] Hurlebaus, S. and Gaul, L. Smart structure dynamiequations (12) and (13)cs, *Mech. Syst. Signal Pr.*, **20** (2), 255–281, (2006). http://dx.doi.org/10.1016/j.ymssp.2005.08.025

[5] Wang, S., Quek, S., Ang, K. Vibration control of smart piezoelectric composite plates, *Smart Mater. Struct.*, **10** (4), 637, (2001). http://dx.doi.org/10.1088/0964-1726/10/4/306

[6] Sabatini, M., Gasbarri, P., Monti, R., and Palmerini, G. B. Vibration control of a flexible space manipulator during on orbit operations, *Acta Astronaut.*, **73** (4), 109–121, (2012). http://dx.doi.org/10.1016/j.actaastro.2011.11.012

[7] Vasques, C. H., da Conceição, S. M., de Abreu, G. L. C. M., et al. Identification and vibration control of a flexible structure, *ABCM Symposium Series in Mechatronics*, **4** (2), 157–165, (2012).

[8] Parameswaran, A. P. and Gangadharan, K. Active vibration control of a smart cantilever beam at resonance: A comparison between conventional and real time control, *Proc. Intelligent Systems Design and Applications (ISDA)*, Kochi, India, (2012), 235–239. http://dx.doi.org/10.1109/isda.2012.6416543

[9] Mahmoodi, S. N. and Ahmadian, M. Modified acceleration feedback for active vibration control of aerospace structures, *Smart Mater. Struct.*, **19** (6), 065015, (2010). http://dx.doi.org/10.1088/0964-1726/19/6/065015

[10] Nima Mahmoodi, S., Craft, M. J., Southward, S. C., and Ahmadian, M. Active vibration control using optimized modified acceleration feedback with adaptive line enhancer for frequency tracking, *J. Sound Vib.*, **330** (7), 1300–1311, (2011). http://dx.doi.org/10.1016/j.jsv.2010.10.013

[11] Kwak, S. K., Washington, G., and Yedavalli R. K. Acceleration feedback-based active and passive vibration control of landing gear components, *J. Aerospace Eng.*, **15** (1), 1–9, (2002). http://dx.doi.org/10.1061/(asce)0893-1321(2002)15:1(1)

[12] Preumont, A. and Loix, N. Active damping of a stiff beam-like structure with acceleration feedback, *Exp. Mech.*, **34** (1), 23–26, (1994). http://dx.doi.org/10.1007/bf02328438

[13] Gatti, G., Brennan, M. J., and Gardonio, P. Active damping of a beam using a physically collocated accelerometer and piezoelectric patch actuator, *J. Sound Vib.*, **303** (3), 798–813, (2007). http://dx.doi.org/10.1016/j.jsv.2007.02.006

[14] Shin, C., Hong C., and Jeong W. B. Active vibration control of beam structures using acceleration feedback control with piezoceramic actuators, *J. Sound Vib.*, **331** (6), 1257–1269, (2012). http://dx.doi.org/10.1016/j.jsv.2011.11.004

[15] Qiu, Z. C., Han, J. D., Zhang, X. M., et al. Active vibration control of a flexible beam using a non-collocated acceleration sensor and piezoelectric patch actuator, *J. Sound Vib.*, **326** (3), 438–455, (2009). http://dx.doi.org/10.1016/j.jsv.2009.05.034

[16] Qiu, Z. C., Wu, H. X., and Ye, C. D. Acceleration sensors based modal identification and active vibration control of flexible smart cantilever plate, *Aerosp. Sci. Tech.*, **13** (6), 277–290, (2009). http://dx.doi.org/10.1016/j.ast.2009.05.003

[17] Chatterjee, S. Vibration control by recursive time-delayed acceleration feedback, *J. Sound Vib.*, **317** (1), 67–90, (2008). http://dx.doi.org/10.1016/j.jsv.2008.03.020

[18] Ramu, I. and Mohanty, S. Study on free vibration analysis of rectangular plate structures using finite element method, *Procedia Eng.*, **38**, 2758–2766, (2012). http://dx.doi.org/10.1016/j.proeng.2012.06.323

[19] Alkhatib, R. and Golnaraghi, M. Active structural vibration control: a review, *Shock Vib. Digest*, **35** (5), 367–383, (2003). http://dx.doi.org/10.1177/05831024030355002

[20] Benjeddou, A. Advances in piezoelectric finite element modeling of adaptive structural elements: a survey, *Comput. Struct.*, 2000, **76** (1), 347–363. http://dx.doi.org/10.1016/s0045-7949(99)00151-0

[21] Yasin, M. Y., Ahmad N., and Alam, M. N. Finite element analysis of actively controlled smart plate with patched actuators and sensors, *Lat. Am J. Solids Struct.*, **7** (3), 227–247, (2010). http://dx.doi.org/10.1590/s1679-78252010000300001

[22] Lam, K., Peng, X., Liu G., and Reddy, J. N. A finite-element model for piezoelectric composite laminates, *Smart Mater. Struct.*, **6** (5), 583–591, (1997). http://dx.doi.org/10.1088/0964-1726/6/5/009

[23] Bandyopadhyay, B., Manjunath, T. C., and Umapathy, M. *Modeling, control and implementation of smart structures: a FEM-state space approach*, Springer-Verlag, Berlin, (2007).

[24] Hung, J. Y., Gao W., and Hung J. C. Variable structure control: a survey, *IEEE Transactions on Indust. Elect.*, 1993, **40** (1), 2–22. http://dx.doi.org/10.1109/41.184817

[25] Fung, E. H. and Lee, C. K. Variable structure tracking control of a single-link flexible arm using time varying sliding surface, *J. Robotic Syst.*, 1999, **16** (12), 715–726. http://dx.doi.org/10.1002/(sici)1097-4563(199912)16:12<715::aid-rob4>3.3.co;2-y

Review and Comparison of Variable Step-Size LMS Algorithms

Dariusz Bismor, Krzysztof Czyz and Zbigniew Ogonowski

Institute of Automatic Control, Silesian University of Technology, ul. Akademicka 16, 44-100 Gliwice, Poland

(Received 4 December 2013; accepted 11 February 2015)

The inherent feature of the Least Mean Squares (LMS) algorithm is the step size, and it requires careful adjustment. Small step size, required for small excess mean square error, results in slow convergence. Large step size, needed for fast adaptation, may result in loss of stability. Therefore, many modifications of the LMS algorithm, where the step size changes during the adaptation process depending on some particular characteristics, were and are still being developed.

The paper reviews seventeen of the best known variable step-size LMS (VS-LMS) algorithms to the degree of detail that allows to implement them. The performance of the algorithms is compared in three typical applications: parametric identification, line enhancement, and adaptive noise cancellation. The paper suggests also one general modification that can simplify the choice of the upper bound for the step size, which is a crucial parameter for many VS-LMS algorithms.

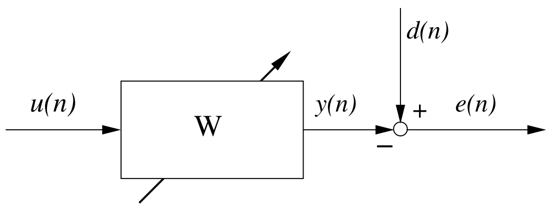

Figure 1. Adaptive filtering problem.

1. INTRODUCTION

In applications where adaptation is needed, the LMS algorithm is probably the most frequently used algorithm. It is simple, fast, and surprisingly robust. Despite its simplicity, the complete mathematical analysis of the LMS algorithm as well as exact rules for the step size adjustment are not currently known, which is probably due to its highly nonlinear character.[1] Therefore, new VS-LMS algorithms appear in the literature every few years with the aim to be useful in practical applications.

The basic block diagram illustrating the LMS algorithm operation is shown on Fig. 1.[1] The adaptive filter $\mathbf{W}$ is fed with the input sequence $u(n)$. The output of the filter, $y(n)$, is compared with the desired signal, $d(n)$, to produce the error signal, $e(n)$. The algorithm adjusts the filter to minimize the error.

If the adaptive filter is of finite impulse response (FIR) type, with the taps stored in a row vector:

$$\mathbf{w}(n) = [w_0(n)\ w_1(n)\ \dots\ w_{L-1}(n)]^T ; \tag{1}$$

where T denotes transpose, the LMS algorithm updates the filter taps according to the well-known formula:[2]

$$\mathbf{w}(n+1) = \mathbf{w}(n) + \mu\mathbf{u}(n)e(n); \tag{2}$$

where μ is the step size parameter and $\mathbf{u}(n)$ is a row vector containing the input signal samples. The latter may be, depending on the application, of spatial type:

$$\mathbf{u}(n) = [u_0(n)\ u_1(n)\ \dots u_{L-1}(n)]^T ; \tag{3}$$

or of temporal type, with regressive samples of the same input signal:

$$\mathbf{u}(n) = [u(n)\ u(n-1)\ u(n-2)\ \dots u(n-L+1)]^T . \tag{4}$$

The problem with the step size choice can be summarized as follows. Large step size allows for fast adaptation, but also gives large excess mean square error (EMSE, see Section 4.1 for definition). Too large step size may lead to the loss of stability of the system using the LMS algorithm. On the other hand, too small step size gives slow convergence, and even if it results in small excess MSE, it cannot be accepted in many practical applications.

At this point a very important remark should be made about theoretical convergence of the LMS algorithm. First of all, there are different types of convergence,[3] e.g. convergence of the mean (the poorest), convergence in the mean, convergence in the mean square sense, etc. However, if convergence in the mean square sense of the LMS algorithm (2) is desired, and the algorithm operates in real conditions (not noise-free environment), such convergence can only be proved for the vanishing step size, i.e. for $\mu \xrightarrow{n\to\infty} 0$.[3,4] In other words, no constant step-size LMS algorithm can result in convergence in the mean square sense, or stronger. On the other hand, it is possible to bound the EMSE within certain limits, depending on the step size.

The idea of variable step-size is not new. Actually, the Normalized LMS (NLMS) algorithm may be considered as the first variable step-size modification of the LMS, and NLMS was proposed in 1967 independently by Nagumo *et al.*[5] and Albert *et al.*[6] Next VS-LMSes were proposed in 1986 by Harris *et al.*,[7] and by Mikhael *et al.*[8] Many VS-LMS algorithms were developed since then: the search for 'variable step LMS' in article titles only on Scopus or IEEEXplore returns more than 130 publications. The research in this field is by no means finished, new results are still being published.[9,10]

The VS-LMS algorithms may be grouped by the techniques they use to adjust the step size. One of these techniques is the adjustment of the step size based solely on the input signal $u(n)$. Historically, it is the oldest idea, because the NLMS acts in this way.[5] Due to popularity of the NLMS, it may also be considered the most popular technique. Another algorithm using this concept is the one proposed by Mikhael[8] (if FIR filter is considered).

The next technique relates the step size to the error signal. This technique is based on the observation that the step size should be small when the error is small in order to provide small EMSE. On the other hand, when the error is large, it is desirable to operate with large step size to adapt the filter taps fast. This technique was used by Kwong,[11] Aboulnasr,[12] Pazaitis[13], and Zou.[14]

Finally, there is a technique combining the use of the input signal and the error signal. It is a technique used by majority of the algorithms presented in this paper, namely by Harris,[7] Shan,[15] Karni,[16] Benveniste,[17] Evans,[18] Mathews,[19] Ang,[20] Benesty,[21] Wahab,[22] Hwang[23] and Wang.[24] In many solutions this technique is based on the *orthogonality principle*, which states that (under some assumptions) the necessary and sufficient condition for the mean-square error to attain its minimum value is that the error signal $e(n)$ and the input signal $u(n)$ are orthogonal.[1]

The VS-LMS algorithms may also be grouped based on the number of additional parameters which have to be adjusted before running each of the algorithms. Surprisingly, the group of algorithms needing no parameters, i.e. algorithms running fully autonomously, has only two members: Mikhael's algorithm[8] and Wang's algorithm.[24] Next follows the group containing only one parameter to adjust, and this group contains only the NLMS algorithm.[5] Very large is the group of the algorithms needing an upper bound for the step size in addition to one or two parameters; this group includes Shan's algorithms[15] (one of them known as the correlation-LMS), Karni's algorithm,[16] Benveniste's algorithms,[17] and Mathews' algorithms.[19] Three parameters, but without an upper bound for the step size, are also required by Benesty's algorithm.[21] The remaining algorithms are parametrized by more than three values, with the maximum of eight in case of Zou's algorithm.[14]

The goal of this paper is to review the VS-LMS techniques developed by different authors for different uses and to compare them in three typical applications: identification, line enhancement, and adaptive noise cancellation. The paper also suggests how to reduce by one the number of parameters required to run those algorithms which use the upper bound for the step size. The paper is organized as follows. In the next section, all the algorithms considered in this paper are detailed to a degree which allow them to be implemented. However, to make the paper of reasonable length, we will omit all the derivations leading to the final formula as well as all the derivations of MSE, learning curves, etc. Section 3 describes a possible way of reduction of the number of parameters in case of some of the algorithms. Section 4.1 describes the results of simulation of the system identification case. Section 4.2 describes the results of simulation of the line enhancer. Section 4.3 describes the results of simulation of the adaptive noise cancellation system. Finally, some concluding remarks are given in Section 5.

2. VS-LMS ALGORITHMS

In this section, VS-LMS algorithms are described in chronological order. The majority of the algorithms described below use common (scalar) step size, and fall under the equation:

$$\mathbf{w}(n+1) = \mathbf{w}(n) + \mu(n)\mathbf{u}(n)e(n); \tag{5}$$

where $\mu(n)$ is the (variable) step size calculated with an appropriate formula.

Some of the algorithms allow for individual step sizes for each of the filter taps; such VS-LMS algorithms are described by:

$$\mathbf{w}(n+1) = \mathbf{w}(n) + \mathbf{M}(n)\mathbf{u}(n)e(n); \tag{6}$$

where $\mathbf{M}(n)$ is a diagonal matrix of the size equal to the adaptive filter length.

2.1. Normalized LMS Algorithm

The first modification of the LMS algorithm which can be considered a variable step-size modification, was developed by Nagumo and Noda,[5] and independently by Albert and Gardner.[6] However, the name "Normalized LMS" was not proposed by the authors, but appears in the literature much later.[1]

The NLMS algorithm uses the following equation for the step size:

$$\mu(n) = \frac{\bar{\mu}}{\mathbf{u}^T(n)\mathbf{u}(n)} = \frac{\bar{\mu}}{\sum_{i=0}^{L-1} u^2(n-i)}; \tag{7}$$

where $\bar{\mu} > 0$ is a scalar which allows for a change of the adaptation speed. The upper limit for $\bar{\mu} > 0$ to provide stability in some cases is equal to two, but lower values must be used in many practical applications.[1]

The NLMS algorithm may be considered as a standard algorithm for the majority of the adaptive signal processing applications. The normalization of the step size with the input signal power estimate makes the algorithm invulnerable to the input signal power changes; therefore, the algorithm does not require the step size readjustment when such changes occur. On the other hand, the division operation required by the normalization may be time-consuming and required to be avoided in some time-critical applications. Nevertheless, the time overhead introduced by the step-size normalization is the smallest when compared to the overhead introduced by other VS-LMS algorithms discussed below.

2.2. VS-LMS Algorithm by Harris *et al.*

The algorithm proposed by Harris *et al.* uses individual step sizes, and the step-size matrix $\mathbf{M}(n)$ is constructed as:

$$\mathbf{M}(n) = 2 \cdot \operatorname{diag}\left[\mu_0(n),\ \mu_1(n),\ \ldots \mu_{L-1}(n)\right];$$
$$\mu_{min} < \mu_i(n) < \mu_{max}, \quad i = 0 \ldots L-1. \tag{8}$$

The authors suggest that $\mu_{max} < 1/\lambda_{max}$, where λ_{max} is the maximum eigenvalue of the autocorrelation matrix $\mathbf{R}_{uu}$ of the input signal. μ_{min}, on the other hand, should be chosen to provide the desired steady-state misadjustment.

With the above restrictions, the individual step sizes are changed as follows:

$$\mu_i(n+1) = \begin{cases} \mu_i(n)/\alpha & \text{if } e(n)u(n-i) \text{ alternates sign} \\ & \text{on } m_0 \text{ successive samples;} \\ \alpha\mu_i(n) & \text{if } e(n)u(n-i) \text{ has the same sign} \\ & \text{on } m_1 \text{ successive samples;} \\ \mu_i(n) & \text{otherwise.} \end{cases} \tag{9}$$

The authors suggest that the typical value for α is 2.

The authors distinguish the following useful cases:

- $m_0 = 1, m_1 = \infty$ — the algorithm decreases the step sizes with every sign change,
- $m_0 > 1, m_1 = \infty$ — the algorithm decreases the step sizes if m_0 consecutive sign changes occur,
- $m_1 > m_0 > 0$ — such algorithm results in general decrease of the step sizes; the authors claim this is useful for stationary input signal processing,
- $m_0 = m_1 \geq 1$ — the symmetric increase or decrease algorithm; the authors claim this is useful for nonstationary input signal processing.

This algorithm is parametrized by five parameters, including the upper bound for the step size.

The algorithm was developed in times when the hardware was many times less powerful than nowadays. The authors admit that they tried to achieve performance comparable with the Recoursive Leas Squares (RLS) algorithm, which was too hardware-demanding to use. The authors claim that the VS-LMS algorithm given above can "provide faster convergence and less misadjustment than the constant μ or LMS algorithm," but that the RLS-type algorithms are still faster to converge. It must be noted, however, that this goal was achieved at the price of four additional parameters, which makes the algorithm difficult to adjust.

This algorithm is also one of the two algorithms that proposed for the first time the individual step sizes for each of the filter taps.

2.3. VS-LMS Algorithm by Mikhael *et al.*

The algorithm proposed by Mikhael *et al.*[8] can be used for FIR filters as well as for infinite impulse response (IIR) filters. It also comes in two flavors: with scalar step size (which the authors call *homogeneous adaptation*), and with individual step sizes. To allow comparison with other algorithms discussed in this paper, we will introduce the FIR version only. Moreover, only individual step sizes will be used. Thus, the algorithm is given by:

$$\mathbf{M}(n) = \mathrm{diag}\left[\mu_0(n),\ \mu_1(n),\ \ldots \mu_{L-1}(n)\right];$$

$$\mu_i(n) = \frac{0.5\,|u(n-i)|}{\sum_{l=0}^{L-1} |u(n-l)|^3}, \quad i = 0 \ldots L-1. \tag{10}$$

As mentioned in the introduction, this algorithm is one of the two that *do not require any parameters to run*, and it is its main advantage. The algorithm is also the second of the two algorithms that proposed the individual step sizes (both the algorithms appeared in the same year). Although the authors allow also for scalar step sizes, they insist that the individual step sizes give better results.

The authors applied the algorithm to the classical adaptive noise cancellation problem (see Section 4.3), with the stationary, white Gaussian noise input. The algorithm resulted in faster convergence rate than the constant step size LMS algorithm.

2.4. VS-LMS Algorithm by Shan *et al.*

The original algorithm by Shan *et al.*[15] is given by:

$$\mu(n+1) = \frac{\alpha|\rho(n)|}{\mathbf{u}^T(n)\mathbf{u}(n)};$$

$$\rho(n) = \lambda\rho(n) + (1-\lambda)\bar{u}(n)e(n);$$
$$\bar{u}(n) = \frac{1}{L}\sum_{l=0}^{L-1} u(n-l); \tag{11}$$

where α is a scaling factor, $\rho(n)$ is an estimate of the correlation between the input and the error at time instance n, λ is a forgetting factor used in calculation of the correlation, and $\bar{u}(n)$ is the mean value of the elements in the input vector. Thus, the algorithm uses the orthogonality principle.[1] Typically, the forgetting factor λ is in range from 0.9 to 1. The value of the scaling factor α, on the other hand, should be chosen experimentally with the knowledge that it affects both the tracking capability and the speed of the convergence of the algorithm.

In its first published form, the original algorithm did not include the absolute value in the numerator of Eq. (11). After comments on their paper[25] the authors added the absolute value and agreed that μ should be bounded ($\mu(n) < \mu_{max}$).[26]

The algorithm by Shan *et al.* was simplified afterwards to the form:

$$\mu(n+1) = \frac{\alpha|\rho(n)|}{\mathbf{u}^T(n)\mathbf{u}(n)};$$

$$\rho(n) = \lambda\rho(n) + (1-\lambda)u(n)e(n); \tag{12}$$

which we currently know under the name *correlation LMS*. The only difference is that the mean value of the elements in the input vector is substituted with the instantaneous input value.

Both the original Shan's algorithm and the correlation LMS are members of the group of algorithms requiring no more than two parameters to adjust in addition to the upper bound for the step size, which is still a reasonable number. The authors claim that their algorithm was developed to address the issue of the robustness of the LMS algorithm to disturbances present in real adaptive systems and to the sudden changes in the noise level. As a response, the algorithm with adaptive gain control similar to the gain control of the RLS algorithm was proposed. Thus, the algorithm is "insensitive to disturbances but sensitive to system changes", i.e. with tracking capabilities.[15]

2.5. VS-LMS Algorithm by Karni *et al.*

The algorithm by Karni *et al.*[16] is given by:

$$0 \le \mu(n) \le \mu_{max};$$
$$\mu(n) = \mu_{max}\left(1 - e^{-\alpha\|\mathbf{u}(n)e(n)\|^2}\right); \qquad (13)$$

where $\alpha > 0$ is the dumping factor. The authors suggest that the $\alpha > 1$ and observe that for $\alpha \to \infty$ the algorithm degenerates to the conventional LMS, with constant step size equal to μ_{max}.

Karni's algorithm requires only one parameter and the upper bound for the step size to run.

The algorithm was developed to address the issue of high misadjustment that is a side effect of fast convergence, or more precisely, of using large step sizes. The authors compare their algorithm with a two-stage method, which uses large values of μ during the initial stage of adaptation to speed up the convergence, and smaller values afterwards to minimize the misadjustment. The authors claim that their algorithm gives better results (both the convergence speed and the misadjustment), especially under nonstationary environment conditions.

2.6. VS-LMS Algorithm by Benveniste *et al.*

Benveniste *et al.* proposed a VS-LMS algorithm in the book.[17] The author of this work failed to find this book; however, as the algorithm was cited by many authors, it is reproduced here after reference[20] and.[27] The algorithm may be used with scalar step size, and in this case it is defined as:

$$\mu(n) = \mu(n-1) + \rho e(n)\mathbf{u}^T(n)\boldsymbol{\phi}(n); \quad \mu(n) < \mu_{max}, \qquad (14)$$

$$\boldsymbol{\phi}(n+1) = \boldsymbol{\phi}(n) - \mu(n)\mathbf{u}(n)\mathbf{u}^T(n)\boldsymbol{\phi}(n) + \mathbf{u}(n)e(n); \qquad (15)$$

where ρ is a small positive value used to control the convergence and MSE, and $\boldsymbol{\phi}(n)$ is an estimate of the gradient vector — the vector of derivatives of the filter coefficients with the respect to the step size. After reference[20] we observe that a larger value of ρ results in faster convergence and may result in lower overall MSE, but may also cause a large fluctuations of MSE in short range of time; we also observe that the behavior of the algorithm is not influenced very much if the value of ρ varies in range $[10^{-4} \ldots 10^{-2}]$.

Benveniste's algorithm can also be used in individual step-sizes form. In this case, the step-size matrix is constructed as:

$$\mathbf{M}(n) = \mathrm{diag}\left[\mu_0(n),\ \mu_1(n),\ \ldots \mu_{L-1}(n)\right]; \qquad (16)$$
$$0 < \mu_i(n) < \mu_{max}, \quad i = 0 \ldots L-1;$$

where:

$$\mu_i(n) = \mu_i(n-1) + \rho e(n)u(n-i)\phi_i(n); \qquad (17)$$
$$\phi_i(n+1) = \phi_i(n) - \mu_i(n)|u(n-i)|^2\phi_i(n) + u(n-i)e(n). \qquad (18)$$

In both its forms, Benveniste's algorithm requires one parameter and the upper bound for the step size to run.

2.7. VS-LMS Algorithm by Kwong *et al.*

The algorithm given by Kwong *et al.*[11] is given by:

$$\mu'(n+1) = \alpha\mu(n) + \gamma e^2(n);$$
$$\mu(n+1) = \begin{cases} \mu_{max} & \text{if } \mu'(n+1) > \mu_{max}; \\ \mu_{min} & \text{if } \mu'(n+1) < \mu_{min}; \\ \mu'(n) & \text{otherwise;} \end{cases} \qquad (19)$$

where $0 < \alpha < 1$ and $\gamma > 0$ are tuning parameters, and $0 < \mu_{min} < \mu_{max}$ are chosen to provide tracking capability and stability, respectively. The authors claim that typical value for α, working well in many simulations they performed, is 0.97. The parameter γ influences both the speed of convergence and the EMSE, and it should be small — $4.8 \cdot 10^{-4}$ was used in the original paper.

The algorithm was developed with the goal to have the step size dependent on the square of the error. The authors' motivation was that the error is frequently large when fast adaptation is required, while the step size may be lowered when the error becomes low. Moreover, simple relation of the step size and the error made it possible to provide theoretical analysis of this VS-LMS algorithm, even in case of the nonstationary environment. The authors compared their results with the results obtained with the algorithms by Harris (Sec. 2.2), and obtained comparable performence.

Kwong's algorithm requires four parameters to run, including the upper bound for the step size. Two of them are the maximum and minimum step size, which usually do not interact with other parameters; therefore, the number of the parameters to adjust is still reasonable.

2.8. VS-LMS Algorithm by Evans *et al.*

The paper by Evans *et al.*[18] discusses two similar algorithms. The first one is identical with Harris's algorithm described in Section 2.2, the second differs only in the step size update equation (9), which is additive rather than multiplicative:

$$\mu_i(n+1) = \begin{cases} \mu_i(n) - \alpha & \text{if } e(n)u(n-i) \text{ alternates sign on } m_0 \text{ successive samples;} \\ \mu_i(n) + \alpha & \text{if } e(n)u(n-i) \text{ has the same sign on } m_1 \text{ successive samples;} \\ \mu_i(n) & \text{otherwise.} \end{cases} \qquad (20)$$

Naturally, the value α can no longer be equal to 2, but should be chosen as some small value (2^{-10} was used for the experiments presented by the authors). The authors claim that this algorithm gives slightly better performance that the algorithm defined by (9). The number of parameters parametrizing the algorithm is identical as in the case of Harris's algorithm.

2.9. VS-LMS Algorithm by Mathews *et al.*

Mathews's algorithm[19] is another algorithm that can use both the individual and common step sizes. In the first case the step-size matrix is again a diagonal matrix with the upper bound on each of the diagonal elements, as in Eq. (16). The individual step sizes are calculated as:

$$\mu_i(n) = \mu_i(n-1) + \rho e(n)e(n-1)u(n-i)u(n-i-1); \qquad (21)$$

where ρ is a small positive value allowing to control the convergence process. The authors used the values in range $10^{-4} \leq \rho \leq 6 \cdot 10^{-3}$ and claim that the choice does not influence the steady-state performance.

In the second case, common step size (also subject to the upper bound μ_{max}) is updated as:

$$\mu(n) = \mu(n-1) + \rho e(n)e(n-1)\mathbf{u}^T(n-1)\mathbf{u}(n). \quad (22)$$

For some hypothetical input sequences, the algorithm may fail to start when $\mu(0) = 0$; therefore, the authors suggest to initialize the step size with some small value. The choice of $\mu(0) > 0$ may also improve the initial speed of convergence of the algorithm.

The concept the algorithm is based on is to change the step size in a manner proportional to the negative of the gradient of the squared estimation error, with respect to the step size. An algorithm offering very good converge speed and small misadjustment resulted. Moreover, the authors claim that this algorithm offers "close-to-the-best-possible performance" when applied in nonstationary conditions.[19]

This algorithm requires two parameters and the upper bound for the step size to run, but one of them is the minimum step size, and the authors claim that the choice the other (ρ) is not critical.

2.10. VS-LMS Algorithm by Aboulnasr *et al.*

The algorithm by Aboulnasr *et al.*[12] is based on the algorithm by Kwong (see Eq. (19)) and the observation that the instantaneous energy of the error signal it uses may lead to unexpected behavior in the presence of measurement noise. Therefore, Aboulnasr proposes to calculate an estimate of the autocorrelation between $e(n)$ and $e(n-1)$, and use this estimate to control the step size instead of $e^2(n)$. The estimate may be calculated as:

$$p(n) = \beta p(n-1) + (1-\beta)\, e(n)e(n-1); \quad (23)$$

where $0 \ll \beta < 1$ is an exponential weighing factor controlling the averaging process. Then, the estimate should be used in calculation of $\mu'(n+1)$ as:

$$\mu'(n+1) = \alpha\mu(n) + \gamma p^2(n). \quad (24)$$

Finally, the same limits on the step size should be applied as in Eq. (19). Also, the meaning of the parameters α and γ is the same as in the case of Kwong's algorithm.

As stated previously, the proposed modification introduced by this algorithm makes it immune to the uncorrelated measurement noise. The authors claim that this raises the performance of the algorithm in case of stationary environments, and offers performance comparable with the algorithms by Kwong and Mathews in case of nonstationary environments. Unfortunately, the modification rises the total number of parameters parametrizing the algorithm up to five, which is a number unsuitable for many practical applications.[28]

2.11. VS-LMS Algorithm by Pazaitis *et al.*

A very original algorithm by Pazaitis *et al.*[13] uses the kurtosis of the error signal to control the step size. The authors propose two different equations for the step size update:

$$\mu(n) = \alpha|\text{Kurt}\,(e(n))\,|; \quad (25)$$

and

$$\mu(n) = \mu_{max}\left(1 - e^{-\alpha|\text{Kurt}(e(n))|}\right); \quad (26)$$

where α is a positive constant controlling both the speed of convergence and the excess MSE. The authors suggest that the value of α should be in range $[1, 10]$ for the update according to Eq. (26), whereas it should be approximately an order smaller for the update according to Eq. (25). The authors also observe that the simpler-to-use update by Eq. (25) may require additional upper bound to ensure convergence; therefore, only the algorithm defined by Eq. (26) will be considered in this paper.

To apply Eqs. (25)–(26) in practice, an estimate of the kurtosis must be calculated. The authors suggest to calculate this estimate as:

$$C_4^e(n) = \hat{E}\left\{e^4(n)\right\} - \rho(n)\hat{E}^2\left\{e^2(n)\right\}; \quad (27)$$

where $C_4^e(n)$ is the estimate, $\hat{E}$ is an estimate of the expected value, and $\rho(n)$ is used to trace the changes in the characteristics of the noise. The latter factor should be calculated recursively as:

$$\rho(n+1) = \rho(n) + \delta\,\text{sgn}\left(\hat{E}\left\{e^4(n)\right\} - \rho(n)\hat{E}^2\left\{e^2(n)\right\}\right)\hat{E}^2\left\{e^2(n)\right\}; \quad (28)$$

where δ is a small positive constant (the authors used $\delta = 0.01$ in their simulations).

The authors suggest to calculate the estimates of the expected values using rectangular window of some size, or to calculate them recursively as:

$$\hat{E}\left\{e^{2i}(n)\right\} = \beta\hat{E}\left\{e^{2i}(n-1)\right\} + (1-\beta)e^{2i}(n), \quad i = 1, 2 \quad (29)$$

(this paper uses the recursive calculation of the estimates).

Both the rectangular window size and the forgetting factor β are additional parameters that need to be selected before application of the algorithm; therefore, the number of parameters to adjust is equal to four, including the upper bound for the step size. This number is rather high and may be unsuitable for some practical applications.

The main advantage of the algorithms lies in the originality of using higher order statistics to adjust the step size. In theory, this should result in the algorithm immune to the disturbance noise, if the noise is Gaussian. However, the main advantage is also a main disadvantage, as in practice higher order statistics are hard to estimate.

2.12. VS-LMS Algorithm by Ang *et al.*

Ang *et al.*[20] proposed a simplification of Benveniste's algorithm given by Eqs. (14)–(15). The simplification applies to the gradient vector Eq. (15), which is now calculated as:

$$\boldsymbol{\phi}(n+1) = \alpha\boldsymbol{\phi}(n) + \mathbf{u}(n)e(n); \quad (30)$$

where α is a constant smaller than but close to one. The authors explain that the algorithm may be viewed as a filtering of the noisy gradient of $\mathbf{u}(n)e(n)$ with a first-order low-pass filter with transfer function $\frac{1}{1-\alpha z^{-1}}$. This should result in a more stable adaptation of the step size. Moreover, for $\alpha = 0$, this algorithm is reduced to Mathews's algorithm (Eq. (22)).

Ang's algorithm may also be used with the individual step sizes, in which case Eq. (18) is simplified to:

$$\phi_i(n+1) = \alpha\phi_i(n) + u(n-i)e(n). \tag{31}$$

Unfortunately, the modification by Ang *et al.* adds another parameter when comparing with Benveniste's algorithm, so the total number of parameters is equal to three, including the upper bound for the step size.

2.13. VS-LMS Algorithm by Benesty *et al.*

The algorithm by Benesty *et al.*[21] is given by:

$$\mu'(n) = \frac{1}{\delta + \mathbf{u}^T(n)\mathbf{u}(n)}\left(1 - \frac{\sigma_v}{\epsilon + \hat{\sigma}_e(n)}\right);$$
$$\mu(n) = \begin{cases} \mu'(n) & \text{if } \hat{\sigma}_e(n) \geq \sigma_v, \\ 0 & \text{otherwise}, \end{cases}; \tag{32}$$

where σ_v is standard deviation of the system noise (see below), $\hat{\sigma}_e(n)$ is an estimate of standard deviation of the error, and δ and ϵ are small positive constants to avoid division by zero.

The authors suggest to estimate the power of the error signal using the recursion:

$$\hat{\sigma}_e^2(n) = \lambda\hat{\sigma}_e^2(n-1) + (1-\lambda)e^2(n); \tag{33}$$

where the exponential parameter λ can be calculated as $\lambda = 1 - \frac{1}{KL}$, with $K \geq 2$.

The concept of the system noise $v(n)$ comes from an assumption that the desired signal $d(n)$ is a sum of the response of some optimal filter W_o and the zero-mean noise $v(n)$:

$$d(n) = \mathbf{w}_o^T\mathbf{u}(n) + v(n); \tag{34}$$

in this case, $\sigma_v^2 = E[v^2(n)]$. In some applications, the standard deviation of the system noise may be known before running the algorithm, but usually it must also be estimated, e.g. using an a posteriori error:

$$\varepsilon(n) = y(n) - \mathbf{w}^T(n+1)\mathbf{u}(n). \tag{35}$$

The estimation of $\hat{\sigma}_v^2 = E[\varepsilon^2(n)]$ may be performed using the recursion in Eq. (33).

The authors showed that the proposed algorithm performs better in acoustic echo cancellation simulations than the NLMS, giving faster convergence and lower excess MSE. However, the authors assumed the knowledge of the variance of the system noise σ_v^2 for these experimets.

The total number of parameters required by this algorithm may be different in different implementations. In the optimistic case, when we fix the δ and ϵ at some small value, and when we estimate both the variances with the same forgetting factor, only one parameter remains to be adjusted (the forgetting factor or the K multiplier). However, if we assume the knowledge of σ_v^2, this variance becomes the second parameter. The second parameter also appears when we decide to estimate both the variances with different forgetting factors. Thus, the author's claim that the algorithm is "nonparametric" should be treated as an exaggeration.

2.14. VS-LMS Algorithm by Wahab *et al.*

The algorithm by Wahab *et al.*[22] was developed by calculation of the optimal step size that minimizes the cost function defined as a quadratic norm of the difference between the new filter weights $w(n+1)$ and the optimal ones. Practical implementation of their algorithm is given by:

$$\mu(n) = \frac{e^2(n) - e(n)\hat{v}(n)}{e^2(n)\|\mathbf{u}(n)\|^2}; \tag{36}$$

where $\hat{v}(n)$ is an estimate of the noise defined as in Eq. (34). The authors propose to estimate the noise as:

$$\hat{v}(n) = g(n)e(n); \tag{37}$$

where

$$g(n) = 1 - \exp\left(\frac{\alpha\hat{\sigma}_v^2}{\hat{\sigma}_u^2(n)(\rho\hat{\sigma}_e^2(n) - \hat{\sigma}_v^2)}\right); \tag{38}$$

where $\hat{\sigma}_v^2$ is the system noise power, $\sigma_u^2(n)$ is the input signal power, $\sigma_e^2(n)$ is the error signal power, $\rho \geq 1$ and α are positive constants used to make a compromise between tracking capabilities and the EMSE (for calculation of $\hat{\sigma}_v^2$ and $\hat{\sigma}_e^2$ see Section 2.13). The authors suggest to estimate the input signal power using rectangular window: $\hat{\sigma}_u^2(n) = \|\mathbf{u}(n)\|^2/L$.

The authors claim that the derivation of their algorithm takes the disturbance noise into account; therefore their algorithm outperforms the algorithms by Ang or Aboulnasr in noisy environments. Moreover, the authors claim that their algorithm is less influenced by inproper choice of the adjustment parameters.

Please note that the algorithm by Wahab is equivalent to the NLMS in case of noise-free environment ($v(n) \equiv 0$). Note also the possible problems in practical implementation of the algorithm introduced by two subtractions, which may make the step size negative. Another disadvantage is that this algorithm is parametrized by as many as four parameters.

2.15. VS-LMS Algorithm by Hwang *et al.*

The algorithm by Hwang *et al.*[23] is based on the algorithm by Kwong given by Eq. (19). The authors observed that the parameter γ from Eq. (19) should be large when fast convergence is required (e.g. at the start of an operation), but should be small during steady-state operation and when the system noise is high. The authors suggest to adjust this parameter using an estimate of the correlation between the input and the error in the vector form:

$$\hat{\mathbf{p}}(n) = \beta\hat{\mathbf{p}}(n-1) + (1-\beta)\mathbf{u}(n)e(n); \tag{39}$$

where $0 < \beta < 1$ is an exponential parameter. Then, the step size should be adjusted as:

$$\mu(n+1) = \alpha\mu(n) + \gamma_s\|\hat{\mathbf{p}}(n)\|^2e^2(n); \tag{40}$$

with $\gamma_s > 0$.

The authors demonstrate the advantages of the algorithm using adaptive channel estimation application: the algorithm converges fast despite of large ranges of γ_s and different levels of noise.

Unfortunately, the modification raises the number of parameters required to run the algorithm up to five, including the upper bound for the step size. This may create a serious disadvantage for many practical applications.[28]

2.16. VS-LMS Algorithm by Wang *et al.*

Algorithm by Wang *et al.*[24] is given by:

$$\mu'(n) = \frac{\sum_{i=1}^{n} \varepsilon(i)e(i-1)\mathbf{u}^T(i-1)\mathbf{u}(i)}{\sum_{i=1}^{n} e^2(i-1)\mathbf{u}^T(i-1)\mathbf{u}(i)}; \tag{41}$$

$$\mu_{min} < \mu'(n) < \mu_{max};$$

$$\mu(n) = \frac{\mu'(n)}{\mathbf{u}^T(n)\mathbf{u}(n)}; \tag{42}$$

where:

$$\varepsilon(n) = d(n) - \mathbf{w}^T(n-1)\mathbf{u}(n). \tag{43}$$

The authors suggest that the lower bound on $\mu'(n)$ may be set to any small positive value, e.g. 10^{-10}, and the upper bound may be set to $\mu_{max} = \mathbf{u}^T(n)\mathbf{u}(n)$. If such values are used, the algorithm is the other algorithm of the two mentioned in Section 1 that *do not require any parameters to run*, which is its greatest advantage. Judging by the simulation results the authors present, this algorithm offers performance comparable with other VS-LMS algorithms, e.g. Aboulnasr's algorithm.

2.17. VS-LMS Algorithm by Zou *et al.*

The algorithm by Zou *et al.*[14] combines the algorithms by Kwong (Eq. (19)) and by Aboulnasr (Eq. (24)) and is composed of three steps. In the first step, the new step size is calculated as:

$$\mu(n+1) = \alpha\mu(n) + \gamma p^2(n);$$

$$\mu_{min} < \mu(n+1) < \mu_{max}; \tag{44}$$

where $0 < \alpha < 1$ and $\gamma > 0$ are tuning parameters (as in Aboulnasr's algorithm). In the next step, the time-averaged correlation between two successive error signal samples $p(n)$ is updated as:

$$p(n+1) = (1 - \beta(n))\, p(n) + \beta(n)e(n)e(n-1). \tag{45}$$

Finally, the new time-averaged error signal power $\beta(n)$ is calculated as:

$$\beta(n+1) = \eta\beta(n) + \lambda e^2(n);$$

$$\beta_{min} < \beta(n+1) < \beta_{max}; \tag{46}$$

where $0 < \eta < 1$ and $\lambda > 0$ are tuning parameters (as in Kwong's algorithm).

The authors observe that $0 < \beta(n) < 1$; therefore, one should choose $\beta_{max} < 1$. The authors claim that the algorithm combines the advantages of the algorithms by Kwong and Aboulnasr: good ability to cope with the noise and good tracking capability. Moreover, the authors claim that very good convergence speed and low misadjustment are achieved, too. However, the algorithm requires *eight parameters* to be adjusted—this is definitely too many to use the algorithm in practical applications.[28]

3. UPPER BOUND FOR THE STEP SIZE

The majority of the algorithms described above require the upper bound for the step size μ_{max}. In fact, the only algorithms that do not require the choice of μ_{max} are NLMS and algorithms by Mikhael (Sec. 2.3), by Benesty (Sec. 2.13) and by Wahab (Sec. 2.14). Please note that μ_{max} must be chosen very carefully in order to guarantee convergence as well as not impose too much restrictions on the step size. Moreover, the upper bound for the step size may depend on the experiment conditions (see Section 4.3 for an example). This is quite opposite of the minimum step size, which can be chosen very roughly.

It is possible to simplify the choice of the upper bound for the step size by assuming it to be similar to the LMS algorithm stability sufficient condition:[29]

$$\mu_{\text{max}}(n) = \varepsilon \frac{2}{\mathbf{u}^T(n)\mathbf{u}(n)}; \tag{47}$$

where $0 < \varepsilon < 1$ is a scaling factor. Although it may seem as substitution of one upper bound by another, there are substantial differences. Namely, contrary to the (constant) μ_{max}, the ε factor may be roughly chosen from a well-defined range $(0 \ldots 1)$ (theoretically) or $[0.5 \ldots 0.9]$ (in practice). For example, a value 0.8 (assumed for the experiments presented below) or 0.9 will work well in many typical applications. The choice of ε is so easy that we may assume that this technique allows us to lower the number of parameters for each algorithm using μ_{max} by one. On the other hand, calculation of the $\mu_{\text{max}}(n)$ in each iteration requires additional processor power.

To check how the proposed modification influences stability and performance of the VS-LMS algorithms, in the next section we will show simulations with constant upper bound for the step size as well as with modification defined by Eq. (47).

4. SIMULATIONS

The VS-LMS algorithms described in the previous section have been tested in three typical applications: system identification, adaptive line enhancement (ALE) and adaptive noise cancellation (ANC).[33] The main problem that occurred during the simulations and concerned especially algorithms with more than two parameters was that it was not easy to adjust the parameters because of parameter interactions. This remark does not apply to the maximum and minimum step sizes, which are relatively easy to choose.

In this sense, the most difficult algorithms to parametrize were those by Aboulnasr, Hwang, Zou, and Wahab. Algorithms presenting moderate complication (two parameters to adjust, except for the minimum and maximum step sizes) are those by Kwong, Shan, Ang and Benesty. This group also includes algorithms by Harris and Evans, which have three parameters, but two of them are integers in the range from 1 to 3.

Another problem was the need to readjust algorithms for different applications. Moreover, the need to readjust the algorithm for one application (ANC) after changing the noise level has also arisen during the experiments.

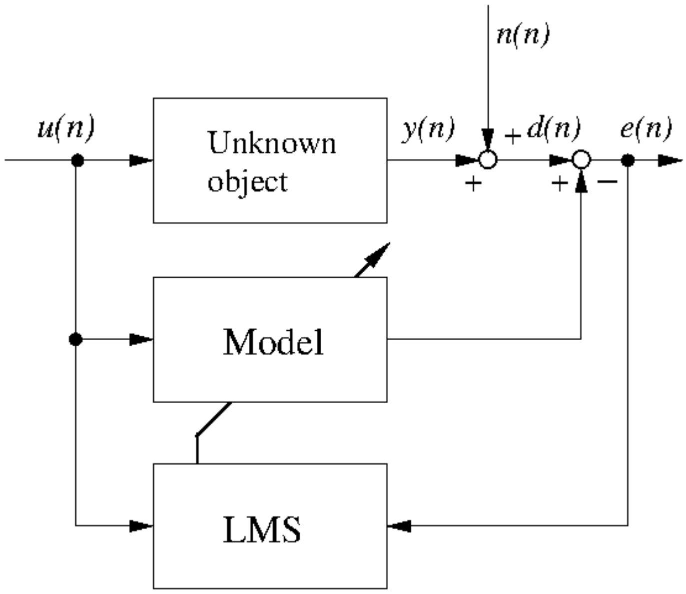

Figure 2. System Identification block diagram.

Despite these difficulties, an effort was taken to adjust the algorithms in a way that allows them to obtain the best possible results with regards to the quantities discussed below. One more remark must be observed: the adjustment of the parameters was performed with the aim of obtaining the behavior which really exhibits the step-size variation. This remark is important because it was very easy to adjust the parameters in the way that the VS-LMS algorithm operated with the (almost) maximum allowed step size. Moreover, this behavior sometimes minimized the sum of MSE — mainly due to maximization of the speed of convergence. However, it did not allow it to minimize the misadjustment and variation of the parameters of an adaptive filter during the steady state. Therefore, such adjustment was considered wrong.

4.1. Simulation of System Identification

The first application the VS-LMS algorithms were tested against is system identification — see Fig. 2. In this application, the LMS algorithm input signal $u(n)$ is the signal used to excite the unknown object, while the LMS algorithm desired signal $d(n)$ is a sum of the object output signal $y(n)$ and the output noise $n(n)$ (the disturbance). Observe that in this case the output noise is the same as the system noise $v(n)$ in Eq. (34). This desired signal is compared to the output of the identified model to produce the error signal $e(n)$.

System identification presents many challenges,[30] but for the purpose of this paper, a relatively simple case of identification of white-noise excited FIR filter was chosen. Moreover, the exact match in the structure of the object and the model was assumed (no modeling error). This, together with the control over the output noise power, allowed us to observe some important differences in the behavior of the VS-LMS algorithms.

It should be noted that in case of an identification of a stationary FIR object, the LMS filter should converge to the Wiener solution.[1] Therefore, it is possible to perform the zero-order analysis of the steady-state phase of the LMS adaptation, with the assumption of the small step size. If we define the instantaneous MSE as:

$$J(n) = E(|e(n)|^2); \tag{48}$$

we may express this MSE as:

$$J(n) = J_{\text{min}} + J_{\text{ex}}(n); \tag{49}$$

where J_{min} is the minimum achievable error, and $J_{\text{ex}}(n)$ is called excess MSE (EMSE).

Assuming that the identified model converges to the original filter, the minimum achievable MSE is equal to the variance of the system noise $n(n)$:

$$J_{\text{min}} = E(n^2(n)). \tag{50}$$

Furthermore, form the small step-size theory it follows that in the steady state the MSE can be expressed as:

$$J(\infty) = J_{\text{min}} + \mu J_{\text{min}} \sum_{k=1}^{L} \frac{\lambda_k}{2 - \mu\lambda_k} \approx J_{\text{min}} + \frac{\mu J_{\text{min}}}{2} \sum_{k=1}^{L} \lambda_k; \tag{51}$$

where λ_k are the eigenvalues of the input signal autocorrelation matrix.[1] Thus, the EMSE is approximately equal to:

$$J_{\text{ex}}(\infty) \approx \frac{\mu J_{\text{min}}}{2} \sum_{k=1}^{L} \lambda_k; \tag{52}$$

which means that it depends on the variance of the system noise. For this reason it is convenient to define additional quantity, called *misadjustment*, as:

$$\mathcal{M} = \frac{J_{\text{ex}}(\infty)}{J_{\text{min}}} \approx \frac{\mu}{2} \sum_{k=1}^{L} \lambda_k. \tag{53}$$

Please note that the misadjustment depends only on the step size and the properties of the input signal $u(n)$ (in the form of the eigenvalues of the autocorrelation matrix), and *does not* depend on the system noise $n(n)$.

In the experiments described below EMSE was used to evaluate each of the algorithms in a quantitative manner in the form of the sum of the EMSE for the whole experiment:

$$\sum \text{EMSE} = \sum_{n=0}^{N} J_{\text{ex}}(n); \tag{54}$$

where N is the number of iterations in each experiment ($N = 4096$ in case of identification experiments). This parameter shows overall performance of the algorithm, combining the speed of convergence and the resulting EMSE. However, to observe the last two quantities separately, the estimate of the misadjustment was also calculated, as the mean value of 100 samples of EMSE, divided by the variance of the system noise. Time of convergence was calculated as a number of samples after which the EMSE falls below the value 10^{-2}:

$$\tau = \min_n \left[J_{\text{ex}}(n) < 10^{-2} \right]. \tag{55}$$

The last quantity calculated for evaluation of the identification performance was the variance of two of the identified

Table 1. Results of identification experiments averaged over 250 runs for SNR = 20 dB. A dash in the 'Modif' column means that the particular algorithm does not use the upper bound for the step size; and thus the modification proposed in Section 3 does not apply.

Algorithm	Excess MSE		End EMSE		Misadjustment		Time		var(w_1)		var(w_2)	
	Orig.	Modif.	Orig.	Modif.	Orig.	Modif.	Orig.	Modif.	Orig.	Modif.	Orig.	Modif.
LMS	357.9	—	4.93e-04	—	4.93e-02	—	329	—	5.02e-05	—	1.91e-05	—
NLMS	356.4	—	6.27e-04	—	6.27e-02	—	324	—	3.71e-05	—	3.89e-05	—
Harris	612.6	344.8	1.14e-03	2.60e-03	1.14e-01	2.60e-01	1115	337	7.04e-05	3.05e-04	1.47e-05	2.62e-05
Mikhael	107.7	—	4.43e-03	—	4.43e-01	—	96	—	5.86e-04	—	4.91e-04	—
Kwong	145.2	107.0	1.48e-04	6.56e-05	1.48e-02	6.56e-03	144	87	5.23e-06	1.80e-06	1.94e-06	8.95e-07
Evans	201.8	117.9	9.20e-04	2.60e-03	9.20e-02	2.60e-01	149	92	1.63e-05	2.00e-04	6.95e-05	2.51e-04
Shan_correlation	174.9	145.4	2.15e-04	8.61e-05	2.15e-02	8.61e-03	131	88	1.03e-05	1.52e-05	3.85e-06	1.52e-05
Shan	239.2	203.0	1.44e-03	2.26e-03	1.44e-01	2.26e-01	201	110	7.11e-07	1.82e-07	4.88e-06	1.40e-05
Benveniste	162.5	112.8	2.23e-04	5.08e-04	2.23e-02	5.08e-02	147	100	6.83e-06	5.27e-05	1.63e-05	6.64e-05
Benveniste_indiv	156.2	∞	4.25e-04	∞	4.25e-02	∞	199	0	8.12e-06	2.07e-04	2.06e-05	5.67e-05
Karni	146.2	116.7	4.19e-04	2.51e-03	4.19e-02	2.51e-01	194	106	7.69e-05	1.91e-04	1.88e-05	2.48e-04
Mathews	223.3	149.8	6.62e-04	7.46e-04	6.62e-02	7.46e-02	204	152	9.11e-06	1.25e-05	6.39e-05	3.15e-06
Mathews_indiv	178.8	126.6	1.11e-03	2.58e-03	1.11e-01	2.58e-01	187	165	1.71e-05	2.87e-04	6.60e-05	3.09e-04
Aboulnasr	164.4	145.7	1.49e-04	1.39e-04	1.49e-02	1.39e-02	134	149	2.13e-09	4.41e-09	8.37e-09	1.10e-09
Ang	160.5	121.7	1.01e-04	2.85e-04	1.01e-02	2.85e-02	145	128	1.25e-06	4.72e-05	1.72e-06	4.29e-05
Ang_indiv	152.3	∞	3.75e-04	∞	3.75e-02	∞	174	0	2.27e-06	1.53e-04	1.15e-05	1.61e-05
Hwang	143.0	128.5	1.05e-04	1.19e-05	1.05e-02	1.19e-03	133	115	3.13e-07	8.70e-08	1.11e-07	3.39e-07
Wang	559.9	—	7.34e-04	—	7.34e-02	—	579	—	7.13e-05	—	7.72e-05	—
Zou	153.3	139.8	9.97e-05	1.20e-04	9.97e-03	1.20e-02	134	113	3.97e-10	1.19e-09	4.69e-10	1.41e-09
Pazaitis	143.3	110.0	3.86e-04	2.35e-04	3.86e-02	2.35e-02	136	151	2.19e-09	2.74e-10	3.21e-09	1.17e-09
Pazaitis	140.1	139.8	1.00e-04	5.21e-05	1.00e-02	5.21e-03	128	486	1.16e-08	2.30e-07	1.78e-08	1.26e-06
Benesty	71.7	—	9.78e-04	—	9.78e-02	—	79	—	1.49e-05	—	6.44e-05	—
Wahab_optimal	95.5	—	1.02e-03	—	1.02e-01	—	103	—	1.28e-04	—	6.27e-05	—

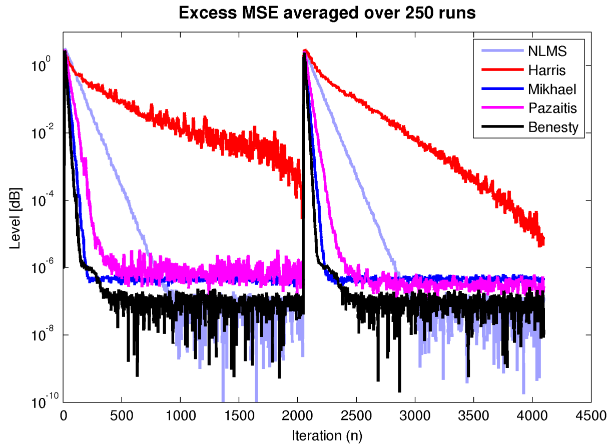

Figure 3. Excess MSE in identification experiments for selected algorithms.

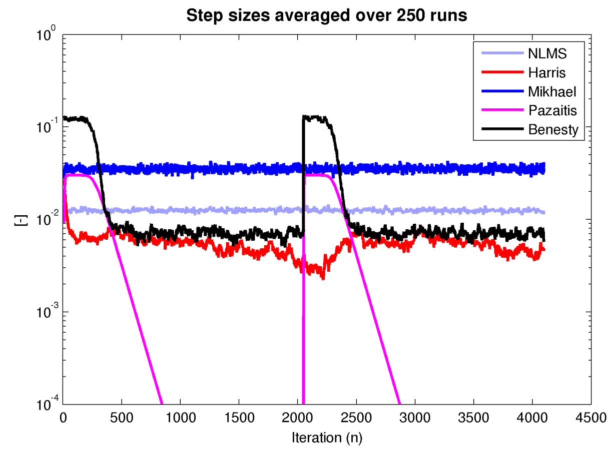

Figure 4. Step sizes in identification experiments for selected algorithms.

coefficients calculated during the steady state at the end of the experiment.

The results of the identification experiments are presented in Table 1. This results were obtained after averaging 250 individual runs, with different excitation sequences and system noise sequences. The identified object was in a form of FIR filter with initial coefficients 0.5, 1.1, 0.8, 0.7, 0.6, 0.5, 0.4, 0.3, 0.2, 0.1. In the middle of the experiment, that is after 2048 iterations, the coefficients were changed to 0.3, -0.5, 0.2, 0.8, 0.5, 0.3, 0.1, 0.1, 0.0, 0.0. The signal to noise ratio was equal to 20 dB, and the assumed minimum and maximum step sizes were equal to 10^{-7} and 0.03. The table presents results for the original algorithm, i.e. the algorithm operating with $\mu_{\max} = 0.03$ as well as for the algorithm operating with variable $\mu_{\max}$, as described in Section 3.

By observing the sum of EMSE for the original algorithms we may conclude that the best algorithm is the algorithm by Benesty, the second is the algorithm by Wahab, and the third the algorithm by Mikhael. By consulting the time of convergence we notice that the algorithm by Benesty is the best due to its speed of convergence (the second by the same criterion is the algorithm by Mikhael, the third by Wahab). On the other hand, the algorithm by Benesty exhibits poor steady-state performance, poorer even than LMS and NLMS — the conclusion that arises after examination of the misadjustment. So, if speed of convergence is not critical, but accuracy is in value, the best algorithm is the one by Zou, beating only slightly the one by Pazaitis (second form, Eq. (26)) and by Hwang. Finally, the variance of the estimates allows us to award the algorithms by Zou, Pazaitis (both forms), and Aboulnasr.

With the analysis of the same quantities for the algorithms using variable maximum step size, we may conclude that this modification usually influences the algorithms positively. Additionally, the speed of convergence can be significantly improved, as can be seen in case of the algorithms by Harris, by Shan, or by Karni. Sometimes, even if the speed of convergence is worse, the overall performance is comparable due to better steady-state performance (e.g. the algorithm by Aboulnasr and by Pazaitis, second form).

Figure 3 presents the excess MSE in the identification experiments for selected algorithms. Considering the NLMS as a reference, we observe that the algorithm by Harris (included here for historical reasons, as the next VS-LMS algorithm after the NLMS) is dramatically slower to converge. On the other hand, the algorithms by Mikhael and Pazaitis, although faster to converge, do not achieve the excess MSE as low as the NLMS. Only the algorithm by Benesty maintains both the fast convergence speed and low excess MSE.

Figure 4 shows the step sizes ($\mu(n)$) used by the algorithms discussed above during the experiments. We observe that the algorithms result in different values of the step sizes, compared to the NLMS. The algorithm by Harris decreases the step size rapidly at the begining of the simulation; therefore, it is very slow to converge. The algorithm by Mikhael uses approximately three times higher value of the step size than the NLMS; thus it converges fast, but results in slightly higher excess MSE in the steady state. The algorithms by Pazaitis and Benesty use what we may consider to be a reasonable approach: they start with higher step sizes, and start to decrease them once the initial convergence is finished (compare with Fig. 3). However, the algorithm by Benesty exploits this technique much more efficiently that the algorithm by Pazaitis, and therefore it achieves both the fast convergence speed and the low excess MSE.

4.1.1. Further observations

More conclusions can be drawn if we analyze the system identification results obtained for different signal to noise ratios (the results of experiments, including the plots of the MSE, the EMSE, the misadjustment and the step sizes, are organized in the form of a web page, and available at http://zpss.aei.polsl.pl/dbismor/vslms/; the results can also be e-mailed as a compressed archive by emailing a request to Dariusz.Bismor@polsl.pl). From Eq. (52), it follows that different EMSE levels should be observed for different SNRs: the lower the system noise, the lower the EMSE should be observed. On the other hand, the misadjustment should not depend on the system noise variance and SNR (Eq. (10)). Such behavior was *not* observed for the algorithms by Harris, by Kwong, by Shan, by Karni, and by Wahab. For those algorithms the EMSE tended to reach similar, high values for different SNRs. This means that the algorithms mentioned above may give higher than expected EMSE values.

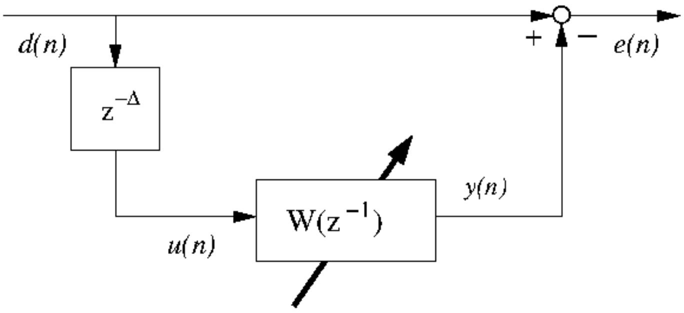

Figure 5. Adaptive line enhancer block diagram.

4.2. Simulation of Adaptive Line Enhancement

The Adaptive Line Enhancement (ALE), introduced by Widrow in 1975, is a technique used to detect highly correlated signals (mainly sinusoids) buried in a wideband noise.[2] Nowadays, ALE is used in many applications, e.g. instantaneous frequency estimation, spectral analysis, and speech enhancement.[31,32] The block diagram of the adaptive line enhancer (ALE) is presented in Fig. 5. The input signal to the ALE, $d(n)$, is usually a mixture of highly correlated signals (e.g. sines) and uncorrelated signals (e.g. white noise or speech recording). This signal is the desired signal for the adaptive LMS filter, while its delayed version constitutes the LMS input signal: $u(n) = d(n - \Delta)$. The delay, Δ, is also called decorrelation delay.[1]

In the experiments presented below, the input signal to the ALE was a short (1.8 s) recording of speech contaminated with four sine signals or with chirp signal. This application tests completely different aspects of the VS-LMS algorithms, as the speech recording can be considered to be a non-stationary signal. Thus, the ALE filter coefficients must be constantly adjusted, except for the short periods between syllables, and only in case of the contamination with the four sines. In case of the chirp signal, its frequency changes during the whole experiment, and no steady state occurs at all.

The performance of the VS-LMS algorithms in the ALE application was evaluated by the means of two quantities. The first one was the sum of MSE during the whole experiment. Please note that excess MSE could not have been used due to the lack of the Wiener filter model, which implies impossibility to calculate the system noise. Moreover, even the calculation of MSE was difficult due to the fact that ALEs may have different amplifications (gains). Therefore, some scaling was necessary before comparing the original speech signal with the ALE output $e(n)$. Scaling by the maximum absolute value was chosen in this case, with the omission of the first 1000 samples to account for the zero initial conditions.

The second quantity used to compare the algorithms performance was the final signal to noise ratio (SNR). This quantity was calculated by the means of the spectrum of the error signal $e(n)$. It was observed that the spectra of the speech recording and the contaminating signals did not overlap during the last 400 ms of the recording. This allowed us to calculate the power of the speech recording and the contaminating signal (after filtration) separately, in different frequency bands.

The speech signal was recorded with the sampling frequently 8 kHz. The ALE had 10 coefficients, and the decorrelation delay was equal to 10. In the case of the four sines, the frequencies were 1.5, 1.8, 2.5 and 3.7 kHz. In case of the chirp signal, the frequency range was 100–3500 Hz. The minimum and maximum step sizes were 10^{-5} and 0.25. The results of the experiments obtained after averaging 250 individual runs, are presented in Table 2.

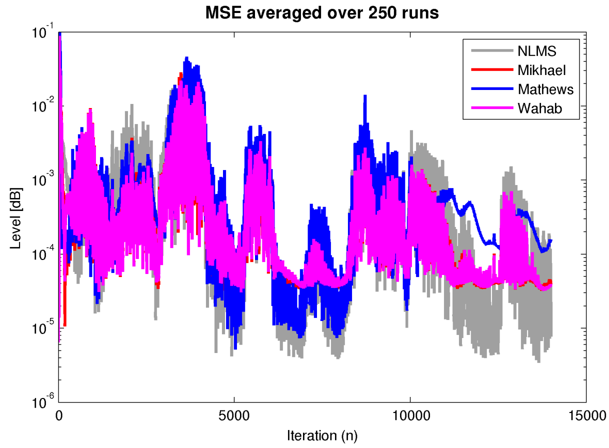

Figure 6. MSE in ALE experiments for selected algorithms.

For the chirp signal, the algorithm by Wahab produced the lowest sum of MSE, while the algorithm by Mikhael was only slightly worse, and the algorithm by Wang was third. However, if the SNR is considered, none of these algorithms perform as well as algorithms by Mathews (with individual step sizes), by Ang (both versions) and even the NLMS.

Figure 6 presents the MSE in the ALE experiments with the chirp signal for the selected algorithms. Treating the NLMS as a reference, we observe that the algorithm by Mathews results in a very similar MSE curve during most of the simulation. Near the end of the experiment, the MSE for this algorithm is noticably higher. The algorithms by Mikhael and Wahab, on the other hand, result in different MSE curves, but very similar to each other. The level of the MSE they produce is comparable with the level produced by the NLMS algorithm.

Figure 7 presents the value of the first filter coefficient during the experiments with the chirp signal. From the figure it is clear that the coefficient does not reach the steady state. However, the values it takes are very similar for all the presented algorithms.

For the four sines signal, and judging by the sum of MSE, the best algorithms are those by Shan, Benveniste, and Benesty. But judging by the SNR, the best algorithms are the one by Evans, Ang, and Benesty.

In the authors' opinion, the SNR better represents the ability of an algorithm to attenuate unwanted contamination — this observation was confirmed by listening to the played error signal. If, for example, the SNR was poor (close to zero or negative), the comprehension of the filtered speech was difficult. Following this observation, we can distinguish VS-LMS algorithms unsuitable for ALE, which certainly are algorithms by Harris, Kwong, Shan, Aboulnasr, Wang, Zou, and Pazaitis. Also, algorithms by Benveniste, Mathews (version with the common step size), and Hwang may not work as well as the others.

Table 2. Results of line enhancer experiments averaged over 250 runs, ALE length: 10. A dash in the 'Modif' column means that the particular algorithm does not use the upper bound for the step size; and thus the modification proposed in Section 3 does not apply.

Algorithm	Chirp				Four sines			
	∑MSE		Final S/N		∑MSE		Final S/N	
	Orig.	Modif.	Orig.	Modif.	Orig.	Modif.	Orig.	Modif.
LMS	14.1	—	26.3	—	20.4	—	18.2	—
NLMS	15.8	—	27.0	—	20.0	—	16.9	—
Harris	22.4	28.4	5.3	5.6	31.5	31.0	-15.7	-18.5
Mikhael	10.5	—	17.7	—	20.1	—	17.3	—
Kwong	43.3	25.1	1.3	1.3	20.9	20.8	8.2	6.4
Evans	24.0	16.6	12.5	13.7	20.6	20.0	18.8	18.0
Shan_correlation	26.2	12.5	-2.1	-2.2	19.4	19.8	12.6	11.4
Shan	22.0	15.0	-3.5	-3.4	19.5	20.0	8.4	10.7
Benveniste	13.1	11.0	20.4	17.5	19.5	19.3	6.7	5.9
Benveniste_indiv	14.9	11.6	22.3	19.7	19.7	19.6	8.2	8.5
Karni	25.5	19.6	12.3	18.1	22.2	22.5	17.6	17.2
Mathews	20.8	19.9	5.6	5.6	24.1	24.8	3.1	7.0
Mathews_indiv	15.8	13.8	27.3	25.8	20.6	20.1	16.5	17.0
Aboulnasr	31.3	28.5	-2.0	-1.7	21.3	21.2	5.0	4.1
Ang	16.4	11.9	27.2	21.8	20.1	19.9	18.1	18.9
Ang_indiv	18.9	12.4	27.2	22.9	20.3	20.0	17.2	17.0
Hwang	48.0	22.4	5.0	5.0	21.4	20.7	6.6	7.1
Wang	12.5	—	7.3	—	113.6	—	-29.9	—
Zou	46.4	35.5	0.8	1.1	21.7	21.4	13.2	13.8
Pazaitis	46.7	26.2	-0.7	-0.0	21.8	22.4	15.7	17.2
Pazaitis	30.5	22.7	-0.6	0.2	21.6	21.9	8.8	18.1
Benesty	12.9	—	26.6	—	19.6	—	18.1	—
Wahab_optimal	9.8	—	16.9	—	20.1	—	17.2	—

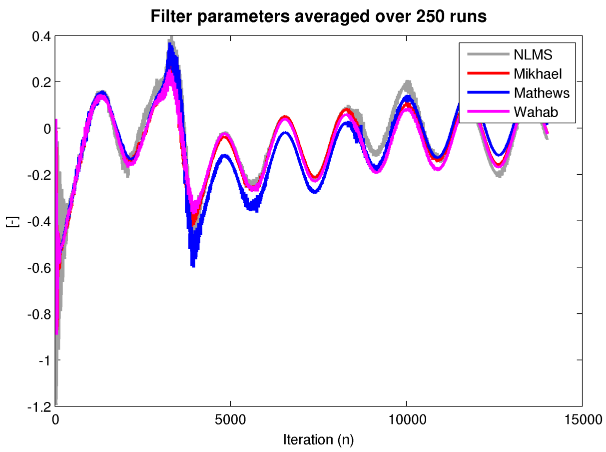

Figure 7. First filter coefficient in ALE experiments for selected algorithms.

It must also be noted that introduction of the variable maximum step-size modification does not always positively influences the performance, especially if we judge the algorithms by the sum of MSE. However, if we consider the SNR only, the set of algorithms for which the performance is significantly reduced is limited to the algorithms by Karni and Ang.

4.2.1. Further observations

The best way to evaluate the ALE performance is by analyzing the spectrograms (available at http://zpss.aei.polsl.pl/dbismor/vslms/). By comparing the spectrograms for the four sines signal, we immediately observe complete failure of the algorithms by Harris and Wang. We also notice very good results obtained with the NLMS and the algorithms by Mikhael, by Evans, by Karni and by Benesty — no trace of the four sines can be observed in the spectrograms for those algorithms. This group may be extended over the algorithms by Pazaitis, if we introduce the variable maximum step size modification discussed in Section 3.

By analyzing the spectrograms for the chirp signal, we observe that it is not possible to remove the constantly changing chirp signal completely with this setup. However, the NLMS and the algorithms by Mathews (individual step sizes), Ang, and Benesty are doing a very good job to weaken the power of the chirp considerably. By analyzing the step sizes, we observe that the most efficient strategy here is to keep the step size as high as possible during the whole experiment.

4.3. Simulation of Adaptive Noise Cancellation

The Adaptive Noise Cancellation (ANC) block diagram is presented in Fig. 8. The diagram is similar to the system identification, except for the presence of the output noise $n(n)$. However, the conditions and goals of operation of the two systems are different. One of the differences is in the unknown system dynamic ($P(z^{-1})$ in Fig. 8). In case of the system identification, we seek for the model of this dynamic, while

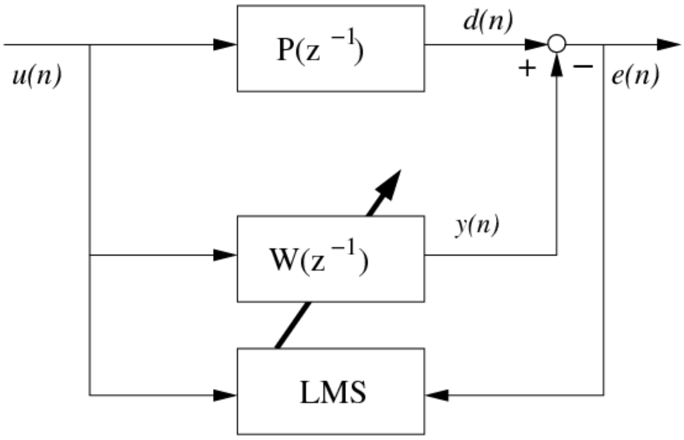

Figure 8. Adaptive noise cancellation block diagram.

in case of the ANC, the dynamic is assumed to be too difficult to be modeled in the whole frequency range. For example, in the experiments described below, the dynamic $P(z^{-1})$ was nonstationary and was implemented as a bank of 300-th order FIR filters switched each 3 seconds, while the ANC filter had only 16 or 128 coefficients.

Another difference is the input signal $u(n)$. In case of the system identification, we usually employ persistently exciting signals of sufficient degree (white noise, if possible). In case of the ANC, we usually have no chance to choose the input signal, which often contains a mixture of narrow-band signals (e.g. single tones) and band-limited noise. In the experiments described below, the input signal consisted of two sines, one with frequency 112 Hz and amplitude 3 and the second with frequency 200 Hz and amplitude 1. The sines were embedded in an amount of white noise with different variances.

The performance of the VS-LMS algorithms in ANC application was evaluated by the means of three quantities. The first one was again the sum of MSE during the whole experiment. The second was the MSE obtained during the steady state of operation, and it will be referred to as 'Final MSE'. Please note that misadjustment cannot be used because there was no additional noise, which means that $J_{\min} = 0$ in Eq. (53). The third quantity used to evaluate the performance of the algorithms was the variance of the ANC filter coefficient w_0 during the steady-state operation.

The results of the experiments, with the ANC filter length 16, obtained after averaging 250 individual runs are presented in Table 3. By analyzing the results for the variance of the wideband noise 10^{-2} we come to a surprising conclusion that none of the VS-LMS algorithms performed better than the NLMS algorithm — this is clear from both the sum of MSE and the Final MSE. Slightly worse results are obtained with the algorithms by Mathews (both versions), Karni, Ang (with individual step sizes), and Evans. Spectacular failure of the algorithm by Wang should also be noted, as it is one of the only two algorithms that does not require any parameters to run. Another conclusion is that very small variance of the coefficients during the steady state, as e.g. in case of the algorithm by Pazaitis, is not correlated with high overall performance.

In case of the wideband noise variance 10^{-4} the advantage of the NLMS algorithm is no more very clear. Although it still produces the smallest final MSE, the sum of MSE

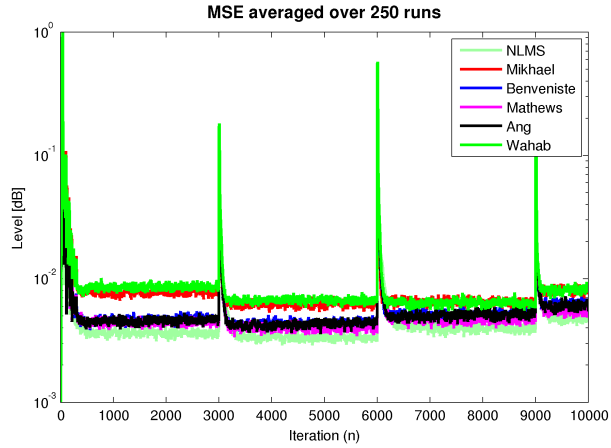

Figure 9. MSE in ANC experiments for selected algorithms.

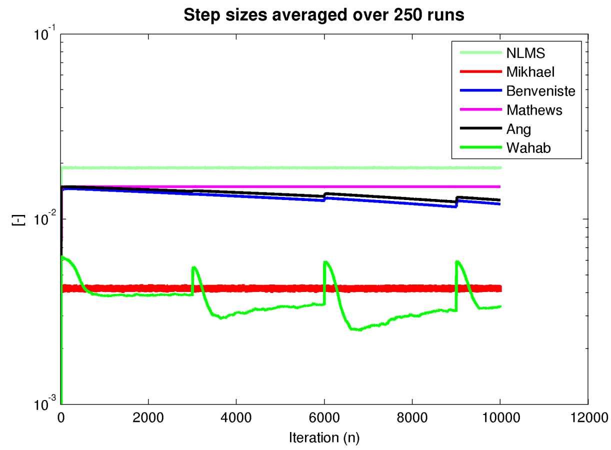

Figure 10. Step sizes in ANC experiments for selected algorithms.

is smaller for other algorithms, such as those by Evans and Karni. Other algorithms with similar performance are correlation LMS and those by Pazaitis, Ang (with individual step sizes), Shan, Benveniste (with individual step sizes), Kwong, and Hwang. Again, the algorithm by Wang failed to operate satisfactorily.

It must be noted that the majority of the algorithms had to be readjusted when switching from the wideband noise variance 10^{-4} to 10^{-2} — because otherwise they failed to maintain convergence. This only does not apply the NLMS and the algorithms by Harris, Mikhael, Evans, Shan, and by Wang. The fact that the NLMS did not need to be readjusted emphasizes its usefulness in ANC applications.

By analyzing the algorithms with variable maximum step-size modification, we may conclude that this modification usually does not degrade the algorithm's performance. On the contrary, the modification usually increased the performance slightly, especially in case of higher wideband noise variance. The algorithms by Karni and Benveniste are the examples.

Figure 9 presents the MSE curves for the wideband noise 10^{-2} for the selected algorithms, and Fig. 10 shows the step sizes for those experiments. From the figures it is clear that, despite different step size strategies, the algorithms show very similar speed of convergence. The only noticable difference is in the final MSE during the stead-state phases, which is slightly higher for the algorithms by Mikhael and Wahab. The step

Table 3. Results of adaptive noise cancellation experiments averaged over 250 runs, ANC filter length: 16. A dash in the 'Modif' column means that the particular algorithm does not use the upper bound for the step size; and thus the modification proposed in Section 3 does not apply.

Algorithm	Noise variance 1e-2						Noise variance 1e-4					
	$\sum$MSE		Final MSE		var(w_1)		$\sum$MSE		Final MSE		var(w_1)	
	Orig.	Modif.	Orig.	Modif.	Orig.	Modif.	Orig.	Modif.	Orig.	Modif.	Orig.	Modif.
LMS	49.1	—	3.9e-03	—	2.2e-05	—	12.0	—	3.9e-05	—	3.5e-07	—
NLMS	49.4	—	4.0e-03	—	2.7e-05	—	12.2	—	4.0e-05	—	3.2e-07	—
Harris	87.7	86.0	7.0e-03	7.2e-03	2.1e-05	2.1e-05	18.4	18.9	7.4e-05	7.4e-05	3.0e-07	3.2e-07
Mikhael	101.8	—	6.4e-03	—	1.1e-05	—	33.2	—	6.5e-05	—	1.0e-07	—
Kwong	113.7	112.5	5.9e-03	6.0e-03	2.4e-07	2.2e-07	14.0	14.4	6.3e-05	6.3e-05	1.4e-08	1.4e-08
Evans	59.6	54.6	4.9e-03	4.5e-03	2.4e-05	3.4e-05	11.9	12.3	4.2e-05	4.5e-05	1.6e-07	2.4e-07
Shan_correlation	88.2	86.6	6.7e-03	6.6e-03	2.9e-06	3.6e-06	12.5	13.1	6.4e-05	6.4e-05	2.1e-08	1.7e-08
Shan	80.8	89.0	7.1e-03	8.3e-03	1.4e-05	2.6e-05	13.3	13.7	6.7e-05	6.7e-05	1.9e-08	1.2e-08
Benveniste	71.4	65.5	6.4e-03	6.2e-03	5.2e-06	1.3e-05	33.9	36.1	4.6e-05	4.7e-05	2.6e-07	2.5e-07
Benveniste_indiv	62.0	56.1	5.3e-03	4.7e-03	1.7e-05	2.5e-05	13.3	13.1	4.4e-05	4.6e-05	2.3e-07	1.8e-07
Karni	57.8	49.4	4.7e-03	3.9e-03	2.3e-05	9.0e-05	12.0	12.8	6.3e-05	6.2e-05	1.5e-07	1.5e-07
Mathews	57.5	53.1	4.7e-03	4.3e-03	2.3e-05	3.1e-05	20.1	23.1	4.1e-05	4.3e-05	5.7e-07	2.6e-07
Mathews_indiv	57.8	53.3	4.7e-03	4.4e-03	1.6e-05	3.1e-05	13.7	13.5	4.2e-05	4.5e-05	2.4e-07	2.4e-07
Aboulnasr	96.4	96.9	6.0e-03	5.9e-03	4.3e-07	6.8e-07	28.5	30.5	5.7e-05	5.7e-05	3.9e-15	4.5e-15
Ang	61.0	57.7	5.2e-03	5.0e-03	1.7e-05	1.8e-05	24.6	22.3	4.3e-05	4.3e-05	1.9e-07	2.6e-07
Ang_indiv	58.2	54.9	4.7e-03	4.5e-03	2.0e-05	3.1e-05	12.9	12.7	4.3e-05	4.5e-05	2.3e-07	2.7e-07
Hwang	87.8	86.6	6.1e-03	6.2e-03	1.3e-06	8.8e-07	14.3	15.2	5.8e-05	5.8e-05	1.5e-10	2.1e-10
Wang	1475.3	—	1.1e-02	—	6.9e-07	—	1386.2	—	5.4e-03	—	6.4e-07	—
Zou	111.5	112.6	6.2e-03	6.1e-03	5.5e-06	2.6e-06	16.7	16.8	5.5e-05	5.4e-05	2.3e-07	1.0e-07
Pazaitis	92.5	92.1	5.7e-03	5.8e-03	1.9e-09	7.3e-09	12.6	13.0	5.8e-05	5.7e-05	1.5e-12	1.0e-12
Pazaitis	116.7	110.0	5.8e-03	5.8e-03	4.1e-10	2.7e-10	14.1	13.8	5.7e-05	5.7e-05	2.2e-16	3.7e-16
Benesty	67.1	—	5.4e-03	—	2.0e-05	—	16.0	—	5.3e-05	—	1.4e-07	—
Wahab_optimal	107.5	—	6.4e-03	—	1.8e-06	—	35.5	—	6.5e-05	—	4.6e-08	—

sizes have similar values for the NLMS and the algorithm by Mikhael, but all the other algorithms presented on the figure use higher values of the step sizes.

5. CONCLUSIONS

The very first conclusion which arises from the above analysis of the seventeen most popular variable step-size modifications of the LMS algorithm presented in this paper is that there is no VS-LMS algorithm which is the best for all the applications. Different applications present different challenges for the adaptation algorithm, thus requiring different step-size update algorithms for the most efficient operation. This is especially apparent with stationary data processing (e.g. the system identification) as opposed to nonstationary data processing (e.g. speech signal processing). However, some general guidelines for the choice of the proper VS-LMS algorithm are as follows:

First of all, the more parameters the algorithm requires to be adjusted prior to operation, the more problematic the use of this algorithm is. Even in simulations, the choice of more than two or three parameters requires many time-consuming trials. This is the effect of parameter interactions: the optimal choice of one parameter is no longer optimal if we change other parameters. Moreover, the optimal set of parameters is likely to be different if experiment conditions (e.g. noise level) change. Thus, the algorithms with more than three parameters should be considered only if very special properties need to be obtained, and probably only for simulations.

The above remark does not apply to the lower and upper bound on the step size, required by many of the algorithms discussed in this paper. The former is very easy to choose and, for properly parametrized VS-LMS algorithm, influences only steady-state error. The latter may easily be substituted with stability sufficient condition bound given by Eq. (47), with low computational cost and almost no influence on the performance.

With the regard to the ease of use, the algorithm by Mikhael (Section 2.3) should be mentioned. This algorithm requires no parameters to run, and performs reasonably well in both the stationary and nonstationary data processing. However, this algorithm resulted in higher error levels in the ANC simulations and may be not very well-suited for this application.

Second, very interesting and original is the algorithm by Pazaitis (Section 2.11). This algorithm performed very well in stationary data processing (the system identification). However, the kurtosis estimation involved in this algorithm requires substantial number of operations; therefore, this algorithm may not be applicable for real-time processing.

Finally, for nonstationary data processing, considering the ease of use, numerical complexity, and performance, the NLMS algorithm still appears to be unrivaled. However, if another algorithm is desired for some reasons, the algorithm by Mathews (Section 2.9) should be considered. This algorithm, based on the orthogonality principle, requires two parameters to be adjusted (excluding the upper bound for the step size), presents moderate degree of numerical complexity, and performs very well in both the ALE and the ANC applications.

To conclude, we will repeat this very important finding that comes from the research reported in this paper: no VS-LMS algorithm appears to be as versatile, easy to use, and well-suited for real-time applications as the NLMS. In our opinion, despite the constant effort to develop new VS-LMS algorithms, the 49-years-old NLMS algorithm is going to dominate the adaptive solutions for many years on, if not forever.

Acknowledgment

The research is within a project financed by the National Science Centre, Poland, based on decision no. DEC-2012/07/B/ST7/01408.

REFERENCES

[1] Haykin, S. *Adaptive Filter Theory, Fourth Edition*. Prentice Hall, New York, (2002). ISBN 0-13-048434-2.

[2] Widrow, B., Glover, J. R., Jr., McCool, J. M., Kaunitz, J., Williams, C. S., Hearn, R. H., Zeidler, J. R., Eugene Dong, Jr., and Goodlin, R. C. Adaptive noise cancelling: Principles and applications. *Proceedings of the IEEE*, 63(12):1692–1716, (1975). ISSN 0018-9219. http://dx.doi.org/10.1109/PROC.1975.10036.

[3] Macchi, O. *Adaptive Processing. The Least Mean Squares Approach with Applications in Transmission.* John Wiley & Sons, Chichester, 1995. ISBN 0 471 93403 8.

[4] Landau, I. D., Lozano, R., M'Saad, M., and Karimi, A. *Adaptive Control. Algorithms, Analysis and Applications*. Springer-Verlag, London, (2011). ISBN 987-0-85729-663-4.

[5] Nagumo, J., and Noda, A. A learning method for system identification. *IEEE Transactions on Automatic Control*, **12**(3):282–287, (1967). ISSN 0018-9286. http://dx.doi.org/10.1109/TAC.1967.1098599.

[6] Albert, A. E., and Gardner,L. S. *Stochastic Approximation and Nonlinear Regression*. MIT Press, Cambridge, MA., (1967).

[7] Harris, R. W., Chabries, D. M., and Bishop, F. A. A variable step (VS) adaptive filter algorithm. *IEEE Transactions on Acoustics, Speech, and Signal Processing*, **ASSP-34**(2):309–316, (1986). http://dx.doi.org/10.1109/TASSP.1986.1164814.

[8] Mikhael, W., Wu, F., Kazovsky, L., Kang, G., and Fransen, L. Adaptive filters with individual adaptation of parameters. *IEEE Transactions on Circuits and Systems*, **33**(7):677–686, (1986). ISSN 0098-4094d. http://dx.doi.org/10.1109/TCS.1986.1085982.

[9] Ao Wei, Xiang Wan-Qin, Zhang You-Peng, Wang Lei, Lv Chun-Ying, and Wang Zheng-Hua. A new variable step size LMS adaptive filtering algorithm. In 2012 International Conference on Computer Science and Electronics Engineering (ICCSEE), volume 2, pages 265–268, (2012). http://dx.doi.org/10.1109/ICCSEE.2012.115.

[10] Tian, F., and Luo, R. *A novel variable step size LMS algorithm based on modified hyperbolic tangent and its simulation*, volume 490–495 of *Advanced Materials Research*, pages 1426–1430. (2012). http://dx.doi.org/10.4028/www.scientific.net/AMR.490-495.1426.

[11] Kwong, R. H., and Johnston, E. W. Variable step size LMS algorithm. *IEEE Transactions on Signal Processing*, **40**(7): 1633–1642, (1992). http://dx.doi.org/10.1109/78.143435.

[12] Aboulnasr, T., and Mayyas, K. A robust variable step-size LMS-type algorithm: Analysis and simulations. *IEEE Transactions on Signal Processing*, **45**(3):631–639, (1997). http://dx.doi.org/10.1109/78.558478.

[13] Pazaitis, D. I., and Constantinides, A. G.. A novel kurtosis driven variable step-size adaptive algorithm. *IEEE Transactions on Signal Processing*, **47**(3):864–872, (1999). ISSN 1053-587X. http://dx.doi.org/10.1109/78.747793.

[14] Zou, K., and Zhao, X. A new modified robust variable step size LMS algorithm. In The 5th IEEE Conference on Industrial Electronics and Applications, pages 2699–2703. Xi'an, China, (2009). http://dx.doi.org/10.1109/ICIEA.2009.5138654.

[15] Shan, T. J., and Kailath, T. Adaptive algorithms with an automatic gain control feature. *IEEE Transactions on Circuits and Systems*, **35**(1):122–127, (1988). ISSN 0098-4094. http://dx.doi.org/10.1109/31.1709.

[16] Karni, S., and Zeng, G. A new convergence factor for adaptive filters. *IEEE Transactions on Circuits and Systems*, **36**(7):1011–1012, (1989). ISSN 0098-4094. http://dx.doi.org/10.1109/31.31337.

[17] Benveniste, A., Métivier, M., and Priouret, P. *Adaptive algorithms and stochastic approximations*. Applications of mathematics. Springer-Verlag, (1990). ISBN 9783540528944. LCCN 91127124.

[18] Evans, J. B., Xue, P., and Liu, B. Analysis and implementation of variable step size adaptive algorithms. *IEEE Transactions on Signal Processing*, **41**(8):2517–2235, (1993). http://dx.doi.org/10.1109/78.229885.

[19] Mathews, V. J., and Xie, Z. A stochastic gradient adaptive filter with gradient adaptive step size. *IEEE Transactions on Signal Processing*, **41**(6):2075–2087, (1993). http://dx.doi.org/10.1109/78.218137.

[20] Ang, W., and Farhang-Boroujeny, B. A new class of gradient adaptive step-size LMS algorithms. *IEEE Transactions on Signal Processing*, **49**(4):805–810, (2001). http://dx.doi.org/10.1109/78.912925.

[21] Benesty, J., Rey, H., Vega, L. R., and Tressens, S. A non-parametric VSS NLMS algorithm. *IEEE Signal Processing Letters*, **13**(10):581–584, oct. (2006). ISSN 1070-9908. http://dx.doi.org/10.1109/LSP.2006.876323.

[22] Wahab, M. A., Uzzaman, M. A., Hai, M. S., Haque, M. A., and Kasan, M. K. Least-squares optimal variable step-size LMS for nonblind system identification with noise. In 5th International Conference on Electrical and Computer Engineering, pages 428–433. Bangladesh, (2008). http://dx.doi.org/10.1109/ICECE.2008.4769245.

[23] Hwang, J., and Li, Y. Variable step-size LMS algorithm with a gradient-based weighted average. *IEEE Signal Processing Letters*, **16**(12):1043–1046, (2009). http://dx.doi.org/10.1109/LSP.2009.2027653.

[24] Wang, P., Kam, P. Y., and Chia, M. W. A novel automatic step-size adjustment approach in the LMS algorithm. In The First International Conference on Wireless VITAE, pages 867–871. Aalborg, Denmark, (2009). http://dx.doi.org/10.1109/WIRELESSVITAE.2009.5172563.

[25] Karni, S., and Zeng, G. Comments on "Adaptive algorithms with an automatic gain control feature". *IEEE Transactions on Circuits and Systems*, **37**(7):974–975, (1990). ISSN 0098-4094. http://dx.doi.org/10.1109/31.55079.

[26] Karni, S., and Zeng, G. Comments, with reply, on "Adaptive algorithms with an automatic gain control feature" by t.j. shan and t. kailath. *IEEE Transactions on Circuits and Systems*, **37**(7):974–975, (1990). ISSN 0098-4094. http://dx.doi.org/10.1109/31.55079.

[27] Kushner,H. J., and Yang, J. Analysis of adaptive step size SA algorithms for parameter tracking. In *Proceedings of 33rd Conference on Decision and Control*, pages 730–737. Lake Buena Vista, Fl, USA, (1994). http://dx.doi.org/10.1109/CDC.1994.410867.

[28] Mazur, K., and Pawelczyk. M. Hammerstein nonlinear active noise control with the Filtered-Error LMS algorithm. *Archives of Acoustics*, **38**(2):197–203, (2013). http://dx.doi.org/10.2478/aoa-2013-0023.

[29] Bismor, D. Extension of LMS stability condition over a wide set of signals. *International Journal of Adaptive Control and Signal Processing*, **29**:653–670, (2015). ISSN 1099-1115. http://dx.doi.org/10.1002/acs.2500.

[30] Söderström, T., and Stoica, P. *System Identification*. Prentice Hall International, Inc., New York, (1989).

[31] Zeidler, J. R. Performance analysis of LMS adaptive prediction filters. *Proceedings of the IEEE*, **78**(12):1781–1806, (1990). ISSN 0018-9219. http://dx.doi.org/10.1109/5.60921.

[32] Latos, M., and Pawelczyk, M. Adaptive algorithms for enhancement of speech subject to a high-level noise. *Archives of Acoustics*, **35**(2):203–212, (2010). http://dx.doi.org/10.2478/v10168-010-0019-z.

[33] Ławryńczuk, M. Nonlinear state–space predictive control with on—line linearisation and state estimation. *International Journal of Applied Mathematics and Computer Science*, **25**(4): 833–847, (2015). http://dx.doi.org/10.1515/amcs-2015-0060.

Modelling and Parameters Study of Piezoceramic Parts of an Electroacoustic Transducers

Nowrouz M. Nouri, Mohammad Riahi and Hamid R. Gharavian

Department of Mechanical Engineering, Iran University of Science and Technology, Narmak, Tehran, Iran, 1684613114.

Ali Valipour

Department of Engineering, Chamran University of Ahvaz, Ahvaz, Iran, 6135783151.

(Received 18 December 2013; accepted 16 February 2015)

Electroacoustic transducers as transmitters and receivers play major role in underwater communication systems. Piezoceramic rings are the most important parts of electroacoustic transducers. In this investigation, attempts were made to use the matrix model and the finite element model to evaluate frequency behaviour of piezoceramic rings. In order to validate the accuracy of the proposed models and the solution algorithm, results obtained from both models were compared with experimental results presented by Radmanović, et al. Upon confirmation of the obtained results from the two models, the effects of the geometrical parameters on the frequency response of the ring and the surrounding domain in which the ring oscillates were studied. Based on the obtained results, the geometrical parameters have effects on both the frequency resonance of the ring, as well as the value of the electrical impedance. It is also noted that the surrounding domain only causes change on the intensity of the ring's electrical impedance.

1. INTRODUCTION

The use of acoustic waves for the recognition and location identification of underwater bodies is called sonar.[1–3] Compared to the other form of wave transmission, acoustic waves are more suitable for underwater applications due to low attenuation.[3–5] Consequently, underwater applications of sonar are related to acoustic fundamentals. Due to military needs, especially during world wars, the related technologies associated with sonar have developed.[6] A transducer is a device capable of converting one form of energy into another.[7] The underwater transducers convert electric energy into a sound wave, which is mechanical energy, and vice versa.[6,8] Careful design and modelling of transducers is necessary, since it is crucial that they perform at the desired level. Moreover, recognition of the frequency behaviour of piezoceramic rings has high importance, since they are the main parts of transducers. The frequency behaviour of a piezoceramic ring is usually obtained by studying its impedance curve and calculating its resonance frequencies.[9]

Traditionally, the design of transducers and the study of the behaviour of their parts, particularly piezoceramic rings, has been done by using lumped parameters models. These models were made on the principle that by assuming one dimension, their different parts could be modelled as a group of masses connected by several springs and dampers.[6,10] Since it is possible to equate mechanical parts with the forming elements of an electric circuit, the next step in modelling is to use equivalent circuits. Through using these circuits, the desired parameters for performance analysis, such as frequency resonance, bandwidth, etc., would be obtained.[11] Another analytical model that can be used is the 2D matrix model. In this model, the relations of forces acting on surfaces, different surface velocities, voltage, and current of a piece like a piezoceramic ring would be expressed in the form of a matrix relation and an impedance matrix of 5*5. This model is also capable of considering the effects of the acoustic environment. For parts like metal rings not containing voltage and current, the size of impedance matrix would be reduced to 4*4.[12,13] Since it was not possible to use analytical models to analyse transducers with complex geometries, finite element methods have been used for the design and analysis of these transducers. So, the main advantages of finite element analysis is the possibility of precise and complete modelling of all parts with complex geometries.[14,15]

In light of the points discussed, the present study utilizes matrix models as well as finite element models, and applies them to simulate a piezoceramic ring. These models can be considered advanced methods in the modelling of the electroacoustic transducers parts. In order to validate the used algorithm, initially for a specified piezoceramic ring, the obtained frequency response was compared to valid results presented by experimental studies in credible references. Then, the frequency response of a piezoceramic ring for several dimensional conditions and different environments were studied. Finally, by interpreting these results through analytical models, fundamentals of vibrations, and circuit analysis, the effects of different parameters on the considered frequency response was evaluated.

2. METHODS OF MODELLING PIEZOCERAMIC RINGS

The design and modelling of underwater transducers is possible through the recognition of piezoceramic rings' behaviour

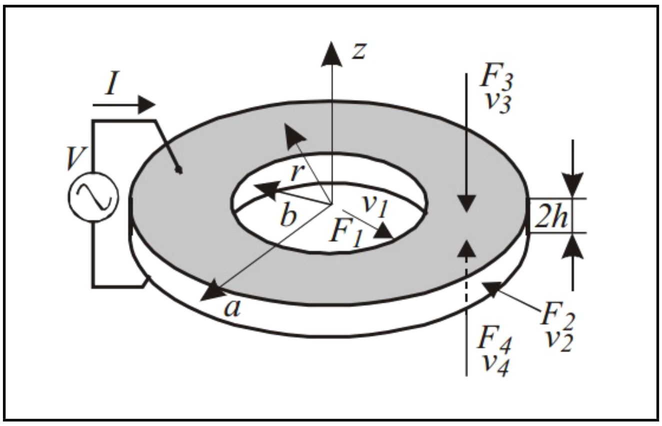

Figure 1. A piezoceramic ring (conventional directions of forces and velocities are shown).

as a major element in these transducers. Moreover, the modelling of a ring with the aim of reducing and improving production costs is rather important. The methods used in this study for the modelling of piezoceramic elements of underwater electroacoustic transducers will be described in this section.

2.1. Matrix Model

The matrix model is known as the most advanced analytical tool for the design and analysis of different elements used in the electroacoustic transducers. In order to better introduce the matrix model, its application in the analysis of a piezoceramic ring is presented. Figure 1 is a schematic view of a piezoceramic ring. This ring has stimulating voltage at its inlet and outlet.

F_i are applied forces on the ring surfaces, and v_i are surface velocities along different directions. By using stress-strain, displacement-strain relations and other related points, the following relations would be presented for impedance of a piezoceramic ring:[16]

$$\begin{bmatrix} F_{10} \\ F_{20} \\ F_{30} \\ F_{40} \\ V_0 \end{bmatrix} = \begin{bmatrix} z_{11} & z_{12} & z_{13} & z_{13} & z_{15} \\ z_{21} & z_{22} & z_{23} & z_{23} & z_{25} \\ z_{13} & z_{23} & z_{33} & z_{34} & z_{35} \\ z_{13} & z_{23} & z_{34} & z_{33} & z_{35} \\ z_{15} & z_{25} & z_{35} & z_{35} & z_{55} \end{bmatrix} \begin{bmatrix} v_{10} \\ v_{20} \\ v_{30} \\ v_{40} \\ I_0 \end{bmatrix}; \qquad (1)$$

$$F_i = F_{i0} e^{j\omega t}; \qquad (2)$$

$$V = V_0 e^{j\omega t}. \qquad (3)$$

In the above relations, z_{ij} is a function of geometrical characteristics and physical structure parameters, as well as the frequency.[6,12] F_{i0} and V_0 are the force spectrum and fluctuating voltage. A matrix comprised of z_{ij} is called the impedance matrix of a piezoceramic ring. In order to obtain the resonance frequencies of this ring, it suffices to equate the determinant of the matrix to zero. ω is the angular frequency, and it equates to

$$\omega = 2\pi f. \qquad (4)$$

In the above relation, f is the frequency in terms of hertz (Hz). More important than defining the matrix impedance is defining the input electrical impedance. The input electrical impedance is the relation of voltage to current in the inlet electrical terminals. The input electrical impedance contains mechanical properties as well as acoustic loading. By drawing this impedance as a function of the frequency, it becomes possible to observe and calculate the resonance frequencies (minimum points) and anti-resonance frequencies (the maximum points).[15] To draw this impedance, first it is necessary to express the relation between force and velocity at the external surfaces by using the acoustic impedance:[12]

$$F_i = -Z_i v_i, \qquad i = 1, 2, 3, 4. \qquad (5)$$

Acoustic impedance is the product of density multiplied by velocity of sound in any acoustic domain. The amount of acoustic impedance for air is about 400, and for water is about 1.5*10^6. A unit of acoustic impedance (external impedance) is $\left(\frac{\text{kg}}{\text{m}^2\text{s}}\right)$ or $\left(\frac{\text{Pa s}}{\text{m}}\right)$, while a unit of obtained z_{ij} impedance of in the matrix impedance is $\left(\frac{\text{kg}}{\text{s}}\right)$. It is evident that in order to unify the acoustic impedance with z_{ij}, acoustic impedance would have to be multiplied by a unit of surface. This surface is equal to the area that impedance enters on it. This means:

$$\begin{aligned} Z_1 &= Z_{1\_\text{acousic}} \times 2 * \pi b * 2h; \\ Z_2 &= Z_{2\_\text{acousic}} \times 2 * \pi a * 2h; \\ Z_3 &= Z_{3\_\text{acousic}} \times \pi(a^2 - b^2); \\ Z_4 &= Z_{4\_\text{acousic}} \times \pi(a^2 - b^2). \end{aligned} \qquad (6)$$

In order to obtain the input electrical impedance as a function of frequency, it is necessary to make some changes to Eq. (1):

$$\begin{bmatrix} F_{10} \\ F_{20} \\ F_{30} \\ F_{40} \\ V_0 \end{bmatrix} = \begin{bmatrix} z_{11} & z_{12} & z_{13} & z_{13} & z_{15} \\ z_{21} & z_{22} & z_{23} & z_{23} & z_{25} \\ z_{13} & z_{23} & z_{33} & z_{34} & z_{35} \\ z_{13} & z_{23} & z_{34} & z_{33} & z_{35} \\ z_{15} & z_{25} & z_{35} & z_{35} & z_{55} \end{bmatrix} \begin{bmatrix} v_{10} \\ v_{20} \\ v_{30} \\ v_{40} \\ I_0 \end{bmatrix} \xrightarrow{F_i = -Z_i v_i}$$

$$\begin{bmatrix} -Z_1 v_{10} \\ -Z_2 v_{20} \\ -Z_3 v_{30} \\ -Z_4 v_{40} \\ V_0 \end{bmatrix} = \begin{bmatrix} z_{11} & z_{12} & z_{13} & z_{13} & z_{15} \\ z_{21} & z_{22} & z_{23} & z_{23} & z_{25} \\ z_{13} & z_{23} & z_{33} & z_{34} & z_{35} \\ z_{13} & z_{23} & z_{34} & z_{33} & z_{35} \\ z_{15} & z_{25} & z_{35} & z_{35} & z_{55} \end{bmatrix} \begin{bmatrix} v_{10} \\ v_{20} \\ v_{30} \\ v_{40} \\ I_0 \end{bmatrix}; \qquad (7)$$

$$\begin{bmatrix} 0 \\ 0 \\ 0 \\ 0 \\ V_0/I_0 \end{bmatrix} = \begin{bmatrix} z_{11}+Z_1 & z_{12} & z_{13} & z_{13} & z_{15} \\ z_{21} & z_{22}+Z_2 & z_{23} & z_{23} & z_{25} \\ z_{13} & z_{23} & z_{33}+Z_3 & z_{34} & z_{35} \\ z_{13} & z_{23} & z_{34} & z_{33}+Z_4 & z_{35} \\ z_{15} & z_{25} & z_{35} & z_{35} & z_{55} \end{bmatrix} \begin{bmatrix} v_{10}/I_0 \\ v_{20}/I_0 \\ v_{30}/I_0 \\ v_{40}/I_0 \\ 1 \end{bmatrix}. \qquad (8)$$

By considering the first four lines of the above matrix and the point that z_{ij} is determined, it becomes possible to find unknowns terms $\{(v_{10}/I_0), (v_{20}/I_0), (v_{30}/I_0), \text{and } (v_{40}/I_0)\}$ in any specific frequency. Then, by using the following equation, which is related to the fifth line of the above matrix, it becomes possible to find the input electrical impedance for a piezoceramic ring:

$$z_{\text{ul}} = V_0/I_0 = z_{15}\frac{v_{10}}{I_0^2} + z_{25}\frac{v_{20}}{I_0^2} + z_{35}\frac{v_{30}}{I_0^2} + z_{35}\frac{v_{40}}{I_0^2} + \frac{z_{55}}{I_0^2}. \qquad (9)$$

In the above equation, z_{ul} is the input electrical impedance. It is evident that in order to calculate z_{ul}, all acoustic impedances would have to be known.[12] By drawing the related curve of the above equation, it becomes possible to analyse the behaviour of the piezoceramic ring caused by the applied voltage.

In addition to the high precision in the matrix method, attention needs to be paid to the fact that in utilizing this method, there are two major limitations. First, by making the geometrical shape more complex, using this method and formation of the impedance matrix becomes more difficult. Second, even in simple geometrical shapes, when a large number of elements are present along each other in a transducer, making correct relationships between impedances of these elements and simultaneously analysing them would be very cumbersome. Therefore, in the present study, an attempt was made to develop a finite element method suitable for both modelling of complex geometrical shapes and for modelling transducers with many elements.

2.2. Finite Element Method

In recent years, due to necessity of using modelling of different and complex geometries, the utilization of finite element methods for analysis of electroacoustic transducers elements has increased.[2] Acoustic analysis in finite elements could take place in both frequency domain and time domain. Of course, for this type of problem, frequency domain is usually used. The major task in the finite element method modelling is the correct and precise defining of the model's boundary conditions. Initially, the propagation domain around the transducer surface could be modelled. In cases where vibrating bodies are axisymmetric, it would be better to use axisymmetric models. This helps to reduce the computational time. Introducing the materials and properties of different parts and domains, as well as determining the base voltage for piezoelectric materials, is the next step in the definition of the problem.[17,18] Figure 2 shows finite element modelling of a single ring along with its acoustic domain.

In Fig. 2, the upper part shows the ring along with its considered spherical acoustic domain. In the lower part, the magnified schematic of ring is shown. The size of the acoustic domain around the vibrating surface of the ring has been made much larger than ring's dimensions. This was done to model infinite domain around the ring. Also, this modelling causes propagated waves to have the chance for receiving the effects of the domain and related boundary conditions.[14] After modelling, the ring and the domain must be meshed. An important point in the size selection of each element is to consider that in acoustical analysis, the size of the largest element must be a function of sound velocity and the highest performing frequency. Therefore, the size of the largest element could be calculated from the following relation:

$$\text{Maximum element size} \leq \frac{c}{n \cdot f_{\max}}. \qquad (10)$$

In the above equation, c is the velocity of sound in the acoustic domain, $f_{\max}$ is the highest frequency within the analysed frequency spectrum, and n is a number between 8 and 12.[19]

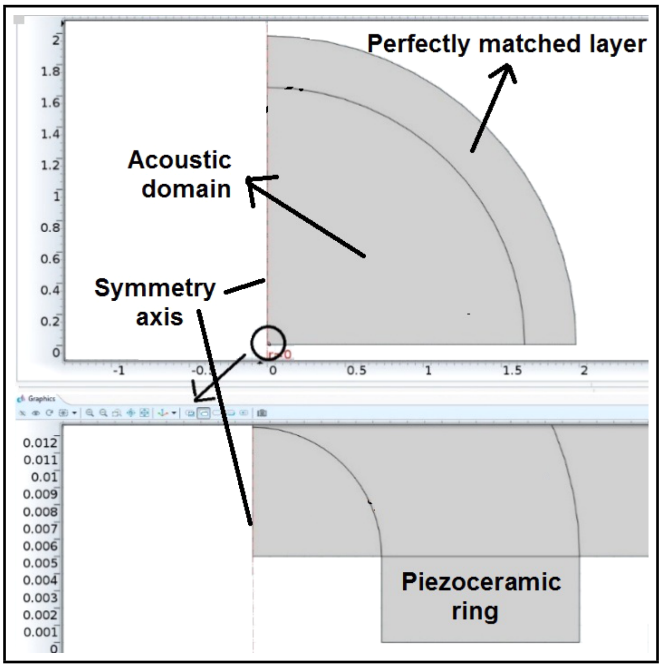

Figure 2. Schematic of acoustical calculation environment model (upper) and piezoceramic ring (lower).

3. VALIDATION

The piezoceramic ring in the simulations has an external diameter equal to 38 mm, an internal diameter of 15 mm, and a thickness 5 mm. The ring's material is PZT8. These dimensions were selected by considering the sample ring tested in the work of Radmanović and Mančić.[16]

It was assumed that the ring passes a 1-volt simulation electrically. In continuation, the frequency analysis of this ring was done through different methods, and the results were compared. Also, in order to verify the obtained results from both methods, these results were compared to the experimental results presented by Radmanović and Mančić.[16] In the matrix model, the first impedance matrix of the considered ring was obtained as a function of frequency. Then, by drawing the matrix for different values of frequency, the curve of the ring impedance was obtained. As mentioned earlier, the effects of the acoustic environment around the ring were entered into the model as acoustic impedance. Also, in the finite element method, after the modelling of the ring and the computational acoustic domain, the behaviour of the ring in the frequency domain was studied. Figure 3 depicts the obtained results from the matrix model and the finite element model next to each other.

The curve in Fig. 3 has many maximum and minimum points. Some of these maximum and minimum points could be representative of resonance and anti-resonance frequencies. As expected, a piezoceramic ring being freely vibrated has several main resonance modes, while other resonance modes like torsional modes, etc., could also be observed. Considering that the matrix model could only model motion along the radius and thickness, only major resonance modes would be observable by it. The finite element model is also two dimensional and axisymmetric. This means that only major resonance modes would be shown. Also, according to the figure,

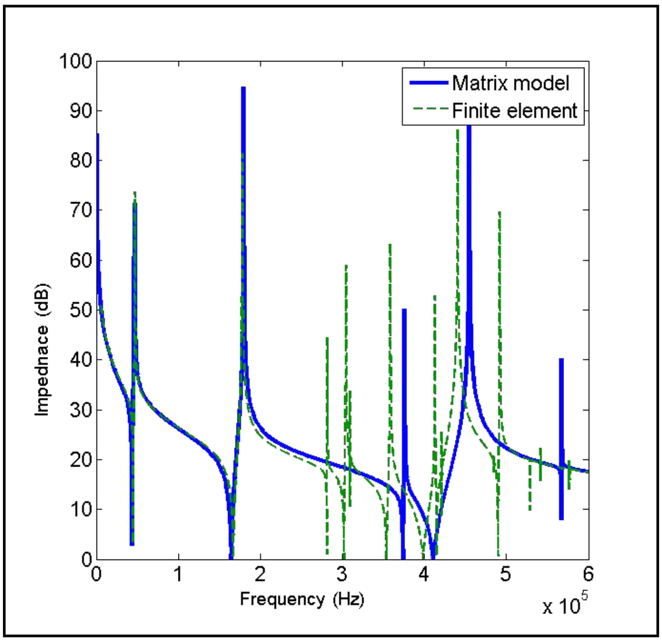

Figure 3. Comparison of the obtained results from the matrix model and the finite element model.

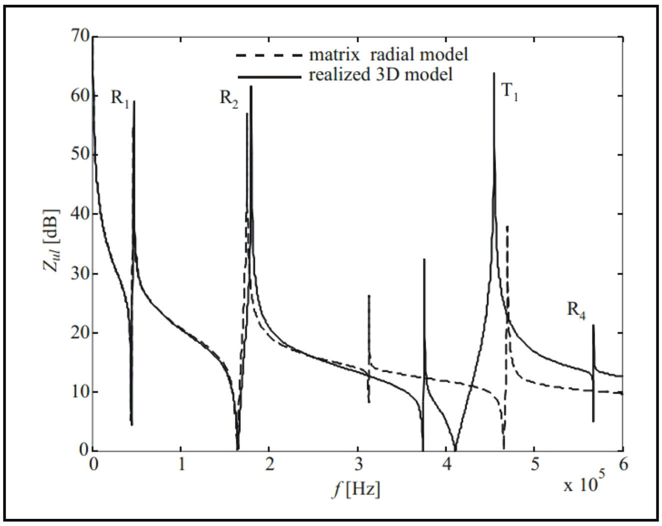

Figure 4. Comparison of obtained results from the matrix model and the experimental results in the work of Radmanović and Mančić.[16]

it is observed that the finite element model shows more resonance modes in a frequency spectrum when compared to the matrix model. The existence of these additional modes could be justified by parameters such as meshing.[15] Thus, they could not be called major modes. It is worth mentioning that, in the above model, the environment surrounding the ring was completely assumed to be air. This means that all acoustic impedances were considered as air impedance:

$$Z_1 = Z_2 = Z_3 = Z_4 = \rho_{\text{air}} \times c_{\text{air}} = 400 \text{ Rayl}.$$

Although the unit of impedance is ohm (Ω), it could be expressed in decibels (dB) by using the following relation:[16]

$$z_{\text{ul}} = 20 \log \left(\frac{Z_{\text{ul}}}{50} + 1 \right). \tag{11}$$

In order to verify the results, they would have to be compared with experimental results. Consequently, the experimental results from the above mentioned ring in the work of Radmanović and Mančić[16] is shown in Fig. 4.

Comparing Figs. 3 and 4 indicates that a suitable fit exists between the results obtained from modelling and these experimental results. In Fig. 4, four resonance modes are named. Three of them are labelled with the letter (R), referring to radius modes, and another one is labelled with the letter (T), related to thickness mode. The number next to each letter represents its number; e.g. R_2 is related to the second resonance radius mode.[16] Recognizing different types of resonance modes has high importance in studying frequency response. Therefore, it should be possible to recognize different modes for a known geometry. One common method to do this for a piezoceramic ring is to use frequency coefficients and utilize semi-empirical simple relations. These relations could provide assistance in the recognition of different modes from a curve. For example, the main thickness mode, the first radius mode, and the second radius mode (circular) for the mentioned ring could be calculated by using the following relations:[20]

$$f_{\text{thickness}} = \frac{N_{\text{thickness}}}{t} = \frac{2070 \text{ Hz m}}{0.005 \text{ m}} = 414 \text{ kHz};$$
$$f_{\text{radial}} = \frac{N_{\text{radial}}}{D} = \frac{1700 \text{ Hz m}}{0.038 \text{ m}} = 44.7 \text{ kHz};$$
$$f_{\text{hoop}} = \frac{N_{\text{hoop}}}{(D-d)/2} = \frac{2000 \text{ Hz m}}{(0.038 \text{ m} - 0.015 \text{ m})/2} = 173.9 \text{ kHz};$$

Table 1. Comparison of obtained results for the sample ring by different methods for modelling with experimental results.

	Radius mode (kHz)	Hoop mode (kHz)	Thickness mode (kHz)
Experimental results	46.0	168.0	418.0
Frequency constants method	44.7	173.9	414.0
Frequency constants method relative error (%)	2.80	3.40	0.95
Matrix model	43.2	179.0	417.3
Matrix model relative error (%)	6.08	1.64	0.16
Finite element method	43.0	178.0	418.2
Finite element method relative error (%)	2.19	6.50	0.04

In order to compare and validate the results quantitatively, the results from the semi-empirical matrix model and the finite element model have been compared to the experimental results in Table 1.

It could be observed that with these semi-empirical relations, it is possible to estimate the main modes easily and precisely. The main advantage of the above calculations is to assist in recognizing different resonance modes. It is noteworthy that the terms N in the above equations are frequency coefficients that could be found by referring to the available table for each standard piezoceramic ring.[21] In Table 1, error values have been found by comparing the results of each model with the experimental results. Therefore, in light of Table 1, it

Table 2. Different conditions based on considered parameters.

No.	Acoustic domain	Thickness t_c (mm)	Inner radius r_{ci} (mm)	Outer radius r_{co} (mm)
1	Air	5	7.5	{15:5:30}
2	Air	{5:5:20}	7.5	19
3	Water	5	7.5	19

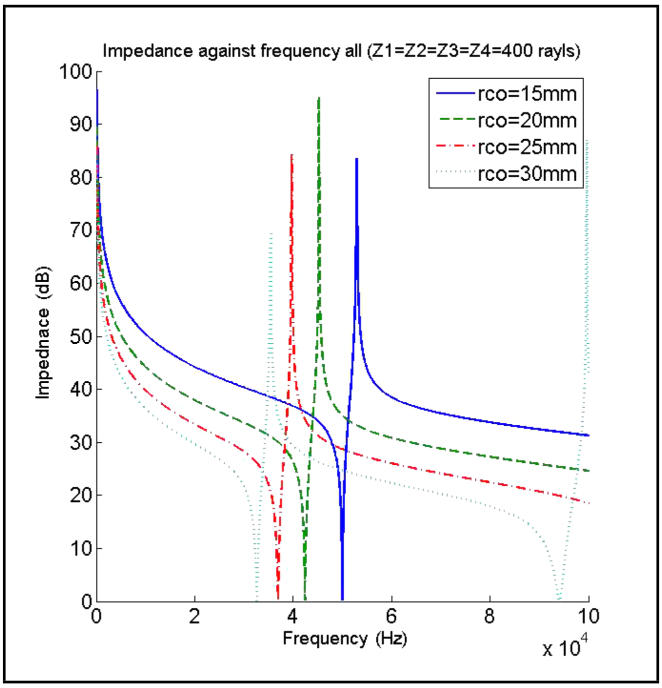

Figure 5. Survey of the effect of change in the external radius of the piezoceramic ring via the matrix model.

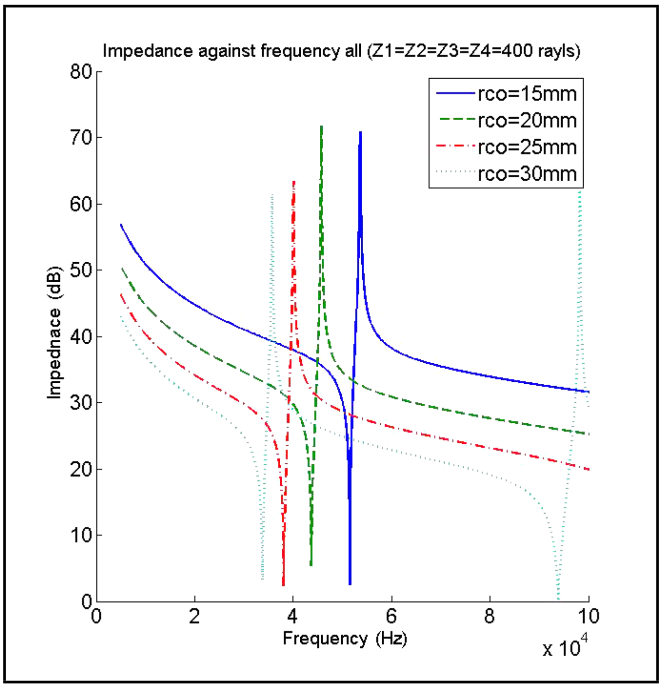

Figure 6. Survey of the effect of change in the external radius of the piezoceramic ring by using the finite element model.

is safe to express that almost all methods present a good precision. Also, it is noticed that for the present problem with a simple geometry, in different modes, results obtained from the matrix models possess the best precision in comparison to other methods. It is obvious that where no difficulties would arise for complex geometries, this method could respond to the need.

4. STUDY OF GEOMETRY AND ENVIRONMENT PARAMETERS EFFECT ON FREQUENCY RESPONSE

In proceeding and in order to determine effect of geometrical dimensions and acoustic domain of surrounding on different resonance modes of a ring, behaviour of the ring in a limited frequency range and in several different modes will be evaluated. Table 2 presents all studied conditions.

It is noteworthy that in row 1, the external radius increases from 15 mm to 30 mm with iteration of 5 mm each. In the second row, the thickness also increases from 5 mm to 20 mm, with 5 mm iterations. As depicted in the table, geometrical changes of the ring include changing in the external radius and its thickness. In order to observe the effect of the surrounding environment in the frequency response of the ring, the results for a certain geometry in two environments of air and water are compared to each other. The results obtained for each change in any of the three parameters, along with their interpretation, will be presented.

5. RESULTS

Obtaining the effect of different parameters in the frequency response of piezoceramic elements has high importance in the optimized and desired design of underwater transducers. In addition, by using a precise simulation of a ring, it would be possible to obtain the necessary knowledge in determining the effect of each parameter in the increase or decrease of the frequency resonance of a piezoceramic ring. In order to survey the effect of each introduced parameter in Table 2, the results obtained from the matrix model, as well as the finite element simulation, were gathered. These results were obtained in response to changes in three parameters: radius, thickness, and the surrounding environment. Through interpreting these results, it was possible to compare the effect value of different parameters.

5.1. Condition 1

In this condition, by assuming constant sizes of internal radii and piezoceramic ring thicknesses, the simulation takes place for four different sizes of the external radius. The selected frequency range is between 0 and 100 kHz. A diagram of the simulation results obtained from the matrix model is presented in Fig. 5, and the results obtained from the finite element model are presented in Fig. 6.

Figure 5 depicts the input electric impedance as a function for four rings with different external radii. This curve was drawn by using the matrix modelling method, and within a frequency range of 0 to 100 kHz. External radii of 15 mm to 30 mm were selected. For the external radius of 15 mm, the first radial resonance frequency mode is approximately 48 kHz. By increasing the external radius and reaching 30 mm, the resonance frequency decreased to 33 kHz. This means that with an increase of 100% in the radius, the resonance frequency decreased around 30%. This is where the intensity of impedance in equal frequencies from the 15 mm radius to the 30 mm radius was decreased around 14 dB. So, it could be stated that by increasing the external radius, the resonance frequency related to the radial mode decreased. Also, the level of input electrical impedance for a similar frequency decreased in

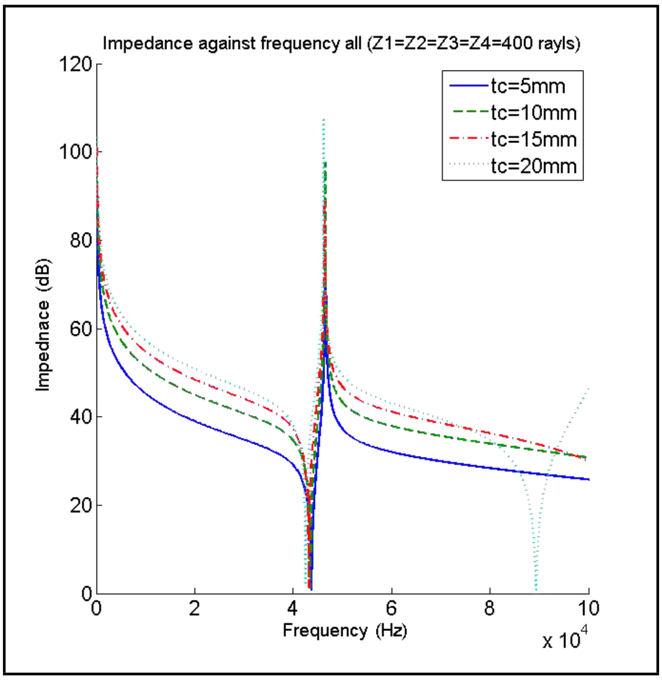

Figure 7. Survey of the effect of change in thickness of the piezoceramic ring through matrix modelling.

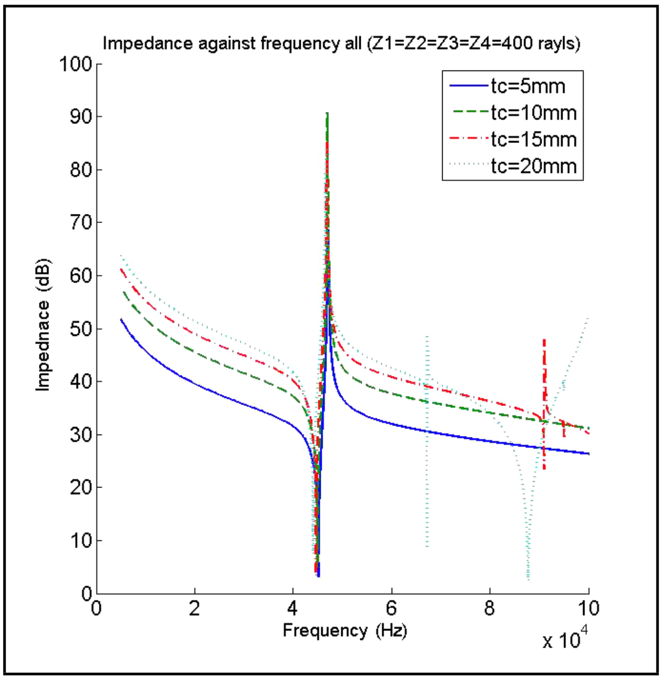

Figure 8. Survey of the effect of change in the piezoceramic ring thickness through FEM modelling.

response to an increase in the external radius. Increasing the external radii translates to a change in the mass and stiffness of a piezoceramic ring. To study causes of this finding, sufficient information is needed about stiffness functions and mass, as well as frequency resonance and electrical impedance. More details about this point and the expression of needed relations will be introduced in the results interpretation section.

Figure 6 is similar to Fig. 5, except that it has been drawn by the finite element model. It is noticeable here that an increase in the external radius from 15 mm to 30 mm has caused the resonance frequency to reduce from 51 kHz to about 35 kHz, meaning that by doubling the external radius, a reduction of 30% in the frequency resonance is noticeable. The reduction in the electric impedance value for this radius reduction is about 14 dB. The objective of presenting this figure is to compare the results between the matrix modelling and the FEM modelling. It is noticeable that the results obtained from both models are in a very agreeable confirmation.

5.2. Condition 2

In this condition, by assuming fixed values for the internal and external radii, a simulation for four different sizes of thickness in a frequency range of 0 to 100 kHz takes place. Figure 7 depicts a simulation by the matrix model on the basis of thickness.

In the above figure, the values of the input electrical impedance for four rings within different thicknesses are shown on the basis of frequency. This diagram was drawn through matrix modelling. It is noticeable that—contrary to the changes in the external radius—along with change in thickness, the frequency resonance related to the radius mode was not changed. This is where, similar to the condition of increase in the external radius with an increase in thickness, the level of the input electrical impedance for a known frequency goes up. Also, along with an increase in thickness, stiffness proportional to thickness decreases intensely. This leads to a reduction in the thickness frequency resonance. It is worth noting that the thickness frequency resonance for the designated ring is high (around 400 kHz), and in light of the selected frequency range, no thickness mode is observed. Similarly, in Fig. 8, also by utilizing the FEM, changes in ring thickness and its effect on the frequency response are shown.

A comparison between Figs. 7 and 8 reveals a good confirmation between the two methods of matrix and FEM modelling.

5.3. Condition 3

In this condition, by assuming fixed geometrical sizes, a simulation for two acoustical environments—water and air—takes place within a 300 kHz to 500 kHz range. The reason for selecting this frequency range is to be able to observe thickness modes as well as radial modes. Considering Fig. 1, the ring is connected to the surrounding domain from four sides. These four sides are radial sides, internal and external, and flat surfaces, upper and lower, along (z) direction (thickness direction). In the first model, the ring is in touch with air from four sides. The second model is similar to the first one, with the difference that the upper flat surface (along the positive direction of (z)) is in contact with the water. Placing the ring in different environments causes different acoustic impedances on ring. The relation of acoustic impedance is as follows:[2,16]

$$Z = \rho c. \tag{12}$$

On the other hand, in the first model, the applied impedance on the different surfaces are:

$$Z_1 = Z_2 = Z_3 = Z_4 = 1\frac{\text{kg}}{\text{m}^3} \times 400\frac{\text{m}}{\text{s}} = 400\frac{\text{Pa s}}{\text{m}}.$$

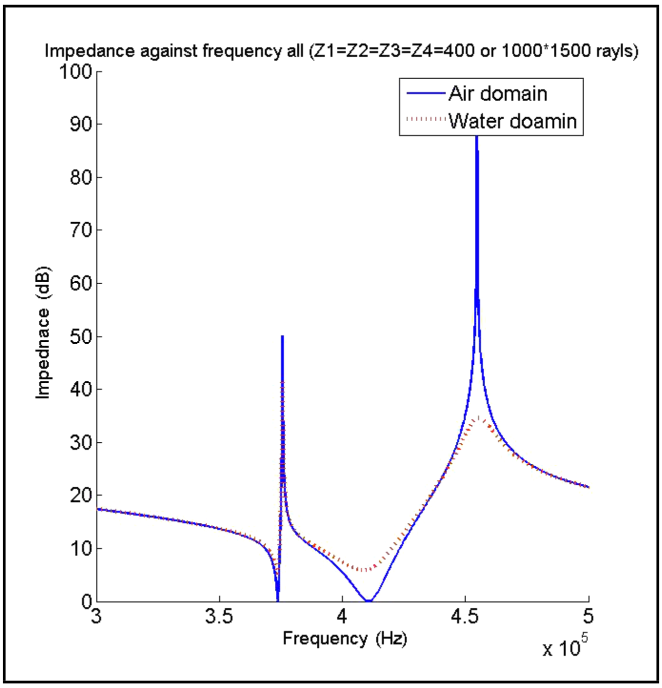

Figure 9. Survey of the effect of change in the acoustic environment material receiving propagation via the matrix model.

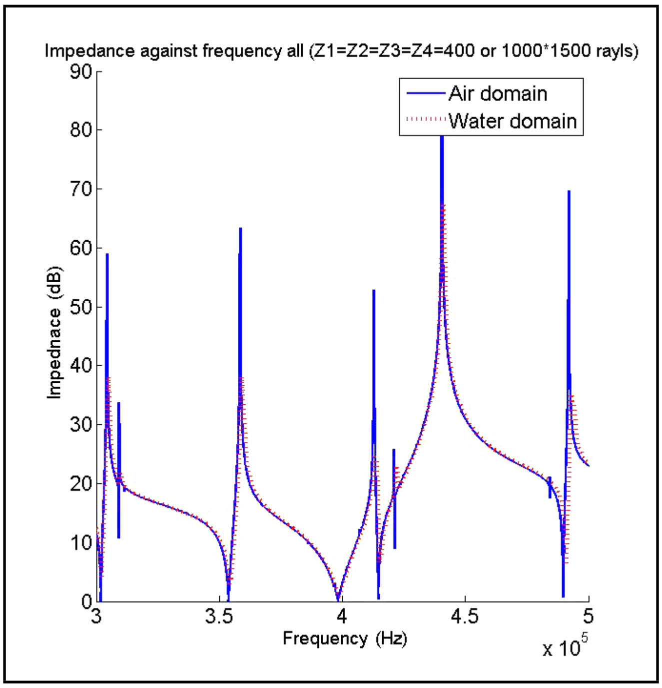

Figure 10. Survey of the effect of change in the material of acoustic environment receiving propagation via FEM model.

In the above equation, z is the acoustic impedance, and indices 1 through 4, according to Fig. 1, are indicative of different directions of the ring. Also, the applied impedance on different surfaces in the second model will be as follows:

$$Z_1 = Z_2 = Z_3 = 1\frac{\text{kg}}{\text{m}^3} \times 400\frac{\text{m}}{\text{s}} = 400\frac{\text{Pa s}}{\text{m}};$$
$$Z_4 = 1000\frac{\text{kg}}{\text{m}^3} \times 1500\frac{\text{m}}{\text{s}} = 1.5 \times 10^6\frac{\text{Pa s}}{\text{m}}.$$

In Figs. 9 and 10, diagrams of electrical impedance of the ring are shown on the basis of the above two models. Figure 9 was obtained using the matrix model, and Fig. 10 was obtained by the FEM model.

According to Figs. 9 and 10, the blue line curve represents the condition in which the ring is in contact with air from four sides, whereas the red line curve represents the condition in which the ring is in contact with water from the upper side. The results are indicative that changes in the acoustic domain have little effect on the location of resonance frequencies. This is where changing the domain along its thickness from air to water has caused the impedance curve to become damped to a great extent. This means that no maximum or minimum points are vividly sharp. The difference between the results of the two models here is greater than in the previous conditions. This is because in higher frequencies, meshing becomes more important and has more effect on results. Perhaps this could mean that unsuitable meshing causes error in the obtained results. However, it is evident that the overall behaviour of results obtained from two models are similar to each other.

6. RESULTS AND INTERPRETATIONS

In order to analyse the effects of change in geometrical dimensions of a piezoceramic ring on impedance and resonance frequency, it is necessary to use analytical models. Any oscillating body in mechanics could be equated with a system of damper, mass, and spring. A piezoceramic ring could be equated with the mechanical system presented in Fig. 11.

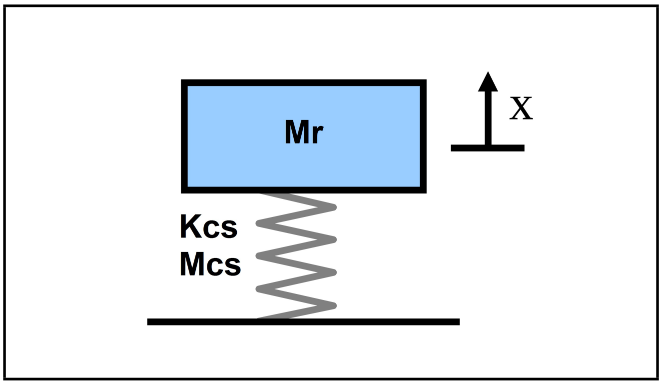

Figure 11. Systems of mass and spring equivalent to a vibrating piezoceramic ring.

Mass resulting from propagation in an acoustical environment is a function of acoustical domain properties, and the cross area of a projector as well as the frequency of propagation would be calculated from Eq. (14). In modelling for each system or structure, an equivalent mass has to be assumed. This mass could be considered as a combination of the mass of the ring (M_{cs}) and the added mass due to the propagation of the wave in the acoustic domain (M_{r}). It is noteworthy that (M_{r}) is usually small. Also for the ring, for every vibration direction, a mass with certain stiffness could be considered. The relation

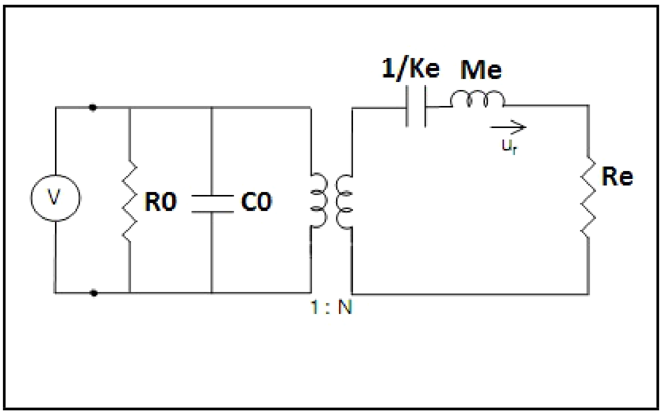

Figure 12. Equivalent electric circuit of a piezoceramic ring having stimulating voltage at both ends.

governing the mass and springs of Fig. 11 are as follows:[10]

$$M_\mathrm{r} = \rho_\mathrm{ac} c_\mathrm{ac} A \left[\frac{2}{\pi} - J_0(ka) + \left(\frac{16}{\pi} - 5 \right) \frac{\sin(ka)}{ka} + \left(12 - \frac{36}{\pi} \right) \frac{1 - \cos(ka)}{(ka)^2} \right] / (ka); \tag{13}$$

$$M_\mathrm{e} = M_\mathrm{r} + \frac{M_\mathrm{cs}}{3}; \tag{14}$$

$$K_\mathrm{e} = \frac{AE}{l}. \tag{15}$$

In the above relations, (A_c) is the cross area of circular portion of the ring's surface, (E) is elasticity modules, and (l) is ring's length along the vibration direction (thickness). (ρ_ac) is the density of the acoustic domain, (c_ac) is the sound velocity in the acoustic domain, (a) is the radius of the projector cross area, (A) is the cross area of the projector, (J_1) is the first order Bessel function, and $k = 2\pi f / c_\mathrm{ac}$ is the wave number.

It was expressed earlier that, in all drawn impedance diagrams for the piezoceramic ring, the vertical axis is the input electrical impedance. The input electrical impedance for a ring stimulating voltage at its ends was obtained from Fig. 12 and based on Eqs. (16)–(22):[19]

$$Z_\mathrm{ul} = \left[\frac{1}{R_0} + j\omega C_0 + \frac{N^2}{Z_\mathrm{mech}} \right]^{-1}; \tag{16}$$

$$R_0 = (\omega C_\mathrm{f} \tan\delta)^{-1}; \tag{17}$$

$$C_0 = \left[\left(\frac{\varepsilon_{33}^\mathrm{T} A_\mathrm{c}}{t_\mathrm{c}} \right) \left(1 - \frac{d_{33}^2}{\varepsilon_{33}^\mathrm{T} s_{33}^\mathrm{E}} \right) \right]; \tag{18}$$

$$N = \frac{F}{V} = \frac{K_\mathrm{c} \Delta t_\mathrm{c}}{E t_\mathrm{c}} = \frac{(A_\mathrm{c}/t_\mathrm{c} s_{33}^\mathrm{E})(S t_\mathrm{c})}{E t_\mathrm{c}} = \frac{S}{E} \frac{A_\mathrm{c}}{t_\mathrm{c} s_{33}^\mathrm{E}} = \frac{d_{33} A_\mathrm{c}}{t_\mathrm{c} s_{33}^\mathrm{E}}; \tag{19}$$

$$Z_\mathrm{mech} = \frac{K_\mathrm{e}}{j\omega} + j\omega M_\mathrm{e} + R_\mathrm{e}; \tag{20}$$

$$R_\mathrm{e} = \rho_\mathrm{ac} c_\mathrm{ac} A \left(1 - J_1(2ka) \right) / (ka); \tag{21}$$

$$\omega_n = \sqrt{\frac{K_\mathrm{e}}{M_\mathrm{e}}}. \tag{22}$$

The unit of the input electrical impedance obtained via Eq. (16) is ohm. By using Eq. (11), it could be calculated in dB. In the above equations, (R_0) is electrical resistance, (C_0) is capacitance volume, (N) is transduction coefficient, (R_e) is resistance terms (in the mass and spring system), (V) is the applied electric voltage, and (F) is the generated force.[10] Other used parameters are introduced in Table 3.[16]

Table 3. Introduction of some parameters of piezoelectric materials.

Symbol	Definition	Unit
C_f	Free capacitance	C/V
$\tan\delta$	Dielectric loss	1
ε_{33}^T	Piezoelectric constant	C/mV
t_c	Piezoceramic ring thickness	m
A_c	Piezoceramic ring cross area	m^2
d_{33}	Piezoelectric strain constant	C/N
s_{33}^E	Compliance matrix member	1/Pa

Now, the results obtained from the three conditions are analysed and interpreted on the basis of the above equations and functions.

6.1. Condition 1

In Eq. (15), by increasing the ring's radius, its stiffness increases in the thickness direction. On the other hand, by increasing the radius, its mass would also be greater. Therefore, in the equation of mechanical impedance, the mass and stiffness terms are increasing. The third term of Eq. (20) also increases in light of enlargement of the cross area. As in this condition, the acoustical environment is air and the radiation impedance is very minute, and hence it is possible to neglect the term resistance in comparison to the term's stiffness and mass in the Eq. (20). However, in Eq. (19), increasing the external radius leads to an increase in the cross area, and N becomes larger. In Eq. (18), C_0 also increases with an increase in the cross area. Considering power 2 on N, it could be stated that this term (N) has a high effect on the final result. Referring to Eq. (16), it becomes obvious that by increasing N and C_0, electrical impedance lowers. (Effect of increase in and is dominant over increase in stiffness and mass). On the other hand, it is obvious that by increasing the radius stiffness and mass, according to Eq. (22), the frequency resonance in which minimum impedance exists has also decreased.

It is noteworthy that by referring to the available relations for the matrix model, it is possible to observe the effect of change in the external radius or any other geometrical parameters on the electrical impedance of a piezoceramic ring. Clearly, by increasing the external radius, the radius resonance mode begins to reduce, such that by a large increase in the external radius, the next radius modes could also be considered within a limited frequency range (as shown by the yellow lines of the above figure).

6.2. Condition 2

First, consider the equation related to mechanical impedance. By increasing the thickness of the ring, its stiffness becomes larger. On the other hand, increasing the thickness causes the stiffness to reduce in the direction of thickness. That is to say, by having fixed values for the internal and external radii and by increasing the thickness, the mass has increased and the stiffness has decreased.

Therefore, the change in the mechanical impedance depends on the numerical values of mass and stiffness. By increasing thickness, N and C_0 will also decrease according to Eqs. (18) and (19). Considering the severe effect of C_0 and particularly N on the electrical impedance, the input electrical impedance increases (see Eq. (16)). In order to survey the change in frequency resonance related to the radius mode, one has to pay attention to the stiffness along the radius. Since the increase in stiffness along the radius and the increase in mass are both proportional to the increase in the side surface of the ring, the ratio related to frequency resonance will remain almost steady. For this reason, the location of the occurrence of frequency resonance becomes noticeable. It is obvious that to calculate the frequency resonance of the thickness mode, in light of having its value expressed by Eq. (15) as length of ring thickness, the stiffness has a large reduction along the thickness, and thus resonance frequency would be reduced in response to an increase in thickness. All this is despite the selected frequency range; no thickness mode around would be observed.

6.3. Condition 3

It is observed that a change in the acoustical environment has no effect on resonance frequencies. It only caused the impedance diagram to be damped. Changing the acoustical environment from air to water with a wave propagated in it causes the value of being mass generated by effect of acoustical environment M_r to increase. However, the main effect of this change in the acoustical environment shows itself in the severe increase in the value of radiating impedance R_e. The role of R_e in the system is similar to that of a damper. Although, in the environment of water, compared to air, the value of M_r has increased some. However, it is possible to neglect the changes in stiffness and mass. This means that in the system shown in Fig. 11, the mass and stiffness have remained almost constant, and the damping term has increased. Therefore, according to Eq. (22), the resonance frequencies of the system would not become changed. On the other hand, it is obvious in a mass and spring system that by an increase in the damping term, the vibration of system moves toward being damped. This means that resonance modes in the impedance diagram begin to disappear. It is for this reason that despite frequency resonance remaining constant, it appears that input electrical impedance has become damped and resonance frequencies responsive to the minimum points in the diagram are no longer sharp and are not vividly noticed.

7. CONCLUSIONS

Modelling of different elements of electroacoustic transducers is an introduction for the modelling of the transducers. Undoubtedly, the most important part, one that has the greatest effect on response of a transducer, is the piezoceramic ring used in it. Precise recognition of the effect of geometrical parameters of a ring helps to reach a desired frequency response based on making necessary changes in its dimensions and sizes. In most studies conducted in the past, the main emphasis has been on the analytical models. However, by considering the limitations of these models, it was attempted herein to extend the modelling to the FEM, as well. In the present paper, attempts were made to use the matrix method and the FEM simultaneously. Differences between them were studied, and the limitations and advantages of each method were analysed. Based on the presented results herein, the following findings could be reviewed as the most noticeable points of this study:

- Comparisons between the results obtained from both the matrix method and the finite element method for modelling a known ring revealed that results are very similar. Also, considering the available experimental results for the same ring and comparing both methods to experimental results indicated that both models are capable of simulating frequency behaviour of a piezoceramic ring.
- By studying the effects of geometric parameters and the surrounding environment on the frequency response of a ring, it could be stated that geometric parameters, besides having effect on electric impedance, also cause noticeable changes in the resonance frequency of a ring. This is where the surrounding environment of the ring only causes changes in the intensity of the electric impedance of the ring.
- Based on the results from both the simulation methods, by increasing the external radius of the circular ring, the resonance frequency related to the radius mode decreases. Through quantitative observation, it could be stated that by doubling the size of the external radius, the resonance frequency decreases around 30%. The reduction of electric impedance responsive to this reducing radius is around 14 dB.
- Based on the obtained results, thickness change in piezoceramic ring has no effect on resonance frequency related to radial mode. Nevertheless, these changes cause the resonance frequency of the thickness mode to be changed. Therefore, the greatest effect of change in the radius is in the resonance frequency of the radial mode, and the greatest effect of the changes in thickness is in the resonance frequency of the thickness mode. Also, by increasing thickness, the level of electrical impedance for a certain frequency would be increased.
- Based on the obtained results, changes in the acoustic environment have little effect on the location of resonance frequency. This is where change in the surrounding environment of a ring in the thickness direction from air to water has caused the shape of the impedance diagram to become damped considerably. In other words, maximum and minimum points could no longer be observed as sharply as they were before. That is to say, some resonance modes begin to disappear.

REFERENCES

[1] Hodges, R. P. *Underwater Acoustics, Analysis, Design and Performance of Sonar*, John Wiley & Sons, Ltd, (2010). http://dx.doi.org/10.1002/9780470665244.

[2] Etter, P. C. *Underwater Acoustic Modelling and Simulation*, Spon Press, (2003), 3rd ed. http://dx.doi.org/10.4324/9780203417652.

[3] Waite, A. D. *Sonar for Practicing Engineering*, John Wiley & Sons, Ltd, (1988), 3rd ed.

[4] Jensen, F. B., Kuperman, W. A., Porter, M. B., and Schmidt, H. *Computational Ocean Acoustics*, Springer, (2011), 2nd ed. http://dx.doi.org/10.1007/978-1-4419-8678-8.

[5] Everst, F. A. *The Master Handbook of Acoustics*, McGraw-Hill, (2001), 4th ed., Chapter 1. http://dx.doi.org/10.1036/0071399747.

[6] Xavier, L. *An Introduction to Underwater Acoustics, Principles and Applications*, Springer, (2010). http://dx.doi.org/10.1007/978-3-642-13835-5.

[7] Wilson, J. S. *Sensor Technology Handbook*, Elsevier, Amsterdam, (2005). http://dx.doi.org/10.1016/b978-075067729-5/50040-9.

[8] Ricón, Y. G.-U. and de Espinosa Freijo, F. M. Piezoelectric modelling using a time domain finite element program, *Journal of the European Ceramic Society*, **27**, 4153–4157, (2007). http://dx.doi.org/10.1016/j.jeurceramsoc.2007.02.127.

[9] Abdel Fattah, A. M., Ali, M. G. S., Elsyed, N. Z., and Gharieb, A. A. Piezocermaic materials for ultrasonic probes, *Egyptian Journal of Solids*, **28**, (2005).

[10] Çepni, K. A Methodology for Designing Tonpilz-Type Transducers, MSc thesis, Middle East Technical University, (2011).

[11] Sherman, C. H. and Butler, J. L. *Transducers and Arrays for Underwater Sound*, Springer, (2007). http://dx.doi.org/10.1007/978-0-387-33139-3.

[12] Jovanović, I., Mančić, D., Paunović, V., Radmanović, M., and Mitić, V. V. Metal rings and discs Matlab/Simulink 3D model for ultrasonic sandwich transducer design, *Science of Sintering*, **44**, 287–298, (2012). http://dx.doi.org/10.2298/sos1203287j.

[13] Mančić, D., Radmanović, M., Petrušić, Z., and Stančić, G. Influence of ultrasonic transducer acoustic impedances and dimensions on its input electrical impedance, *Working and Living Environmental Protection*, **5**, 59–72, (2008).

[14] Kocbach, J. Finite Element Modelling of Ultrasonic Piezoelectric Transducers: Influence of Geometry and Material Parameters on Vibration, Response Functions and Radiated Field, PhD dissertation, University of Bergen, (2000).

[15] Bayliss, C. Application and Development of Finite Element Techniques for Transducers Design and Analysis, PhD dissertation, University of Birmingham, (1998).

[16] Radmanović, M. D. and Mančić, D. D. *Designing and Modelling of the Power Ultrasonic Transducers*, M.P. Interconsulting, (2004).

[17] Nygren, M. W. Finite Element Modelling of Piezoelectric Ultrasonic Transducers, MSc thesis, Norwegian University of Science and Technology, (2011).

[18] Chung, G.-S. and Phan, D.-T. Finite element modelling of surface acoustic waves in piezoelectric thin films, *Journal of the Korean Physical Society*, **57**, 446–450, (2010). http://dx.doi.org/10.3938/jkps.57.446.

[19] Nguyen, K. K. Design and Comparison of Single Crystal and Ceramic Tonpilz Transducers, MSc thesis, University of Texas at Austin, (2010).

[20] Leping, F. and Ramanathan, S. K. On application of radiation loss factor in the prediction of sound transmission loss of a honeycomb panel, *International Journal of Acoustics and Vibration*, **17**, 47–51, (2011).

[21] Pantea, C., Osterhoudt, C. F., and Sinha, D. N. Determination of acoustical nonlinear parameter β of water using the finite amplitude method, *Ultrasonics*, **53**, 1012–1019, (2013). http://dx.doi.org/10.1016/j.ultras.2013.01.008.

Experimental Evaluation of Flank Wear in Dry Turning from Accelerometer Data

R. Serra

INSA Centre Val de Loire, Laboratoire de Mécanique et Rhéologie / CEROC, Blois, France

W. Rmili

Université François Rabelais, Laboratoire de Mécanique et Rhéologie / CEROC, Tours, France

(Received 18 December 2013; accepted 14 November 2014)

This paper presents an experimental evaluation of cutting tool wear based on vibration signals to study the wear development of the cutting tool insert in order to increase machining performance. To achieve this purpose, tool life tests according to ISO standard 3685 have been performed in turning operation under dry cutting conditions. The wear development was studied for thirty cutting tool inserts selected from the same production batch, and used in strictly identical experimental conditions for a statistical study. The vibration signatures acquired during cutting processes have been analysed and contrasted using three signal processing techniques: statistical, temporal and spectral analysis. Results have shown that the dynamic characteristics of tool vibration changed with cutting tool wear development. Furthermore, this vibration analysis exhibited a strong correlation, during machining, between the evolution of flank wear land and vibration responses.

1. INTRODUCTION

In the machining process, the quality of the workpiece, like dimensional accuracy and surface roughness, depends mainly on the state of the cutting tool. Monitoring of the cutting tool condition therefore plays a significant role in achieving consistent quality and controlling the overall cost of manufacturing. High performance machining consequently requires a good evaluation of the cutting tool wear.[1] A wide variety of sensors, modelling, and data analysis techniques have been developed for this purpose.[2–4] In general, the cutting tool wears on the two contact zones, and the wear phenomenon appears in several forms, such as flank wear, crater wear, chipping, etc.[5] These forms depend essentially on cutting tool characteristics, workpiece material, cutting conditions, and types of machining.[6] Crater wear occurs on the rake face of the tool (see Fig. 1) where the chip moves with a frictional force under heavy loads and high temperatures, leading to wear. Crater wear is usually avoided or minimized by selecting cutting conditions and a cutting tool that does not have an affinity for diffusion with the workpiece material. Flank wear is caused by friction between the flank face of the cutting tool (see Fig. 1) and the machined workpiece surface. At the tools flank-workpiece interface, tool particles adhere to the workpiece surface and are periodically sheared off. This leads to the loss of cutting edge and affects the dimensional accuracy and surface finish quality. An established industrial standard on tool wear is ISO 3685 (1993).[7] Figure 1 shows the typical tool wear profile according to this standard. In this figure, the wear of the major cutting edges of the tool can be divided into four regions:

- Region C is the curved part of the cutting edge at the tool corner, which marks the outer end of the wear land;
- Region B is the remaining straight part of the cutting edge between Region C (consisting of uniform wear land);
- Region A is the quarter of the worn cutting edge length farthest away from tool corner;
- Region N extends beyond the area of mutual contact between the tool workpiece for approximately 1 to 2 mm along the major cutting edge. The wear in this region is of the notch type and contributes significantly to surface roughness.

Under normal machining conditions, flank wear is regarded as the most preponderant. According to ISO 3685 (1993), measurement of the width of flank wear land (VB) is the most commonly used parameter to evaluate cutting tool lifespan.[5,6] If the profile is uniform, the tool can be used unless the average value of VB is greater than 0.3 mm. For uneven wear, the maximum wear land width (VBmax) should be less than 0.6 mm.

The development of this wear form on the cutting tool is not a random phenomenon. A typical evolution of flank wear land (VB) with cutting time for different cutting velocities is shown in Fig. 2.[5] The curve can be divided into three zones during its lifetime:

- Initial wear zone, where the initial flank wear land is established (primary wear zone);
- Steady wear zone, where wear progresses at a uniform rate (secondary wear zone);
- Accelerated wear zone, where wear occurs at a gradually increasing rate (tertiary wear zone).

Generally, the evaluation of cutting tool wear can be made in two ways: direct and indirect methods. The direct methods involve measuring the state of tool wear by the classical vision or optical systems such as CCD-based cameras, equipped optical microscopes, and/or white light interferometers.[8,9] These methods have an advantage of measuring exact

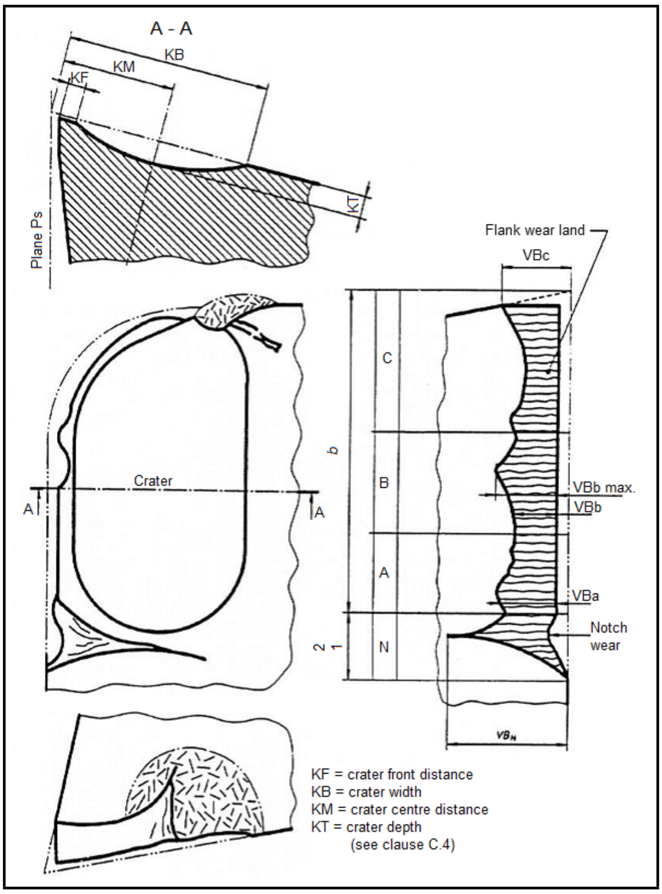

Figure 1. Progressive tool wear geometry according to ISO standard 3685 (1993).

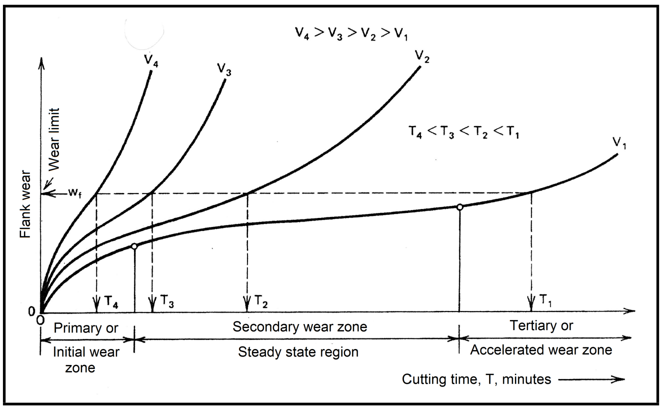

Figure 2. Evolution of flank wear related to cutting time (Altintas, 2000).

geometric changes due to wearing of the cutting tool. However, these methods require production to stop for the evaluation of the cutting tool wear, and in most cases it is too late to limit its effects. The indirect methods are achieved by the correlation of suitable sensors to cutting tool wear.[10] In this case, the cutting tool wear is not obtained directly, but estimated from the signal of the measurement feature. The features are extracted through signal processing techniques for evaluating its corresponding wear state. Direct and indirect methods, discussed in the work by Byrne, et al.,[11] are based on tool wear measurement using various tool wear sensors, radio isotopes as tracers, chemical analysis of tool particles carried by chips, detection probe microscopes, and weighing of the tool before and after machining,[12] acoustic emissions,[13] cutting forces,[14,15] optical displacement sensors,[16] spindle current,[17] strain measurements,[18] tool vibrations,[2,18,19] etc. But many of them are difficult to implement in the real-time monitoring of a production system. However, sensing accelerometer signals from the cutting process is one of the most promising methods. The wide range of techniques available for characterizing the tool wear, either during the machining process or after, indicates that no technique has gained widespread acceptance, either in research or in industrial practice. This is not surprising, since it is clear that each method suffers from numerous disadvantages. The final decision on what method is appropriate for a particular application rests with the user.

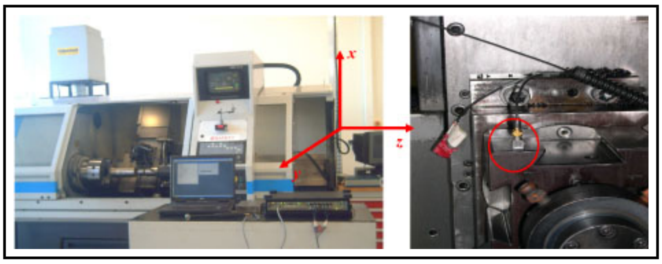

Figure 3. Machine tool used, data acquisition system, directions and localization of a tri-axial accelerometer mounted on tool holder.

In this context, a collaboration project between a world leader in cutting tool insert manufacturing and our laboratory was carried to develop a reliable and applicable evaluation based on vibratory analysis to characterize in terms of wear a new cutting tool insert. In this study, the vibratory signatures produced during the turning process and acquired by a tri-axial accelerometer, mounted on the tool holder, were analysed using three signal processing methods: statistical analysis, time domain analysis, and spectral analysis. The selected processing methods are simple to operate in an industrial environment, and do not require protracted computing time. The results issued from vibratory analysis were compared with the off-line direct control of cutting tool wear and contrasted in a sensitivity matrix.

2. METHODOLOGY

2.1. Experimental Set-up and Data Acquisition

2.1.1. Machining Details

In this study, experiments were conducted for the turning process, and the machining operations have been achieved on a 2.4 kW power SOMAB model 500 lathe (CNC), as shown in Fig. 3. The cast iron workpiece material chosen was an AISI CL 40 gray iron for its good machinability, wear resistance, and vibration damping capacity. The cutting tool insert was made by Safety Company of the ISO CNMG 1204 08 with a MT-CVD inner coating (TiCN/Al2O3/TiN multilayer structure) and mounted on ISO DCLNL 2525M12 tool holder.

Cutting operations were performed in dry conditions (without applying coolant). All cutting experiments were performed under the following cutting conditions according to manufacturer recommendations and held under the same cutting conditions in order to examine the experimental repeatability: cutting speed $V_c = 340$ m/min, feed rate $f = 0.18$ mm/rev, and depth of cut $a_p = 1.5$ mm.[6,20]

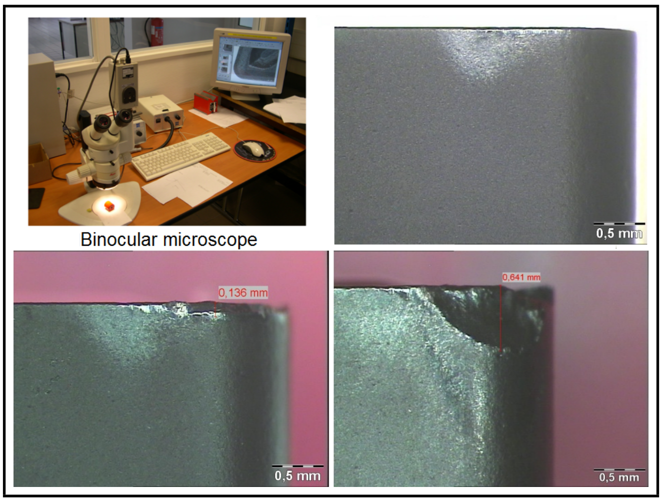

Figure 4. Binocular optical microscope of flank wear insert after machining 1 minutes: (a) 8 minutes (b) and 11 minutes (c) of tool life (4× magnification).

2.1.2. Flank Wear Measurement

Tool life tests according to ISO 3685 (1993) were performed.[7] The assessment of flank wear is accomplished by its direct measurement. From the first use up to the end of its lifespan, the cutting tool state was controlled over regular intervals (after each cutting test). Tool wear was measured carefully using a modern CCD Camera linked to a binocular optical microscope for the picture acquisition in an integrated desktop PC with a commercial digital image processing software installed (AnalySIS). A high resolution picture (768 pixels × 576 pixels) of the flank face at 4× zoom was taken and imported into AnalySIS software, in order to further measure VB. Wear measurements were made along the length of the active cutting edge. Each test was repeated three times, and an average was calculated to ensure precision and repeatability, as shown in Fig. 4.

A specific optical technique based on white light interferometry is a modern technique for accurately and precisely measuring the 3D surface of the cutting tools. This technique uses the vertical scanning interferometer (VSI) performed on a Wyko NT-2000 optical profiler. To evaluate the degree of tool wear, the mean of the flank wear width (VB) was measured by scanning the major flank (scanning size is 0.60×0.46 mm^2), as illustrated in Fig. 5 below.

2.1.3. Accelerometer Data Acquisition

In order to study the correlation between tool vibration and tool wear, it is necessary to first analyse how tool vibration acts on a machined workpiece. As mentioned by Tobias[21] and after by Thomas, et al.,[22] the variation of cutting forces generated when the tool and workpiece come into contact produce significant structural deflections. Consequently, the chip thickness varies in proportion to the tool deflection $x(t)$. Assuming a simple model, the vibration of the tool structure may be described by the following dynamic equation:

$$m\ddot{x}(t) + c\dot{x}(t) + kx(t) = f(t); \tag{1}$$

where m, c, and k are the effective mass, damping, and stiffness, respectively, of the tool structure. The tool deflections $x(t)$ are obtained by measuring the acceleration amplitudes on the tool during the machining process, using a B&K tri-axial

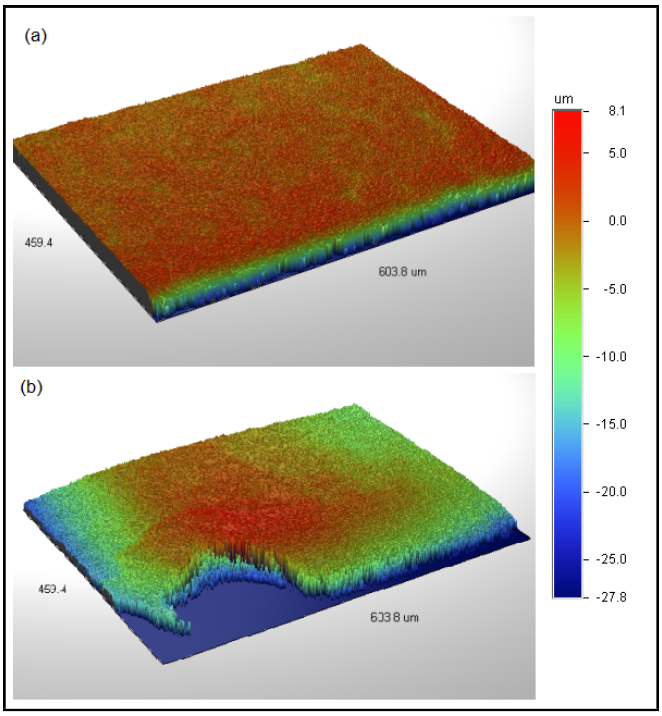

Figure 5. 3D interferometer scanning of new insert (a) and worn insert (b).

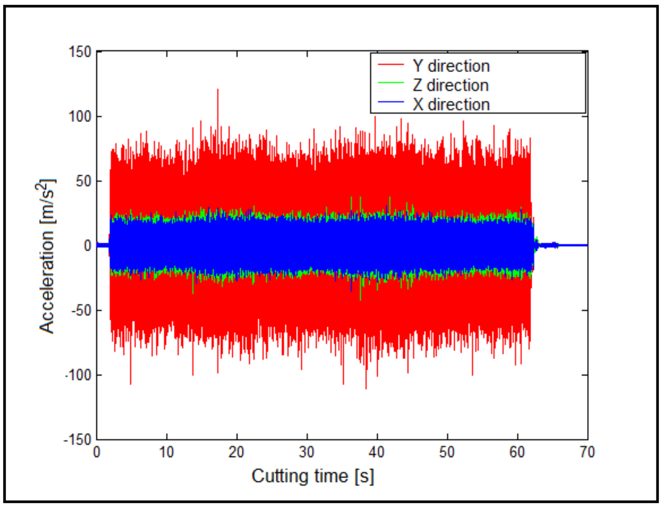

Figure 6. 3D interferometer scanning of new insert (a) and worn insert (b).

piezoelectric accelerometer (type 4520) with a sensitivity of 1.032 mV/ms^{-2} according X direction, 1.067 mV/ms^{-2} according Y direction, and 1.045 mV/ms^{-2} according Z direction. This accelerometer was fixed on the tool holder, to be in the fixed part of the machine and near of the cutting area, as shown in Fig. 3.

All vibratory signatures produced during the dry turning process were measured in real time, recorded, and analysed with a B&K Pulse Multi-channel analyser connected directly to the desktop PC in the three directions: the axial or feeding direction (Z), the tangential (to the rotating workpiece) or cutting direction (Y), and the radial direction (X), as shown in Fig. 6. This generates a large number of features, which was helpful to acquire maximum information about the cutting tool wear.

Signals issued from the accelerometer were acquired for a 70 seconds (including 60 seconds of cutting time) and sampled at 16,384 Hz. Each signal contained 1,146,600 samples.

Collected data were stored directly on the PC hard drive. Signal processing methods were performed from raw data using our interactive MATLAB interface.

2.2. Signal Processing Analysis

Exploiting vibratory signals acquired during machining allows the estimation of the cutting tool wear and the follow-up of its evolution by calculating several parameters. Three signal processing techniques based on statistical analysis (variance), time domain analysis (envelope), and spectral analysis (smoothed mean periodogram) are chosen to evaluate a flank wear from accelerometer data. These techniques are very common and do not require qualified personnel or investment in expensive equipment. The sensitivity matrix will compare these methods.

2.2.1. Statistical Analysis

The variance σ^2 of the accelerometer signal recorded x_q such as $x_q[n] = (x_q(1), x_q(2), x_q(3), , x_q(N))$, where n is a sample and N is the number of samples obtained at periodic time intervals of T seconds, maintains the relevant information about the process and tool conditions. It is defined by:

$$\sigma^2 = E[x_q^2] - (E[x_q])^2. \qquad (2)$$

2.2.2. Time Domain Analysis

The time domain method described below provides a rapid quantification of the tool wear during the turning process. The envelope represents the slowly varying features of the signal and is calculated from the magnitude discrete-time analytic signal modulus $|Z_q|$, defined by:

$$Z_q = x_q + j\tilde{x}_q; \qquad (3)$$

where a real part x_q is the original data, and the imaginary part $\tilde{x}_q$ contains the Hilbert transform of the signal implemented in a MATLAB as function "hilbert()".

In fact, the analytic signal Z_q for a sequence x_q has a one-sided discrete Fourier transform — that is, negative frequencies are zeros. To approximate the analytic signal, Hilbert calculates the Fast Fourier transform (FFT) of the input sequence, replaces those FFT coefficients that correspond to negative frequencies with zeros, and calculates the inverse FFT of the result. Recall that the convolution kernel $h[n]$ for the transfer function of the Hilbert transform can be calculated through the inverse Fourier transform:[23]

$$h = \begin{cases} \dfrac{2}{\pi}\dfrac{\sin^2(\pi n)}{n}, & n \neq 0 \\ 0, & n = 0 \end{cases}. \qquad (4)$$

The analytic signal is useful as an estimates for the amplitude envelope $\mathbf{A}$ of the signal x_q in discrete-time domain. Notably, it was used to evaluate the tool wear from onset to the ending of tool life.

2.2.3. Spectral Analysis

The simplest way to determine the frequency domain information is by using the Fast Fourier Transform (FFT) of the

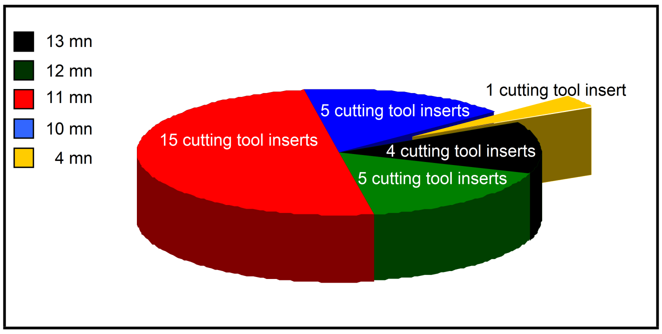

Figure 7. Lifespan of thirty cutting tool inserts used in experiments.

measured signal. But more advanced statistical signal processing techniques, such as computing the smoothed mean periodogram so-called power spectral density (PSD) with Welchs method,[23] can yield better results. In spectral domain, the PSD $S_X(f)$ of the signal $X(t)$ is determined by the relation:

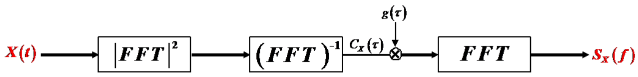

where $C_X(\tau)$is the correlation function of $X(t)$, and $g(\tau)$ is a Hanning window.

3. RESULTS AND DISCUSSION

3.1. Tool Wear Control

As expected, the experimental results showed that the dominant tool wear was the flank wear (VB). Damage observed on the rake face, such as width and depth of crater wear, indicates that the crater wear was not affected by wear mechanisms except some frictions due to chip contact during cutting process. It is relatively weak comparing to flank wear (VB) in accordance with the other studies used in this paper, and therefore the chosen criterion of tool life is the flank wear.

In accordance with the ISO Standard 3685, an average width of flank wear land (VB) of 0.3 mm (considered to be regularly worn) is adopted for the tool life criterion, as shown in Fig. 5(b). For the same insert, if the criterion is not achieved, the tests continue in order to provide wear data for use in the wheel wear evaluation procedure, as shown Figs. 4(a) and (c). Then, experiments were stopped when flank wear (VB) reached or exceeded the value of flank wear limit. Figure 4(c) shows the flank wear after the eleventh cutting passes. It can be seen that the flank wear was quite severe. The list of all experiments in which the flank wear limit is measured is shown in Table 1.

3.2. Dispersion Analysis

The result obtained shows that although the cutting tool inserts belong to the same production batch and are used under the same experimental conditions, their end of lifetime varies from 4 to 13 minutes, which shows the complexity of the phenomenon of wear in an industrial context and the manufacturing process dispersion.

In accordance with the results given in Table 1, the lifespan dispersion of the same thirty cutting tool inserts studied in the same conditions is shown in Fig. 7.

From the representation shown in Fig. 7, the thirty cutting tool insert lifespan dispersion could be divided into four prin-

Table 1. List of all experiments.

Insert N^o	Machined work-piece diameter [mm]	Machined length [mm]	Time limit [min]	Flank wear limit [mm]
1	185	105.30	13	0.31
2	182	107.04	13	0.30
3	179	108.83	12	0.32
4	176	110.69	13	0.40
5	173	112.60	13	0.40
6	170	114.59	11	0.40
7	167	116.65	11	0.32
8	164	118.78	11	0.60
9	161	121.00	11	0.30
10	158	123.29	11	0.37
11	155	125.68	12	0.40
12	152	128.16	11	0.41
13	149	130.74	12	0.74
14	146	133.43	11	0.71
15	143	136.23	10	0.57
16	140	139.15	11	0.62
17	137	142.19	11	0.64
18	134	145.38	4	0.40
19	131	148.71	11	0.60
20	128	152.19	11	0.40
21	125	155.84	10	0.40
22	122	159.68	11	0.42
23	119	163.70	10	0.34
24	116	167.94	12	0.52
25	113	172.39	10	0.32
26	110	177.10	11	0.55
27	107	182.06	12	0.41
28	104	187.31	11	0.60
29	101	192.88	11	0.53
30	98	198.78	10	0.40

cipal duration groups: 10, 11, 12 and 13 minutes (an insert which lasted 4 minutes was considered an anomaly and was not taken into account in this study).

3.3. Flank Wear Analysis

Flank wear evolution was tracked by plotting a mean of flank wear width (VB) versus cutting time, as illustrated in Fig. 8, for each group. It was observed that the flank wear propagation was almost linearly related to the cutting time and then increased again quite rapidly, indicating that the severity of degradation was increased until tool collapse.

In order to provide wear data for use in the wheel wear evaluation procedure, the tool life was split into three regions (see Fig. 8). It can be clearly seen that the wear trend obeys the universal wear law of any mechanical workpiece (initial wear zone, steady state wear zone, and accelerated wear zone), according to the research referenced in this study (see Fig. 2).

Indeed, the wear-time diagram shows that it is possible to distinguish the three domains for all groups: initial wear phase of the insert, from the first experiment up to the 3rd experiment; a wear stabilization zone where the flank wear increase uniformly, from the 3rd experiment up to the cutting time between 8th and 10th experiment; and finally a tool wear acceleration phase where the wear rate increases rapidly, crossing the exceeded value of flank wear. Furthermore, all cutting tool inserts had the same behaviour before reaching the wear acceleration. Each group was characterized by its own local and specific stabilization/acceleration transition. However, using the direct control, all these transitions could be localized between 9 and 10 minutes of cutting time. In the following section, the application of signal processing methods is shown,

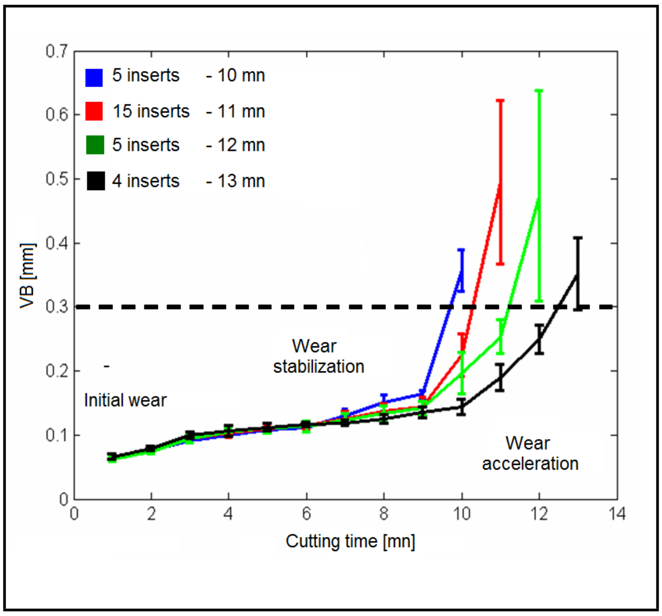

Figure 8. Flank wear (VB) according to the cutting experiment for each insert group.

which can be used to precisely determine the flank wear. This is helpful in industrial applications to predict the end of tool life and preserve a good quality of the product.

3.4. Signal Analysis

The evaluation of the cutting tool wear development was conducted by analysing the vibratory signature generated during the dry turning process. The estimation of the cutting tool wear was obtained by calculating three signal processing analyses: variance (Fig. 9), envelope (Fig. 10), and PSD (Fig. 11), in order to be considered as tool wear indicators in real time monitoring strategies.

3.4.1. Variance and Tool Wear

In Fig. 9, the Y-direction is difficult to exploit because of high levels of the recorded signal. In the X- and Z-directions, the evolution of the variance from the beginning to the end of machining is very close; all the groups have the same behaviour. The transition, or collapse, can be estimated at the 10th minute. From this state, each group has its own evolution up to the end of the tool life. In fact, as the flank wear increased, the variance increased gradually. Hence, the variance can be used as a significant parameter for the evaluation of the cutting tool wear.

3.4.2. Envelope and Tool Wear

As for the variance, the levels recorded in the Y-direction for the envelope parameter were raised and did not allow us to establish a correlation with the cutting tool wear. The evolution of the envelope according to the X-direction was most sensitive to the deterioration of the tool state. The three conventional phases of tool wear (initial wear zone, stabilization wear zone, and acceleration wear zone) could be distinguished. It can be seen that the envelope increased gradually as the flank wear. Consequently, the envelope can be used as a significant parameter for the evaluation of the cutting tool wear. Finally for this method, of the three directions, X-direction seems to

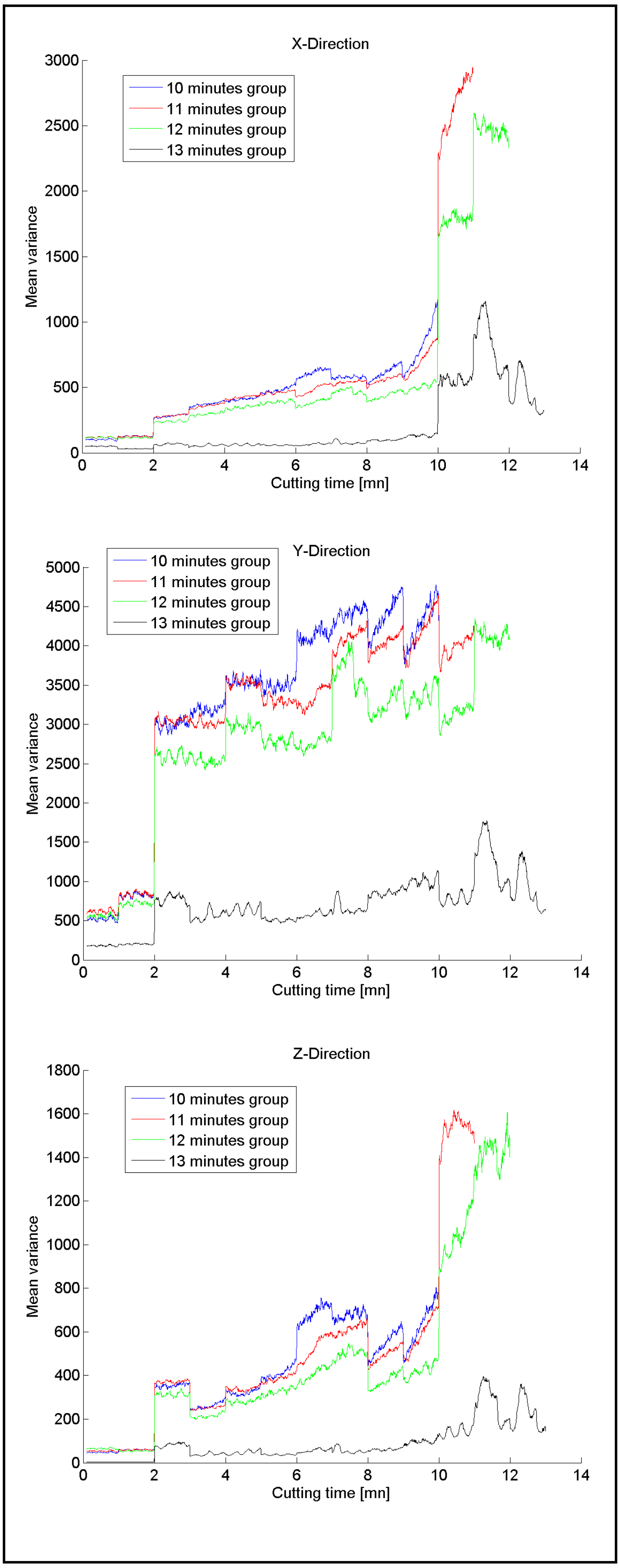

Figure 9. Variance versus experiments for each insert group.

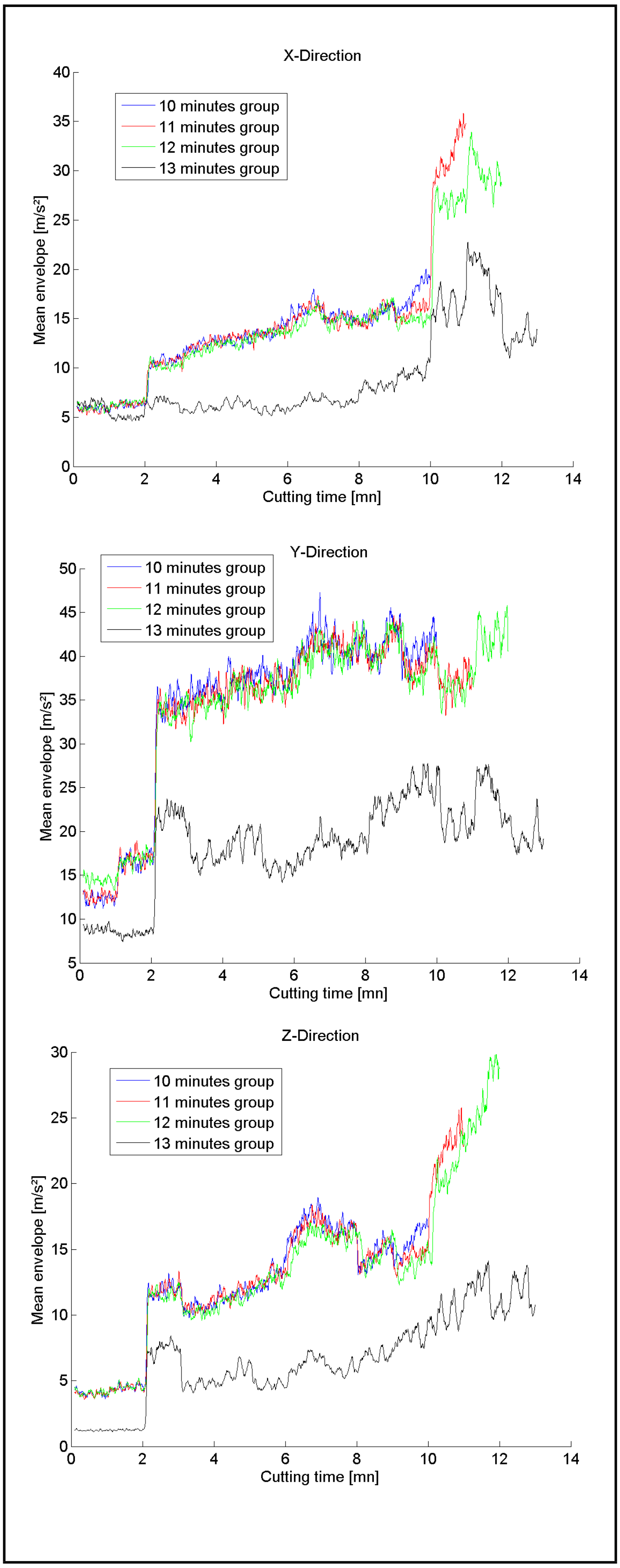

Figure 10. Envelope versus experiments for each insert group.

be the most adapted direction to the evaluation of the wear of the cutting tool.

In addition, for both statistical and temporal analysis, the level of the group of 13 minutes is definitely different from the other groups, whereas the tests were strictly identical, and the measuring chain has been the same during all the tests (same sensor, same cable, same analyser, same process, and same configuration). This shows the complexity of the manufacturing process phenomenon. It can be noted that the groups having longest tool life were also those having the lowest acceleration level.

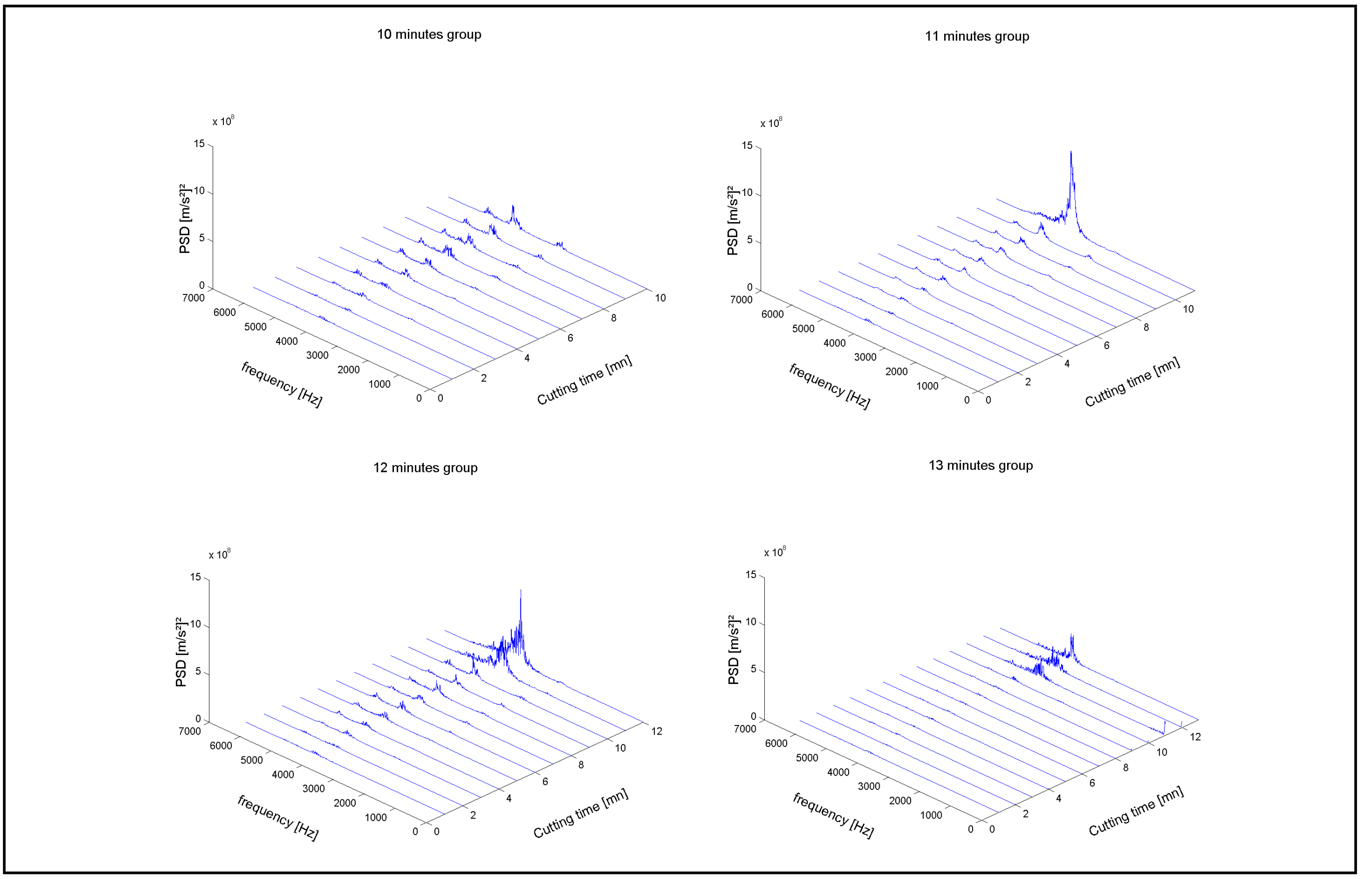

Figure 11. PSD vibration spectra vs experiments for each insert group, respectively, according to X-direction.

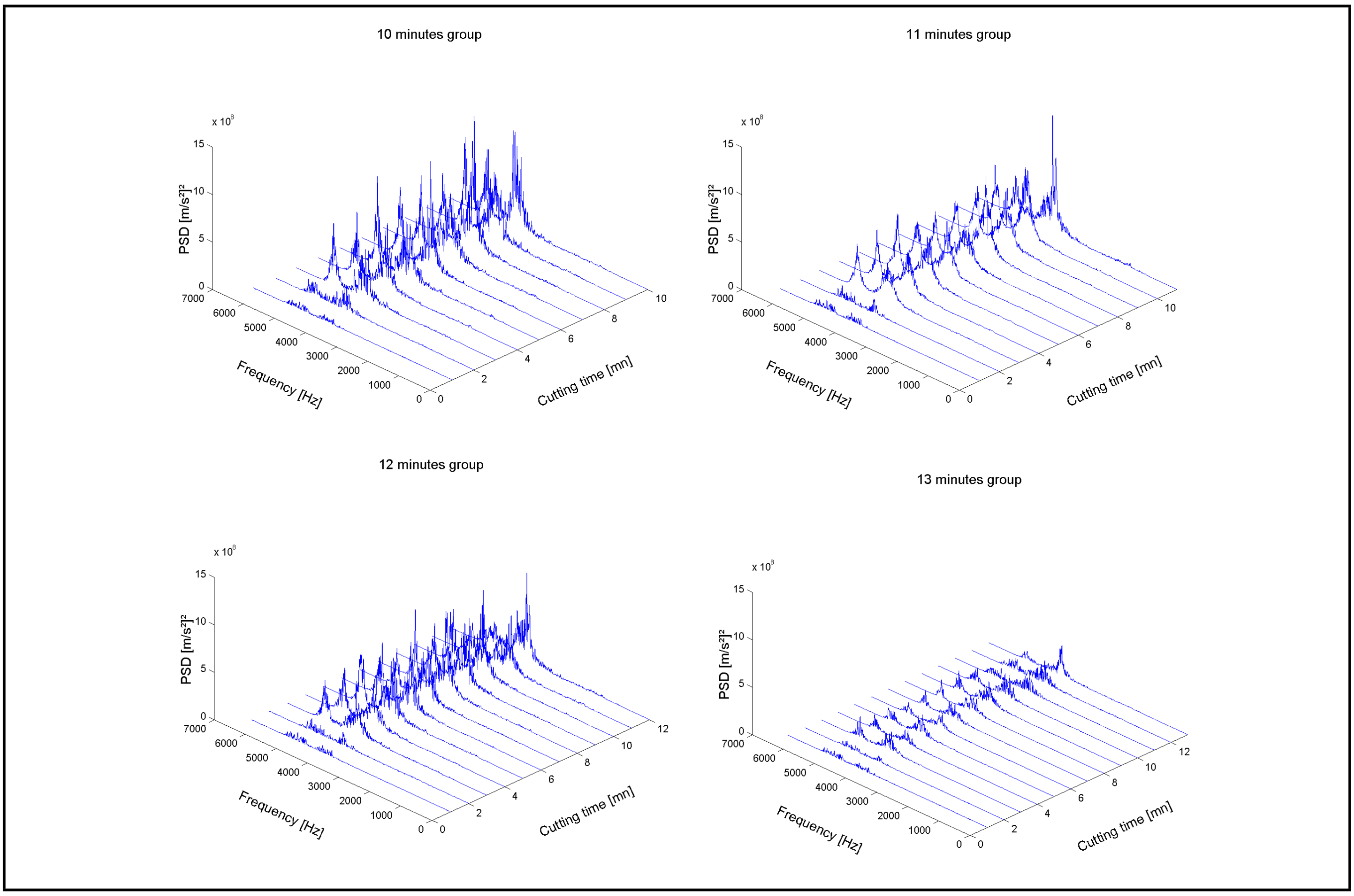

Figure 12. PSD vibration spectra vs experiments for each insert group, respectively, according to Y-direction.

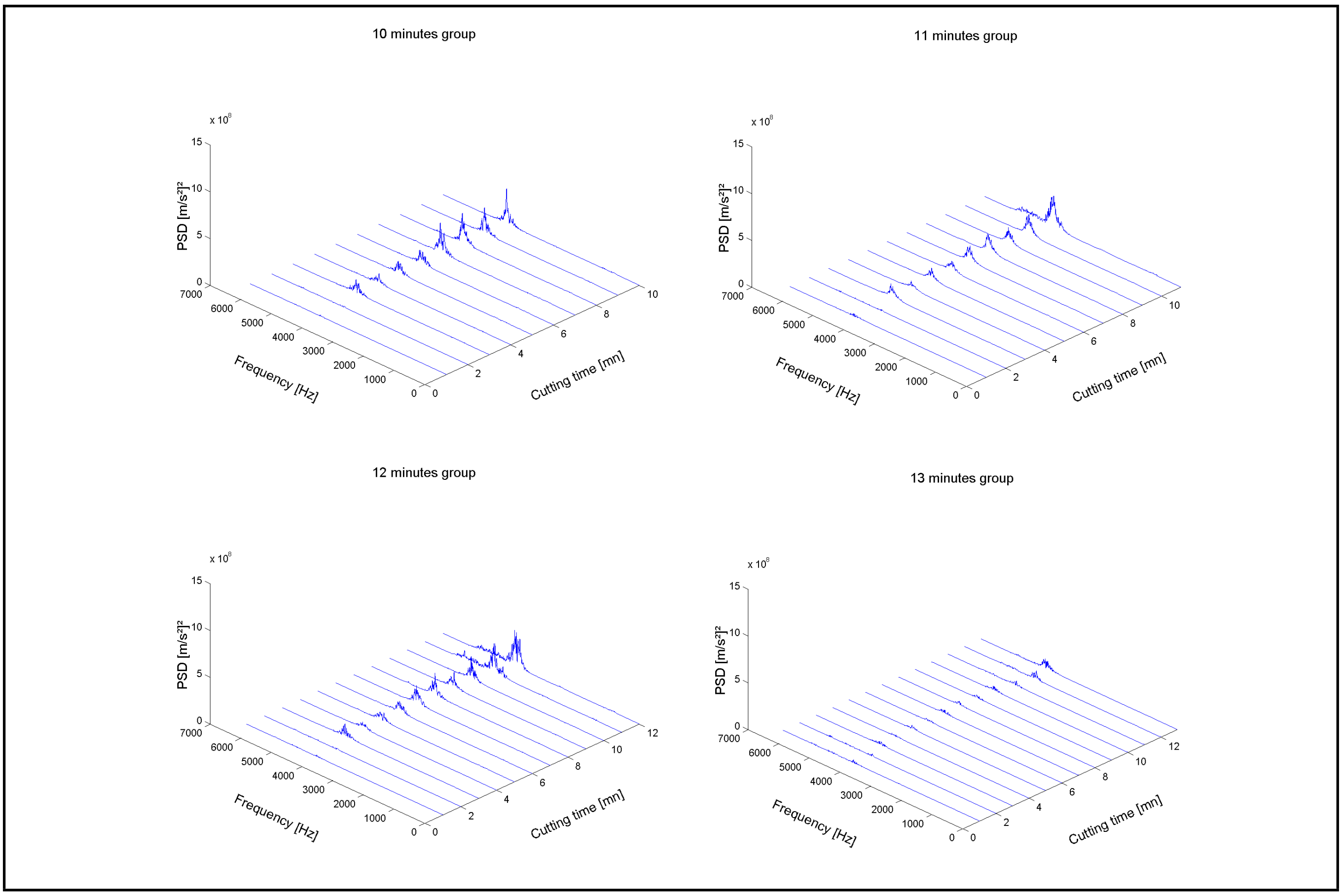

Figure 13. PSD vibration spectra vs experiments for each insert group, respectively, according to Z-direction.

3.4.3. PSD and Tool Wear

In order to characterize the evolution of vibratory energy according to the cutting tool wear, the PSD vibration spectra (waterfall plot) is respectively represented in Figs. 11, 12 and 13, respectively in X-, Y-, and Z-directions.

In these figures, it was possible to visualize the amplitude variations and their corresponding frequencies, and the two frequency bands (one to 4200 Hz and the other to 5100 Hz) were distinguished quite clearly. A third frequency (2600 Hz) is slightly visible in X-direction of the 11 minutes group (Fig. 11). A previous modal analysis of the cutting tool (tap test) has shown that these three frequencies correspond to the first three natural frequencies of the cutting tool. These frequencies increased steadily, peaking before falling just before the tool collapse.

As illustrated in Fig. 12, the Y-direction imposes the highest levels when compared to the others directions, which is in agreement with the research used in this paper, because it corresponds to the direction of cut where the cutting energy is highest. The magnitude of vibration is higher in the main cutting Y-direction than that of the radial X-direction.

The evolution of these PSD according to the X-direction of acquisition was significant to the deterioration of the tool state. The three conventional phases of tool life (initial wear zone, stabilization, and acceleration of wear) can be distinguished.

Finally, it is clear that the amplitude of vibration increases steadily with increasing flank wear, as it was established for the variance or envelope analysis.

Table 2. Sensitivity matrix of vibration components.

	Vibration components		
Criteria	X-Direction	Y-Direction	Z-Direction
Variance	3	1	2
Envelope	3	1	1
Power Spectral Density	3	1	2
Total	9	3	5

3.4.4. Comparative Evaluation of Signal Processing Methods

For the best performance evaluation of the three adapted signal processing methods used, a sensitivity criterion to tool wear was obtained by building a sensitivity index table. Table 2 was constructed using the following score: 3 = most sensitive; 2 = moderately sensitive; 1 = least sensitive; and 0 = not sensitive at all.

All the components of the vibratory signal were sensitive to flank wear, but the X-Direction component was the most sensitive, regardless of the cutting conditions, to all the adapted signal processing used, i.e. the variance, envelope, and power spectral density.

4. CONCLUSIONS

The present study investigates the use of vibration measurement to perform the evaluation of cutting tool wear during the dry turning process. To achieve this objective, tool life tests according to ISO standard 3685 were conducted. The flank wear width of the cutting tool insert was measured using a binocular optical microscope and a 3-D optical profiler after each machining. Thirty inserts used under the same experimental protocol were classified into four groups associated with different lifespans, which demonstrated the complexity of the wear phenomenon in an industrial context.

Generally, all cutting tool inserts had the same behaviour according to the tool life law. The level progressively increases with the time of machining. The cutting tool wear may be split, then, into three regions as expected.

From accelerometer data acquired during the dry turning process, three signal processing analyses based on the calculation of the variance, the envelope, and the smoothed mean periodogram of the signals were evaluated. This demonstrated that the variance, the envelope, and the smoothed mean periodogram were relevant parameters for the evaluation of the cutting tool wear from accelerometer data in the X-direction. For any parameter selected, each group respects a certain order. Indeed, the groups which last longest are those whose vibratory level is lowest. In addition, the highest levels were obtained in the cut direction in agreement with the studies used in this paper. Finally, a sensitivity criterion was proposed to choose the most sensitive direction for signal processing analysis from accelerometer signals.

REFERENCES

[1] Dan, L. and Mathew, J. Tool wear and failure monitoring techniques for turning: A review, *Int. J. Mach. Tool. Manu.*, **30** (4), 579598, (1990). http://dx.doi.org/10.1016/0890-6955(90)90009-8

[2] Dimla, E. Sensor signals for tool-wear monitoring in metal cutting operations a review of methods, *Int. J. Mach. Tool. Manu.*, **40**, 10731098, (2000). http://dx.doi.org/10.1016/s0890-6955(99)00122-4

[3] Lim, G. H. Tool wear monitoring in machine turning, *J. Mater. Process. Tech.*, **51** (14), 2536, (1995). http://dx.doi.org/10.1016/0924-0136(94)01354-4

[4] Braun, S. and Lenz, E. *Machine tool wear monitoring: mechanical signature analysis: theory and applications*, Academic Press Ltd., 321342, (1986).

[5] Altintas, Y. *Manufacturing Automation*, Cambridge University Press, 2000.

[6] Cheng, K. *Machine dynamics: fundamentals, applications and practices*, Springer series in advanced manufacturing, Springer-Verlag London Limited, UK, (2009). http://dx.doi.org/10.1007/978-1-84628-368-0

[7] ISO 3685:1993: Tool-life testing with single-point turning tools, (1993), 2nd edition.

[8] Kurada, S. and Bradley, C. A review of machine vision sensors for tool condition monitoring, *Comput. Ind.*, **34** (1), 5572, (1997). http://dx.doi.org/10.1016/s0166-3615(96)00075-9

[9] Wang, W. H., Hong, G. S., Wong, Y. S., and Zhu, K. P. Sensor fusion for online tool condition monitoring in milling, *Int. J. Prod. Res.*, **45** (21), 50955116, (2007). http://dx.doi.org/10.1080/00207540500536913

[10] Srinivas, J. and Kotaiah, K. Rama. Tool wear monitoring with indirect methods, *Manu. Tech. Today (India)*, **4**, 79, (2005).

[11] Byrne, G., Dornfeld, D., Inasaki, I., Ketteler, G., Knig, W., and Teti, R. Tool condition monitoring (TCM) The status of research and industrial applications, *CIRP Annals*, **44** (2), 541568, (1995). http://dx.doi.org/10.1016/s0007-8506(07)60503-4

[12] Micheletti, G. F., et al., In process tool wear sensors for cutting operations, *CIRP Annals*, **25**, 483495, (1976).

[13] Rice, J. A. and Wu, S. M. On the feasibility of catastrophic cutting tool fracture prediction via acoustic emission analysis, *Transactions of the ASME J. Eng. Ind.*, **115**, 400403, (1993). http://dx.doi.org/10.1115/1.2901781

[14] Ravindra, H. V., Srinivasa, Y. G., and Krishnamurthy, R. Modelling of tool wear based on cutting forces in turning, *Wear*, **169**, 2532, (1993). http://dx.doi.org/10.1016/0043-1648(93)90387-2

[15] Oraby, S. E. and Hayhurst, D. R. Tool life determination based on the measurement of wear and tool force ratio variation, *Int. J. Mach. Tool. Manu.*, **44**, 12611269, (2004). http://dx.doi.org/10.1016/j.ijmachtools.2004.04.018

[16] Choudhury, S. K. and Ramesh, S. On-line tool wear sensing and compensation in turning, *J. Mater. Process. Tech.*, **49**, 247254 (1995). http://dx.doi.org/10.1016/0924-0136(94)01350-a

[17] Cuppini, D. and Errico, G. Tool wear monitoring based on cutting power measurement, *Wear*, **139** (2), 303311, (1990). http://dx.doi.org/10.1016/0043-1648(90)90052-c

[18] Scheffer, C. and Heyns, P. S. Wear monitoring in turning operations using vibration and strain measurements, *Mech. Syst. Signal Pr.*, **15**, 11851202, (2001). http://dx.doi.org/10.1006/mssp.2000.1364

[19] Rmili, W., Ouahabi, A., Serra, R., and Kious, M. Tool wear monitoring in turning process using vibratory analysis, *Int. J. Acoust. Vib.*, **14** (1), 411, (2009).

[20] Coromant, S. *Turning tools general turning*, 2007.

[21] Tobias, S. A. *Machine tool vibration*, Blackie and Son Ltd, London, UK, (1965).

[22] Thomas, M., Beauchamp, Y., Youssef, Y. A., and Masounave, J. Effect of tool vibration on surface roughness during lathe dry turning process, *Comput. Ind. Eng.*, **31** (3), 637644, (1995). http://dx.doi.org/10.1016/s0360-8352(96)00235-5

[23] Oppenheim, A. V. and Schafer, R. W. *Discrete-time signal processing*, 3rd Edition, Pearson, Boston, (2010).

[24] Welch, P. D. The use of fast Fourier transform for the estimation of power spectra: a method based on time averaging over short, modified periodograms, *IEEE T. Acoust. Speech*, **15** (2), 7073, (1967). http://dx.doi.org/10.1109/tau.1967.1161901

Nonlinear Torsional Vibration Modeling and Characteristic Study of Planetary Gear Train Processing Device

Sun Zhijun, Hou Li, Chang Qinglin and Wei Yongqiao

School of Manufacturing Science and Engineering, Sichuan University, Chengdu 610065, China

Li Wei

School of Mechanical Engineering & Automation, Xihua University, Chengdu 610039, China

(Received 19 December 2013; accepted 20 May 2014)

A nonlinear torsional vibration model with meshing errors, time varying meshing stiffness, damping coefficients, and gear backlashes was presented to analyse the nonlinear dynamic behaviour of the planetary gear train system, which was used to machine the Circular-Arc-Tooth-Trace cylindrical gear. Its dimensionless equations of the system were derived, and the solution of the equations was carried out by using the method of numerical integration. The bifurcation diagrams indicated that the system had abundant bifurcation properties with the dimensionless speed, and the damping ratios of meshing pairs could influence the vibration amplitudes and bifurcation characteristic greatly. The phase plane plots and Poincar maps revealed that the motion state of the system would through the regions such as harmonic response, non-harmonic response, 2T-periodic harmonic response, 4T-periodic harmonic response, quasi-harmonic response, and chaotic response. The chaotic regions will cause the system failure and instabilities, so these regions should be avoided.

1. INTRODUCTION

The planetary gear was used in the processing device for machining the Circular-Arc-Tooth-Trace cylindrical gear (CATT gear—it is a new type gear) due to its advantages, such as compactness, large torque-to-weight ratio, large transmission ratios, reduced vibrations, and translational property.[1] The processing device consists of planetary gear sets that have translational and rotary motions, which can form the ideal tooth profile of the CATT gear,[2] and its vibration influences the correct manufacturing of the tooth profile. That is the reason why this paper focuses on the vibration of the planetary gear transmission system. The structures of the processing device of the CATT gear are shown in Figs. 1 and 2. Similarly, there have been numerous studies about the vibration of planetary gears in recent decades. The factors influencing the vibration- and noise-related dynamic responses of planetary gear systems have been investigated by many researchers. Velex and Flamand,[3] Kahraman and Blankenship,[4] and Lin and Parker[5] investigated the time-varying mesh stiffness. Kahraman, Parker, et al. analysed the natural modes of planetary gears with unequally spaced planets and an elastic ring gear.[6,7] Ericson and Parker[8,9] investigated the effects of torque on the dynamic behavior and system parameters of planetary gears by experimental measurement and finite element analysis, and the study provided good methods for the CATT gear research. The transmission errors, the spacing, and backlash-related nonlinear dynamics were the main focus in much published research.[10–12] Xihui, Liang, et al.[13] investigated the vibration properties of a planetary gear set and evaluated the mesh stiffness effectively. Li, Wu, and Zhang[14] formulated a nonlinear time-varying dynamic model for a multi-stage planetary gear train. However, these published studies investigated the vibration based on the conventional planetary gears. Fewer studies are available about the investigations on the translational planetary gear train.

Although many models in previous research are different from this planetary gear set, some studies can provide many available methods, as in some of the work referenced in this paper. A. Kahraman used a family of torsional dynamic models of compound gear sets to predict the free vibration characteristics under different kinematic configurations resulting in different speed ratios, but he investigated the planetary gear sets without nonlinear models.[15] Robert G. Parker examined the effectiveness of planet phasing to suppress planetary gear vibration in certain harmonics of the mesh frequency based on the physical forces acting at the sun-planet and ring-planet meshes.[16] This research proposed a method to suppress the vibration of the planetary gears. J. Lin and R. G. Parker also investigated the natural frequency and vibration mode sensitivities to system parameters for both tuned and mistuned planetary gears.[17,18] V. K. Ambarisha, et al. investigated the complex, nonlinear dynamic behaviour of spur planetary gears using two models: a lumped-parameter model and a finite element model.[19] In this paper, mesh phasing rules to suppress rotational and translational vibrations in planetary gears were valid even when nonlinearity formed tooth contact loss occurs. Sun Zhimin, et al. used a clearance-type nonlinear dynamic model of a 2K-H planetary gear train to analyse the nonlinear dynamic behaviour of the gear train excited by a static transmission error in addition to a mean torque.[20] His research results indicate that the backlash induces complicated nonlinear dynamic behaviour in the 2K-H planetary gear train. Simi-

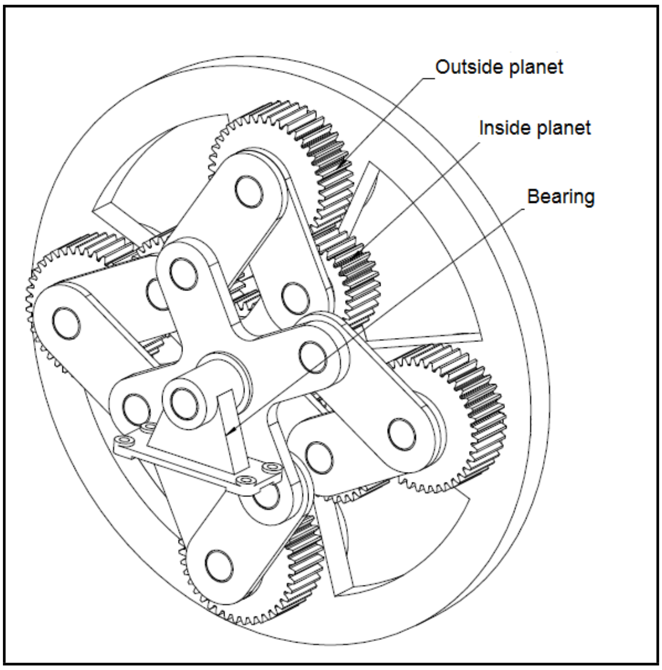

Figure 1. 3D model of the CATT gear processing device.

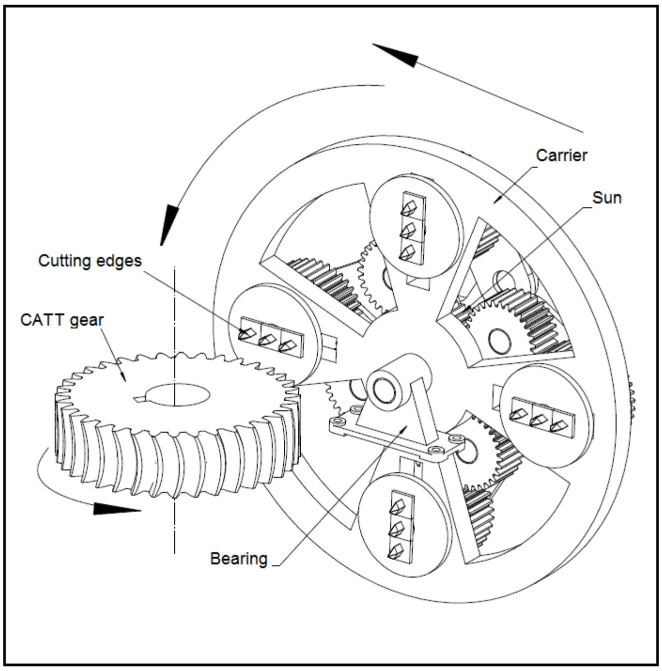

Figure 2. The CATT gear and its planetary gear train processing device.

larly, Li Tongjie, et al. established a nonlinear torsional vibration model of a planetary gear train with errors of transmission, time varying stiffness, and gear backlashes. His study results revealed that the systems motion state would change into chaos in the way of crisis as speed increased, and a smaller damping coefficient would make the systems periodic motion state change into a complex state.[21]

This study proposes a planetary gears device whose planetary gear centre could move with translational motion. Then, a nonlinear torsional vibration model of the planetary gear train is established. This model includes the transmission, time varying meshing stiffness, and gear backlashes. By using the method of numerical integration, the frequency content and geometry of the dynamic response of spur planetary gears in the rotating and stationary reference frames are investigated. This paper tries to improve the stability of the planetary gear train processing device by examining the vibration characteristics of the model.

2. MODELLING METHODOLOGY

The planetary gear train processing device consists of a sun gear (s), N inside planetary gears (q), N outside planetary gears (p), and a carrier (c) without a ring gear. Figures 1 and 2 are the 3D models of the CATT gear processing device with four gear sets, and these gear sets have to be evenly distributed around the sun gear. All gears are spur gears, and the motion of the sun gear is constrained. Each element has one rotational degree-of-freedom without considering translations.

The planetary gear dynamic model used is based on the one developed by Lin and Parker.[5,18] But the structure and the motions of the model are different from those in previous research. According to the motion properties of the planetary gear device, the vibration system can be a simplified spring-damping vibration system with meshing errors and gear backlashes. The torsional vibration model is shown in Fig. 3.

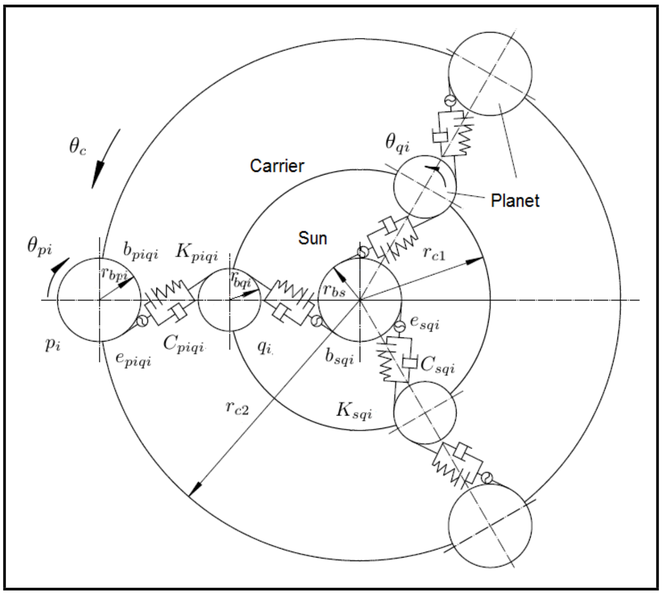

Figure 3. Torsional vibration model of planetary gears.

The model is normally selected with three or four gear sets for vibration analysis. Rotational motions of the carrier, inside planets, and outside planets are denoted by $\theta_h, h = c, q, p,$ and $1...N$, where N indicates the number of planets. The gear bodies are assumed to be rigid with moments of inertia $J_c, J_{qi}, J_{pi}(i = 1, 2, ..., N)$. Not only the sun and inside planet tooth meshes, but also the inside planet and the outside planet tooth meshes, are modelled as linear springs with time-varying stiffness $K_{sqi}(t), K_{piqi}(t)(i = 1, 2, ..., N)$. Simultaneously, the non-linear factors such as the damping C_{sqi}, C_{piqi}, clearance b_{sqi}, b_{piqi} , and meshing error $e_{sqi}(t), e_{piqi}(t)$ are considered in the determination of instability boundaries. By using the Lagrange equation, the systems equations of motion are

$$\begin{cases} J_{qi}\ddot{\theta}_{qi} - (D_{sqi} + P_{sqi} - D_{piqi} - P_{piqi})\, r_{bqi} = 0 \\ J_{pi}\ddot{\theta}_{pi} + T_{L1} = (P_{piqi} + D_{piqi})\, r_{bpi} \\ \left(J_c + \sum_{i=1}^{N} (m_{pi} r_{c2} + m_{qi} r_{c1})\right) \ddot{\theta}_c + T_{L2} \\ + \sum_{i=1}^{N} (D_{sqi} + P_{sqi})\, r_{bs} \cos\alpha = T_D \end{cases}; \quad (1)$$

where $r_{bs}, r_{bqi}, r_{bpi} (i = 1, 2, , N)$ are the base circle radii of the sun, inside planets and outside planets, respectively. The parameters r_{c1} and r_{c2} are the radii of the circle passing through the planets centres for the carrier. m_s, m_{qi}, m_{pi}, m_c are the masses of the sun gear, inside planet, outside planet, and carrier. T_d, T_{L1}, T_{L2} are external torques. $P_{sqi}, P_{piqi} (i = 1, 2, ..., N)$ are the elastic meshing forces, and $D_{sqi}, D_{piqi} (i = 1, 2, ..., N)$ are the viscous meshing forces.[16] They can be expressed as

$$\begin{cases} P_{sqi} = K_{sqi}(t) f\left(\theta_c r_{c1} - \theta_{qi} r_{bqi} - e_{sqi}(t), b_{sqi}\right) \\ P_{piqi} = K_{piqi}(t) f\left(\theta_{qi} r_{bqi} - \theta_{pi} r_{bpi} - e_{piqi}(t), b_{piqi}\right) \end{cases}; \quad (2)$$

$$\begin{cases} D_{sqi} = C_{sqi}\left(\dot{\theta}_c r_{c1} - \dot{\theta}_{qi} r_{bqi} - \dot{e}_{sqi}(t)\right) \\ D_{piqi} = C_{piqi}\left(\dot{\theta}_{qi} r_{bqi} - \dot{\theta}_{pi} r_{bpi} - \dot{e}_{piqi}(t)\right) \end{cases}; \quad (3)$$

where $f(x, b)$ is the nonlinear function of clearance, and it can be represented by[22]

$$f(x, b) = \begin{cases} x - b, & (x > b) \\ 0, & (-b \le x \le b) \\ x + b, & (x < -b) \end{cases}. \quad (4)$$

For spur gears, rectangular waves are often used to approximate mesh stiffness alternating between n and $n + 1$ pairs of teeth in comtact.[5] Each mesh stiffness is represented by

$$\begin{cases} K_{sqi}(t) = K_{msqi} + K_{asqi} \sin(\omega t + \varphi_{sqi}) \\ K_{piqi}(t) = K_{mpiqi} + K_{apiqi} \sin(\omega t + \varphi_{piqi}) \end{cases}; \quad (5)$$

where $K_{msqi}, K_{mpiqi} (i = 1, 2, ..., N)$ are mean values, and $K_{asqi}, K_{apiqi} (i = 1, 2, ..., N)$ are time-varying components of ith the sun to inside planet, and inside planet to outside planet meshes. ω is the mesh frequency of the sun-planet, and $\varphi_{sqi}, \varphi_{piqi} (i = 1, 2, ..., N)$ are the phases.

C_{sqi}, C_{piqi} are the damping coefficients, and they can be expressed as[20]

$$\begin{cases} C_{sqi} = 2\xi_1 \sqrt{K_{msqi}/(1/M_s + 1/M_{qi})} \\ C_{piqi} = 2\xi_2 \sqrt{K_{mpiqi}/(1/M_{pi} + 1/M_{qi})} \end{cases}; \quad (6)$$

where ξ_1, ξ_2 are the damping ratios of meshing pairs for the sun to inside planet, and the inside planet to outside planet. M_c, M_{qi}, M_{pi}, M_s are the equivalent masses of the sun, planets, and carrier. Their expressions will be written in the following part of the paper. $e_{sqi}(t), e_{piqi}(t)$ are the gear backlashes, and can be represented by[20]

$$\begin{cases} e_{sqi}(t) = E_{sqi} \sin(\omega t + \phi_{sqi}) \\ e_{piqi}(t) = E_{piqi} \sin(\omega t + \phi_{piqi}) \end{cases}; \quad (7)$$

where E_{spi}, E_{piqi} are the synthetical meshing errors, and ϕ_{spi}, ϕ_{piqi} are the phase angles.

In order to eliminate the displacement of the rigid body, the generalized coordinates are introduced as

$$\begin{cases} X_{sqi} = x_c - x_{qi} - e_{sqi}(t) \\ X_{piqi} = x_{qi} - x_{pi} - e_{piqi}(t) \end{cases}. \quad (8)$$

Eq. (8) can also be expressed as

$$\begin{cases} X_{sqi} = \theta_c r_{c1} - \theta_{qi} r_{bqi} - e_{sqi}(t) \\ X_{piqi} = \theta_{qi} r_{bqi} - \theta_{pi} r_{bpi} - e_{piqi}(t) \end{cases}. \quad (9)$$

Substituting Eqs. (2), (3), and (9) into Eq. (1), we obtain the following:

$$\begin{cases} \ddot{X}_{sqi} = \frac{r_{c1}}{M_c {r_{bc}}^2}\Bigg(T_D - T_{L2} \\ \quad - \left(\sum_{i=1}^{N} K_{sqi}(t) f(X_{sqi}, b_{sqi}) \right. \\ \quad \left. + \sum_{i=1}^{N} C_{sqi}\dot{X}_{sqi}\right) r_{bs}\cos\alpha\Bigg) \\ \quad - \frac{1}{M_{qi}}\Big(C_{sqi}\dot{X}_{sqi} + K_{sqi}(t) \\ \quad \cdot f(X_{sqi}, b_{sqi}) - C_{piqi}\dot{X}_{piqi} \\ \quad -K_{piqi}(t) f(X_{piqi}, b_{piqi})\Big) - \ddot{e}_{sqi}(t) \\ \ddot{X}_{piqi} = \frac{1}{M_{qi}}\Big(C_{sqi}\dot{X}_{sqi} + K_{sqi}(t) f(X_{sqi}, b_{sqi}) \\ \quad -C_{piqi}\dot{X}_{piqi} - K_{piqi}(t) f(X_{piqi}, b_{piqi})\Big) \\ \quad - \frac{1}{M_{pi} r_{bpi}}\Bigg(\Big(K_{piqi}(t) f(X_{piqi}, b_{piqi}) \\ \quad +C_{piqi}\dot{X}_{piqi}\Big) r_{bpi} - T_{L1}\Bigg) \\ \quad - \ddot{e}_{piqi}(t) \end{cases}; \quad (10)$$

where M_c, M_{qi}, M_{pi}, M_s can be expressed as

$$\begin{aligned} &M_c = (J_c + \sum_{i=1}^{N} (m_{pi} r_{c2} + m_{qi} r_{c1})) / r_{bc}^2; \\ &M_{qi} = J_{qi}/r_{bqi}^2; \\ &M_{pi} = J_{pi}/r_{bpi}^2; \qquad M_s = J_s/r_{bs}^2. \end{aligned} \quad (11)$$

In order to simplify the solutions of the equations and the analysis of the results, we use dimensionless variables, introducing the parameters

$$\begin{aligned} &\omega_n = \sqrt{K_{msqi}(1/M_s + 1/M_c)}; \quad \bar{X} = X/b_c; \\ &\dot{\bar{X}} = \dot{X}\Big/\omega_n b_c; \quad \ddot{\bar{X}} = \ddot{X}\Big/{\omega_n}^2 b_c; \\ &\bar{b} = b/b_c; \qquad \ddot{\bar{e}} = \ddot{e}/{\omega_n}^2 b_c; \\ &\Omega = \omega/\omega_n; \qquad \tau = \omega_n t; \end{aligned} \quad (12)$$

where τ is dimensionless time and b_c is the nominal size of displacement.

Substituting Eq. (12) into Eq. (11), we obtain the following:

$$\begin{cases} \ddot{\bar{X}}_{sqi} = \frac{r_{c1}}{M_c r_{bc}{}^2 \omega_n{}^2 b_c}(T_D - T_{L2}) \\ \quad - \frac{r_{c1} r_{bs} \cos\alpha}{M_c r_{bc}{}^2 \omega_n{}^2} \sum\limits_{i=1}^{N} K_{sqi}(\tau) f(\bar{X}_{sqi}, \bar{b}_{sqi}) \\ \quad - \frac{r_{c1} r_{bs} \cos\alpha}{M_c r_{bc}{}^2 \omega_n} \sum\limits_{i=1}^{N} C_{sqi} \dot{\bar{X}}_{sqi} \\ \quad - \frac{1}{M_{qi}\omega_n} C_{sqi} \dot{\bar{X}}_{sqi} \\ \quad - \frac{1}{M_{qi}\omega_n{}^2} K_{sqi}(\tau) f(\bar{X}_{sqi}, \bar{b}_{sqi}) \\ \quad + \frac{1}{M_{qi}\omega_n} C_{piqi} \dot{\bar{X}}_{piqi} + \frac{1}{M_{qi}\omega_n{}^2} \\ \quad \cdot K_{piqi}(\tau) f(\bar{X}_{piqi}, \bar{b}_{piqi}) - \ddot{\bar{e}}_{sqi}(\tau) \\ \ddot{\bar{X}}_{piqi} = \frac{1}{M_{qi}\omega_n} C_{sqi} \dot{\bar{X}}_{sqi} + \frac{1}{M_{qi}\omega_n{}^2} K_{sqi}(\tau) \\ \quad \cdot f(\bar{X}_{sqi}, \bar{b}_{sqi}) - \frac{1}{M_{qi}\omega_n} C_{piqi} \dot{\bar{X}}_{piqi} \\ \quad - \frac{1}{M_{qi}\omega_n{}^2} K_{piqi}(\tau) f(\bar{X}_{piqi}, \bar{b}_{piqi}) \\ \quad - \frac{1}{M_{pi}\omega_n{}^2} K_{piqi}(\tau) f(\bar{X}_{piqi}, \bar{b}_{piqi}) \\ \quad - \frac{1}{M_{pi}\omega_n} C_{piqi} \dot{\bar{X}}_{piqi} + \frac{T_{L1}}{M_{pi} r_{bpi} \omega_n{}^2 b_c} \\ \quad - \ddot{\bar{e}}_{piqi}(\tau) \end{cases} ; \quad (13)$$

where $K_{sqi}(\tau), K_{piqi}(\tau), \bar{e}_{sqi}(\tau), \bar{e}_{piqi}(\tau)$ can be represented by

$$\begin{cases} K_{sqi}(\tau) = K_{msqi} + K_{asqi}\sin(\Omega\tau + \varphi_{sqi}) \\ K_{piqi}(\tau) = K_{mpiqi} + K_{apiqi}\sin(\Omega\tau + \varphi_{piqi}) \end{cases} ; \quad (14)$$

$$\begin{cases} \bar{e}_{sqi}(\tau) = \frac{E_{sqi}}{b_c}\sin(\Omega\tau + \phi_{sqi}) \\ \bar{e}_{piqi}(\tau) = \frac{E_{piqi}}{b_c}\sin(\Omega\tau + \phi_{piqi}) \end{cases} . \quad (15)$$

3. THE STEADY-STATE RESPONSE OF THE SYSTEM

In order to investigate the vibration characteristics of the planetary gear processing device, this paper uses a set of basic parameters: $m = 3.0$ mm, $\alpha = 20°$, $E_{sqi} = E_{piqi} = 10$ μm, $\varphi_{sqi} = \varphi_{piqi} = 0$, $\phi_{sqi} = \phi_{piqi} = 0$, $z_s = 40$, $z_{qi} = 30$, $z_{pi} = 40$, $N = 3$, $b_c = 10$ μm, $B = 15$ mm, $b_{sqi} = b_{piqi} = 50$ μm, $K_{msqi} = 0.8256$ GN/m, $K_{mpiqi} = 1.06$ GN/m, $K_{asqi} = K_{apiqi} = 0.2$ GN/m, $T_D = 1100$ Nm, $T_{L1} = 100$ Nm, and $T_{L2} = 1000$ Nm.

This paper uses a numerical integration algorithm to solve the nonlinear Eq. (13) with the four order Runge-Kutta method, and investigates the steady-state responses of the planetary gear system. The bifurcation diagram of the system with the non-dimensional speed is shown in Fig. 4.

Figure 4 shows that the system is stable excepting the critical speed $\Omega = 0.75$ to 2.3, and the region is also called the chaotic region. Simultaneously, when the non-dimensional speed is at $\Omega = 0.75$ to 2.3, the non-dimensional displacement $\bar{X}_s pi$ has a magnitude of nearly 2 to 4.

Figure 5 shows that the bifurcation diagram of the vibration system changes with the dimensionless speed Ω when the damping ratios are at $\xi_1 = \xi_2 = 0.1$. The bifurcation diagram is different from the diagram in Fig. 4. The amplitude range of the non-dimensional displacement shows a sharp decline compared to the system in Fig. 5. In addition, the vibration system only passes through a short chaotic region with the speed Ω form 1 to 2, and the displacement amplitudes in Fig. 4 change

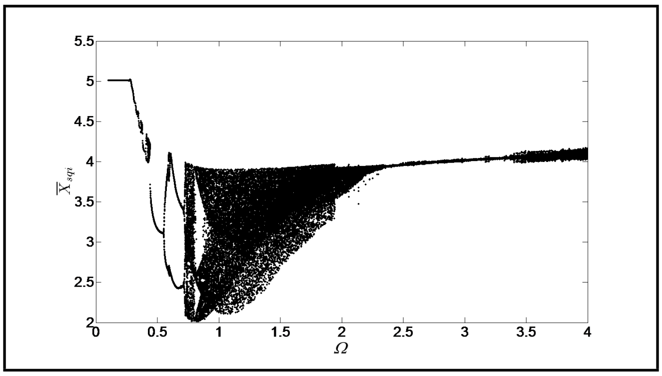

Figure 4. Bifurcation diagram of the system with non-dimensional planetary speed Ω ($\xi_1 = \xi_2 = 0.05$).

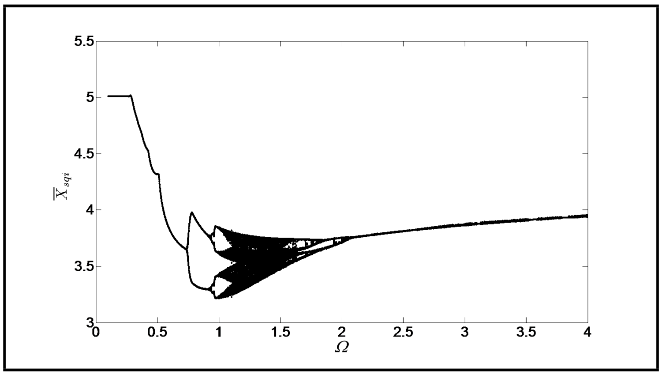

Figure 5. Bifurcation diagram of the system with non-dimensional planetary speed Ω ($\xi_1 = \xi_2 = 0.1$).

more than those in Fig. 5. Simultaneously, the vibration state is in the stage of aperiodic motion. So, this paper pays more attention to the vibration with $\xi_1 = \xi_2 = 0.05$.

Figure 6 shows that the vibration of the system is a harmonic response by the excitation for $\Omega = 0.2$. The time histories are sinusoidal waves, and the phase plot shows an ellipse. Whats more, the Poincar map is a single scatter, and the Fourier spectra shows that the frequency occurs at Ω. The results indicates that the system is stable.

Figure 7 shows that the vibration of the system is a non-harmonic response by the excitation for $\Omega = 0.4$. The time histories are nearly single periodic motions, which consist of different sinusoidal waves, but the phase plot does not show an ellipse. The Poincar map has many scatters that are close to each other. The Fourier spectra shows that the frequency occurs at $k\Omega$ (k is a positive integer). The results indicate that the system response is a super-harmonic response.

Figure 8 indicates that the vibration of the system is a 2T-periodic harmonic response by the excitation for $\Omega = 0.56$. The time histories are nearly two periodic motions, which consist of sinusoidal waves, and the phase plot shows two ellipses. The Poincar map has two scatters that are not close to each other. The Fourier spectra shows that the frequency occurs at . The results indicate that the system response is stable.

Figure 9 shows that the system creates a 4T-periodic harmonic response by the excitation for $\Omega = 0.72$. The time histories are nearly four periodic motions which consist of sinusoidal waves, and the phase plot shows four quasi ellipses. The Poincar map has four scatters that are not close to each other. The Fourier spectra shows that the frequency occurs at Ω. The

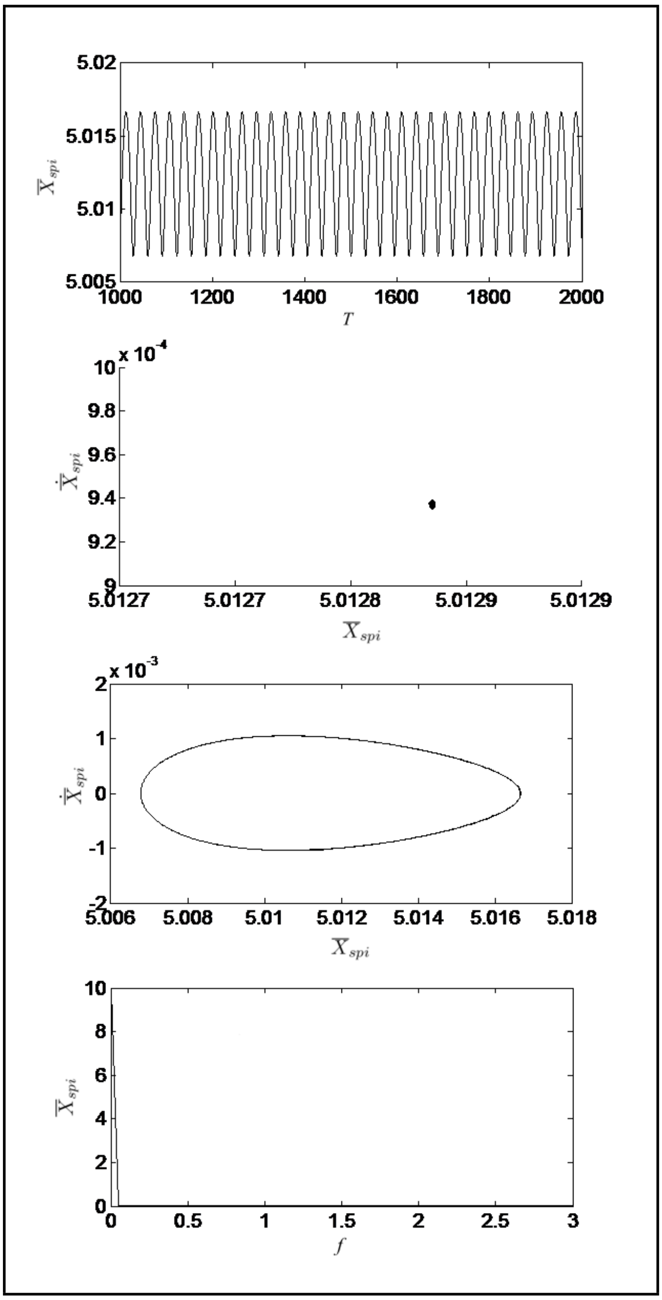

Figure 6. Harmonic response ($\Omega = 0.2$). (a) Time histories; (b) Poincaré map; (c) Phase plant plot; (d) Fourier spectrum.

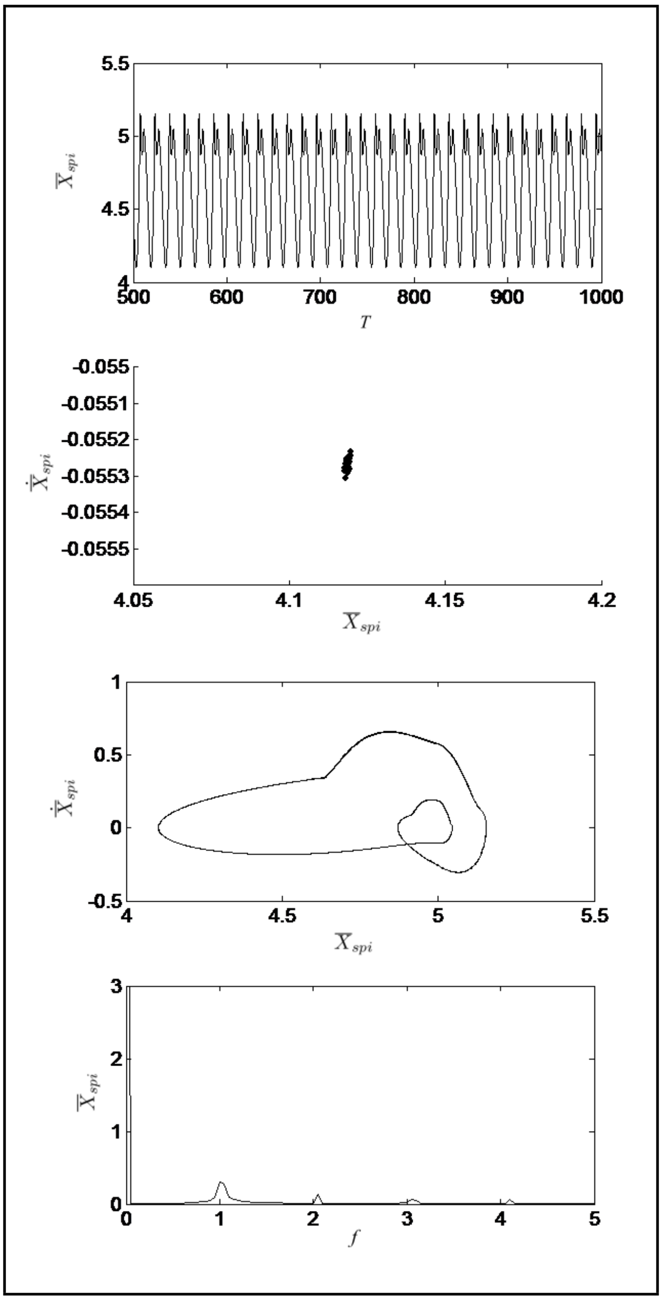

Figure 7. Non-harmonic response ($\Omega = 0.4$). (a) Time histories; (b) Poincaré map; (c) Phase plant plot; (d) Fourier spectrum.

results indicate that the system response is still stable.

Figure 10 shows that the vibration of the system is a quasi-periodic response by the excitation for $\Omega = 0.74$. The time histories are quasi-periodic motions which consist of different kinds of sinusoidal waves, and the phase plot consists of many analogical ellipses. The Poincar map has many scatters, which form the instability attractor. The results indicate that the system response is in a critical state, and the results reveal that the device is easy to work in the next state.

Figure 11 shows that the system creates the chaotic responce by the excitation for $\Omega = 1.5$. The time histories are not periodic motions which consist of different kinds of waves, and the phase plot consists of many different ellipses or spiral lines. The Poincar map has many scatters, which form the instability attractor and irregular shape. The results indicate that the system response is not stable, and the device is easily damaged. That is to say, the planetary gear processing device will be damaged in the form of fatigue.

Figure 12 shows that the vibration of the system returns to the harmonic response by the excitation for $\Omega = 3$. The time histories are still periodic motions which consist of sinusoidal waves, and the phase plot consists of only one ellipse. The Poincar map has many scatters, which are close to each other. The results illstrate that the system response is stable, and the planetary gear processing device will vibrate in the form of harmonic motion.

4. CONCLUSIONS

This paper analyszed the planetary gear processing device and established the nonlinear dynamic model. This vibration model considered errors of transmission, time varying meshing stiffness, and gear backlashes. Then, the solution of the dimen-

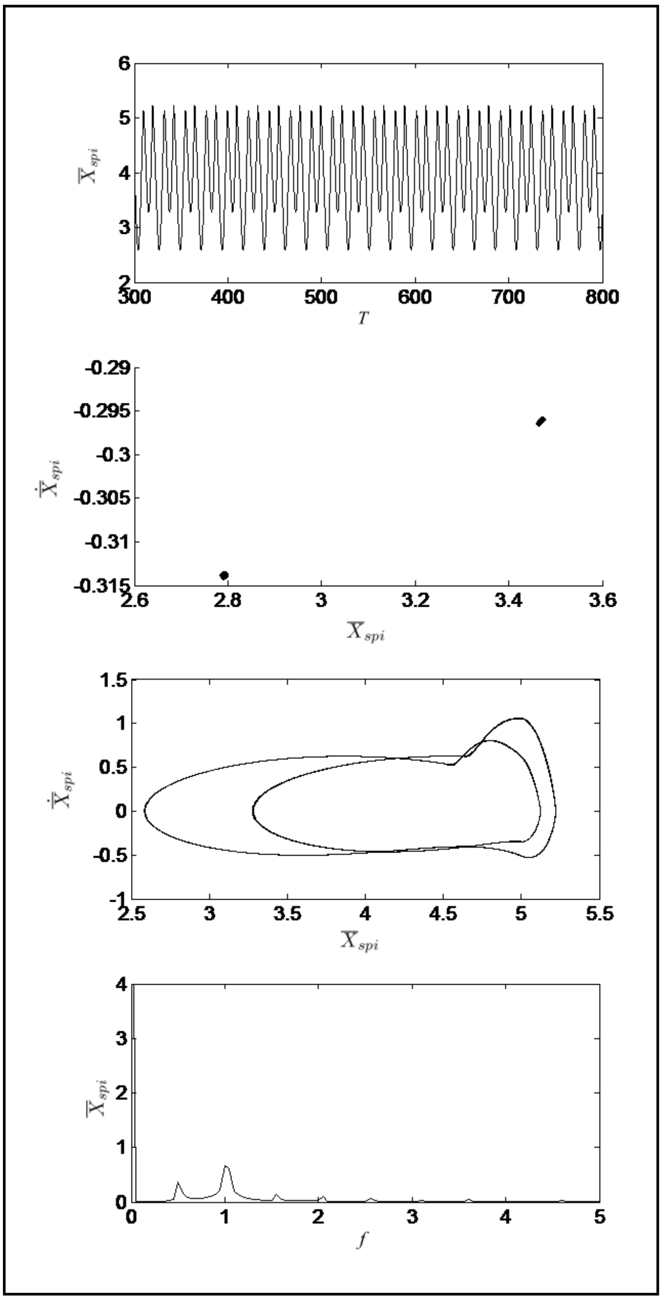

Figure 8. The 2T-periodic harmonic response ($\Omega = 0.56$). (a) Time histories; (b) Poincaré map; (c) Phase plant plot; (d) Fourier spectrum.

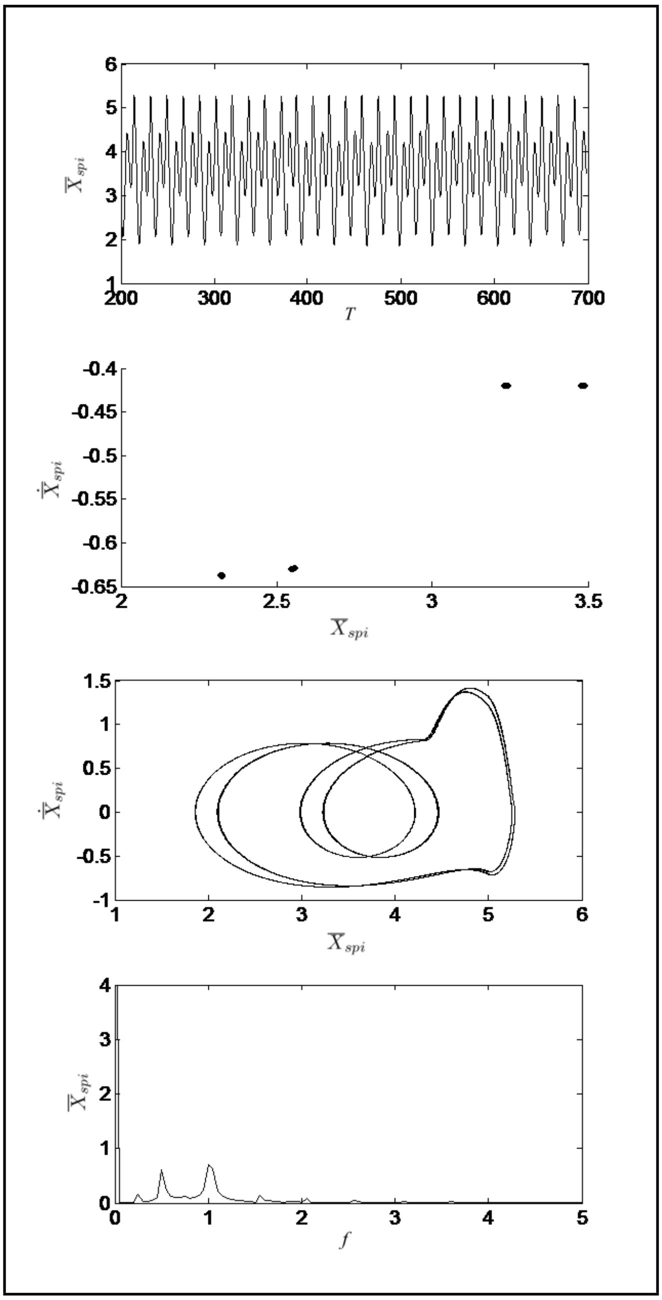

Figure 9. The 4T-periodic harmonic response ($\Omega = 0.72$). (a) Time histories; (b) Poincaré map; (c) Phase plant plot; (d) Fourier spectrum.

sionless equations of the system was carried out by using the method of numerical integration. By comparison to Poincar maps and bifurcation diagrams, the vibration properties of the planetary gear system were investigated, and the following results were found:

1. The planetary gear train system with translational motion has abundant bifurcation characteristics because of the complex inflluences of many nonlinear factors. The results reveal that the motion state of the system will change into chaos in the way of crisis as the dimensionless speed increases.

2. The system will be in the chaotic state when the dimensionless speed is increased to a certain value range. Therefore, the system should avoid these critical regions for reducing fatigue-failure of the processing device.

3. The time histories, phase plane plots, Poincar maps, and Fourier spectras prove the planetary gear train system has a harmonic response, a 2T-period harmonic response, a 4T-period harmonic response, a quasi-harmonic response, and a chaotic response, but the chaotic state is not stable and should be avoided.

4. The damping ratio can influence the vibration amplitudes greatly, and it should be increased when the processing device is designed. Also, the damping ratio can easily influence the bifurcation characteristics.

ACKNOWLEDGMENTS

This paper was supported by National Natural Science Foundation of China (Grant No.51375320). The authors would like to acknowledge their financial support.

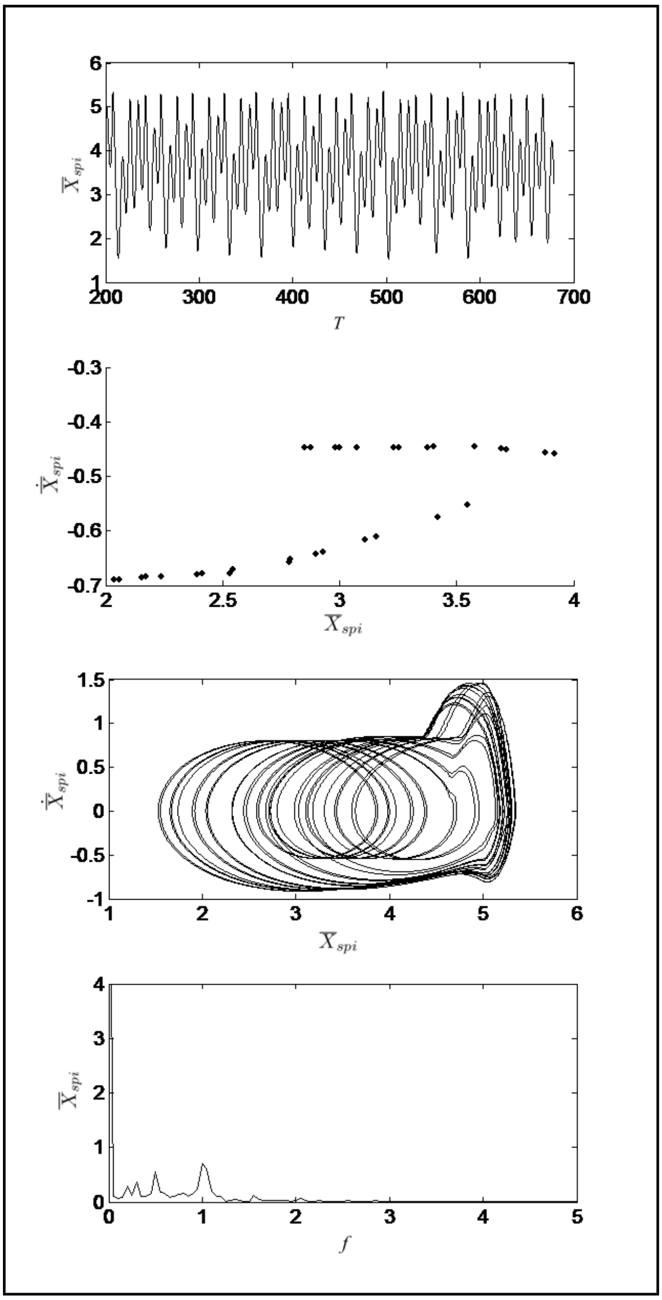

Figure 10. The quasi periodic response ($\Omega = 0.74$). (a) Time histories; (b) Poincaré map; (c) Phase plant plot; (d) Fourier spectrum.

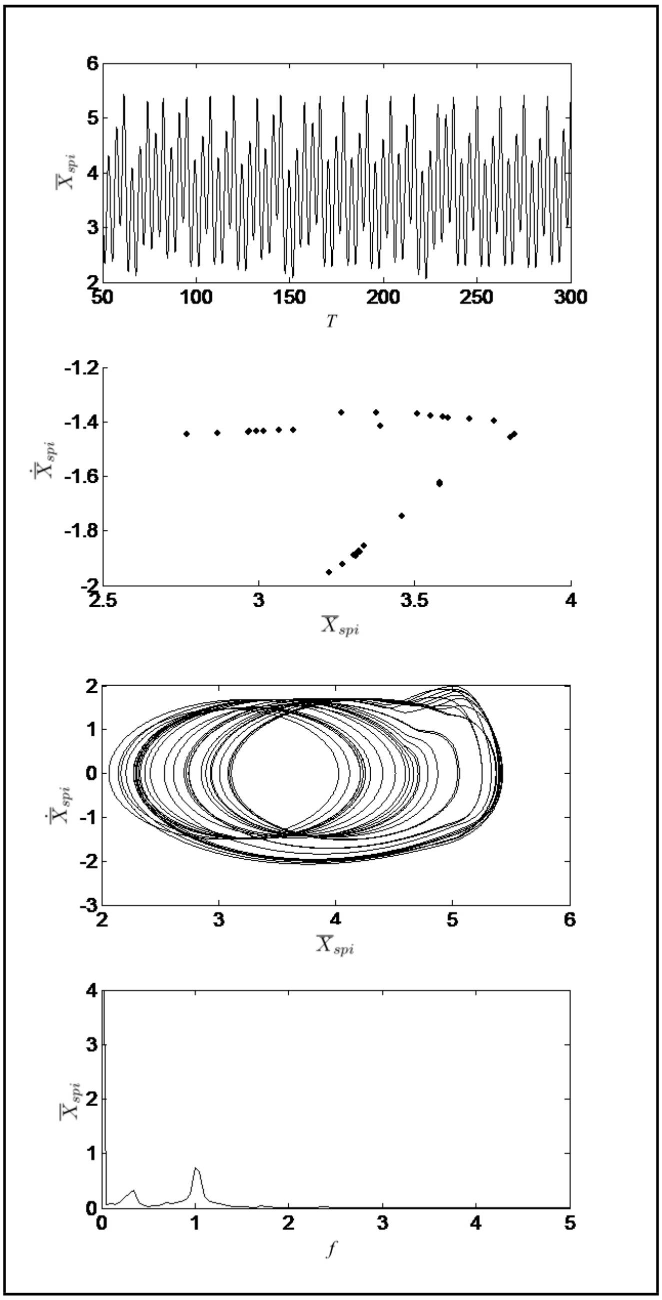

Figure 11. The chaotic resonance ($\Omega = 1.5$). (a) Time histories; (b) Poincaré map; (c) Phase plant plot; (d) Fourier spectrum.

REFERENCES

1 Chen, Z. and Shao, Y. Dynamic simulation of planetary gear with tooth root crack in ring gear, *Eng. Fail. Anal.*, **31**, 818, (2013). http://dx.doi.org/10.1016/j.engfailanal.2013.01.012

2 Song, A., Wu, W., Gao, S., and Gao, W. The ideal geometry parameters of arch cylindrical gear and its process method, *J. Shanghai Jiaotong U.*, **44** (12), 17351740, (2010).

3 Velex, P. and Flamand, L. Dynamic response of planetary trains to mesh parametric excitations, *J. Mech. Des.*, **118**, 714, (1996). http://dx.doi.org/10.1115/1.2826860

4 Kahraman, A. and Blankenship, G. W. Experiments on nonlinear dynamic behavior of an oscillator with clearance and periodically time-varying parameters, *J. Appl. Mech.*, **64**, 217226, (1997). http://dx.doi.org/10.1115/1.2787276

5 Lin, J. and Parker, R. G. Planetary gear parametric instability caused by mesh stiffness variation, *J. Sound Vib.*, **249** (1), 129145, (2002). http://dx.doi.org/10.1006/jsvi.2001.3848

6 Kahraman, A. Natural modes of planetary gear trains, *J. Sound Vib.*, **173** (1), 125130, (1994). http://dx.doi.org/10.1006/jsvi.1994.1222

7 Parker, R. G. and Wu, X. Vibration modes of planetary gears with unequally spaced planets and an elastic ring gear, *J. Sound Vib.*, **329**, 22652275, (2010). http://dx.doi.org/10.1016/j.jsv.2009.12.023

8 Ericson, T. M. and Parker, R. G. Experimen-

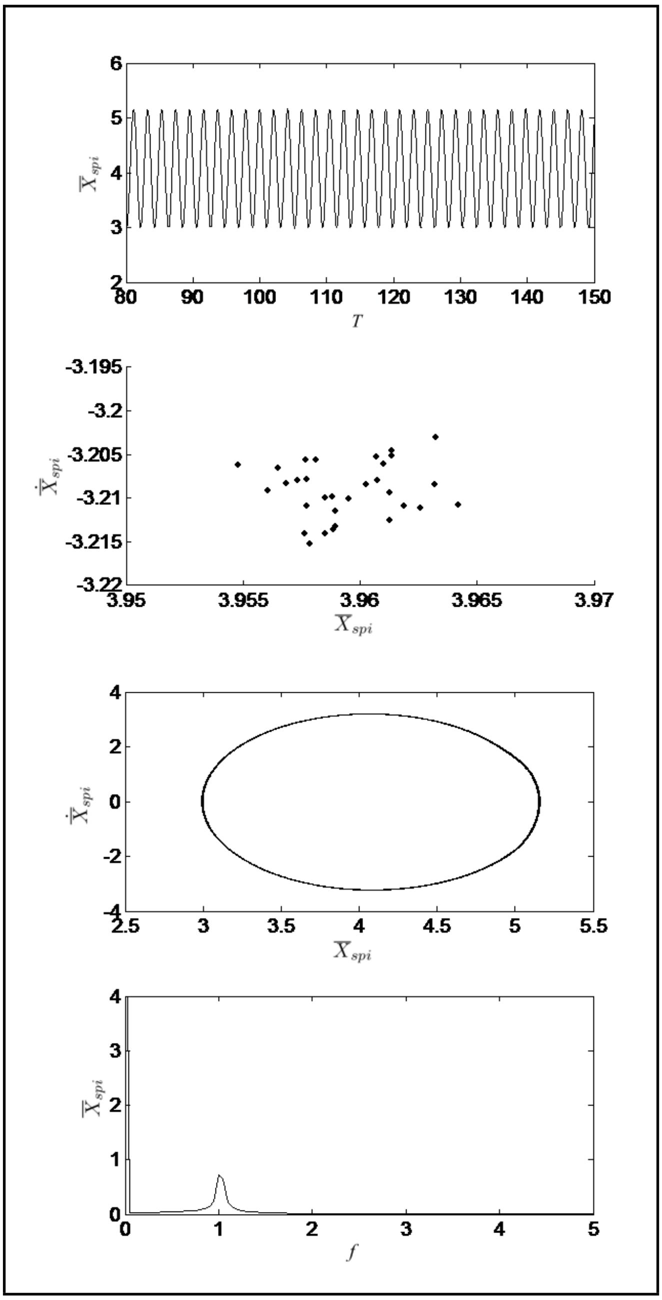

Figure 12. The harmonic response ($\Omega = 3$). (a) Time histories; (b) Poincaré map; (c) Phase plant plot; (d) Fourier spectrum.

tal measurement of the effects of torque on the dynamic behavior and system parameters of planetary gears, *Mech. Mach. Theory*, **74**, 370389, (2014). http://dx.doi.org/10.1016/j.mechmachtheory.2013.12.018

[9] Ericson, T. M. and Parker, R. G. Planetary gear modal vibration experiments and correlation against lumped-parameter and finite element models, *J. Sound Vib.*, **332**, 23502375, (2013). http://dx.doi.org/10.1016/j.jsv.2012.11.004

[10] Chaari, F., Fakhfakh, T., Hbaieb, R., Louati, J., and Haddar, M. Influence of manufacturing errors on the dynamical behavior of planetary gear, *Int. J. Adv. Manuf. Tech.*, **27**, 738746, (2006). http://dx.doi.org/10.1007/s00170-004-2240-2

[11] Lin, J. and Parker, R. G. Structured vibration characteristics of planetary gears with unequally spaced planets, *J. Sound Vib.*, **233** (5), 921928, (2000). http://dx.doi.org/10.1006/jsvi.1999.2581

[12] Chen, Z. G., Shao, Y. M., and Lim, T. C. Non-linear dynamic simulation of gear response under the idling condition, *Int. J. Automot. Techn.*, **13** (4), 541552, (2012). http://dx.doi.org/10.1007/s12239-012-0052-1

[13] Xihui, L., Zuo, M. J., and Pandey, M. Analytically evaluating the influence of crack on the mesh stiffness of a planetary gear set, *Mech. Mach. Theory*, **76**, 2038, (2014). http://dx.doi.org/10.1016/j.mechmachtheory.2014.02.001

[14] Li, S., Wu, Q., and Zhang, Z. Bifurcation and chaos analysis of multistage planetary gear train, *Nonlinear Dynam.*, **75** (12), 217233, (2014). http://dx.doi.org/10.1007/s11071-013-1060-z

[15] Kahraman, A. Free torsional vibration characteristics of compound planetary gear sets, *Mech. Mach. Theory*, **36**, 953971, (2001). http://dx.doi.org/10.1016/s0094-114x(01)00033-7

[16] Parker, R. G. A physical explanation for the effectiveness of planet phasing to suppress planetary gear vibration, *J. Sound Vib.*, **236** (4), 561573, (2000). http://dx.doi.org/10.1006/jsvi.1999.2859

[17] Lin, J. and Parker, R. G. Sensitivity of planetary gear natural frequencies and vibration modes to model parameters, *J. Sound Vib.*, **228** (1), 109128, (1999). http://dx.doi.org/10.1006/jsvi.1999.2398

[18] Lin, J. and Parker, R. G. Analytical characterization of the unique properties of planetary gear free vibration, *J. Vib. Acoust.*, **121** (3), 316321, (1999). http://dx.doi.org/10.1115/1.2893982

[19] Ambarisha, V. K. and Parker, R. G. Nonlinear dynamics of planetary gears using analytical and finite element models, *J. Sound Vib.*, **302**, 577595, (2007). http://dx.doi.org/10.1016/j.jsv.2006.11.028

[20] Zhimin, S., Linhong, J., and Yunwen, S. Nonlinear dynamics of 2K-H planetary gear train, *J. Tsinghua U. (Science & Technology)*, **43** (5), 636639, (2003).

[21] Li, T. Nonlinear torsional vibration modeling and bifurcation characteristic study of a planetary gear train, *J. Mech. Eng.*, **47** (21), 7683, (2011). http://dx.doi.org/10.3901/jme.2011.21.076

[22] Runfang, L. and Jiangjun, W. *Dynamics of gear system: Vibration, shock and noise*, Science Press, Beijing, (1997).

Seat-to-Head Transmissibility and Reading Discomfort of the Seated Subjects Exposed to Whole Body Vibration

Vikas Kumar

Mechanical and Automation Engineering Department, Amity University Uttar Pradesh, India

V. H. Saran

Mechanical and Industrial Engineering Department, Indian Institute of Technology Roorkee, Uttarakhand India

(Received 19 January 2014; accepted 18 September 2014)

The transmission of vibration from the vibrating interface to various organs of the human body may influence their functioning during the vibration exposure. Therefore, an experimental study on a vibration simulator has been performed to find the effects of vibration on reading performance, and also to establish the relationship between seat-to-head transmissibility (STHT) with reading difficulty and reduction in reading performance. Twelve seated male subjects were exposed to sinusoidal vibration with three magnitudes (0.5, 1.0 & 1.5 m/s2 rms) at seven different frequencies (4, 5, 6.3, 10, 16, 20, and 25 Hz) in three independent directions (vertical, fore-and-aft, and lateral). The results show that three output measures - STHT, reduction in reading performance, and perceived difficulty in reading - are significantly affected by the frequency of vibration in each direction. All three measures have shown the peak at 4 or 5 Hz in three independent directions of vibration. Another peak at 25 Hz has also been observed for reduction in performance and perceived reading difficulty in vertical direction vibration. The results also show decrease in resonance frequency of the transmissibility with an increase in vibration magnitude, which represents nonlinear behaviour in biodynamic response by the human body.

1. INTRODUCTION

There are diverse effects of whole body vibration (WBV) exposure on the human body, such as discomfort, performance difficulty in various sedentary activities, and health effects. The biodynamic response of the human body to WBV may be used for the quantification of the diverse effects of vibration exposure.[10] Biodynamic responses are measured in terms of two functions: the 'to the body' function, and the 'through the body' function. The 'through the body' function describes the transmission of vibration from the input point to the various segments of the human body during the WBV exposure. The STHT measurement has been found to be appropriate for describing seated body responses to higher frequency vibration.[27]

The STHT measurement may be considered for the quantification of the activity discomfort in the WBV environment. The transmissibility is measured as the ratio of output acceleration to the input acceleration.[10]

$$\text{STHT}T_{STH}(f) = \frac{a_{head}(f)}{a_{seat}(f)}; \tag{1}$$

where $a_{head}(f)$ is acceleration at the head, and $a_{seat}(f)$ acceleration at the seat.

A large number of experimental studies[6,7,11,17,18,21,22,25] have focused on the transmissibility of vibration to various parts of the human body, such as seat-to-head, pelvis, lumber/cervical, etc., with a broad range of experimental conditions. Griffin and Whitham have observed the significant effect of individual variability on transmissibility of WBV through the seated subjects.[6] Many previous studies[17,19,27] have shown the relationship between STHT and Apparent Mass (APMS) of the seated subjects exposed to WBV with various experimental conditions, *e.g.* vibration magnitude, frequency range, vibration type, subject's anthropometric data, etc. The measured data in these studies have revealed nonlinearities in both APMS and STHT responses, and also shows stronger effects of hand position, backrest conditions, etc. In the field studies of Bhiwapurkar, *et al.*[1] and studies of Indian and Swedish trains by Khan and Sundström,[12] reading activity has been found to be the most preferable of all sedentary activities- *i.e.* writing, sketching, eating, etc.- to the passengers while travelling. Also, most passengers reported reading discomfort due to the train vibrations in response to a questionnaire used in these studies. Bhiwapurkar, *et al.*,[3,4] conducted the laboratory experiment on reading of a word chain in English, a Hindi newspaper, and an English e-paper under vibration exposure by measuring subjective and objective responses. The results revealed a strong influence of the WBV on the performance reduction in reading performance and increase in perceived difficulty. Experiments on reading and writing activity[3,4,8,12] show the strong influence of vibration amplitude and vibration frequency on the performance of these activities. The studies also show that a moderate level of discomfort has been found at low magnitudes of WBV. These results depend upon various conditions, such as sitting posture, direction of vibration, type of task to be performed, etc. Wollstrom observed a decrease in the reading performance in fore-and-aft (x-axis) vibrations between 5.6 and 11 Hz frequencies; however, the effect was only present when a seat with a backrest was used.[29] So backrests may be a critical part for vibration transmitted to the head, and may be the cause of the problem.

Most of the human body sensors, *e.g.* the eyes, tongue, etc., are located in the head and play a crucial role in the reading tasks performed by the seated subjects. The functioning of these organs of human body during the task performance is also affected by the WBV exposure.[10] In the present experimental study, an attempt has been made to establish the relationship between STHT and perceived difficulty and decrement in reading performance for the seated subjects in the vibration environment. It was hypothesized that the transmission of vibration to the head would affect reading difficulty, and this would also be reflected in the reading performance.

2. METHODOLOGY

2.1. Experimental Setup

This experimental study has been conducted on the vibration simulator available in the vehicle dynamics laboratory, MIED, IIT Roorkee, India. This vibration simulator was developed as a mock-up of a train compartment, and was used in many previous studies.[1–4,7,13] The vibration simulator consists of a platform of the size 2 × 2 m, made of stainless steel sheets, and can be excited with the help of three electrodynamic vibration shakers in three directions: vertical (z-axis), lateral (y-axis) and fore-and-aft (x-axis). The sinusoidal vibration can be generated by each vibration shaker having a capacity of 1000 N force and maximum stroke length (peak-peak) of 25 mm. These shakers are computerized and controlled with the help of three amplifiers and three controllers. An accelerometer is attached to the shaker to provide continuous motion feedback to each individual controller via a signal conditioning unit. A table and two rigid chairs have been fixed rigidly on the platform of the vibration simulator (shown in Fig. 1). The height of the seat surface from the floor is 45 cm. None of the accessories attached to the platform had shown any resonance within the frequency range under study, in any of three directions. The platform vibrations were measured for the monitoring of the vibration signals by using a tri-axial accelerometer (PCB PEZIOTRONICS-356A32), and the signals were conveyed to the LabVIEW software via a data acquisition device (NI cDAQ-9174). The air conditioned environment at 26 °C temperature was maintained in the simulator lab with working illumination well above 250 Lux. The illumination from all the direct and indirect light sources was well distributed. The two test subjects were seated on the chairs at a specific time and were excited with the same frequency as the platform. The frequency of the vibrations produced on-board railway vehicles ranges from 1 to 25 Hz, which is also a critical range for human beings.[10,20]

2.2. Subjects and Methods

A total of twelve healthy male subjects were involved in the present experimental study. The details of the anthropometric

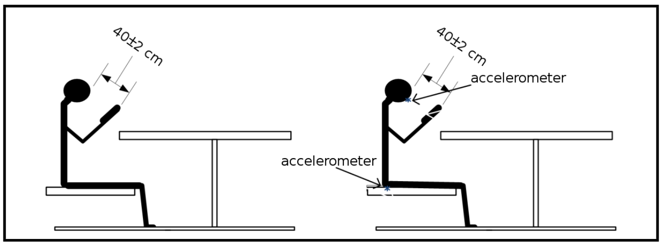

Figure 2. Erect upright posture maintained during the (a) reading task, and (b) measurement of STHT.

data of the subjects are given in the Table 1. All the participants were students (either undergraduates, graduates, or research scholars) of the institute, had normal eyesight (normal visual acuity 6/6 vision), and were fluent in reading the English language. All the subjects participated voluntarily, and before participation, all the subjects were required to sign the written consent letter. Approval for conducting the experiment on the subjects was obtained from the Institute Human Ethical Committee of IIT Roorkee. A screening questionnaire was filled by the participating subjects related to their personal backgrounds, levels of education, fitness, and musculoskeletal disorders.[14] All the subjects were free from any musculoskeletal disorders and were found to be suitable for the experimental task.

The sinusoidal vibration in each independent axis was generated at frequencies 4, 5, 6.3, 10, 16, 20, and 25 Hz with the help of computerized controllers at three levels of vibration magnitude: 0.5, 1 and 1.5 m/s^2 rms (un-weighted). A total of 63 vibration conditions (7 vibration frequencies, 3 vibration magnitudes in 3 mono axes) were given to the vibrating platform, and three responses to STHT - perceived difficulty in reading and reading performance - were measured. For one vibration condition, a one-minute break was provided to the subject to reduce fatigue. The whole experiment was completed in two different sessions of 2 hours each.

Both the subjects maintained an erect upright posture throughout the experiment for the reading task, and had the reading material in their hands, as shown in Fig. 2. The normal viewing distance of 40±2 cm between the subjects' eyes and the reading material was maintained by each subject throughout the experimentation.[15,16]

The experimental task performed by the subjects involved reading a printed paragraph in English on A4 size paper at a normal speed. The paragraphs of 300 words were selected from leading English newspapers. Most of the leading newspapers use Nimrod MT font type and 7.5- to 10-point font sizes for the news content. For the present study, Nimrod MT font type and 8 font sizes had been selected for the reading task. To avoid learning the effect, different articles were used for the reading task for each vibration exposure. The test subjects were asked to sit in the prescribed posture.

The reading performance was assessed on the basis of the time taken to complete the reading task at various vibration conditions. A digital stopwatch was used to count the time taken for task completion. The perceived difficulty in the reading task was assessed with the help of Borg's CR-10 scale, which consists of nine labelled and eight unlabelled points (depicted in Table 2). The value ranges from a minimum of '0' to

Table 1. Anthropometric data of 12 volunteer male subjects who participated in the study

	Age (Years)	Height (cm)	Seated Height (cm)	Weight (Kg)	Seated weight (Kg)	Arm length (cm)	Lower leg length (cm)
Mean	26.5	172.1	133.5	70.9	53.6	58.9	50.8
Standard deviation	2.4	5.7	1.9	4.0	2.5	1.7	1.1

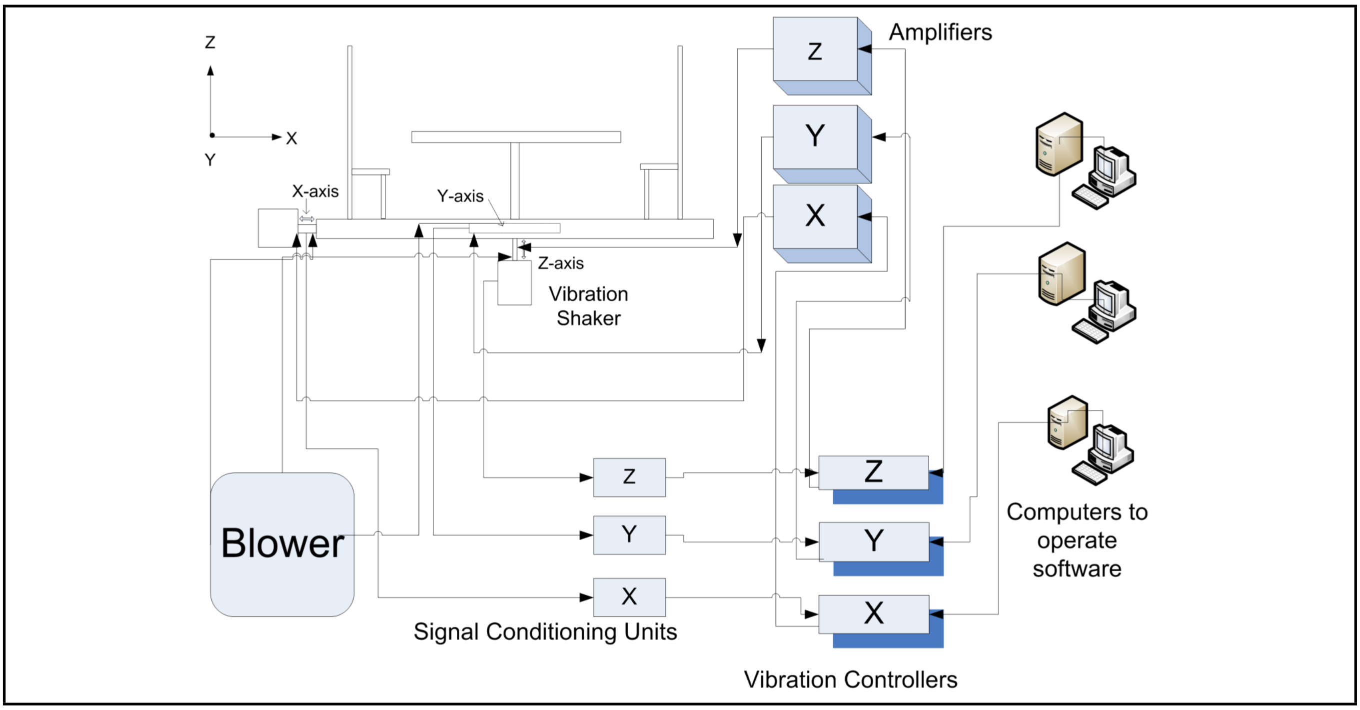

Figure 1. Schematic diagram of computerized controlled vibration simulator.

Table 2. Borg's CR-10 scale.

0	Nothing at all
0.3	
0.5	Extremely weak
0.7	
1	Very weak
1.5	
2	Weak
2.5	
3	Moderate
4	
5	Strong
6	
7	Very strong
8	
9	
10	
•	Absolute maximum

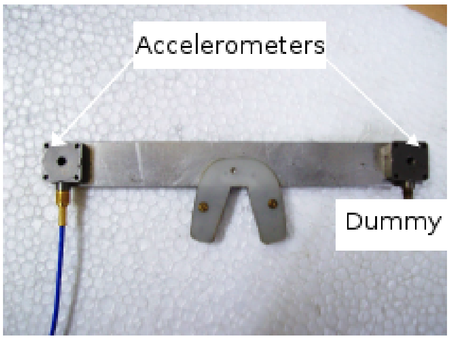

Figure 3. Sterilize bite-bar.

a maximum of '10' for this scale. The point after 10 can also be selected by the subjects depending upon their choice.[5]

For the measurement of acceleration at the seat and Ischial-tuberosite interface, a seat-pad accelerometer was placed on the seat. The acceleration of the head was measured with the help of a bite bar on which an accelerometer was mounted. The bite bar consisted of a light-weight, alloy steel strip, approximately 21 cm long, which was screwed on to a U-shaped bite plate made of Perspex material, as illustrated in Fig. 3. The weight of the accelerometer was balanced by mounting the dummy accelerometer. The sterilized bite bar was gripped by the subjects in their teeth during the measurement of the STHT responses. The signals from the accelerometers were acquired with the help of a nine-channel data acquisition system (**NI cDAQ-9174**) and further processed with the help of LabVIEW software.

The effects of various factors, such as vibration magnitude, frequency, and direction, were analysed by the general linear model (GLM) for repeat measurements. A factorial analysis of variance (ANOVA) was performed using a statistical package for social sciences (SPSS Inc., Chicago, USA, version 16). The results at the level of $p<0.05$ and $p<0.01$ were considered 'Significant' and 'highly significant', respectively. To analyse all the gathered responses, these were manually fed to the statistical software SPSS 16.

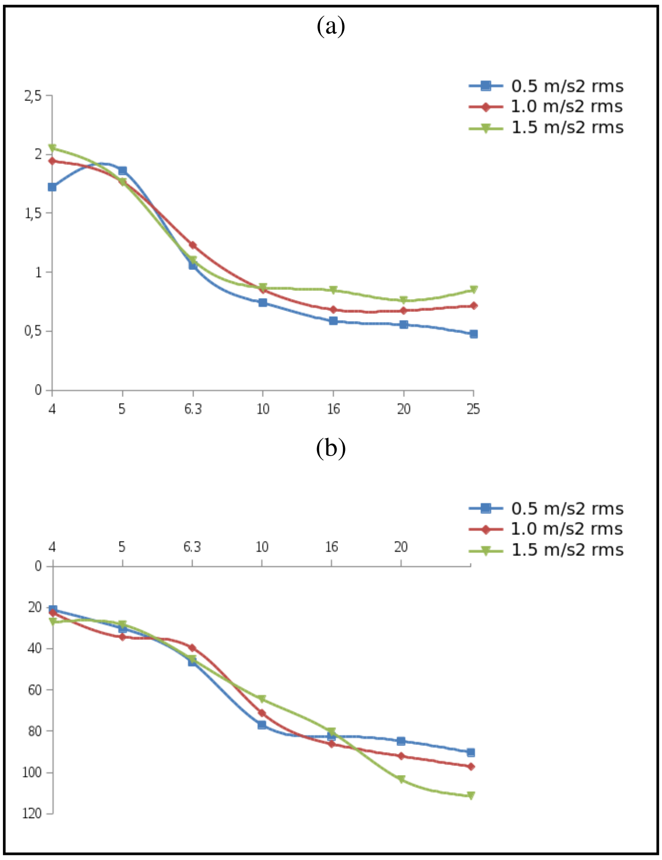

Figure 4. (a) Mean STHT and (b) phase (degree) of 12 subjects measured at 0.5, 1.0, 1.5 m/s^2 rms in vertical direction.

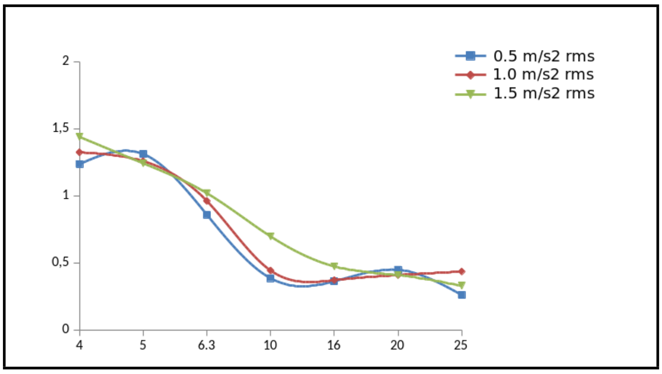

Figure 5. Mean STHT of 12 subjects measure at 0.5, 1.0, 1.5 m/s^2 rms in lateral direction.

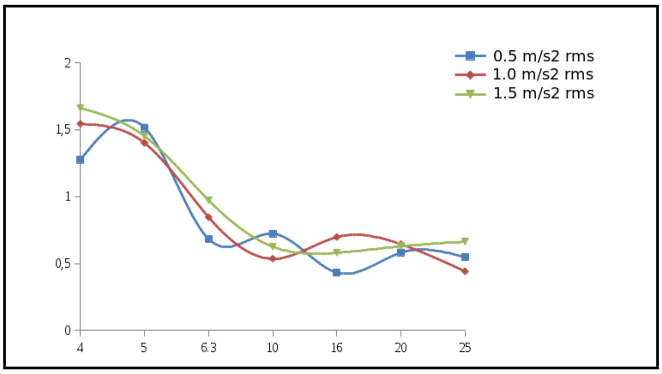

Figure 6. Mean STHT of 12 subjects measure at 0.5, 1.0, 1.5 m/s^2 rms in fore-and-aft direction.

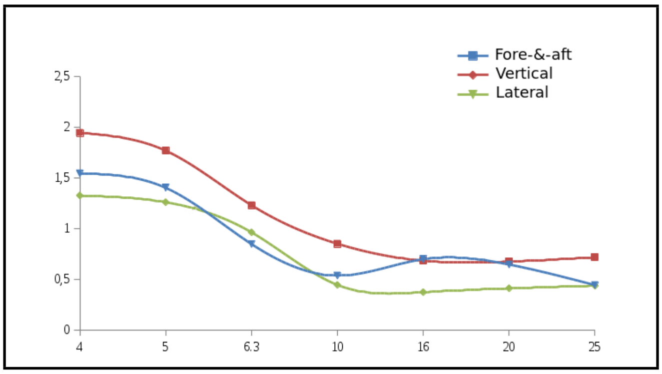

Figure 7. Comparisons of mean STHT responses for 1.0 m/s^2 rms in vertical, fore-and-aft, and lateral vibration.

3. RESULTS

3.1. Effect of Vibration on STHT

The mean STHT and phase responses were shown for all the three vibration magnitudes in vertical, lateral, and fore-and-aft directions, and are depicted in Figs. 4–6. Only the values of the phase for the vertical direction are shown in Fig. 4(b). The peak was observed around 4–5 Hz for the mean STHT responses for vibration in all the three directions, as shown in Figs. 4–6.

The STHT was found to decrease after 5 Hz frequency in the vertical direction of vibration for all vibration magnitudes. Statistically, highly significant differences have been observed between STHT responses at 4–5 Hz and other frequencies of vibration ($p<0.01$). The STHT responses at 4 and 5 Hz frequency are not found to be significantly different ($p>0.05$). The overall effect of the frequency of vibration is highly significant ($p<0.01$), as specified in Table 3.

No significant differences were observed in STHT responses for lateral and fore-and-aft vibrations. At a vibration magnitude of 0.5 m/s^2 rms, the peak in STHT was observed at 5 Hz frequency for all the considered directions. At vibration magnitudes 1.0 and 1.5 m/s^2 rms, the peak was observed around 4 Hz for the vertical and lateral directions. There is a decrease in resonance frequency with an increase in vibration magnitude, which is also evident in many previous studies.[7,17,19] This shows the nonlinear softening characteristics of three human body under the exposure of vibration.

The results also revealed that STHT for vertical vibration was significantly higher than that in lateral and fore-and-aft vibration at 1 m/s^2 rms vibration magnitude up to the 1ower frequency range, *i.e.* up to 10 Hz only ($p<0.05$), as shown in Fig. 7.

3.2. Effect of Vibration on Reduction in Reading Performance

Figures 8–10 show the effect of vibration frequency on the reduction in reading performance for all the vibration magnitudes. The decline in reading performance was found to be greater with the increase in vibration magnitude in all the directions of vibration, as shown in Figs. 8–10. The greatest drop in reading performance was observed around 4–5 Hz frequency for all directions and vibration magnitudes ($p<0.01$). The decline in reading performance decreases with the increase in

Table 3. Test of within-subject effects of experimental variables in repeated-measure analysis.

Source	Type III Sum of Squares	df	Mean Square	F	Sig.
Seat-to-head Transmissibility (STHT)					
Direction	10.404	2	5.202	11.478	.000
Magnitude	2.972	2	1.486	5.649	.010
Frequency	164.401	6	27.400	84.697	.000
Direction * Magnitude	.145	4	.036	.172	.951
Direction * Frequency	3.239	12	.270	.879	.570
Magnitude * Frequency	3.065	12	.255	1.365	.191
Direction * Magnitude Frequency	2.355	24	.098	.518	.972
Percentage Reduction in reading performance					
Direction	189.410	2	94.705	2.554	.012
Magnitude	3848.626	2	1924.313	48.872	.000
Frequency	30159.175	6	5026.529	135.100	.000
Direction * Magnitude	255.200	4	63.800	1.719	.043
Direction * Frequency	905.005	4.971	182.075	2.764	.027
Magnitude * Frequency	2678.784	12	223.232	6.635	.000
Direction * Magnitude Frequency	798.303	24	33.263	1.128	.113
Perceived Difficulty in reading					
Direction	39.784	2	19.892	43.061	.000
Magnitude	635.722	2	317.861	627.932	.000
Frequency	839.779	6	139.963	322.900	.000
Direction * Magnitude	8.179	1.000	8.179	7.512	.018
Direction * Frequency	20.975	1.000	20.975	5.721	.034
Magnitude * Frequency	469.164	12	39.097	124.990	.000
Direction * Magnitude Frequency	12.147	1.000	12.147	1.785	.206

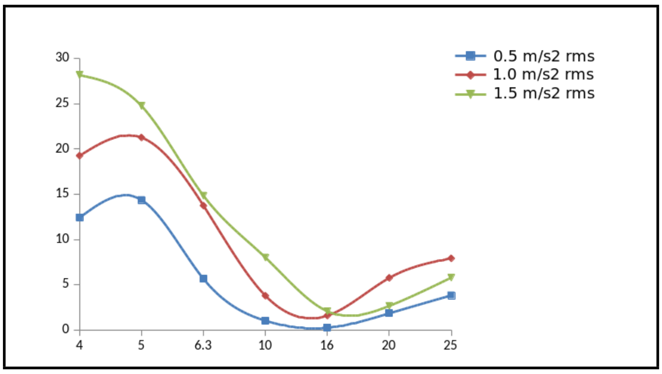

Figure 8. Mean percentage reduction in reading performance of 12 subjects measure at 0.5, 1.0, 1.5 m/s^2 rms in vertical direction.

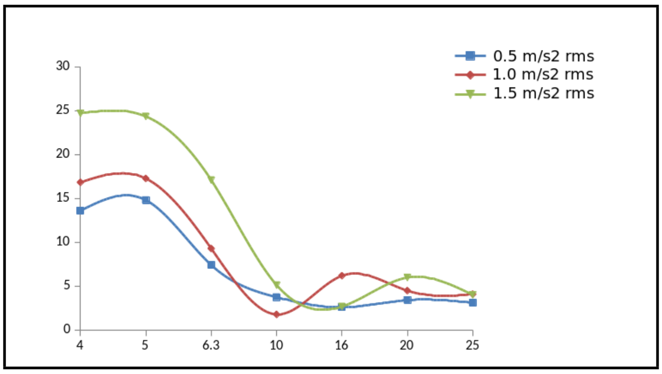

Figure 9. Mean percentage reduction in reading performance of 12 subjects measure at 0.5, 1.0, 1.5 m/s^2 rms in lateral direction.

frequency up to 16 Hz frequency. The comparable decline in reading performance was observed at 25 Hz for all vibration magnitudes in the vertical direction only. Comparing the vibration in three directions, the decline in reading performance in the vertical direction is significantly higher at lower frequencies ($p<0.05$), as shown in Fig. 11.

3.3. Effect of Vibration on Perceived Difficulty in Reading

Figures 12,–14 show the effect of vibration frequency on the perceived difficulty in reading for all three vibration magnitudes. The perceived difficulty in reading progressively increases with an increase in vibration magnitude in each direction. Highly significant differences were observed for the perceived difficulty in reading for all the considered vibration magnitudes in each direction, up to the lower frequency range, *i.e.* 10 Hz ($p<0.01$). The perceived difficulty in reading for vertical vibration is significantly greater than in lateral and fore-and-aft directions up to lower frequencies, *i.e.* up to 10 Hz ($p<0.05$) (Figure 15). The maximum perceived difficulty has been observed at 5 Hz for all the considered vibration magnitudes in all directions. Considerable reading difficulty was also observed at 25 Hz, but in the vertical direction only. The perceived difficulty in reading is very low at higher frequencies for lateral and fore-and-aft vibration.

3.4. Results from Statistical Analysis

The within-subject design of repeated measurement analysis was used to evaluate the overall effects of all the independent variables, *i.e.* vibration magnitude, direction, and frequency, of the three dependent variables such as STHT, perceived difficulty in reading, and reduction in reading performance. The overall effects of the independent variables and their interaction on dependent variables are shown in Table 3. Table 3 shows the significance value ($p<0.05$) of all the independent variable and their interaction for the measured re-

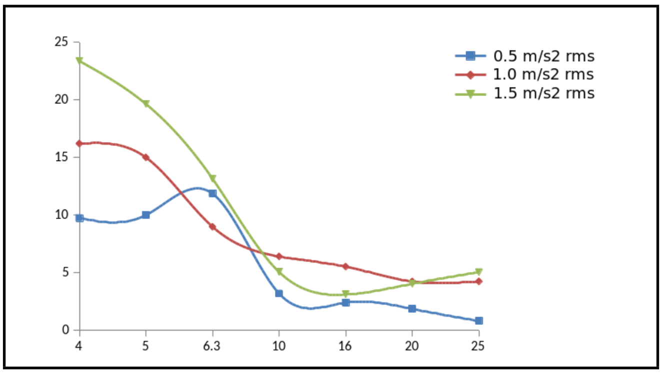

Figure 10. Mean percentage reduction in reading performance of 12 subjects measure at 0.5, 1.0, 1.5 m/s^2 rms in fore-and-aft direction.

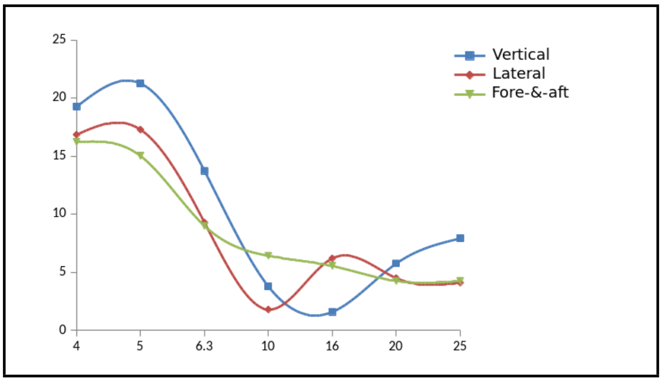

Figure 11. Comparisons of mean percentage reduction responses for 1.0 m/s^2 rms in vertical, fore-and-aft and lateral vibration.

sponses, which indicate that the variables and their interactions are strongly responsible for the results. The vibration direction, magnitude, and frequency have significant effects on the STHT, reduction in performance, and perceived difficulty responses ($p<0.05$), as illustrated in the Table 3. The interactions of variables, *i.e.* vibration direction, magnitude, and frequency, have insignificant effects on the STHT responses. The two-way interactions of variables, *i.e.* vibration direction, magnitude, and frequency, have significant effects on the reduction in performance and perceived difficulty responses.

4. DISCUSSION

In the research used in this paper, none of the studies were observed to relate STHT to reading discomfort at the same vibration environment and posture from the best knowledge of the author. This study has shown that the STHT and reading discomfort are related to each other during the vibration exposure. The STHT, percentage reduction in reading performance, and perceived difficulty in reading have shown higher values around 4–5 Hz frequency for all the vibration directions and magnitudes. The results also revealed that the response decreases with an increase in frequency up to 10–16 Hz, and it is almost constant at least up to 25 Hz.

The results show the various trends between STHT, reduction in performance, and perceived difficulty responses. As the vibration magnitude increases, the peak in STHT responses occurs at lower frequencies. This decrease in STHT resonance frequency with an increase in vibration magnitude has been observed in the present study, which shows the nonlinear behaviour of transmissibility. The nonlinear behavior of

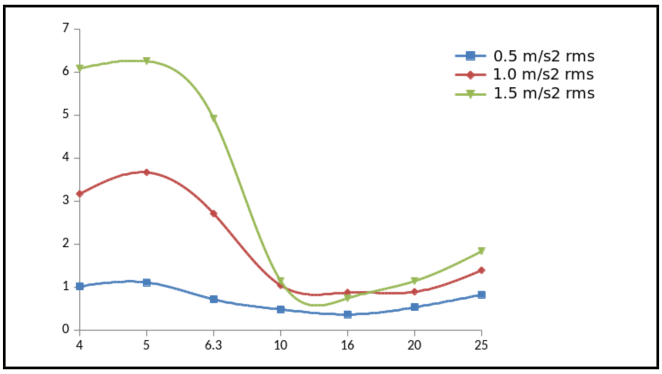

Figure 12. Mean level of perceived difficulty in reading of 12 subjects measured at 0.5, 1.0, 1.5 m/s^2 rms in the vertical direction.

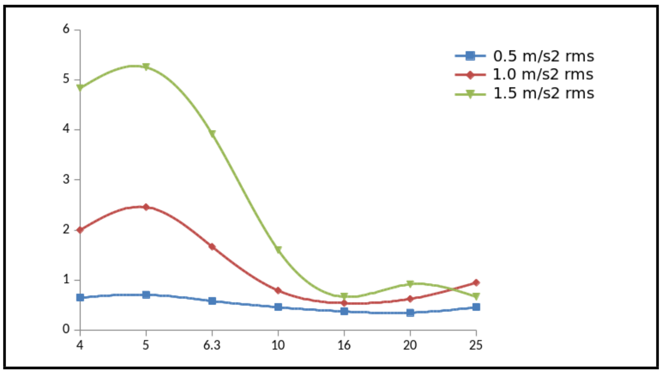

Figure 13. Mean level of perceived difficulty in reading of 12 subjects measured at 0.5, 1.0, 1.5 m/s^2 rms in the lateral direction.

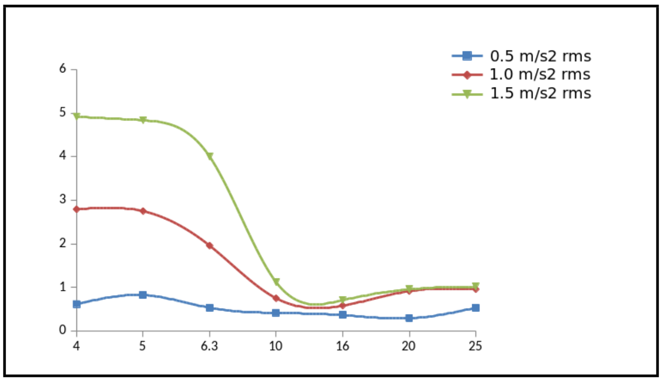

Figure 14. Mean level of perceived difficulty in reading of 12 subjects measured at 0.5, 1.0, 1.5 m/s^2 rms in fore- and-aft direction.

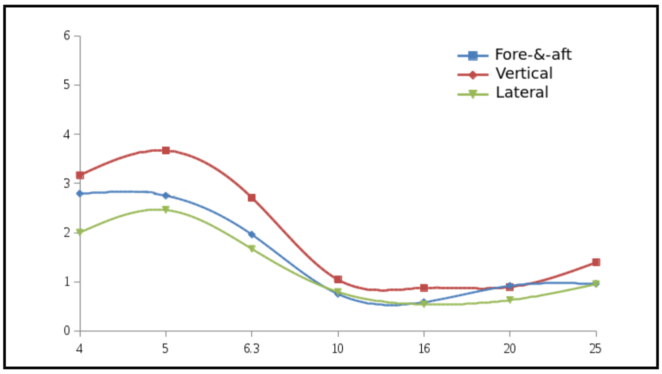

Figure 15. Comparisons of mean level of perceived difficulty in reading for 1.0 m/s^2 rms in vertical, fore-and-aft and lateral vibration.

transmissibility has been discussed previously in many studies.19,26,27 Mansfield and Griffin,[19] showed the nonlinear behaviour of apparent mass and transmissibility to the viscera, pelvis, and lumbar spine, and it was observed that the dynamics of tissues, the bending and buckling of the spine, and some complex responses of the body may be the cause for nonlinearity in biodynamic responses.

The results show that both the percentage reduction in reading performance and the perceived difficulty are found to increase with an increase in vibration magnitude in each independent direction. This finding is consistent with many previous studies.[2,3,28,29] The frequency of vibration also has highly significant effects on the reduction in reading performance and the perceived difficulty in reading. The reduction in reading performance and perceived difficulty have the highest value around 4–5 Hz. Eye movements of the subjects are affected by the whole body vibration depending upon the magnitude and vibration frequency. The performance with respect to reading is largely dependent upon the eye movements of the subjects.[10] The legibility reduces as the image moves faster across the retina, which is due to the unstable image on the retina.[24] The lines which make up the letters and rows overlap with each other at higher magnitudes of whole body vibration, which in turn reduces the reading performance of the subjects.

The results show a considerable decline in reading performance and an increase perceived difficulty in reading at 25 Hz frequency in the vertical direction. Most of the subjects feel agitation in the eyes at around 20–25 Hz frequency. This agitation in the eyes may be attributed to the resonance of the eyeballs or the internal structure of the head of the seated subjects under the exposure to WBV at 25 Hz frequency.

The reading discomfort is quantified with the help of the percentage reduction in reading performance and perceived difficulty in reading. The results for these two quantifying parameters show the maximum value of reading discomfort occurs around 4–5 Hz frequency of WBV in three independent axes. The STHT also observed the peak around 4–5 Hz frequency in all the three considered directions of vibration. So, both STHT and reading discomfort show the maximum values at the resonant frequency of the human body. Considerable reading discomfort was also shown around 25 Hz frequency, which may be attributed to the resonance of the eyeballs of the subjects. The reading discomfort may be affected by other frequencies which may be the resonance frequencies for the subjects' internal organs or structure of the head. The vibrations for the internal organs and eyes are difficult to measure. At the resonance frequencies, *i.e.* around 4–5 Hz of human body, the seated test subjects feel higher reading discomfort during WBV exposure.

5. CONCLUSION

The extent of decline in the reading performance depends upon magnitude, direction, and frequency of vibration. Vibration magnitude and frequency contribute most to the reduction in reading performance and perceived difficulty in reading. The decline in reading performance increases with an increase in vibration magnitude in each direction of vibration. The three measured responses - STHT, percentage reduction in reading performance, and perceived difficulty in reading - are most affected around 4–5 Hz frequency of whole body vibration, which means that the, transmission of vibration to the head and various parts of the head affects the reading performance of the seated subjects. In vertical vibration, reading performance is to some extent affected around 25 Hz frequencies. STHT has shown nonlinear behaviour with respect to vibration magnitude. Principal resonance in STHT occurs at around 4–5 Hz for seated subjects.

REFERENCES

1. Bhiwapurkar, M. K., Singh, P. P., Yana, J., Saran V. H., and Harsha, S. P. Influence of vibration on passenger comfort — a survey on Indian train, *Proc. Int. Conf. Adv. Ind. Eng. Appl.*, Chennai, India, (2009).

2. Bhiwapurkar, M. K., Saran, V. H., Harsha, S. P., Goel, V. K., and Berg, M. Influence of mono-axis random vibration on reading activity, *Ind. Health*, **48**, 675–681, (2010). http://dx.doi.org/10.2486/indhealth.mswbvi-09

3. Bhiwapurkar, M. K., Saran, V. H., Harsha, S. P. Objective and subjective responses of seated subjects while reading Hindi newspaper under multi axis whole-body vibration, *Int. J. Ind. Ergonom.*, **141**, 625–633, (2011).http://dx.doi.org/10.1016/j.ergon.2011.06.004

4. Bhiwapurkar, M. K., Saran, V. H., and Harsha, S. P. Interference in reading an e-paper under whole body vibration exposure with subject posture, *Int. J. Acoust. Vib.*, **17**, 100–107, (2012).

5. Borg, E., *On Perceived Exertion and its Measurement* (Doctoral dissertation), Dept. of Psychology, Stockholm University, (2007). http://dx.doi.org/10.1037/e529832013-001

6. Demic, M. and Luki, J. Investigation of the transmission of fore-and-aft vibration through the human body, *Appl. Ergon.*, **40**, 622–629, (2009). http://dx.doi.org/10.1016/j.apergo.2008.05.002

7. Desta, M., Saran, V. H., and Harsha S. P. Effects of intersubject variability and vibration magnitude on vibration transmission to head during exposure to whole-body vertical vibration, *Int. J. Acoust. Vib.*, **16**, 88–97, (2011).

8. Griffin, M. J., and Hayward, R. A. Effects of horizontal whole-body vibration on reading, *Appl. Ergon.*, **25**, 165–169, (1994). http://dx.doi.org/10.1016/0003-6870(94)90014-0

9. Griffin, M. J., and Whitham, M. E. Individual variability and its effect on subjective and biodynamic response to whole-body vibration, *J. Sound Vib.*, **58** (2), 239–250, (1978). http://dx.doi.org/10.1016/s0022-460x(78)80078-9

10. Griffin, M. J. *Handbook of Human Vibration*, Academic Press, London, (1990). http://dx.doi.org/10.1016/B978-0-12-303040-5.50001-5

[11] Hinz, B., Menzel, G., Blüthner, R., and Seidel, H. Seat-to-head transfer function of seated men — determination with single and three-axis excitations at different magnitudes, *Ind. Health*, **48**, 565–583, (2010). http://dx.doi.org/10.2486/indhealth.mswbvi-03

[12] Khan, S. and Sundstrm, J. Vibration comfort in Swedish inter-city trains — a survey on passenger posture and activities, *Proc. 17th Int. Conf. Acoust. (ICA)*, Kyoto, Japan, 3733–3736, (2004).

[13] Kumar, V. and Saran, V. H. Influence of reading format on reading activity under uniaxial whole body vibration, *Int. J. Ind. Ergonom.*, **44**, 520–527, (2014). http://dx.doi.org/10.1016/j.ergon.2014.05.004

[14] Kuorinka, I., Jonsson, B., Kilbom, A., Vinterberg, H., Biering-Srensen, F. Andersson, G., and Jrgensen, K. Standardised Nordic questionnaires for the analysis of musculoskeletal symptoms, *App. Ergon.*, **18** (3), 233–237, (1987). http://dx.doi.org/10.1016/0003-6870(87)90010-x

[15] Legge, G. E., Pelli, D. G., Rubin, G. S., and Schleske, M. M. Psychophysics of reading—I. Normal vision, *Vision Res.*, **25** (2), 239–252, (1985). http://dx.doi.org/10.1016/0042-6989(85)90117-8

[16] Legge, G. E., Rubin, G. S., Pelli, D. G., and Schleske, M. M. Psychophysics of reading—II. Low vision, *Vision Res.*, **25** (2), 253–265, (1985). http://dx.doi.org/10.1016/0042-6989(85)90118-x

[17] Mandapuram, S., Rakheja, S., Boileau, P-., Maeda, S., and Shibata, N. Apparent mass and seat-to-head transmissibility responses of seated occupants under single and dual axis horizontal vibration, *Ind. Health*, **48**, 698–714, (2010). http://dx.doi.org/10.2486/indhealth.mswbvi-15

[18] Mandapuram, S., Rakheja, S., Boileau, P-É., and Maeda, S. Apparent mass and head vibration transmission responses of seated body to three translational axis vibration, *Int. J. Ind. Ergonom.*, **42**, 268–277, (2012). http://dx.doi.org/10.1016/j.ergon.2012.02.002

[19] Mansfield, N. J. and Griffin, M. J. Nonlinearities in apparent mass and transmissibility during exposure to whole-body vertical vibration, *J. Biomech.*, **33**, 933–941, (2000). http://dx.doi.org/10.1016/s0021-9290(00)00052-x

[20] Mansfield, N. J. *Human Response to Vibration.* CRC Press, London, (2005).

[21] Matsumoto, Y. and Griffin, M. J. Movement of upper body of seated subjects exposed to vertical whole-body vibration at the principle resonance, *J. Sound Vib.*, **215**, 743–762, (1998). http://dx.doi.org/10.1006/jsvi.1998.1595

[22] Matsumoto, Y. and Griffin, M. J. Comparison of biodynamic responses in standing and seated human bodies, *J. Sound Vib.*, **238** (4), 691–704, (2000). http://dx.doi.org/10.1006/jsvi.2000.3133

[23] Magnusson, M., Pope, M., Rosredt, M., and Hansson, T. Effect of backrest inclination on the transmission of vertical vibrations through the lumbar spine, *Clin. Biomech.*, **8**, 5–12, (1993). http://dx.doi.org/10.1016/s0268-0033(05)80003-8

[24] Moseley, M. J. and Griffin, M. J. Effects of display vibration and whole body vibration on visual performance, *Ergonomics*, **29**, 977–983, (1986). http://dx.doi.org/10.1080/00140138608967211

[25] Paddan, G. and Griffin, M. The transmission of translational seat vibration to the head—I. Vertical seat vibration, *J. Biomech.*, **21**, 191–197, (1988). http://dx.doi.org/10.1016/0021-9290(88)90169-8

[26] Pranesh, A. M., Rakheja, S., and Demont, R. Influence of support conditions on vertical whole-body vibration of the seated human body, *Ind. Health*, **48**, 682–697, (2010). http://dx.doi.org/10.2486/indhealth.mswbvi-25

[27] Wang, W., Rakheja, S., and Boileau, P-É. Effect of back support condition on seat to head transmissiblities of seated occupants under vertical vibration, *Low Freq. Noise, Vib. Act. Cont.*, **25** (4), 239–259, (2006). http://dx.doi.org/10.1260/026309206779884874

[28] Sundström, J. and Khan, S. Influence of stationary lateral vibrations on train passengers-difficulty to read and write, *Appl. Ergonom.*, **39**, 710–718, (2008). http://dx.doi.org/10.1016/j.apergo.2007.11.009

[29] Wollstrom, M. *Effects of vibrations on passenger activities: reading and writing: a literature study.* TRITA- FKT Report, **64**, (2000).

[30] Zimmermann, C. L. and Cook, T. M. Effects of vibration frequency and postural changes on human responses to seated whole-body vibration exposure, *Int. Arch. Occ. Env. Hea.*, **69**, 165–179, (1997). http://dx.doi.org/10.1007/s004200050133

On the Instabilities in a Switchable Stiffness System for Vibration Control

Diego Francisco Ledezma-Ramírez

Universidad Autónoma de Nuevo León, Facultad de Ingeniería Mecánica y Eléctrica, San Nicolás de los Garza, Nuevo León, México, 66456

Neil Ferguson

University of Southampton, Institute of Sound and Vibration Research, University Road, Highfield, Southampton, Great Britain, SO17 1BJ

Michael Brennan

Departamento de Engenharia Mecanica, UNESP, Ilha Solteira, Brazil

(Received 30 January 2014; accepted 22 September 2014)

A strategy for vibration control in which the stiffness is switched on and off between a minimum and a maximum value within each oscillation cycle is considered in this study. The strategy has been shown to help greatly in decreasing residual vibrations, thus increasing the effective damping ratio in lightly-damped systems. This work explores the effect of the delay during the stiffness switching. In this study, it is predicted theoretically how a certain value of delay could cause instabilities, and experimental results are presented.

1. INTRODUCTION

Mechanical vibration is an undesirable condition that could lead to fatigue, noise, damage, and other harmful effects to structures, machines, and humans. There are different methods for vibration suppression, either through control of the vibration source, structural modifications, or vibration isolation. The vibration isolation method involves the use of a resilient element located between the vibration source and the receiver, normally modelled mathematically as an elastic element and viscous damper in parallel.[1] When the properties of these elements, i.e. damping and stiffness, have a fixed value, the isolator is said to be passive. However, there are some isolators in which the properties are able to change in real time depending upon the excitation, the so-called semi-active vibration isolators. Lately, there has been a growing interest in the use of semi-active isolation systems mainly for random and deterministic vibration, while few works exist on shock isolation. Most of the work has been done in the field of variable damping; for instance, some switchable or semi-active damping strategies based on the skyhook damper concept have been studied,[2] and Waters, et al. showed that reducing the damping to a lower value during a shock input can lead to better isolation performance.[3]

In the field of switchable stiffness strategies, Winthrop presented an important review in which different methods to achieve variable stiffness were documented.[4] A control strategy for transient vibrations was proposed by Onoda[5] considering an on/off logic aimed to extract energy, based on the switchable stiffness concept presented by Chen for structural vibration control.[6] A resetting technique was considered by Jabbari, et al.[7] and Leavitt, et al.,[8] also based on switchable stiffness with the objective of extracting energy from a mechanical system while having a high stiffness value at all times. Switchable stiffness control has recently been investigated theoretically and experimentally by the authors of this paper, as a means of energy dissipation in lightly damped systems.[9,10] The strategy developed by Ledezma, et al.[9] comprises a mass supported by two springs, one of which can be disconnected. Switching in and out of the spring involves a two-stage control strategy — stiffness control during the shock to reduce the maximum response of the payload, and reduction of the residual vibration after the shock has occurred. The theoretical simulations presented demonstrate that it is possible to obtain better shock isolation by switching the stiffness in lightly damped systems, and this concept was demonstrated experimentally.

This paper explores the second part of the strategy presented previously by the authors,[9,10] namely the residual control of vibrations, which involves switching in real time the actual stiffness of the system. It was found that a delay in the switching could lead to instabilities. Time delays in active vibration control may result in the unstable motion of a controlled oscillating system and hence limit the development and application of vibration control. Haiyan,[11] and later Gu,[12] summarized the recent studies on the dynamics of controlled systems with time delay. Due to the possibility of instabilities as a result of delays, this work gives an insight into the stability of the system, prediction of the maximum delay, and some of the practical issues involved.

2. SWITCHABLE STIFFNESS BACKGROUND THEORY

The switchable stiffness strategy presented by the authors is described briefly here, focusing on the residual vibration control. It is important to mention that residual vibration is the

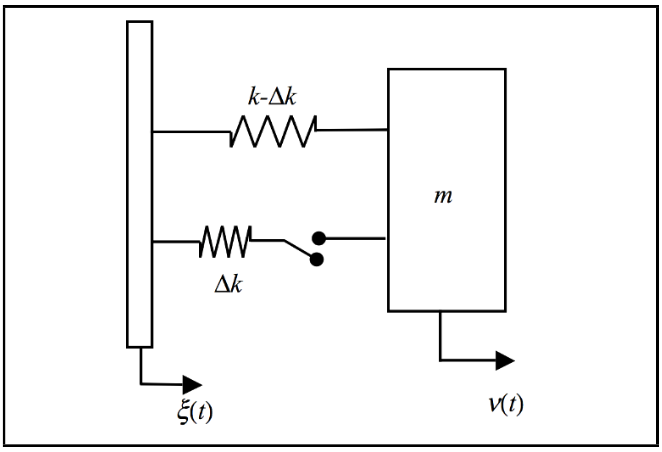

Figure 1. Schematic of a SDOF system with switchable stiffness under excitation $\xi(t)$ applied to the base. The two stiffnesses in parallel have stiffness Δk and $k - \Delta k$, respectively, and m is the mass with absolute displacement v.

result of a transient excitation, such as a pulse, i.e. a versed sine pulse. The analysis of shock isolation is normally divided in two stages: the forced response during the shock pulse, and the subsequent free vibrations at the natural frequency of the system. This paper focuses on what happens after the pulse, and it is assumed for simplicity that an impulse is applied when the system is at rest, so there is an initial velocity applied. The switching strategy considers an undamped system supported by two springs, one of which can be disconnected during free transient vibration, in order to quickly dissipate the energy stored by the elastic element without adding an external damping mechanism, as shown in Fig. 1. The control strategy is given by

$$k_{\text{effective}} = \begin{cases} k & \text{for } v\dot{v} \geq 0 \\ k - \Delta k & \text{for } v\dot{v} < 0 \end{cases}; \tag{1}$$

where $\dot{v}$ is the velocity of the suspended mass. The stiffness is maximum and equal to k when the product $v\dot{v}$ is positive, and it is minimum and equal to $k - \Delta k$ when $v\dot{v}$ is negative. As a result, the secondary spring, Δk, is disconnected when the absolute value of the displacement of the mass is a maximum. It is connected again when the system passes through its equilibrium position. The effective stiffness change in the system is quantified with the stiffness ratio, defined as $\sigma = \frac{\Delta k}{k}$. This parameter varies between 0 and 1, where 0 means no stiffness reduction, and 1 means total stiffness removal. The schematic model is depicted in Fig. 1, where a base excitation $\xi(t)$ is applied and the response is $v(t)$. It is also important to introduce the mean period of the system, given by $T_{\text{m}} = \frac{T_{\text{on}}}{2} + \frac{T_{\text{off}}}{2}$, where T_{on} is the natural period for the ON state, i.e. high stiffness, and T_{off} is the period for the OFF state, i.e. low stiffness.

The typical behaviour of the switching strategy can be easily explained with the phase plane plot presented in Fig. 2(a) showing the switching and how the energy is dissipated at every stiffness reduction point. Figure 2(b) depicts a time history corresponding to this example. The comprehensive study of this strategy presented in a previous paper[9] concludes that a greater stiffness reduction leads to greater rate of decay of the residual vibrations.

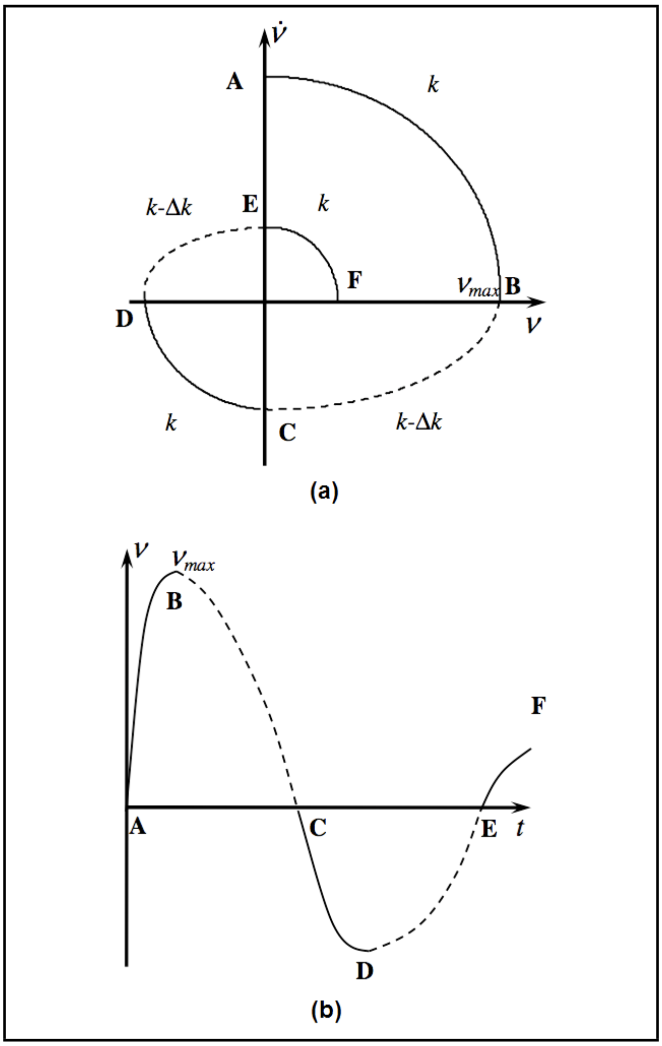

Figure 2. Effect of the switchable control strategy on the residual vibration. (a) Phase plane plot, and (b) Time history of the displacement response. (—— High stiffness; - - - - - Low stiffness).

3. EXPERIMENTAL DEVICE FOR VIBRATION CONTROL USING SWITCHABLE STIFFNESS

An experimental prototype was designed to validate the theoretical strategy discussed before.[10] Considering the results previously referenced, the experimental model has to be capable of achieving a high stiffness change — at least a factor of two — and perform this change rapidly, i.e. four times during a full oscillation cycle. It was also designed bearing in mind that the system should behave as a lightly-damped single degree-of-freedom system, for which predictions had been previously obtained.

To create a system with these characteristics, an electromagnetic element was used to achieve a switchable stiffness. The experimental system is shown in Fig. 3; a schematic of the system is given in Fig. 3(a), and a photograph of the system is shown in Fig. 3(b). The device comprises two disc-shaped neodymium magnets suspended between two electromagnets using four tensioned nylon wires attached to the main frame, providing additional stiffness in parallel with the stiffness given by the magnets. The total isolated mass (payload) in the experimental system was 0.0753 kg.

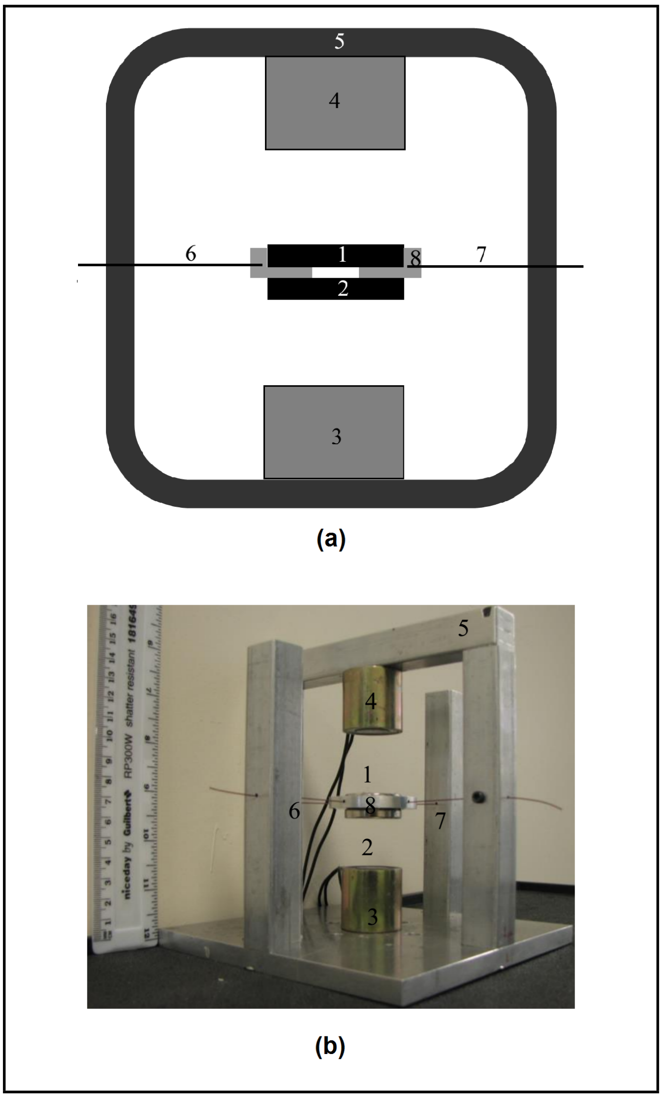

Figure 3. (a) Diagram of the switchable stiffness experimental system in the vertical position. The permanent magnets (1, 2) are suspended between two electromagnets (3, 4) using four wires (6, 7) that also join the magnet to the main frame (5). The permanent magnets are held by an aluminium disc (8). (b) Photograph of the rig.

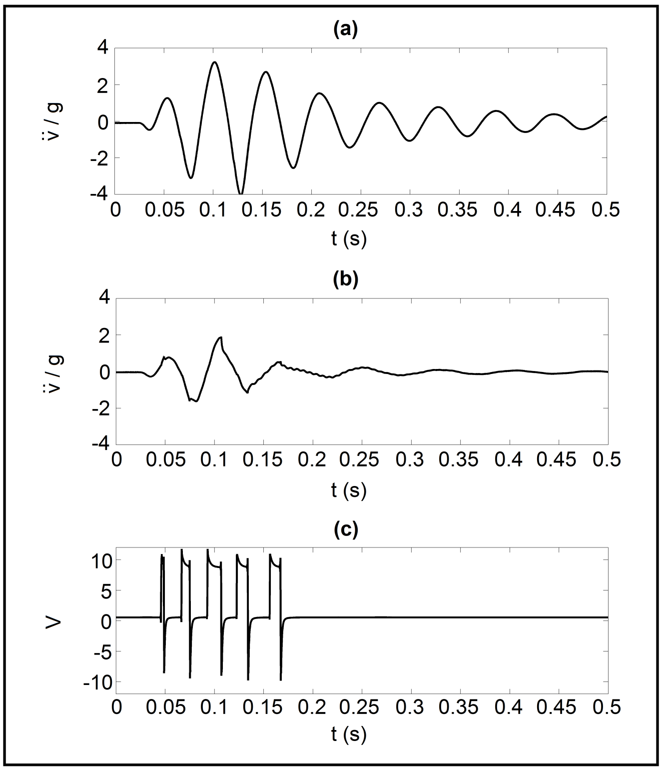

Figure 5. Switching stiffness response for residual vibration suppression. (a) Passive acceleration response for high stiffness state, (b) switching response and (c) the voltage supplied to the electromagnets. All acceleration time histories are normalized by g.

The low stiffness state was achieved when the electromagnets are turned off, whilest the high stiffness state was obtained by applying a constant DC voltage of 12 V to the electromagnet, using a Hameg triple voltage source HM7042-5. The properties of the system were measured by attaching the device to an electrodynamic shaker with a random signal generated by a Data Physics Mobilizer analyser through a power amplifier. The response was acquired using two PCB teardrop miniature accelerometers type 352C22, and the frequency response function was measured. It was found that the maximum and minimum values of the natural frequencies were 17.75 Hz and 12.75 Hz, respectively, corresponding to an effective stiffness change of 48%. The full results for these properties and the procedure are available in a previously published paper.[10] It is also important to mention that the magnetic forces are nonlinear by nature, and as a result, the oscillation of the system was kept within a linear range for which coherence and static measurements were performed, as stated in previous work.[10]

For the control of residual vibrations, an electronic circuit was designed in order to perform the switching strategy given by Eq. (1). The acceleration signal measured in the suspended mass was amplified and then split into two in order to have acceleration and velocity signals. Then, both signals were multiplied, and the product was compared with respect to zero. If the product is greater than zero, the voltage is set to zero. Otherwise, a voltage is applied to the electromagnets. A block diagram is shown in Fig. 4(a), while a circuit diagram is shown in Fig. 4(b).

The system was subjected to a very short pulse and then the responses were measured. An example is presented in Fig. 5. Figure 5(a) depicts the free vibration acceleration response of the passive system in the high stiffness state, which is taken as a basis for comparison. The switching response is presented in Fig. 5(b), and the voltage applied to the electromagnets is given in Fig. 5(c).

It can be seen from the voltage plot that the stiffness is switched from a high state to a low state twice during each cycle of vibration. The voltage supply turned off when the response was at a maximum, and turned on when the response passed through the static equilibrium position. It can also be seen that there were only four cycles of stiffness change. This was because the circuit was set to switch only when the input signals were at a minimum voltage level of 0.7 V. However, even though the stiffness switched during the first two cycles of vibration, the vibration decayed at a much faster rate than the passive case, as can be seen by comparing Figs. 5(a) and 5(b).

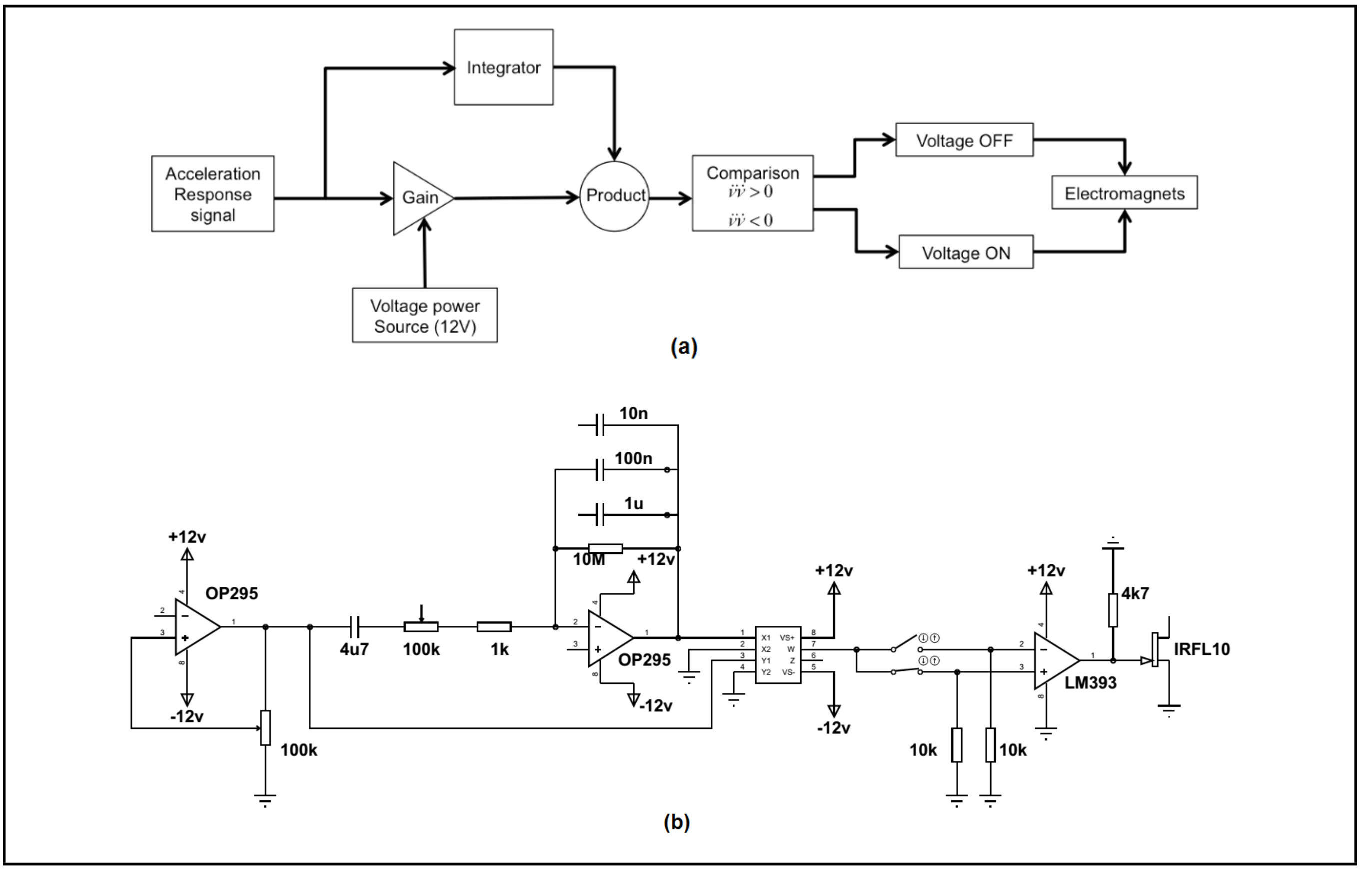

Figure 4. Electrical circuit used for the switching stiffness during residual vibration. (a) Block diagram. (b) Circuit diagram.

4. EFFECT OF DELAY ON THE CONTROL STRATEGY

4.1. Stability of the System

Using Lyapunov's direct method,[12] one can construct an energy-like function of the system and, examining its derivatives, the condition of stability can be evaluated. An energy function for the switching stiffness model can be written in terms of the total energy of the system, where the energy is considered after the disconnection of the secondary spring, being the sum of the kinetic energy of the mass and the potential energy stored in the effective low stiffness, as follows:

$$V = \frac{1}{2}m\dot{v}^2 + \frac{1}{2}(k - \Delta k)\, v^2. \tag{2}$$

The first time derivative of equation Eq. (2) can be written as:

$$\dot{V} = m\ddot{v}\dot{v} + k\dot{v}v - \Delta k\dot{v}v. \tag{3}$$

This can be further simplified using the equation of motion of the system given by $m\ddot{v} + k_{\text{effective}}v = 0$ and rewritten as

$$\dot{V} = -\Delta k\dot{v}v. \tag{4}$$

As stated in the control theory[13] as V is a positive definite function, and $\dot{V}$ is negative semidefinite, it can be said that the system is asymptotically stable. However, it is interesting to note the behaviour of the system when the control law is inverted as:

$$k_{\text{v}} = \begin{cases} k & \text{for } v\dot{v} \leq 0 \\ k - \Delta k & \text{for } v\dot{v} > 0 \end{cases}. \tag{5}$$

In this case, the energy function of the system is expressed as:

$$V = \frac{1}{2}m\dot{v}^2 + \frac{1}{2}(k + \Delta k)\, v^2; \tag{6}$$

and the derivative is given by:

$$\dot{V} = \Delta k\dot{v}v. \tag{7}$$

The derivative is a positive function, and as a result the system is unstable. This can also be observed in Eq. (6), as its second term means that energy is added to the system instead of being dissipated. In fact, at the stiffness reduction points, the system is going from a low energy state to a higher energy state. In a real system, this energy, which causes instabilities, must come from a certain source. This phenomenon will be discussed later.

4.2. Effect of Delay on Stability

An interesting point in the study for the stability of this particular strategy is to determine if a delay in the reduction or recovery of the stiffness will cause any possible instability condition. In order to investigate this, a numerical simulation was performed in MATLAB. The simulation comprises an iterative test that evaluates the amplitude of the system and compares it with the previous cycle. If the amplitude of the next cycle increases with respect to the previous one, the system will be unstable. The comparison is made for values of the stiffness ratio σ, i.e. the factor of stiffness reduction from 0 to 1, where 0 is no stiffness reduction and 1 means total stiffness removed. Then, a delay in the implementation of the strategy is

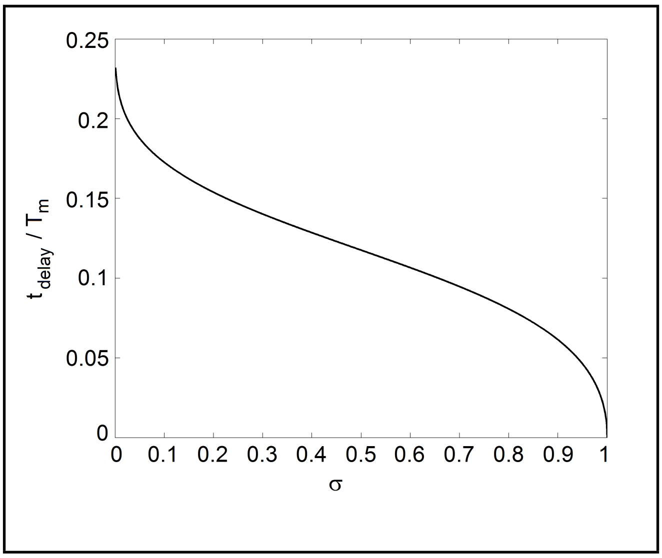

Figure 6. Maximum delay permissible in order to guarantee stability in the switching strategy presented as a function of the stiffness ratio σ. Values of delay above the curve will cause the system to become unstable.

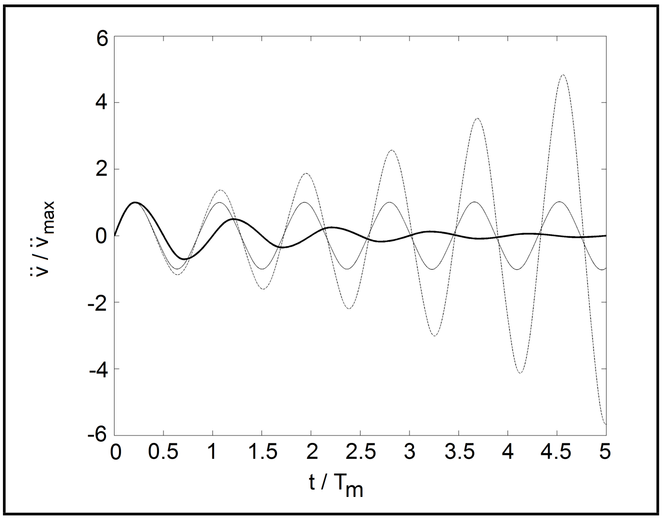

Figure 7. Theoretical acceleration response of the switching system showing the effect of delay in the switching stiffness strategy. This example shows no delay (continuous bold line), limiting value of delay $d = 0.1176\,T_{\mathrm{m}}$ (continuous thin line), and $d = 0.15\,T_{\mathrm{m}}$ (dotted line).

introduced on purpose. This delay is given as a fraction of the mean period of the system $T_{\mathrm{m}} = \frac{T_{\mathrm{on}}}{2} + \frac{T_{\mathrm{off}}}{2}$. The resulting plot is presented in Fig. 6.

Figure 6 represents the limiting value of delay that is permissible in order to achieve stability. The area below the curve represents a "safe" zone where the system is stable. However, it is important to note that although small delays will not cause instabilities, the performance of the system might decrease. The maximum value of delay depends upon the value of the stiffness reduction ratio σ. As the stiffness ratio increases, smaller delays are permitted. A time response example for $\sigma = 0.5$ is shown in Fig. 7, for three situations. The continuous bold line gives the response of the system with no delay, the continuous thin line represents the limiting value of delay $d = 0.1176\,T_{\mathrm{m}}$ for this value of the stiffness ratio, and the dotted line indicates a value exceeding the limit $d = 0.15\,T_{\mathrm{m}}$.

This phenomenon is attributed to two factors. First, as the

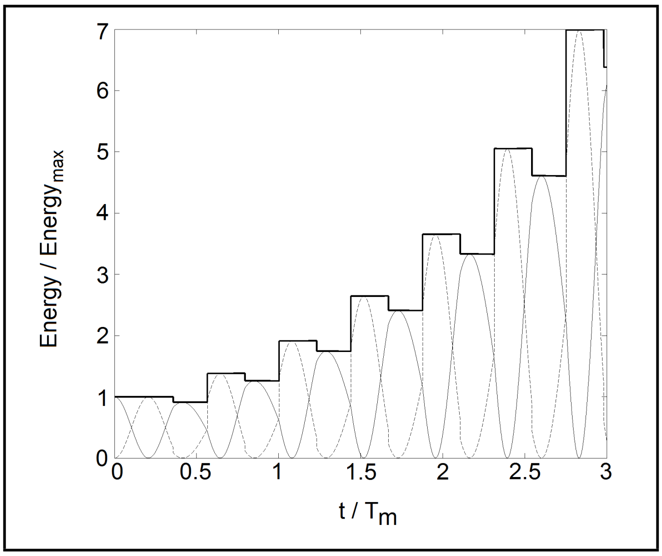

Figure 8. Energy levels in a switchable stiffness system with delay of $d = 0.15\,T_{\mathrm{m}}$ enough to cause instabilities. The bold line represents the total energy in the system, the thin line represents the kinetic energy, and the dotted line is for the potential energy.

stiffness reduction is not made at the point of maximum displacement, the energy dissipated is not maximized. Secondly, the stiffness recovery is performed after the point of equilibrium position. As a result, the secondary spring Δk has a certain deformation at the moment of reconnection. This means the secondary spring Δk has some energy stored that is returning to the system. If the delay causes the energy returned to be greater than the energy dissipated during the stiffness reduction, the amplitude will grow. Figure 8 shows the energy levels in the unstable system, showing that at some point the energy returned is higher than the energy removed. This will in fact violate energy conservation, which means that in a real system, the energy needed to cause the instability must come from an external source. In practice, this phenomenon has not been observed because the delay in the real-time implementation of the strategy is very small.

If the delay is large enough to cause instabilities, in a real system the energy must come from an external source. For the experimental setup used in this project, the electromagnets as inductive devices are capable of storing and releasing energy resulting from sudden voltage or current changes. In practice, the presence of damping in the system could help to reduce the effect of delay and the possible instabilities.

Finally, an experimental test was performed considering the opposite control law as expressed by Eq. (5). Figure 9 shows the response of the actual system using the inverted control law. In this case, the amplitude of the system is bounded. However, the vibration of the system is sustained, and while the voltage is supplied, the amplitude never decays away. The energy responsible of this behaviour is believed to come from the electromagnets and the voltage source used in the system. As a result, a constant amplitude of vibration is sustained.

5. CONCLUSIONS

This study presents an overview of a switching stiffness strategy for vibration control. The strategy is based on a con-

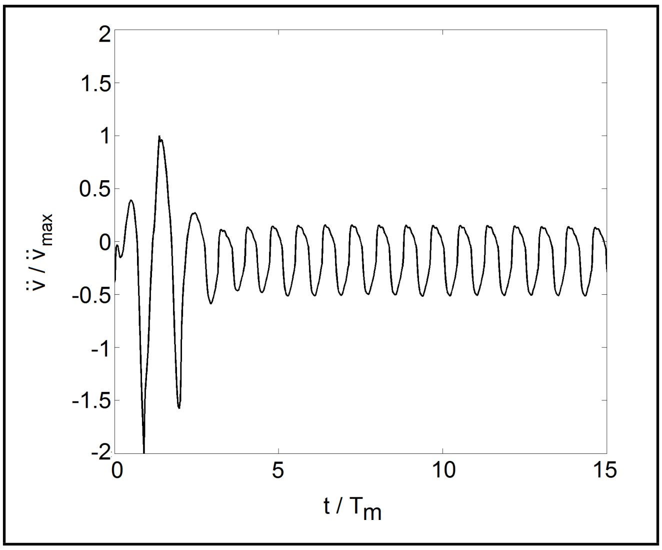

Figure 9. Actual response of the switching system considering the opposite control law as specified by Eq. (5). Time is normalised considering natural period of the system.

trol law that switches off the stiffness at points of maximum and minimum displacement and restores the stiffness when the isolated mass passes through equilibrium. Theoretical and experimental evidence was presented showing improved vibration control for lightly-damped systems.

The stability issues were discussed, and it was shown how a delay in the implementation of the strategy could lead to potential instabilities. The limiting value of permissible delay was calculated numerically and presented in the form of time histories showing the increase of amplitude due to energy cumulating. This phenomenon was not observed in the experimental rig, but it was shown experimentally how the inverted control law is indeed as unstable as the theory predicts. The development of an analytical study to predict the effect of delay is suggested for future work.

6. AKNOWLEDGEMENTS

The first author would like to acknowledge the Mexican Council of Science and Technology, CONACyT for the financial support given to develop this project, as well as Universidad Autonoma de Nuevo Leon.

REFERENCES

[1] Harris, C. M. and Crede, C. E. *Shock and Vibration Handbook*, McGraw-Hill, New York, (1996).

[2] Ledezma, D. F., Ferguson, N. S., and Brennan, M. J. Shock performance of different semi-active damping strategies, *Journal of Applied Research and Technology*, **8** (2), 249–259, (2010).

[3] Waters, T. P., Hyun, Y., and Brennan, M. J. The effect of dual-rate suspension damping on vehicle response to transient road inputs, *Transactions of the ASME, Journal of Vibration and Acoustics*, **131** (1), (2009). http://dx.doi.org/10.1115/1.2980370.

[4] Winthrop, M. F., Baker, W. P., and Cobb, R. G. A variable stiffness device selection and design tool for lightly damped structures, *Journal of Sound and Vibration*, **287** (4–5), 667–682, (2005). http://dx.doi.org/10.1016/j.jsv.2004.11.022.

[5] Onoda, J., Endo, T., Tamaoki, H., and Watanabe, N. Vibration suppression by variable-stiffness members, *AIAA Journal*, **29** (6), 977–983, (1991). http://dx.doi.org/10.2514/3.59943.

[6] Chen, J. C. Response of large spacecraft structures with stiffness control, *Journal of Spacecrafts and Rockets*, **21** (5), 163–167, (1984). http://dx.doi.org/10.2514/3.25681.

[7] Jabbari, F. and Bobrow, J. E. Vibration suppression with a resettable device, *Journal of Engineering Mechanics*, **128** (9), 916–924, (2002). http://dx.doi.org/10.1061/(ASCE)0733-9399(2002)128:9(916).

[8] Leavitt, J. L., Jabbari, F., and Bobrow, J. E. Optimal performance of variable stiffness devices for structural control, *ASME Journal of Dynamic Systems, Measurement and Control*, **129** (2), 171–177, (2007). http://dx.doi.org/10.1115/1.2432360.

[9] Ledezma-Ramirez, D. F., Ferguson, N. S., and Brennan, M. J. Shock isolation using an isolator with switchable stiffness, *Journal of Sound and Vibration*, **330** (5), 868–882, (2011). http://dx.doi.org/10.1016/j.jsv.2010.09.016.

[10] Ledezma-Ramirez, D. F., Ferguson, N. S., and Brennan, M. J. An experimental switchable stiffness device for shock isolation, *Journal of Sound and Vibration*, **331** (23), 4987–5001, (2012). http://dx.doi.org/10.1016/j.jsv.2012.06.010.

[11] Haiyan, H. On dynamics in vibration control with time delay, *Journal of Vibration Engineering*, **3**, (1997).

[12] Gu, K. and Niculescu, S. I. Survey on recent results in the stability and control of time-delay systems, *Journal of Dynamic Systems, Measurement, and Control*, **125** (2), 158–165, (2003). http://dx.doi.org/10.1115/1.1569950.

[13] Ogata, K. *Modern Control Engineering*, Prentice-Hall, New Jersey, (1990).

Vibroacoustic Analysis and Response Suppression of a Rectangular Sandwich Electrorheological Panel

Seyyed M. Hasheminejad, S. M. Parvasi and A. Fadavi-Ardakani

Acoustics Research Laboratory, Center of Excellence in Experimental Solid Mechanics and Dynamics, School of Mechanical Engineering, Iran University of Science and Technology, Narmak, Tehran 16844 Iran

(Received 19 February 2014; accepted 17 January 2015)

A modal summation method based on far-field sound intensity is used to study the average radiation efficiency and the corresponding radiation power of a point-excited, simply-supported, rectangular sandwich plate containing a tunable electrorheological fluid (ERF) core, and set in an infinite rigid baffle. In addition, a classical analytical procedure based on the Rayleigh integral equation method is adopted to investigate the sound transmission characteristics (TL) of the adaptive plate insonified by plane pressure waves at an arbitrary angle of incidence, or excited by a perfectly diffuse sound field with a Gaussian directional distribution of energy. Numerical results reveal the imperative influence of an applied electric field strength (0–3.5 kV/mm) on controlling acoustic radiation from (or sound transmission through) the smart panel in a wide frequency range. In addition, an effort is made to find the optimal electric field which yields improved sound radiation and transmission characteristics for each excitation frequency. Limiting cases are considered and good agreements with the solutions available in the literature used in this study are obtained.

1. INTRODUCTION

Plates are one of the most extensively used structural components in industrial applications. Many civil, industrial, and modern aerospace and aeronautical structures (*e.g.*, walls and floors, ship hulls, machine elements, and aircraft sidewalls) can be practically modelled, to a first approximation, as a finite baffled panel. Throughout the past few decades, vibroacoustic problems involving acoustic radiation from (or sound transmission through) finitely bounded isolated panel structures have been subject to intense research. In particular, numerous efforts have been concentrated on studying the sound radiation and transmission characteristics of rectangular plates with various complications since early 1960s.[1] Maidanik[2] was the first to apply the concept of power flow and statistical energy analysis to derive several approximate asymptotic expressions for calculating the modal radiation resistance in different wavenumber regions for a simply-supported, rectangular isotropic plate placed in an otherwise rigid co-planar baffle. Wallace[3] subsequently used the Rayleigh integral to derive analytical expressions for the modal radiation efficiency of a simply-supported baffled rectangular panel. Leppington, *et al.*[4] provided a detailed mathematical analysis of the modal radiation from a simply-supported panel, and used the assumption of high modal densities to revise some of Maidanik's results for large acoustic wavenumbers, especially in the ranges close to the critical frequency.

Roussos[5] developed an analytical procedure for an efficient solution of sound transmission through a rectangular, simply-supported, isotropic or symmetrically laminated composite plate in an infinite rigid baffle and under arbitrary plane wave incidence. Panneton and Atalla[6] used a three-dimensional finite element model coupled with a boundary element approach to predict the sound transmission loss through multi-layer structures made of elastic, acoustic, and poroelastic (Biot) media. Lee and Kondo[7] presented analytical and experimental studies of noise transmission loss of a three-layered simply-supported baffled rectangular plate with a viscoelastic core. Foin, *et al.*[8] proposed a variational model to analyse the vibroacoustic behaviour of a rectangular, baffled, simply-supported plate covered by a free or a constrained viscoelastic layer and immersed in either a light or a heavy fluid. Foin, et al.[9] investigated the vibroacoustic behaviour of an elastic, simply-supported rectangular plate covered by a locally reacting decoupling layer immersed in water and subjected to a point force disturbance. Sgard, *et al.*[10] employed the finite element method to predict sound-transmission loss across finite- sized, double-panel sound barrier with poroelastic linings. Berry, *et al.*[11] investigated the vibroacoustic response of a finite, simply-supported rectangular plate covered by a thick layer of decoupling material and immersed in a heavy fluid. Park, *et al.*[12] used the Rayleigh-Ritz method to investigate the effects of the support properties (stiffness and damping) on the forced vibration response and the associated radiated sound of viscoelastically supported rectangular plates.

Chiello, *et al.*[13] used a free-interface component mode synthesis technique associated with the finite element method to study the vibroaocoustic behaviour of an elastically-supported baffled plate excited by a plane wave or a diffuse field. Xie, *et al.*[14] used results from a modal summation method based on the farfield sound intensity to investigate the average radiation efficiency of point-excited baffled rectangular plates, including those with a very large aspect ratio (strips). Au and Wang[15] investigated sound radiation from forced vibration of rectangular orthotropic plates with general boundary conditions traversed by moving loads. Park and Mongeau[16] used the Mindlin plate theory and the Rayleigh-Ritz method to investigate the vibroacoustic characteristics of sandwich panels with viscoelastic supports. Assaf and Guerich[17] used a finite element formulation coupled to a boundary element method to predict noise transmission loss (TL) through viscoelastically-damped sandwich rectangular plates subjected to an acoustic plane wave or a diffuse sound field excitation.

Chazot and Guyader[18] used the so-called patch-mobility method to predict vibroacoustic behaviour of (or sound transmission through) double panels filled with porogranular materials. Assaf, *et al.*[19] presented a finite element formulation to analyse the vibroacoustic response of plates with a constrained-layer damping treatment immersed in a light or heavy fluid. Zhou and Crocker[20] used two different boundary element analyses to investigate the sound transmission characteristics of foam-filled honeycomb sandwich panels excited by a random incidence acoustic field. Loredo, *et al.*[21] used Rayleigh–Ritz's method for vibroacoustic analysis of baffled rectangular plates with constrained-layer damping (viscoelastic) patches. Li[21] studied active modal control of the vibroacoustic response of a fluid-loaded baffled rectangular plate using piezoelectric actuators and sensors and negative velocity feedback. He showed that the proposed method increases the modal damping ratio of the controlled mode and achieves notable reductions in the associated sound power and mean square velocity. Just recently, Kam, *et al.*[23] presented a semi-analytical approach based on the Rayleigh–Ritz method and the first Rayleigh integral for vibroacoustic analysis of elastically-restrained shear deformable stiffened rectangular orthotropic plates, and validated their results by carrying out experiments.

Vibration and sound radiation and transmission control of elastic structures is a crucial issue in many engineering systems, ranging from ground-based vehicles to machinery, civil structures, ships, aircrafts, aerospace vehicles, space-based platforms, and buildings. Two different approaches are normally used - passive control and active control. In the passive control approach, the material properties of the structure itself, such as damping and stiffness, are customized so as to modify the structural response. However, the material properties of such structures are preset in their design or construction stage, which can hardly be adapted to unanticipated environmental variations. Over the past few decades, intelligent materials such as piezoelectric materials, shape memory alloys, or electro- or magneto-rheological materials have been incorporated into conventional structures in order to adjust to the changes of the environment.[24,25] The latter materials have recently gained increasing recognition, as their rheological properties (damping and stiffness) can swiftly and reversibly be varied when subjected to an electrical field.[26]

Other valuable features of these materials include simplicity, compactness, low cost, low-energy loss, robustness, and easy controllability by computers,[27] which makes them an ideal methodology for noise and vibration control in various spheres of engineering. Consequently, numerous investigators have thoroughly studied the use of smart electro- or magneto-rheological-based structures for vibration control in various spheres of engineering.[28–32] There are, however, comparatively fewer authors who have investigated the sound radiation and insulation characteristics of these structures. Among them, Choi, *et al.*[33] formulated a fuzzy control logic on the basis of field-dependent sound pressure levels to experimentally investigate noise control of a rectangular closed cabin featuring one side of an ER fluid-based smart plate. Szary[34] examined the sound transmission loss for various kinds of electrorheological suspensions placed between two specially designed barriers under a variable alternative electric field density in a frequency range from 100 Hz to 2 kHz. Lu, *et al.*[35] experimentally studied the dynamic and acoustic characteristics of a sandwich cylindrical shell structure with an electrorheological fluid core, excited by an internal high frequency noise source. In a series of experimental investigations, Tang, *et al.*[36] devised sandwiched flexible electrorheological gel layers and studied the tunable behaviour of the transmitted sound-pressure levels with respect to the external electric field. More recently, Hasheminejad and Shabanimotlagh[37] employed the linear theory of elasticity in conjunction with the classical structural damping model, involving complex-valued field-dependent material constants, to develop a two-dimensional analytic solution for sound transmission control through an MRE-based adaptive sandwich infinite panel of arbitrary thickness.

The above review indicates that while there exists a notable body of literature on vibroacoustic characteristics of composite panels, rigorous analytical or numerical solutions for the sound radiation or transmission characteristics of finitely-bounded ERF-based sandwich structures seems to be absent. Thus, in this paper, we employ the equations of motion for a simply-supported ERF-filled rectangular sandwich plate,[38] the classical complex modulus approach for describing the viscoelastic behaviour of the ER core fluid,[31] the pertinent wave field expansions, and the modal summation method[14] along with the Rayleigh integral equation approach[1] to fill this gap. The proposed model is of noble interest, largely due to its inherent value as a canonical problem in structural acoustics. It can lead to further understanding of the acoustic behaviour of ER-material- based adaptive structures. It is also of practical value for noise control engineers involved in the development of reliable analytical and/or experimental tools for the design and analysis of ERF- based plates or panels with optimal acoustical characteristics.[33–37] Lastly, the presented analytical solution can serve as the benchmark for a comparison to solutions obtained by strictly numerical or asymptotic approaches.

2. FORMULATION

2.1. Governing Equations for the ERF Plate

The problem configuration is shown in Fig. 1. A sandwich rectangular plate ($a \times b$) consisting of a base plate (thickness h_3), a constraining layer (thickness h_1), and a tunable fluid core layer (thickness h_2), with simply-supported edge conditions, is considered. The skin layers are assumed to be cross-ply elastic composite laminates, with no slipping with respect to the core layer, and where identical transverse displacements are assumed at every point across the cross section for all three layers $w(x, y, t)$. Using Hamilton's principle, after some tedious manipulations, the displacement equations of motion for the ERF-sandwich plate can readily be obtained, as outlined in details in the work of Hasheminejad and Maleki.[38] To consider the steady state vibrational response of the simply-supported adaptive plate, one may advantageously assume a harmonic normal resultant force acting on the upper surface of the plate (e.g., see Fig. 1(a)) which, along with the relevant displacement components, can be expanded in double Fourier series as[39]

$$q(x,y,t) = q_0(x,y)e^{i\omega t} = \sum_{m=1}^{\infty}\sum_{n=1}^{\infty} q_{mn}\sin(\alpha_m x)\sin(\beta_n y)\,e^{i\omega t};$$
$$u_i(x,y,t) = \sum_{m=1}^{\infty}\sum_{n=1}^{\infty} U_{mn}^{(i)}\cos(\alpha_m x)\sin(\beta_n y)\,e^{i\omega t};$$
$$v_i(x,y,t) = \sum_{m=1}^{\infty}\sum_{n=1}^{\infty} V_{mn}^{(i)}\sin(\alpha_m x)\cos(\beta_n y)e^{i\omega t};$$
$$w(x,y,t) = \sum_{m=1}^{\infty}\sum_{n=1}^{\infty} W_{mn}\sin(\alpha_m x)\sin(\beta_n y)e^{i\omega t}; \quad (1)$$

where ω is the excitation frequency, $\alpha_m = m\pi/a$, $\beta_n = n\pi/b$, u_i and $v_i (i = 1,3)$ are the mid-plane deformations of the skin layers in the x and y directions, respectively, $U_{mn}^{(i)}$, $V_{mn}^{(i)} (i = 1,3)$ and W_{mn} are unknown modal coefficients, and $q_{mn} = \frac{4}{ab}\int_0^b\int_0^a q_0(x,y)sin(\alpha_m x)sin(\beta_n y)dxdy$ $(m,n = 1,2,3,...)$ are the Fourier coefficients associated with the harmonic distributed normal force of amplitude $q_0(x,y)$. By direct substitution of the displacement expansions in Eq. (1) into the governing equations of motion for the ERF plate (see Eq. 19 in Hasheminejad's and Maleki's work[38]), after some manipulations, one obtains (2) (see the top of the next page), where $i = 1,3$; $\delta_i = 1$ if $i = 1$; and $\delta_i = 1$ if $i = 3$, $\rho_i (i = 1,2,3)$ denotes the mass density in the i-th layer; $I_2 (= \rho_2 h_2^3/12)$ is the mass moment of inertia of the ER fluid interlayer; $G^{(2)}$ is the viscoelastic shear modulus of the ER fluid layer; $d = h_1/2 + h_2 + h_3/2$; and $\left(A_{jk}^{(i)}, B_{jk}^{(i)}, D_{jk}^{(i)}\right) = \int_{-h_i/2}^{h_i/2}(1, z_i, z_i^2)\overline{Q}_{jk}dz_i$ are the rigidity constants in which the indices j and k can be 1, 2, or 6; z_i is the transverse coordinate in the local coordinate system of the skin layers positioned at their associated mid-planes; and one should note that $B_{jk}^{(i)} = 0$ when the planes are symmetrically laminated with respect to their mid-plane. Besides, $\overline{Q}_{11}^{(i)} = \overline{Q}_{22}^{(i)} = \frac{E_i}{1-v_i^2}$, $\overline{Q}_{12}^{(i)} = \frac{v_i E_i}{1-v_i^2}$, and $\overline{Q}_{66}^{(i)} = \frac{E_i}{2(1+v_i)}$, where E_i and v_i are the Young modulus and Poisson ratio of the base and constraining layer, respectively. The equations of motion (2) can conveniently be written in a matrix form

$$\mathbf{Z}_{mn}\boldsymbol{\xi}_{mn} = \mathbf{q}_{\text{mn}}; \quad (3)$$

where $\boldsymbol{\xi}_{mn} = [U_{mn}^{(1)} \quad U_{mn}^{(3)} \quad V_{mn}^{(1)} \quad V_{mn}^{(3)} \quad W_{mn}]^T$, $\mathbf{q}_{mn} = [0 \quad 0 \quad 0 \quad 0 \quad q_{mn}]^T$, and the elements of the (5×5) coefficient matrix $\mathbf{Z}_{mn} = \mathbf{a}_{mn} + \omega^2\mathbf{b}_{mn}$ are given in the Appendix.

2.2. The Acoustic Radiation Problem

Let the simply-supported sandwich ERF plate be set in an infinite rigid baffle, and subjected to a harmonic point force excitation at point (x_0, y_0) with frequency ω, i.e. $q_0(x,y) = F_0\delta(x - x_0)\delta(y - y_0)$, where the associated Fourier coefficients are simply obtained as $q_{mn} = \frac{4}{ab}\int_0^b\int_0^a q_0(x,y)sin(\alpha_m x)sin(\beta_n y)dxdy = \frac{4F_0}{ab}sin(\alpha_m x_0)sin(\beta_n y_0)$ (see Fig. 1(a)). Also, the total acoustic power radiated from the adaptive plate can be determined by integrating the far-field sound intensity over a hemisphere of radius r to get[1]

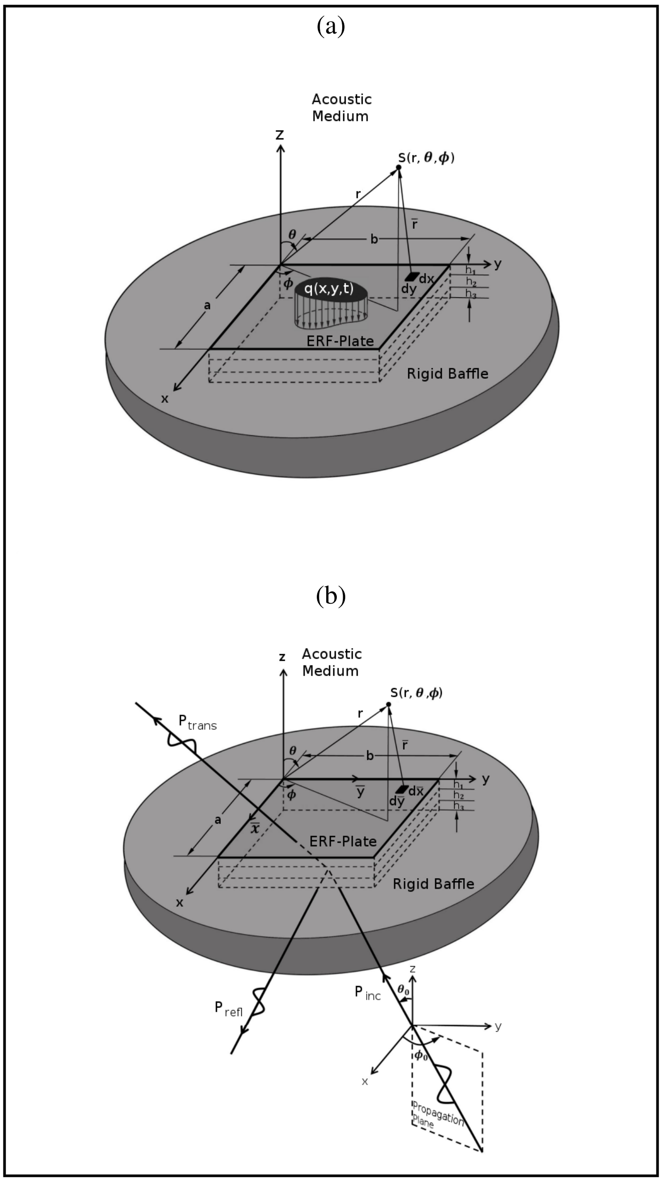

Figure 1. Problem geometry. (a) The acoustic radiation problem. (b) The sound transmission problem.

$$\Pi = \int_0^{2\pi}\int_0^{\pi/2}\frac{|P(r,\theta,\phi,t)|^2}{2\rho c}r^2\sin\theta \mathrm{d}\theta\mathrm{d}\phi; \quad (4)$$

where c is the speed of sound in the external acoustic fluid, and P is the complex acoustic pressure at location "S" in space, expressed in spherical coordinates (r,θ,π), which can be written in terms of the plate surface velocity through the well-known Rayleigh integral in the form[40]

$$P(r,\theta,\phi,t) = \int_0^a\int_0^b \frac{i\rho kc}{2\pi\,\overline{r}}\frac{\partial w(x,y,t)}{\partial t}e^{-ik\,\overline{r}}\mathrm{d}y\mathrm{d}x; \quad (5)$$

where $k = \omega/c$ is the acoustic wave number, $\overline{r}$ is the vector connecting a representative element of the plate (dx, dy) to the field point "S" (see Fig. 1a), and using Eq. (3) with $q_{mn} = \frac{4F_0}{ab}sin(\alpha_m x_0)sin(\beta_n y_0)$, the transverse plate velocity may be

$$\left(-\alpha_m^2 A_{11}^{(i)} - \beta_n^2 A_{66}^{(i)} + \rho_i h_i \omega^2\right) U_{mn}^{(i)} + \delta_i \left(-\frac{G^{(2)}}{h_2} + \frac{I_2\omega^2}{h_2^2}\right)\left(U_{mn}^{(1)} - U_{mn}^{(3)}\right) - \alpha_m\beta_n\left(A_{12}^{(i)} + A_{66}^{(i)}\right) V_{mn}^{(i)}$$
$$+ \left[\alpha_m^3 B_{11}^{(i)} + \alpha_m\delta_i\left(\frac{I_2 d\omega^2}{h_2^2} - \frac{G^{(2)}d}{h_2}\right) + \alpha_m\beta_n^2\left(B_{12}^{(i)} + 2B_{66}^{(i)}\right)\right] W_{mn} = 0;$$
$$\left(-\alpha_m^2 A_{66}^{(i)} - \beta_n^2 A_{22}^{(i)} + \rho_i h_i \omega^2\right) V_{mn}^{(i)} + \delta_i \left(-\frac{G^{(2)}}{h_2} + \frac{I_2\omega^2}{h_2^2}\right)\left(V_{mn}^{(1)} - V_{mn}^{(3)}\right) - \alpha_m\beta_n\left(A_{12}^{(i)} + A_{66}^{(i)}\right) U_{mn}^{(i)}$$
$$+ \left[\beta_n^3 B_{22}^{(i)} + \delta_i\beta_n\left(\frac{I_2 d\omega^2}{h_2^2} - \frac{G^{(2)}d}{h_2}\right) + \alpha_m^2\beta_n\left(B_{12}^{(i)} + 2B_{66}^{(i)}\right)\right] W_{mn} = 0;$$
$$\sum_{i=1,3}\left[\alpha_m^3 B_{11}^{(i)} + \alpha_m\beta_n^2\left(B_{12}^{(i)} + 2B_{66}^{(i)}\right) + \delta_i\alpha_m\left(-\frac{G^{(2)}d}{h_2} + \frac{I_2 d\omega^2}{h_2^2}\right)\right] U_{mn}^{(i)}$$
$$+ \sum_{i=1,3}\left[\alpha_m^2\beta_n\left(B_{12}^{(i)} + 2B_{66}^{(i)}\right) + \beta_n^3 B_{22}^{(i)} + \delta_i\beta_n\left(-\frac{G^{(2)}d}{h_2} + \frac{I_2 d\omega^2}{h_2^2}\right)\right] V_{mn}^{(i)}$$
$$+ \left\{\sum_{i=1,3}\left[-\alpha_m^4 D_{11}^{(i)} - 2\alpha_m^2\beta_n^2\left(D_{12}^{(i)} + 2D_{66}^{(i)}\right) - \beta_n^4 D_{22}^{(i)}\right] - \left(\alpha_m^2 + \beta_n^2\right)\left(\frac{G^{(2)}d^2}{h_2} - \frac{I_2 d^2\omega^2}{h_2^2}\right)\right.$$
$$\left. + \left(\rho_1 h_1 + \rho_2 h_2 + \rho_3 h_3\right)\omega^2\right\} W_{mn} = q_{mn}; \qquad (2)$$

written in the form

$$\frac{\partial w(x,y,t)}{\partial t} = \sum_{m=1}^{\infty}\sum_{n=1}^{\infty} u_{mn}\sin(\alpha_m x)\sin(\beta_n y)e^{\mathrm{i}\omega t}; \qquad (6)$$

in which $u_{mn} = \left(\frac{4i\omega F_0}{ab}\right)\psi(\omega)sin(\alpha_m x_0)sin(\beta_n y_0)$, where $\psi(\omega)$ is a complex (unknown) function of frequency that should be obtained by a numerical solution of the linear system of Eq. (3). Directly substituting Eq. (6) into (5), after some tedious manipulations, one obtains the final expression for the far-field acoustic pressure in the external fluid medium:[3]

$$P(r,\theta,\phi,t) = \sum_{m=1}^{\infty}\sum_{n=1}^{\infty} u_{mn}T_{mn}(r,\theta,\phi)\,e^{\mathrm{i}\omega t}; \qquad (7)$$

where

$$T_{mn}(r,\theta,\phi) = \frac{\mathrm{i}\rho kabc}{2\pi^3 mn}\left(\frac{e^{-\mathrm{i}kr}}{r}\right)\left[\frac{(-1)^m e^{\mathrm{i}\mu} - 1}{\left(\frac{\mu}{m\pi}\right)^2 - 1}\right]\left[\frac{(-1)^n e^{\mathrm{i}\chi} - 1}{\left(\frac{\chi}{n\pi}\right)^2 - 1}\right]; \qquad (8)$$

in which $\mu = ka\cdot sin\theta\cdot cos\phi$, and $\chi = kb\cdot sin\theta\cdot sin\phi$. Next, direct substitution of Eq. (7) into Eq. (4), leads to the expression for total radiated power from the adaptive plate due to the action of a harmonic point force at point (x_0, y_0) in the form Eq. (9) (see the top of the next page). Now, by considering the average of all possible locations of the uncorrelated point loads acting on the plate, the total averaged radiated power is defined as[14]

$$\overline{\Pi} = \frac{1}{ab}\int_0^a\int_0^b \Pi(x_0,y_0)\,dy_0 dx_0 = \sum_{m=1}^{\infty}\sum_{n=1}^{\infty}\overline{\Pi}_{mn}; \qquad (10)$$

where the modal components of the total averaged radiated power can be found by direct substitution of Eq. (9) into Eq. (10), after some manipulations, in the form[14]

$$\overline{\Pi}_{mn} = \overline{|u_{mn}|^2}\int_0^{2\pi}\int_0^{\pi/2}\frac{T_{mn}(r,\theta,\phi)\,T_{mn}^*(r,\theta,\phi)}{2\rho c}r^2\sin\theta\mathrm{d}\theta\mathrm{d}\phi; \qquad (11)$$

in which the cross-modal terms have been eradicated by using the classical orthogonality of transcendental eigenfunctions, and $\overline{|u_{mn}|^2}$, which is the modulus squared of the modal velocity amplitude averaged over all force positions, is derived in the form $\overline{|u_{mn}|^2} = \frac{1}{ab}\int_0^a\int_0^b u_{mn}u_{mn}^*\mathrm{d}y_0\mathrm{d}x_0 = \left(\frac{2F_0\omega}{ab}\right)^2\Psi_{mn}(\omega)\,\Psi^*{}_{mn}(\omega)$. Next, using Eq. (11), the modal radiation efficiency can be written as[14]

$$\sigma_{mn} = \frac{\overline{\Pi}_{mn}}{\frac{1}{2}\rho cab\overline{\langle v_{mn}^2\rangle}} = 4\int_0^{2\pi}\int_0^{\pi/2}\frac{T_{mn}(r,\theta,\phi)\,T_{mn}^*(r,\theta,\phi)}{(\rho c)^2 ab}r^2\sin\theta\mathrm{d}\theta\mathrm{d}\phi; \qquad (12)$$

where $\overline{\langle v_{mn}^2\rangle}$ represents the spatially-averaged modal mean square velocity, averaged over all possible force positions, obtained in the form

$$\overline{\langle v_{mn}^2\rangle} = \frac{1}{ab}\int_0^a\int_0^b|u_{mn}|^2\sin^2(\alpha_m x)\sin^2(\beta_n y)\mathrm{d}y\mathrm{d}x = \left(\frac{F_0\omega}{ab}\right)^2\Psi_{mn}(\omega)\,\Psi^*{}_{mn}(\omega). \qquad (13)$$

Direct substitution of Eq. (8) into right-hand side of Eq. (12), after some manipulations, leads to the final expression for the modal radiation efficiency in Eq. (14) (see the top of the next page). Thus, by using Eq. (12), the total average radiation efficiency of the plate is obtained in the final form

$$\sigma = \frac{\overline{\Pi}}{\frac{1}{2}\rho cab\overline{\langle v^2\rangle}} = \frac{\sum_{m=1}^{\infty}\sum_{n=1}^{\infty}\overline{\Pi}_{mn}}{\frac{1}{2}\rho cab\overline{\langle v^2\rangle}} = \frac{\sum_{m=1}^{\infty}\sum_{n=1}^{\infty}\sigma_{mn}\overline{\langle v_{mn}^2\rangle}}{\overline{\langle v^2\rangle}}; \qquad (15)$$

where $\overline{\langle v^2\rangle} = \sum_{m=1}^{\infty}\sum_{n=1}^{\infty}\overline{\langle v_{mn}^2\rangle}$ is the spatially-averaged mean square velocity of the plate. Here, it is noteworthy that because

$$\Pi\left(x_0, y_0\right)=\sum_{m=1}^{\infty} \sum_{n=1}^{\infty} \sum_{\bar{m}=1}^{\infty} \sum_{\bar{n}=1}^{\infty} u_{mn} u_{\bar{m}\bar{n}}^{*} \int_0^{2\pi} \int_0^{\pi/2} \frac{T_{mn}(r, \theta, \phi) T_{\bar{m}\bar{n}}^{*}(r, \theta, \phi)}{2 \rho c} r^2 \sin\theta \mathrm{d}\theta \mathrm{d}\phi; \tag{9}$$

$$\sigma_{mn}=\frac{64 k^2 a b}{\pi^6 m^2 n^2} \int_0^{\pi/2} \int_0^{\pi/2}\left\{\frac{\sin\left(\frac{\mu}{2}+\frac{m \pi}{2}\right) \sin\left(\frac{\chi}{2}+\frac{n \pi}{2}\right)}{\left[\left(\frac{\mu}{m \pi}\right)^2-1\right]\left[\left(\frac{\chi}{n \pi}\right)^2-1\right]}\right\}^2 \sin\theta \mathrm{d}\theta \mathrm{d}\phi. \tag{14}$$

of the averaging over all possible force locations (see Eq. (10)), the average radiation efficiency depends only on the self-modal radiation.

2.3. The Sound Transmission Problem

In this subsection, the transmission loss through the simply-supported rectangular sandwich ERF plate, subjected to an obliquely incident harmonic plane wave, P_{inc}, of amplitude p_0, and the incidence angle (θ_0, ϕ_0), as depicted in Fig. 1(b), is investigated. Also, P_{refl} and P_{trans} denote the reflected and transmitted pressure waves, respectively. These three pressure waves may be rewritten as the combination of the so-named blocked pressure (*i.e.*, the pressure on the incident side when the plate is regarded as a rigid wall) and the reradiated pressure (*i.e.*, the pressure exclusively due to the plate vibration). Making the standard assumption that the reradiated pressure is negligible compared to the blocked pressure in the equation of motion for the plate,[5] one can arrive at accurate solutions over a large frequency range, excluding the frequencies near the plate fundamental resonant frequency.

Adopting the three dimensional Cartesian coordinate system (x, y, z) (or equivalently the spherical coordinate system (r, θ, ϕ)) attached to the top surface of the plate for a point S in the far- field (see Fig. 1(b)), along with the two dimensional auxiliary coordinate system $(\overline{x}, \overline{y})$ referring to a point on the ERF plate, one can consider the equations of motion of the ERF plate (Eq. (2)) with the blocked pressure as the only forcing function in the form $q(\overline{x}, \overline{y}, t) = P_{inc}(\overline{x}, \overline{y}, t) + P_{refl}(\overline{x}, \overline{y}, t) - P_{trans}(\overline{x}, \overline{y}, t) \approx P_b(\overline{x}, \overline{y}, t)$, in which the blocked pressure P_b is generally assumed to be twice the incident pressure (i.e., $P_b(\overline{x}, \overline{y}, t) = 2P_{inc}(\overline{x}, \overline{y}, t)$).[5] Also, the incident travelling plane wave may be represented as in Eq. (16) (see the top of the next page),[41] where, with no loss of generality, the amplitude p_0 of the incident pressure is taken to be a real constant. Furthermore, the generalized modal amplitude of the transverse load due to the external forcing pressure may simply be obtained from $q\left(\bar{x}, \bar{y}, t\right) = 2P_{\text{inc}}\left(\bar{x}, \bar{y}, t\right) = \sum_{m=1}^{\infty}\sum_{n=1}^{\infty} q_{mn} \sin\left(\alpha_m \bar{x}\right) \sin(\beta_n \bar{y}) e^{\mathrm{i}\omega t}$, where $q_{mn} = 8p_0 \overline{I}_m \overline{I}_n$, in which $\underset{m}{\bar{I}} = \frac{m\pi\left[1-(-1)^m e^{-\mathrm{i}ka\sin\theta_0\cos\phi_0}\right]}{(m\pi)^2-[ka\sin\theta_0\cos\phi_0]^2}$, $\underset{n}{\bar{I}} = \frac{n\pi\left[1-(-1)^n e^{-\mathrm{i}kb\sin\theta_0\sin\phi_0}\right]}{(n\pi)^2-[kb\sin\theta_0\sin\phi_0]^2}$, The vibration of the plate causes the reradiated pressure to be transmitted by the plate. The Rayleigh integral is known to relate plate velocity to the transmitted pressure, *i.e.*,[40]

$$P_{\text{trans}}\left(r, \theta, \phi, t\right) = \int_0^a \int_0^b \frac{\mathrm{i}\rho k c}{2\pi \bar{r}} \frac{\partial w(\bar{x}, \bar{y}, t)}{\partial t} e^{-\mathrm{i}k\bar{r}} \mathrm{d}\bar{y} \,\mathrm{d}\bar{x}\,. \tag{17}$$

Here, noting that $r^2 = x^2 + y^2 + z^2, x = r \cdot sin\theta cos\phi$ and $y = r \cdot sin\theta sin\phi$, one can arrive at the useful expression $\overline{r} = r\sqrt{1 - 2\frac{sin\theta cos\phi}{r}\overline{x} - 2\frac{sin\theta sin\phi}{r}\overline{y} + \left(\frac{\overline{x}}{r}\right)^2 + \left(\frac{\overline{y}}{r}\right)^2}$ (see Fig. 1(b)). As a result, a closed form evaluation of the integral shown in Eq. (17) can be obtained in the far-field by using the approximations $1/\overline{r} \approx 1/r, (\overline{x}/r)^2 \to 0$ and $(\overline{y}/r)^2 \to 0$, leading to the following expression for the far-field transmitted pressure in (18) (see the top of the next page), where the transverse plate velocity may be expanded in the form

$$\frac{\partial w\left(\bar{x}, \bar{y}, t\right)}{\partial t} = \mathrm{i}\omega \sum_{m=1}^{\infty}\sum_{n=1}^{\infty} W_{mn} \sin\left(\alpha_m \bar{x}\right) \sin(\beta_n \bar{y}) e^{\mathrm{i}\omega t}. \tag{19}$$

Direct substitution of the expansion in Eq. (19) into the integral representation in Eq. (18), after some manipulations, leads to

$$P_{\text{trans}}\left(r, \theta, \phi, t\right) = \frac{-\omega^2 \rho a b}{2\pi r} \exp\left[\mathrm{i}\omega\left(t - \frac{r}{c}\right)\right] \sum_{m=1}^{\infty}\sum_{n=1}^{\infty} W_{mn} I_m I_n; \tag{20}$$

where $I_m = \frac{m\pi\left[1-(-1)^m e^{-\mathrm{i}ka\sin\theta\cos\phi}\right]}{(m\pi)^2-[ka\sin\theta\cos\phi]^2}$, $I_n = \frac{n\pi\left[1-(-1)^n e^{-\mathrm{i}kb\sin\theta\sin\phi}\right]}{(n\pi)^2-[kb\sin\theta\sin\phi]^2}$, Now, the total transmitted acoustic power, Π_{trans}, can be calculated by integrating the far-field transmitted intensity over a large hemisphere in the form[1]

$$\Pi_{\text{trans}} = \int_0^{2\pi}\int_0^{\pi/2} I_{\text{trans}} r^2 \sin\theta \mathrm{d}\theta \mathrm{d}\phi; \tag{21}$$

where the far-field transmitted intensity, I_{trans}, is given as the product of the far-field transmitted acoustic pressure and the complex conjugate of the far-field radial fluid particle velocity, $u_r = \frac{P_{trans}}{pc}$[5] which, by using the expansion shown in Eq. (20), reduces into

$$I_{\text{trans}} = \frac{1}{2}\mathrm{Re}\left[P_{\text{trans}} u_r{}^*\right] = \frac{\left|P_{\text{trans}}\left(r, \theta, \phi, t\right)\right|^2}{2\rho c} = \frac{\rho\omega^4 a^2 b^2}{8\pi^2 r^2 c}\left|\sum_{m=1}^{\infty}\sum_{n=1}^{\infty} W_{mn} I_m I_n\right|^2. \tag{22}$$

$$P_{\text{inc}}\left(\bar{x},\bar{y},t\right)=p_0\exp\left[\mathrm{i}\left(\omega t-k\,\bar{x}\sin\theta_0\cos\phi_0-k\,\bar{y}\sin\theta_0\sin\phi_0\right)\right];\tag{16}$$

$$P_{\text{trans}}\left(r,\theta,\phi,t\right)=\frac{\mathrm{i}\rho\omega}{2\pi r}\int_0^a\int_0^b\frac{\partial w(\bar{x},\bar{y},t)}{\partial t}\exp\left[-\mathrm{i}kr\left(1-\frac{\sin\theta\cos\phi}{r}\bar{x}-\frac{\sin\theta\sin\phi}{r}\bar{y}\right)\right]\mathrm{d}\,\bar{y}\,\mathrm{d}\,\bar{x};\tag{18}$$

Thus, the final expression for the total transmitted acoustic power can be found by simple substitution of Eq. (22) into Eq. (21) as

$$\Pi_{\text{trans}}=\int_0^{2\pi}\int_0^{\pi/2}\frac{\rho\omega^4a^2b^2}{8\pi^2c}\left|\sum_{m=1}^{\infty}\sum_{n=1}^{\infty}W_{mn}I_mI_n\right|^2\sin\theta\mathrm{d}\theta\mathrm{d}\phi;\tag{23}$$

Where, for a given $q_{mn}=8p_0\overline{I}_m\overline{I}_n$, the unknown displacement coefficients W_{mn} can readily be obtained from the linear system of Eq. (3). Finally, the acoustic transmission loss (TL) for the baffled ERF plate can be determined from

$$TL=10\log\left(\frac{1}{\tau}\right);\tag{24}$$

where $\tau=\Pi_{trans}/\Pi_{inc}$ is the transmission coefficient, and since the incident disturbance is a plane wave, the incident acoustic power, Π_{inc}, can simply be determined from the incident intensity multiplied by the area of the plate in the form[41]

$$\Pi_{\text{inc}}=\left(\frac{ab}{2\rho c}\right)p_0^2\cos\theta_0.\tag{25}$$

In the case of a diffuse sound field, Kang, *et al.*[42] introduced a directional weighting function for the incident energy, leading to accurate calculation of the plate transmission loss from $TL=10log(\frac{1}{\tau_d})$, where the angle-averaged diffuse-field transmission coefficient, $\tau_d(\omega)$, which takes into account the angular characteristic of incident energy, is defined as[43]

$$\tau_d\left(\omega\right)=\frac{\int_0^{2\pi}\int_0^{\pi/2}D\left(\theta,\phi\right)\tau\left(\theta,\phi,\omega\right)\sin\theta\cos\theta\mathrm{d}\theta\mathrm{d}\phi}{\int_0^{2\pi}\int_0^{\pi/2}D\left(\theta,\phi\right)\sin\theta\cos\theta\mathrm{d}\theta\mathrm{d}\phi};\tag{26}$$

in which $D(\theta,\phi)$ signifies the directional distribution of incident sound energy, which is generally taken to be of Gaussian form with zero mean and vertical symmetry of the incident energy, *i.e.*, $D(\theta,\phi)=e^{-\beta\theta^2}$, where $1\leq\beta\leq 2$ is a constant depending on measurement parameters such as frequency, facilities dimensions, geometry, source and microphone positions.[44] Here, it should be noted that, in many physical situations, the diffuse sound field can be a very practical approximation to the real sound field.[13,42–44]

3. NUMERICAL RESULTS

In order to illustrate the nature and general behaviour of the solution, we consider some numerical examples in this section. Noting the large quantity of parameters and the relatively intense computations involved here, while realizing the drawbacks in accessibility of experimental input data, our attention will be focused on a specific model. A square sandwich aluminium/ERF/aluminium panel of fixed length ($a=b=0.5$ m) with equal skin layer thicknesses ($h_1=h_3=0.0005$ m) set in an infinite rigid baffle is considered, while, the thickness of the ER layer is assumed to be twice that of each skin layer ($h_2=0.001$ m). The material parameters for the aluminium layers are selected as $\rho_1=\rho_3=2700$ kgm^3; $E_1=E_3=70$ GPa; $v_1=v_3=0.3$. Also, using the accessible information on the ER material pre-yield rheology, the electric field dependence of ER material in the pre-yield regime is considered. In particular, the complex modulus for a typical ER fluid is adopted from Yalcintas and Coulter's work[45] in the form

$$G^{(2)}\left(E\right)=G'\left(E\right)+\mathrm{i}G''\left(E\right);\tag{27}$$

where $G'(E)=50{,}000$ E^2 is the shear storage modulus, $G''(E)=2600$ E + 1700 is the loss modulus, and $0\leq E(t)\leq 3.5$ kV/mm is the electric field strength. Also, $\rho_2=1700$ kg/m^3 is the mass density of the ER fluid. In addition, the surrounding fluid medium is assumed to be air at atmospheric pressure and ambient temperature ($\rho=1.2$ kg/m^3, $c=340$ m/s).

A Mathematica code was constructed for treating the linear system of Eq. (3), solving for the unknown transverse modal displacement coefficients W_{mn} as functions of the incident wave angles and frequency (or external loading frequency in the radiation problem) as well as the electric field magnitude, and ultimately calculating the spatially-averaged mean square velocity of the plate, $\overline{\langle v^2\rangle}$, the total average radiation efficiency, σ , and the acoustic transmission loss, TL, for the above selected geometric parameters. Also, the value of the exponential parameter, $\beta=2$, is selected for a perfectly diffuse sound field,[44] and the integrals in Eqs. (23) and (26) were numerically evaluated using the Mathematica built-in function "NIntegrate." The convergence of results was systematically checked in a simple trial-and-error manner, by increasing the truncation constants in the Fourier expansions, while looking for steadiness or stability in the numerical value of the solutions. Using a maximum number of thirty modes, ($m_{max}=n_{max}=30$) was found to yield satisfactory results for the selected geometric parameters in all loading situations.

Before presenting the main numerical results, we shall briefly check the overall validity of the work. To do this, we first used our general "sound transmission" Mathematica code to compute the sound transmission loss for a three-layered aluminium-ERF-aluminium plate (with its physical properties as given in Table 1), under a selected electric field strength ($E=0.5$ kV/mm) and incidence angles ($\theta_0=\phi_0=60°$), as shown in the first subplot of Fig. 2(a). Furthermore, we used our general "sound radiation" Mathematica code to compute the mean square velocity, $\overline{\langle v^2\rangle}$, for the three-layered adaptive plate, under a selected electric field strength ($E=0.5$ kV/mm) and for a unit amplitude harmonic load ($F_0=1$), as shown in the second subplot of Fig. 2(a). It is clear that the ERF plate resonance frequencies show up as dips in the Transmis-

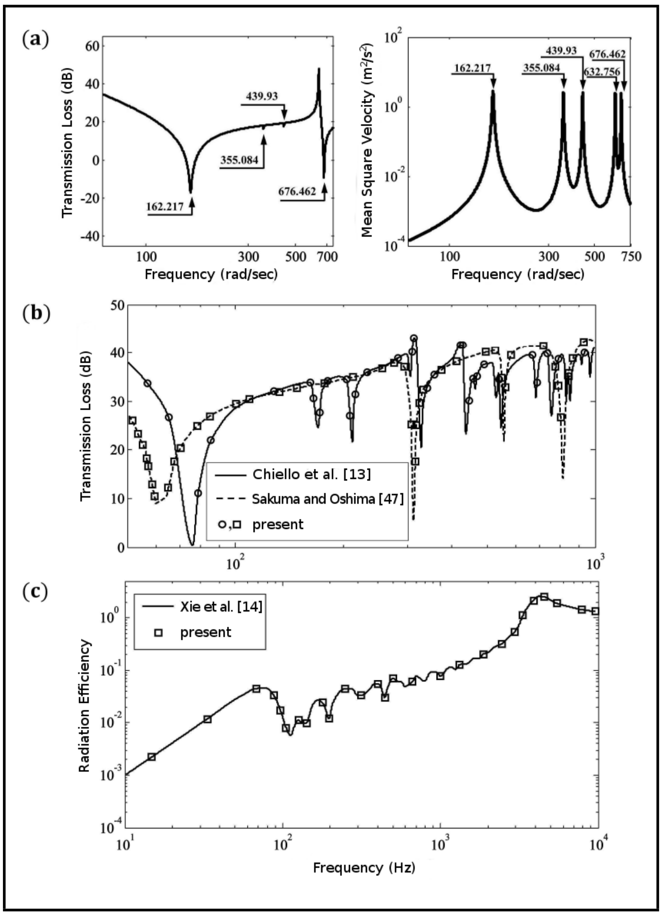

Figure 2. (a) Sound transmission loss and mean square velocity spectrum for a three-layered aluminium-ERF-aluminium plate under selected electric field strength ($E = 0.5$ kV/mm) and incidence angles ($\theta_0 = \phi_0 = 60°$; $F_0 = 1$). (b) Comparison of the calculated sound transmission loss of a single-layer panel with those available in the literature. (c) Comparison of the calculated radiation efficiency of a single-layer panel with that available in the literature.

sion Loss (TL) subplot and peaks in the mean square velocity subplot, as marked in the figures, and demonstrate very good agreements with the natural frequencies displayed in Fig. 5 of the work of Yeh and Chen,[46] which were obtained by means of the finite element method. As a further verification, we let the bottom and midlayer thickness values of the adaptive plate approach zero ($h_2 = h_3 \approx 0$) in our general "sound transmission" code, and calculated the Transmission Loss (TL) spectra for normal incidence as well as for the diffuse case ($D(\theta, \phi) = 1$) for single-layered aluminium plates with their physical properties, as shown in Table 2. The outcome, as displayed in Fig. 2(b), shows very good agreement with the Transmission Loss (TL) data presented in Figs. 3 and 6 in the works of Chiello, Sgard, and Atalla[13] and Sakuma and Oshima,[47] respectively. Lastly, we let the bottom and mid-layer thickness values approach zero in our general "sound radiation" code, and calculated the average radiation efficiency, σ, for a single-layered aluminium plate with its physical properties as given in Table 3. The outcome, as shown in Fig. 2(c) shows excellent agreement with the data presented in Fig. 3 of the study conducted by Xie, Thompson, and Jones.[14]

Figure 3 shows the variation of sound transmission loss (TL) with incident wave frequency for selected angles of incidence ($\theta_0 = 0$, 45, 80; $\phi_0 = 0$, 45°), and for applied electric field strengths (E = 0, 1, 2, 3.5 kV/mm). Also shown are the TL spectra calculated for the ERF panel in a perfectly diffuse

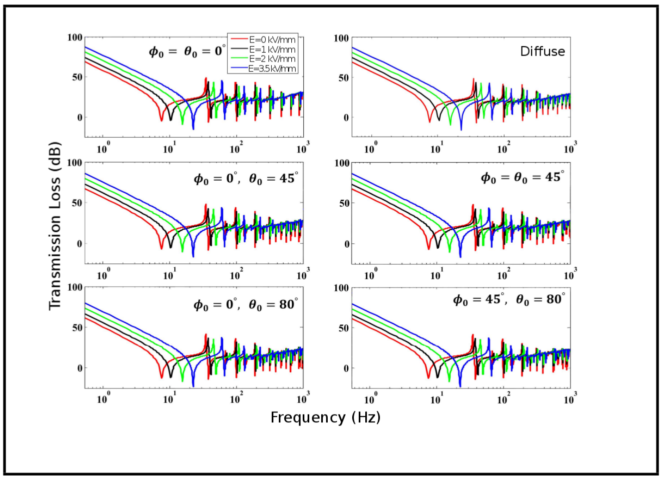

Figure 3. Variation of sound transmission loss with incident wave frequency for selected angles of incidence (including the perfectly diffuse situation) and applied electric field strengths.

Table 1. Input physical properties used for the verification example presented in Fig. 2(a).

$a = 0.3$ m
$b = 0.25$ m
$h_1 = 0.00005$ m
$h_2 = h_3 = 0.0005$ m
$E_1 = E_3 = 70$ GPa
$v_1 = v_3 = 0.3$
$\rho_1 = \rho_3 = 2700$ kg/m^3
$\rho = 1.2$ kg/m^3
$c = 340$ m/s
$\theta_0 = \phi_0 = 60°$
$E = 0.5$ kV/mm

Table 2. Input physical properties used for the verification examples presented in Fig. 2(b).

Chiello, Sgard, and Atalla[13]
$a = 0.48$ m
$b = 0.4$ m
$h_1 = 0.003$ m
$h_2 = h_3 = 3\times10^{-7}$ m
$E_1 = E_3 = 200(1+0.01i)$ GPa
$v_1 = v_3 = 0.3$
$\rho_1 = \rho_3 = 7800$ kg/m^3
$\rho = 1.2$ kg/m^3
$c = 340$ m/s
$E = 0$ kV/mm
Sakuma and Oshima[47]
$a = b = 0.9$ m
$h_1 = 0.01$ m
$h_2 = h_3 = 10^{-6}$ m
$E_1 = E_3 = 75(1+0.002i)$ GPa
$v_1 = v_3 = 0.22$
$\rho_1 = \rho_3 = 2500$ kg/m^3
$\rho = 1.2$ kg/m^3
$c = 340$ m/s
$\theta_0 = \phi_0 = 0°$
$E = 0$ kV/mm

Table 3. Input physical properties used for the verification example presented in Fig. 2(c).

$a = 0.5$ m
$b = 0.6$ m
$h_1 = 0.003$ m
$h_2 = h_3 = 3\times10^{-7}$ m
$E_1 = E_3 = 71(1+0.1i)$ GPa
$v_1 = v_3 = 0.3$
$\rho_1 = \rho_3 = 2700$ kg/m^3
$\rho = 1.2$ kg/m^3
$c = 340$ m/s
$E = 0$ kV/mm

sound field. The most important observations are as follows: The application of the electric field appears to have an appreciable effect on sound transmission, especially in the very low frequency range ($f < 30$ Hz). In particular, increasing the electric field strength at such low frequencies leads to a distinct monotonic increase in the TL amplitudes, nearly regardless of the angle of incidence. This may clearly be linked to the increase in the overall structural stiffness of the system in the so-named stiffness controlled region.[1] As the incident wave frequency increases, the effect of the electric field gradually decreases, especially for the case of normal incidence, where there is minimum shear effect induced in the ERF core layer. In the very high frequency range ($f > 1000$ Hz), increasing the electric field has a small effect on the TL amplitudes for all angles of incidence. This is perhaps due to the fact that at such high frequencies, the plate inertia effects overwhelms the electric field effects.

Also, it is well known that the incidence angle has a notable effect on the excitation of panel vibrational modes. In the case of normal incidence, the sound pressure imposed on the panel is uniform, and thus only the odd-odd panel modes are expected to be excited (to transmit sound power). Furthermore, in the case of oblique incidence with the incident wave traveling parallel to the x-axis (*i.e.*, for $\phi_0 = 0°$), the radiated power for even-even or odd-even modes of the panel is rather small, and the resonance dips in the calculated TL take place at the resonance frequencies whose y-axis mode numbers are odd. Likewise, the resonance dips in the calculated TL for incident waves travelling parallel to the y-axis (i.e., for $\phi 0 = 90°$) happen at the resonance frequencies whose x-axis mode numbers are odd. Keeping the above discussion in mind, one can readily see from Fig. 3 that for non-normal incident wave fields, many more plate resonance frequencies get involved (note the numerous dips appearing in the sub-figures), as either the inclination angle, θ_0, or the azimuth angle, ϕ_0, increases, nearly regardless of the electric field strength. Moreover, the smallest TL levels are observed in case of the near-grazing ($\theta_0 = 80°$) incident wave field, while decreasing the inclination angle, θ_0, has a slight amplification effect on the panel sound transmission loss, especially at low incident wave frequencies (thus, the largest overall TL levels are observed in case of the normally incident, or $\theta_0 = 0°$, sound field). The TL curves for the perfectly diffuse or random sound field behave rather differently, recalling that a diffuse sound field superposes a series of equal-amplitude uncorrelated progressive plane waves, with all directions of sound propagation arising with the same probability, and the phase relations of the waves being arbitrary at any given point in space.[42–44]

In particular, in the low frequency region ($f < 100$ Hz), the TL levels associated with the diffuse field are very close to those of the normally incident ($\theta_0 = 0°$) case, where mainly the uniform odd-odd panel modes seem to be excited. In the higher frequency range ($f > 100$ Hz), on the other hand, the TL curves of the diffuse sound field behave very similarly to those of the near-grazing ($\theta_0 = 80°$) incident sound field, where the appearance of the numerous dips indicate that increasingly more panel resonance frequencies get involved (*i.e.*, sound transmission is mainly controlled by panel resonant effects[48]). This similarity in the sound transmission characteristics of the diffuse and near-grazing incidence problems can also be observed in Fig. 5 of the work of Schiller and Beck.[49] Therefore, in the mid- to high-frequency range, it may be sufficient to use the near-grazing incidence TL with an acceptable error (or with a correction factor) in order to predict the diffuse field transmission loss, nearly regardless of the electric field strength.

At each incident wave frequency, there is only one electric field level which leads to a maximum or a minimum transmission loss amplitude, denoted here by E_{max} (kV/mm) or E_{min} (kV/mm), respectively. The left column in Fig. 4 displays the variations in sound transmission loss (TL) amplitude with the incident wave frequency associated with such electric field strengths, for the adaptive plate under selected angles of incidence ($\theta_0 = 45°$; $\phi_0 = 0, 45°$) as well as for the perfectly diffuse field (note that the TL associated with the $E = 0$ kV/mm case is also shown in the figure by black lines). Moreover, the right column of Fig. 4 depicts the frequency spectrums of the corresponding input electric field amplitudes required for maximizing or minimizing sound transmission loss. The most important observations are as follows: Perfect coincidence of the black curves ($E = 0$) with the blue curves ($E = E_{min}$) in the entire low frequency range (*i.e.*, in the stiffness-controlled region) as well as in some relatively small frequency patches in the moderate and high frequency range leads to the important conclusion that maintaining a null electric field level (*i.e.*, keeping the panel stiffness low) can significantly deteriorate the sound transmission performance of the ERF-based plate, primarily in the low frequency range.

In other words, it is clear that inappropriate application of the electric field (*e.g.*, note the blue curves associated with $E = E_{min}$) may even lead to minimum sound transmission loss levels in a wide frequency range. The most interesting observation is perhaps the fact that by selecting $E = E_{max}$ (*i.e.*, the red colored curves), one can advantageously avoid the commonly occurring sharp (resonant) dips in the uncontrolled ($E = 0$) or non-optimally controlled ($E \neq E_{max}$) adaptive structure, leading to maximum transmission loss in the entire frequency range, nearly irrespective of incident wave direction. Moreover, the maximum or minimum electrical field pattern (shown in the second column of the figure) resembles a repeating ramp type curve, while the effect of incident wave direction on the electric field strength is not very prominent. Furthermore, repeated zones of a null electric field ($E = 0$ kV/mm) are observed in the entire frequency range, which are associated with either a maximum or a minimum sound transmission loss level. Thus, one can conversely conclude that applying a non-zero electric field (*i.e.*, increasing the structural stiffness and damping), does not necessarily lead to an improvement in the system's sound transmission characteristics.

Figures 5(a) and (b) show the variation of total average radiation efficiency, σ, as well as the average mean square velocity, $\overline{\langle v^2 \rangle}$, with the external load frequency ($F_0 = 1$ N), for selected applied electric field strengths ($E = 0$, 1, 2, 3.5 kV/mm). The most important observations are as follows: While the electric field strength has little or nearly no effect on the average radiation efficiency spectrum at low and high frequency ends (Fig. 5(a)), it is of significant influence on the average mean square velocity in the entire frequency range (Fig. 5(b)). In particular, the electric field seems to be of major consequence on the radiation efficiency only in the intermediate frequency range (*i.e.*, increasing the electric field strength has a notable

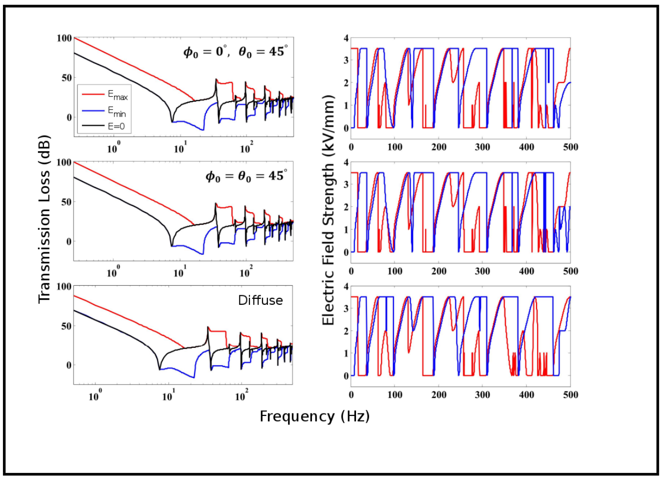

Figure 4. Calculated maximum and minimum sound transmission loss spectrums for selected angles of incidence (including the perfectly diffuse field) along with the associated applied electric fields.

amplification effect on the sandwich plate radiation efficiency roughly in the range of $10 < f < 100$ Hz; see Fig. 5(a)). This may be explained by comparison with Fig. 5(b), where it is clear that increasing the electric field level (increasing or decreasing the overall system stiffness and displacement amplitudes) leads to a notable rightward shift in the resonance frequencies of an adaptive plate (*i.e.*, the peaks in the mean square velocity curves) to the higher frequency range (see Hasheminejad and Maleki[38]).

Moreover, there is a notable decrease in the oscillation amplitude of the mean square velocity curves with increasing the electric field strength towards $E = 3.5$ kV/mm (or increasing overall system stiffness) at intermediate and low frequencies, which may be linked to the overall decrease in the system kinetic energy. Thus, one may conclude that while direct application of an electric field can perceptibly influence the radiation efficiency of an adaptive panel in the intermediate frequency range, it can effectively reduce the average mean square velocity in the entire frequency range. Lastly, as the excitation frequency further increases, approaching the system critical frequency ($f_c = \omega_c 2\pi \approx 11.9$ kHz; as observed from Fig. 5(a)), the occurrence of 'edge' modes dominate the so-called corner modes,[1] and the electric field strength almost entirely loses its effect on the sound radiation efficiency, which gradually increases towards its maximum level slightly beyond the critical frequency and then makes a small drop towards the asymptotic value of unity.[43]

As in the case of the previously discussed sound transmission problem (see Fig. 4), at each excitation frequency there is only one electric field level which causes a maximum or minimum average radiation efficiency or a maximum or minimum mean square velocity, denoted here by $E^{\sigma}_{max}/E^{\sigma}_{min}$ kV/mm or E^{v}_{max}/E^{v}_{min} kV/mm, respectively. The left column in Fig. 6 displays the variations in the total average radiation efficiency, σ, as well as the average mean square velocity, $\langle\overline{v^2}\rangle$, with the excitation frequency associated with such electric field strengths (note that the results associated with the $E = 0$ kV/mm case are also shown in the subplots by black lines). Moreover, the right column of Fig. 6 depicts the frequency spectrums of the corresponding electric field amplitudes calculated for maximizing or minimizing the average radiation efficiency or the mean square velocity. Here, the nearly

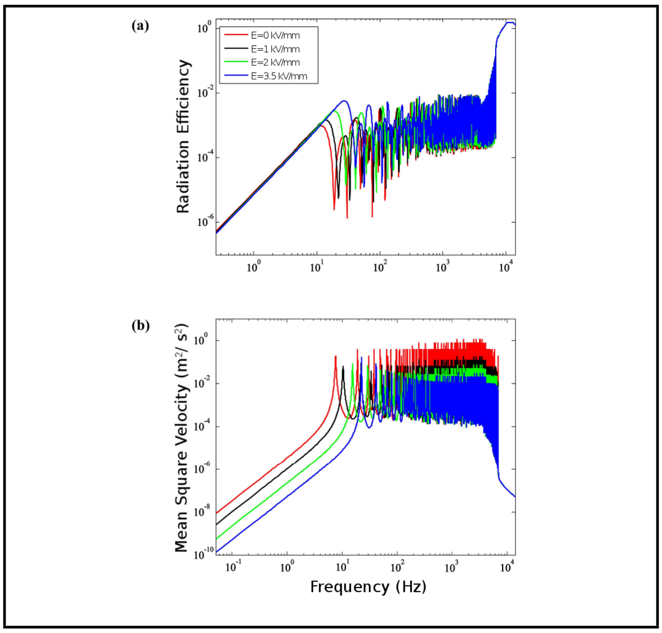

Figure 5. (a) Variation of the total average radiation efficiency with the external load frequency for selected applied electric field strengths. (b) Variation of the average mean square velocity with the external load frequency for selected applied electric field strengths.

perfect coincidence of the black curve ($E = 0$) with the red and blue curves ($E = E^{\sigma}_{min,max}$) in the entire low frequency range (*i.e.*, in the stiffness-controlled region) once again leads to the important conclusion that the electric field level has nearly no effect on the sound radiation performance of the ERF-based plate in the low frequency range.

Furthermore, almost perfect coincidence of the maximum mean square velocity ($E = E^{v}_{max}$ or the red) curve with that of the null field ($E = 0$ or the black curve) in the low frequency range demonstrates that decreasing the electric field strength (system stiffness) leads to a natural increase in the system mean square velocity. Also, it is clear that as in the case of the sound transmission problem (Fig. 4), inappropriate application of the electric field may deteriorate sound radiation efficiency in a wide frequency range (*i.e.*, note the blue curve associated with $E = E^{\sigma}_{min}$. Another interesting observation is the fact that by selecting $E = E^{\sigma}_{max}$ or $E = E^{v}_{max}$ (*i.e.*, the red colored curves), one can respectively avoid the commonly occurring sharp dips or peaks in the uncontrolled or non-optimally controlled adaptive structure, leading to maximum radiation efficiency (or mean square velocity) in the entire frequency range.

4. CONCLUSIONS

The three-dimensional sound radiation and transmission control from and through an electrorheological fluid-based rectangular sandwich plate, set in an infinite rigid baffle, and subjected to a periodic transverse excitation or an arbitrary incident plane wave, is considered in this study. The problem solution is based on the equations of motion for a simply-supported ERF-based plate, the classical complex modulus approach for the viscoelastic behaviour of ER core fluid, the pertinent wave field expansions, and the modal summation method along with the Rayleigh integral equation approach. Special attention is paid to the influence of electric field strength, incident wave angle (including the perfectly diffuse

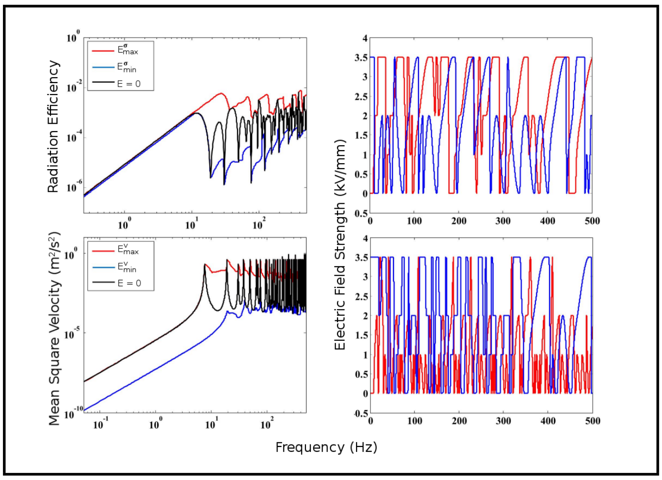

Figure 6. Calculated maximum and minimum average radiation efficiency and mean square velocity spectrums along with the associated applied electric fields.

situation) and excitation frequency on the sound transmission and radiation characteristics of the adaptive panel. The most important observations regarding the sound transmission and radiation problem are respectively summarized in the following two paragraphs.

Increasing the electric field strength at very low incident wave frequencies (*i.e.*, in the stiffness controlled region) leads to a distinct monotonic increase in the sound transmission amplitudes, nearly regardless of angle of incidence, caused by the increase in the overall structural stiffness of the system. As the incident wave frequency increases, the electric field effect gradually decreases, especially in cases of normal incidence, where there is minimum shear effect induced in the ERF core layer. In the very high frequency range ($f > 1000$ Hz), the plate inertia effects dominate the electric field effects and the electric field level is observed to have a small influence on the sound transmission loss, almost regardless of the angle of incidence. In case of normal incidence, only the odd-type plate modes are observed to get excited, while for oblique incidence (non-zero inclination angle), even-type modes can also get involved, the extent of which depends on the azimuth angle. Also, as the oblicity of the incident wave increases, the sound transmission loss amplitudes generally decrease, nearly regardless of the electric field strength, especially at high incident wave frequencies. In particular, the largest TL levels are found in case of the normally incident sound field.

Furthermore, in the low frequency range, the TL levels associated with the diffuse sound field are observed to be very close to those of the normally incident case, while the panel resonant effects dominate at higher frequencies, and the TL curves of the diffuse field behave very similarly to those of the near-grazing incidence situation. Therefore, in order to approximate the diffuse field transmission loss with an acceptable error in the mid- to high-frequency range, it may be sufficient to use the near-grazing incidence TL, nearly regardless of the electric field strength. Lastly, maintaining a null electric field level is shown to significantly deteriorate the sound transmission performance of the ERF-based plate, primarily in the low frequency range, while applying a non-zero electric field does not necessarily lead to an improvement in the system's overall sound transmission characteristics.

The electric field strength has little or nearly no effect on the average radiation efficiency spectrum at low and high frequency ends, while it can effectively reduce the average mean square panel velocity in the entire frequency range. In particular, increasing the electric field strength is demonstrated to have a notable amplification effect on the adaptive plate radiation efficiency in the intermediate frequency region ($10 < f < 100$ Hz). It also causes a notable rightward shift in the resonance frequencies appearing in the mean square velocity plot of the adaptive plate in addition to a general drop in velocity amplitudes. As the excitation frequency approaches the system critical frequency, the occurrence of 'edge' modes dominate the so-called corner modes, and the electric field strength almost entirely losses its effect on the system sound radiation efficiency, which gradually increases towards its maximum level slightly beyond the critical frequency and then makes a small drop towards the asymptotic value of unity. Lastly, by adopting the optimal electric field strength, one can advantageously avoid the commonly occurring sharp resonant peaks and dips in the radiation spectrum of the uncontrolled or non-optimally controlled adaptive structure, resulting in major improvements in the system's overall sound radiation characteristics. It is hoped that the present study will provide designers the basic information required in practical noise control applications of ER fluid-embedded smart structures.

APPENDIX

$$
\begin{aligned}
a_{mn}^{11} &= -\alpha_m^2 A_{11}^{(1)} - \beta_n^2 A_{66}^{(1)} - G^{(2)}/h_2,\\
a_{mn}^{12} &= G^{(2)}/h_2,\\
a_{mn}^{13} &= -\alpha_m\beta_n \left(A_{12}^{(1)} + A_{66}^{(1)}\right),\\
a_{mn}^{14} &= 0,\\
a_{mn}^{15} &= \alpha_m^3 B_{11}^{(1)} - \alpha_m G^{(2)} d/h_2 + \alpha_m\beta_n^2 \left(B_{12}^{(1)} + 2B_{66}^{(1)}\right),\\
a_{mn}^{21} &= G^{(2)}/h_2,\\
a_{mn}^{22} &= -\alpha_m^2 A_{11}^{(3)} - \beta_n^2 A_{66}^{(3)} - G^{(2)}/h_2,\\
a_{mn}^{23} &= 0,\\
a_{mn}^{24} &= -\alpha_m\beta_n \left(A_{12}^{(3)} + A_{66}^{(3)}\right),\\
a_{mn}^{25} &= \alpha_m^3 B_{11}^{(3)} + \alpha_m G^{(2)} d/h_2 + \alpha_m\beta_n^2 \left(B_{12}^{(3)} + 2B_{66}^{(3)}\right),\\
a_{mn}^{31} &= -\alpha_m\beta_n \left(A_{12}^{(1)} + A_{66}^{(1)}\right),\\
a_{mn}^{32} &= 0,\\
a_{mn}^{33} &= -\alpha_m^2 A_{66}^{(1)} - \beta_n^2 A_{22}^{(1)} - G^{(2)}/h_2,\\
a_{mn}^{34} &= G^{(2)}/h_2,\\
a_{mn}^{35} &= \alpha_m^2\beta_n \left(B_{12}^{(1)} + 2B_{66}^{(1)}\right) + \beta_n^3 B_{22}^{(1)} - \beta_n G^{(2)} d/h_2,\\
a_{mn}^{41} &= 0,\\
a_{mn}^{42} &= -\alpha_m\beta_n \left(A_{12}^{(3)} + A_{66}^{(3)}\right),\\
a_{mn}^{43} &= G^{(2)}/h_2,\\
a_{mn}^{44} &= -\alpha_m^2 A_{66}^{(3)} - \beta_n^2 A_{22}^{(3)} - G^{(2)}/h_2,\\
a_{mn}^{45} &= \alpha^2\beta_n \left(B_{12}^{(3)} + 2B_{66}^{(3)}\right) + \beta_n^3 B_{22}^{(3)} + \beta_n G^{(2)} d/h_2,\\
a^{51_{mn}} &= \alpha_m^3 B_{11}^{(1)} + \alpha_m\beta_n^2 \left(B_{12}^{(1)} + 2B_{66}^{(1)}\right) - \alpha_m G^{(2)} d/h_2,\\
a_{mn}^{52} &= \alpha_m^3 B_{11}^{(3)} + \alpha_m\beta_n^2 \left(B_{12}^{(3)} + 2B_{66}^{(3)}\right) + \alpha_m G^{(2)} d/h_2,\\
a_{mn}^{53} &= \alpha_m^2\beta_n \left(B_{12}^{(1)} + 2B_{66}^{(1)}\right) + \beta_n^3 B_{22}^{(1)} - \beta_n G^{(2)} d/h_2,\\
a_{mn}^{54} &= \alpha_m^2\beta_n \left(B_{12}^{(3)} + 2B_{66}^{(3)}\right) + \beta_n^3 B_{22}^{(3)} + \beta_n G^{(2)} d/h_2,
\end{aligned}
$$

$$a^{55}_{mn} = -\alpha^4_m \left(D^{(1)}_{11} + D^{(3)}_{11}\right) + \\ -2\alpha^2_m\beta^2_n \left(D^{(1)}_{12} + D^{(3)}_{12} + 2D^{(1)}_{66} + 2D^{(3)}_{66}\right) \\ -\beta^4_n \left(D^{(1)}_{22} + D^{(3)}_{22}\right) - \left(\alpha^2_m + \beta^2_n\right) G^{(2)} d^2/h_2,$$

and

$$b^{11}_{mn} = \rho_1 h_1 + I_2/h^2_2,$$
$$b^{12}_{mn} = -I_2/h^2_2,$$
$$b^{13}_{mn} = b^{14}_{mn} = 0,$$
$$b^{15}_{mn} = \alpha_m I_2 d/h^2_2,$$
$$b^{21}_{mn} = -I_2/h^2_2,$$
$$b^{22}_{mn} = \rho_3 h_3 + I_2/h^2_2,$$
$$b^{23}_{mn} = b^{24}_{mn} = 0,$$
$$b^{25}_{mn} = -\alpha_m I_2 d/h^2_2,$$
$$b^{31}_{mn} = b^{32}_{mn} = 0,$$
$$b^{33}_{mn} = \rho_1 h_1 + I_2/h^2_2,$$
$$b^{34}_{mn} = -I_2/h^2_2,$$
$$b^{35}_{mn} = \beta_n I_2 d/h^2_2,$$
$$b^{41}_{mn} = b^{42}_{mn} = 0,$$
$$b^{43}_{mn} = -I_2/h^2_2,$$
$$b^{44}_{mn} = \rho_3 h_3 + I_2/h^2_2,$$
$$b^{45}_{mn} = -\beta_n I_2 d/h^2_2,$$
$$b^{51}_{mn} = \alpha_m I_2 d/h^2_2,$$
$$b^{52}_{mn} = -\alpha_m I_2 d/h^2_2,$$
$$b^{53}_{mn} = \beta_n I_2 d/h^2_2,$$
$$b^{54}_{mn} = -\beta_n I_2 d/h^2_2,$$
$$b^{55}_{mn} = \left(\alpha^2_m + \beta^2_n\right) I_2 d^2/h^2_2 + (\rho_1 h_1 + \rho_2 h_2 + \rho_3 h_3).$$

REFERENCES

[1] Fahy, F. and Gardonio, P. *Sound and structural vibration: Radiation, transmission and response*, Academic Press, Oxford, 2007, 2nd ed. http://dx.doi.org/10.3397/1.2741307

[2] Maidanik, G. Response of ribbed panels to reverberant acoustic fields, *J. Acoust. Soc. Am.*, **34** (6), 809–826, (1962). http://dx.doi.org/10.1121/1.1918200

[3] Wallace, C. E. Radiation resistance of rectangular panel, *J. Acoust. Soc. Am.*, **51** (3), 946–952, (1972). http://dx.doi.org/10.1121/1.1912943

[4] Leppington, F. G., Broadbent, E. G., and Heron, K. H. The acoustic radiation efficiency of rectangular panels, *Proc. Roy. Soc. London, Ser. A*, **382** (1783), 245–271, (1982). http://dx.doi.org/10.1098/rspa.1982.0100

[5] Roussos, L. A. Noise transmission loss of a rectangular plate in an infinite baffle, *J. Acoust. Soc. Am.*, **75** (S1), S2, (1984). http://dx.doi.org/10.1121/1.2021367

[6] Panneton, R. and Atalla, N. Numerical prediction of sound transmission through finite multilayer systems with poroelastic materials, *J. Acoust. Soc. Am*, **100** (1), 346–354, (1996). http://dx.doi.org/10.1121/1.415956

[7] Lee, C. and Kondo, K. Noise transmission loss of sandwich plates with viscoelastic core, *40th Struct., Struct. D., and Mat. Conf. and Ex., Struct., Struct. D., and Mat. and Co-located Conf.*, 2137–2147, (1999). http://dx.doi.org/10.2514/6.1999-1458

[8] Foin, O., Nicolas, J., and Atalla, N. An efficient tool for predicting the structural acoustic and vibration response of sandwich plates in light or heavy fluid, *Appl. Acoust.*, **57** (3), 213–242, (1999). http://dx.doi.org/10.1016/S0003-682X(98)00059-0

[9] Foin, O., Berry, A., and Szabo, J. Acoustic radiation from an elastic baffled rectangular plate covered by a decoupling coating and immersed in a heavy acoustic fluid, *J. Acoust. Soc. Am.*, **107** (51), 2501–2510, (2000). http://dx.doi.org/10.1121/1.428638

[10] Sgard, F. C., Atalla, N., and Nicolas, J. A numerical model for the low frequency diffuse field sound transmission loss of double-wall sound barriers with elastic porous linings, *J. Acoust. Soc. Am.*, **108** (6), 2865–2872, (2000). http://dx.doi.org/10.1121/1.1322022

[11] Berry, A., Foin, O., and Szabo, J. P. Three-dimensional elasticity model for a decoupling coating on a rectangular plate immersed in a heavy fluid, *J. Acoust. Soc. Am.*, **109** (6), 2704–2714, (2001). http://dx.doi.org/10.1121/1.1372224

[12] Park, J., Mongeau, L., and Siegmund, T. Influence of supported properties on the sound radiated from the vibration of rectangular plates, *J. Sound Vib.*, **275** (1–2), 249–265, (2004). http://dx.doi.org/10.1016/S0022-460X(02)01215-4

[13] Chiello, O., Sgard, F. C., and Atalla, N. On the use of a component mode synthesis technique to investigate the effects of elastic boundary conditions on the transmission loss of baffled plates, *Comput. Struct.*, **81** (28–29), 2645–2658, (2003). http://dx.doi.org/10.1016/S0045-7949(03)00326-2

[14] Xie, G., Thompson, D. J., and Jones, C. J. C. The radiation efficiency of baffled plates and strips, *J. Sound Vib.*, **280** (1–2), 181–209, (2005). http://dx.doi.org/10.1016/j.jsv.2003.12.025

[15] Au, F. T. K. and Wang, M. F. Sound radiation from forced vibration of rectangular orthotropic plates under moving loads, *J. Sound Vib.*, **281** (3–5), 1057–1075, (2005). http://dx.doi.org/10.1016/j.jsv.2004.02.005

[16] Park, J. and Mongeau, L. Vibration and sound radiation of viscoelastically supported Mindlin plates, *J. Sound Vib.*, **318** (4–5), 1230–1249, (2008). http://dx.doi.org/10.1016/j.jsv.2008.04.045

[17] Assaf, S. and Guerich, M. Numerical prediction of noise transmission loss through viscoelastically damped sandwich plates, *J. Sandw. Struct. Mater.*, **10** (5), 359–384, (2008). http://dx.doi.org/10.1177/1099636207088444

[18] Chazot, J. D. and Guyader, J. L. Transmission loss of double panels filled with porogranular materials, *J. Acoust. Soc. Am.*, **126** (6), 3040–3048, (2009). http://dx.doi.org/10.1121/1.3245033

[19] Assaf, S., Guerich, M., and Cuvelier, P. Vibration and acoustic response of damped sandwich plates immersed in a light or heavy fluid, *Comput. Struct.*, **88** (13–14), 870–878, (2010). http://dx.doi.org/10.1016/j.compstruc.2010.04.006

[20] Zhou, R. and Crocker, M. J. Boundary element analyses for sound transmission loss of panels, *J. Acoust. Soc. Am.*, **127** (2), 829–840, (2010). http://dx.doi.org/10.1121/1.3273885

21 Loredo, A., Plessy, A., Hafidi, A. E., and Hamzaoui, N. Numerical vibroacoustic analysis of plates with constrained-layer damping patches, *J. Acoust. Soc. Am.*, **129** (4), 1905–1918, (2011). http://dx.doi.org/10.1121/1.3546096

22 Li, S. Active modal control simulation of vibro-acoustic response of a fluid-loaded plate, *J. Sound Vib.*, **330** (23), 5545–5557, (2011). http://dx.doi.org/10.1016/j.jsv.2011.07.001

23 Kam, T. Y., Jiang, C. H., Lee, B. Y. Vibro-acoustic formulation of elastically restrained shear deformable stiffened rectangular, *Compos. Struct.*, **94** (11), 3132–3141, (2012). http://dx.doi.org/10.1016/j.compstruct.2012.04.031

24 Chopra, I. Review of state of art of smart structures and integrated systems, *AIAA J.*, **40** (11), 2145–2187, (2002). http://dx.doi.org/10.2514/2.1561

25 Haddad, Y. Intelligent materials for engineering applications: A review, *AES-ATEMA International Conference Series, Advances and Trends in Engineering Materials and their Applications*, 151–162, (2011).

26 Sims, N. D., Stanway, R., and Johnson, A. R. Vibration control using smart fluids: A state-of-the-art review, *Shock Vib. Digest*, **31** (3), 195–205, (1999). http://dx.doi.org/10.1177/058310249903100302

27 Yalcintas, M., Coulter, J. P., Don, D. L. Structural modeling and optimal Control of electrorheological material based adaptive beams, *Smart Mater. Struct.*, **4** (3), 207–214, (1995). http://dx.doi.org/10.1088/0964-1726/4/3/008

28 Yeh, J. Y., Chen, L.W., Wang, C. C. Dynamic stability of a sandwich beam with a constrained layer and electrorheological fluid core, *Comput. Struct.*, **64** (1), 47–54, (2004). http://dx.doi.org/10.1016/S0263-8223(03)00212-5

29 Yeh, J. Y. and Chen, L. W. Dynamic stability analysis of a rectangular orthotropic sandwich plate with an electrorheological fluid core, *Comput. Struct.*, **72** (1), 33–41, (2006). http://dx.doi.org/10.1016/j.compstruct.2004.10.010

30 Yeh, J. Y. and Chen, L. W. Finite element dynamic analysis of orthotropic sandwich plates with an electrorheological fluid core layer, *Comput. Struct.*, **78** (3), 368–376, (2007). http://dx.doi.org/10.1016/j.compstruct.2005.10.010

31 Narayana, V. G. and Ganesan, N. Critical comparison of viscoelastic damping and electrorheological fluid core damping in composite sandwich skew plates, *Comput. Struct.*, (2), 221–233, (2007). http://dx.doi.org/10.1016/j.compstruct.2006.05.004

32 Rajamohan, V., Sedaghati, R., and Rakheja, S. Optimal vibration control of beams with total and partial MR-fluid treatments, *Smart Mater. Struct.*, **20** (11), (2011). http://dx.doi.org/10.1088/0964-1726/20/11/115016

33 Choi, S. B., Seo, J. W., Kim, J. H., and Kim, K. S. Electrorheological fluid-based plate for noise reduction in a cabin: experimental results, *J. Sound Vib.*, **239** (1), 178–185, (2001). http://dx.doi.org/10.1006/jsvi.2000.3051

34 Szary, M. L. The phenomena of electrorheological fluid behavior between two barriers under alternative voltage, *Arch. Acoust.*, **29** (2), 243–258, (2004).

35 Lu, H., Meng, G., and Zhang, T. Dynamic and acoustic characteristics high frequency region for sandwich cylindrical cavity embedded with ER fluid, *J. Vib. Eng.*, **17** (4), 457–461, (2004).

36 Tang, H., Luo, C., and Zhao, X. Sonic resonance in a sandwiched electrorheological panel, *J. Appl. Phys.*, **98** (1), (2005). http://dx.doi.org/10.1063/1.1941466

37 Hasheminejad, S. M. and Shabanimotlagh, M. Magnetic-field-dependent sound transmission properties of magnetorheological elastomer-based adaptive panels, *Smart Mater. Struct.*, **19** (3), (2010). http://dx.doi.org/10.1088/0964-1726/19/3/035006

38 Hasheminejad, S. M. and Maleki, M. Free vibration and forced harmonic response of an electrorheological fluid-filled sandwich plate, *Smart Mater. Struct.*, **18** (5), (2009). http://dx.doi.org/10.1088/0964-1726/18/5/055013

39 Leissa, A. W. *Vibration of Plates*, (1969), NASA SP-160, NASA, Washington, D.C. Reprinted by the Acoustical Society of America, Woodbury, NY, (1993).

40 Rayleigh, L. *The Theory of Sound*, Macmillan, London, (1896).

41 Kinsley, L. E. and Frey, A. R. *Fundamentals of Acoustics*, John Wiley & Sons, Inc., New York, (1962).

42 Kang, H. J., Ih, J. G., Kim, J. S., and Kim, H. S. Prediction of sound transmission loss through multilayered panels by using Gaussian distribution of directional incident energy, *J. Acoust. Soc. Am.*, **107** (3), 1413–1420, (2000). http://dx.doi.org/10.1121/1.428428

43 Fahy, F. J. *Foundations of Engineering Acoustics*, UK: Academic, 2001.

44 Pellicier, A. and Trompette, N. A review of analytical methods, based on the wave approach, to compute partitions transmission loss, *Appl. Acoust.*, **68** (10), 1192–1212, (2007). http://dx.doi.org/10.1016/j.apacoust.2006.06.010

45 Yalcintas, M. and Coulter, J. P. Electrorheological material based adaptive beams subjected to various boundary conditions, *J. Intel. Mat. Syst. Str.*, **6** (5), 700–717, (1995). http://dx.doi.org/10.1177/1045389X9500600511

46 Yeh, J. Y and Chen, L. W. Vibration of a sandwich plate with a constrained layer and electrorheological fluid core, *Compos. Struct.*, **65** (2), 251–258, (2004). http://dx.doi.org/10.1016/j.compstruct.2003.11.004

47 Sakuma, T. and Oshima, T. Numerical vibro-acoustic analysis of sound insulation performance of wall members based on a 3-D transmission model with a membrane/plate, *Acoust. Sci. Tech.*, **22** (5), 367–369, (2001). http://dx.doi.org/10.1250/ast.22.367

48 Tewes, S. Active trim panel attachments for control of sound transmission through aircraft structures, PhD diss., Institute of Lightweight Structures, Technische Universitt Mnchen, Germany, (2005).

49 Schiller, N. and Beck, B. Numerical study of transmission loss through a slow gas layer adjacent to a plate, *NASA Technical Report No. NF1676L-16143*, (2013).

An Inverse Approach for the Determination of Viscous Damping Model of Fibre Reinforced Plastic Beams using Finite Element Model Updating

Subhajit Mondal and Sushanta Chakraborty

Department of Civil Engineering, Indian Institute of Technology Kharagpur, Kharagpur- 721 302, India

(Received 3 March 2014; accepted 9 April 2015)

Investigations have been carried out both numerically and experimentally to settle with a practically feasible set of proportional viscous damping parameters for the accurate prediction of responses of fibre reinforced plastic beams over a chosen frequency range of interest. The methodology needs accurate experimental modal testing, an adequately converged finite element model, a rational basis for correct correlations between these two models, and finally, updating of the finite element model by estimating a pair of global viscous damping coefficients using a gradient-based inverse sensitivity algorithm. The present approach emphasises that the successful estimate of the damping matrix is related to a-priori estimation of material properties, as well. The responses are somewhat accurately predicted using these updated damping parameters over a large frequency range. In the case of plates, determination of in-plane stiffness parameters becomes easier, whereas for beam specimens, transverse material properties play a comparatively greater role and need to be determined. Moreover, for damping matrix parameter estimation, frequency response functions need to be used instead of frequencies and mode shapes. The proposed method of damping matrix identification is able to reproduce frequency response functions accurately even outside the frequency ranges used for identification.

1. INTRODUCTION

The accurate determination of dynamical responses is very important from the viewpoint of safety, serviceability, and operation of any structure. The geometrical complexities, material property distributions, existing boundary conditions, and applied loading are the key factors that influence the dynamic responses. The elastic and inertial properties are somewhat correctly represented through finite element modelling with suitable simplifying assumptions, whereas uncertainties in response prediction still remain due to imperfect boundary conditions and the presence of damping, which are difficult to deal with. No generally acceptable modelling techniques for damping have been proposed in previous research that can be confidently used for complicated structures. The damping mechanism may comprise three effects — material damping resulting from micro-structural behaviour, friction damping resulting from looseness at boundaries, and environmental damping effects, such as interaction with the surrounding fluid. Depending on the practical situation, one or more component may be less significant than the others, making the modelling effort easier for the particular structure under consideration.

Although the phenomenon of damping is mostly nonlinear, the assumption of small damping makes many equivalent linear models practically acceptable. For example, Dowell and Schwartz[1] presented a methodology for accounting for dry friction damping arising from axial sliding of surfaces inside supports, and concluded from studies on plates and beams that an equivalent linear viscous damping ratio can be agreed upon, even if nonlinear Coulomb law for the friction and geometric nonlinearity of beams are present. Tang and Dowell[2] further investigated experimentally to verify the theory presented in the previous paper. It was concluded that the methodology works well in lower mode ranges, especially with the fundamental mode. Sometimes, it will be possible to accept on practical terms the linear damping models for much more complicated environmental effects, such as interaction of a beam with the surrounding air, etc. Filipiak, et al.[3] presented such an approach to determine the effects of air damping on small beams housing miniature sensors. How far such efforts are applicable to realistic full scale structures remain an open question.

If linear damping is agreed upon with small damping assumptions, it can be modelled as a multiplier of conveniently chosen state variables with constant coefficients. The success of such a model can be judged by its ability to replicate the actual observable responses over a frequency range of interests. Then, the entire domain of linear modal testing can be employed and a damping matrix can finally be put forward in the model to be treated in a fashion similar to the stiffness and mass matrices. Mostly, instantaneous velocity is chosen as the state variable, and the damping can be stated to be viscous.[4]

Fibre Reinforced Plastics (FRP) have long been used in weight-sensitive aerospace, naval, automotive, and high performance sports applications. However, it took some time for the engineering community to appreciate the other positive aspects of FRPs, such as durability, fatigue, and corrosion resistance to pave the way for its infrastructural applications. Recently, many standard structural forms such as various beam sections, plates, and shells have been routinely manufactured and employed for structural applications. Pultruded sections in regular forms such as rectangular, angle, 'T', etc., are likely to replace most of the current infrastructures made of conventional material such as steel. Condition assessment and health monitoring of such huge infrastructures made of FRPs will be a challenge in the future, especially if they degrade over long periods of time, but still remain serviceable. The existing stiffness and damping properties need to be correctly assessed from time to time using a reliable non-destructive inverse technique. Unlike the stiffness and inertia parameters, uncertainties in damping parameters will further increase, as the mechanism may include one or more effects which were initially absent. For example, loosening of joints and supports may result in increased friction component of damping as time passes.

Literature related to the modelling of damped FRP structures is very scant. Zhuang and Crocker[5] presented a review on the damping of composite structures. Gelman, et al.[6] proposed a methodology of diagonalisation of the damping matrix based on measured frequency response functions (FRF). Akrout, et al.[7] conducted numerically simulated investigations of vibroacoustic behaviour of two thin film-laminated glass panels in the presence of a fluid layer. Assaf[8] analysed sandwich composite beams and investigated the effects of ply-stacking sequences, core-to-face stiffness ratio, etc. on natural frequencies and modal damping.

The current literature is very rich in information related to inverse detection of stiffness parameters from measured vibration responses,[9] whereas only limited attempts have been made to inversely estimate the damping parameters for FRP type of structures. The main reason is that for small damping, the resonant frequencies and mode shapes change very little with damping coefficients, but the responses change drastically, especially near resonances. Literature related to damping identification using a beam type of specimen is very rare. Reix, et al.[10] used the FRF information of a beam to update the damping matrix using a nonlinear least square optimization technique.

Inverse detection of damping using an iterative procedure demands proper forward simulation of the damped responses of the FRP structures in the iterative loop. The most popular forward damping model is due to Rayleigh, in which the damping matrix is assumed as a weighted linear combination of the mass and stiffness matrix

$$C = a_0 M + a_1 K. \tag{1}$$

A more generalised viscous proportional damping matrix has been proposed by Caughey and Kelly,[11] and can be written as

$$C = M \sum_{n=0}^{r-1} a_n \left[M^{-1}K\right]^n . \tag{2}$$

Woodhouse[12] has given an account of various linear damping models useful for structural applications. The main difficulty of all such models is that the damping parameters remain somewhat insensitive to frequency variations. Moreover, stiffness and mass distributions should be exactly determined a-priori, which is impossible in most practical cases. Adhikari[13] incorporated the frequency variation of damping factors within the framework of a generalised damping model. As a continuation of the above methodology, Adhikari and Phani[14] proposed a proportional damping matrix obtained from a single driving point FRF. Minas and Inman[15] used incomplete experimental modal data and reduced mass and stiffness matrices to identify a non-proportional damping matrix in a weighted least square sense. Lancaster and Prells[16] used the inverse spectral method to estimate the damping matrix from complex eigenvectors. Pilkey[17] proposed direct and iterative approaches for damping matrix reconstruction. Friswell, et al.[18] used a direct approach to identify damping and the stiffness matrix together using FRF information. Chen and Tsuei[19] distinguished between the viscous and structural damping components from the measured complex FRF matrix. Some investigators tried to estimate mass, stiffness, and damping matrices together.[20]

The main drawback of the investigations on damping matrix identification proposed in a great deal of research is that they demand availability of accurate information about the stiffness and mass of the system, as well as the availability of accurate modal properties. Even in newly built FRP structures, there are large variations between the predicted stiffness parameters as compared to those existing, due to the fact that the structural fabrication and material fabrication are one unified process for FRP, and the actual existing material properties vary greatly from those mentioned in manufacturer's manual or in standard handbooks. For the FRP type of anisotropic layered composites, such uncertainties are greater as compared to similar constructions made of isotropic and homogeneous materials. It thus appears that a proper inverse regularised technique augmented by a-priori stiffness estimation procedure will be appropriate for realistic damping parameter identification. If the damping is small, which is the case in most practical structures, a linear model will suffice.

The objective of the present investigation is to apply a gradient-based model updating technique to estimate viscous damping parameters along with the stiffness parameters for pultruded FRP beams using measured FRFs. The efficiency of the algorithm will be judged by comparing the regenerated FRFs to the experimentally obtained values to examine if the responses match accurately. Information related to FRF-based updating is abundant in current literature,[21] although most of it is related to the estimation of stiffness parameters as far as applications to FRP structures are concerned.

The complete process for identification of damping of FRP beams includes a-priori estimate of stiffness parameters using measured modal and FRF data, converged finite element modelling, correlations between them, and finally updating the global proportional damping parameters using the gradient-based inverse sensitivity technique in a nonlinear least square sense.[22] The methodology is first established through a numerically simulated example, followed by real experimental case studies involving different boundary conditions.

2. MATHEMATICAL FORMULATION

The equation of motion of a multiple-degrees-of-freedom system in a discretized form can be written as

$$M\ddot{x}(t) + C\dot{x}(t) + Kx(t) = f(t); \tag{3}$$

where M, K, and C are the mass, stiffness, and damping matrix, respectively. Here, equivalent viscous damping has been considered as the major dissipation mechanism. In modal coordinates, the equation can be written as a set of single-degree-of-freedom (SDOF) uncoupled equations

$$[m]\ddot{x}(t) + [c]\dot{x}(t) + [k]x(t) = \{u\}(t); \tag{4}$$

where

$$[m] = \phi^T[M]\phi = \text{modal mass matrix},$$
$$[k] = \phi^T[K]\phi = \text{modal stiffness matrix},$$
$$[c] = \phi^T[C]\phi = \text{modal damping matrix}. \quad (5)$$

The free vibration equation can be expressed as

$$\left(-\omega^2[m] + i\omega[c] + [k]\right)\{u\} = 0. \quad (6)$$

If damping is neglected, the undamped equation of motion can be solved from the eigenequation

$$Ku = \omega^2 Mu. \quad (7)$$

These undamped eigenvalues and eigenvectors can be used to form the acceleration FRFs, and can be expressed as a function of modal damping factor

$$H_{ij}(\omega) = -\omega^2 \sum_{k=1}^{N} \frac{\phi_{ik}\phi_{jk}}{\omega_k - \omega + 2i\omega\omega_k\xi_k}. \quad (8)$$

It is to be noted that the Rayleigh damping coefficients can be related to the modal damping factor, as shown below:

$$\xi_i = \frac{1}{2}\left(\frac{a_0}{\omega_1} + a_1\omega_i\right). \quad (9)$$

The disadvantage of Rayleigh damping is that the effects of the higher modes are usually weighted more than the lower modes. As only two modes are used at a time for the estimation of modal damping, the effects of other modes cannot be taken care of. The present investigation is focused on removing this difficulty by including the effects of multiple modes through measured FRFs within a frequency range of interest for a FRP beam.

The expression for the FRF can be modified to include the damping coefficients as

$$H_{ij}(\omega) = -\omega^2 \sum_{k=1}^{N} \frac{\phi_{ik}\phi_{jk}}{\omega_k - \omega + i\omega\left(a_1\omega^2 + a_0\right)}; \quad (10)$$

where H_{ij} is the acceleration response at point i due to excitation at point j. As it is a common practice to deploy accelerometers for measuring accelerations directly and compute displacement and velocities as derived quantities as and when required, all response quantities are expressed in terms of accelerations in this paper. In case of other measurement techniques employing measured displacements as first hand information, such as in full field measurements using scanning Laser Doppler Vibrometer types of non-contact devices, the formulations can be modified to deal with displacements directly.

Since the order of magnitude of the terms of the damping matrix is much lower as compared to the stiffness and mass matrices, it will be efficient to have the stiffness properties updated prior to the updating of the damping parameters. Thus, a two-stage model updating algorithm is implemented here. Moreover, the global stiffness properties can be updated more efficiently with the help of measured natural frequencies and mode shapes, whereas updating the damping matrix coefficients a_1 and a_0 requires the information from measured FRFs. At present, the inertia properties are assumed to be determined accurately, as this is generally the case in practice.

The objective functions involving the measured and modelled FRFs can be written in a weighted least square sense

$$E = \sum_{i=1}^{q} w_{ii}\,||H_{\text{exp}}(\omega) - H_{\text{nu}}(\omega)||^2; \quad (11)$$

where w_{ii} are the weights and q is the number of FRFs considered. The sensitivities of these FRFs with respect to the damping or elastic parameters can be computed using

$$S_{ij} = \left[\frac{\partial H(\omega)}{\partial r_j}\right]; \quad (12)$$

where $i = 1$ to n and $j = 1$ to m. Here, the order of the sensitivity matrix is $n \times m$. The linearized first order approximation of the relationship between changes in measured modal properties (i.e. frequencies, mode shapes or FRFs) and the changes in the parameters to be updated can be related through the first order sensitivity matrix

$$\{\Delta f\} = [S]\{\Delta r\}. \quad (13)$$

In the updating process, changes (Δr) are made to the initial guesses of parameters within reasonable bounds, and the finite element model of the pultruded FRP beam is updated as follows:

$$\{r\}_{i+1} = \{r\}_i + \{\Delta r\}_i. \quad (14)$$

The error between the experimental observation and the finite element modelling is thus minimised through this inverse sensitivity method. In the present investigation, the parameters can be the in-plane elastic material constants, such as the Young's modulus and the shear modulus, the out-of-plane shear modulus, and the modal damping coefficients. A Block Lanczos Algorithm has been implemented for the eigensolutions.

In an inverse problem related to anisotropic materials, mode sequences need to be properly checked using certain established correlation criteria. In the present investigation, Modal Assurance Criteria (MAC) is used at each step of iteration to determine how similar or dissimilar the analytical modal vector is as compared to the experimentally measured modes; a value close to 1 indicates good correlations:[23]

$$MAC(\phi_{\text{nu}}, \phi_{\text{exp}}) = \frac{\left|\{\phi_{\text{nu}}\}^T\{\phi_{\text{exp}}\}\right|^2}{\left(\{\phi_{\text{nu}}\}^T\{\phi_{\text{exp}}\}\right)\left(\{\phi_{\text{exp}}\}^T\{\phi_{\text{exp}}\}\right)}. \quad (15)$$

Here, ϕ represents the realised eigenvectors from the measured complex modes. The analytical and experimental FRFs are similarly correlated using Signature Assurance Criteria (SAC),[22] which is basically a global Frequency Response Assurance Criteria (FRAC):[24]

$$SAC(H_{\text{nu}_i}, H_{\text{exp}_i}) = \frac{\left(\left|H_{\text{exp}_i}^T\right|\left|H_{\text{nu}_i}\right|\right)^2}{\left(\left|H_{\text{exp}_i}^T\right|\left|H_{\text{exp}_i}\right|\right)\left(\left|H_{\text{nu}_i}^T\right|\left|H_{\text{nu}_i}\right|\right)}. \quad (16)$$

Furthermore, Cross Signature Assurance Criteria (CSAC) is the correlation function, checking the FRF correlations[22] lo-

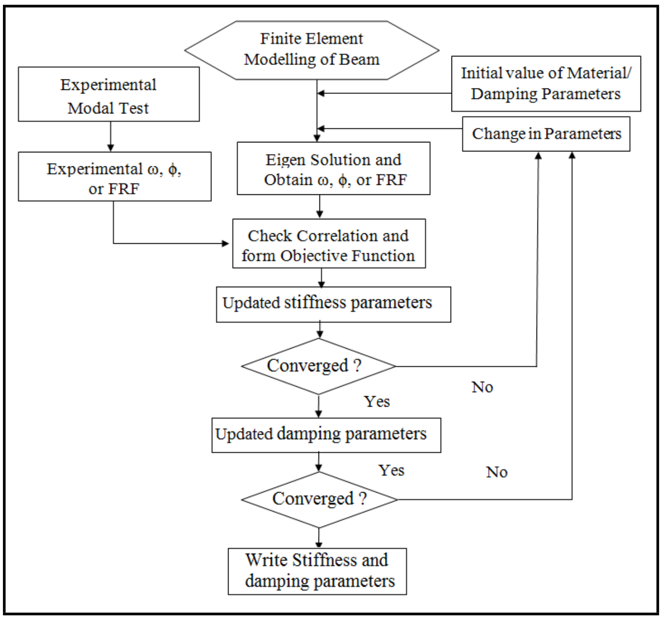

Figure 1. Flow chart of the model updating algorithm.

cally:

$$CSAC(\omega_k) = \frac{\left|H^T_{\text{exp}_i}(\omega_k)H_{\text{nu}_i}(\omega_k)\right|^2}{\left(H^T_{\text{exp}_i}(\omega_k)H_{\text{exp}_i}(\omega_k)\right)\left(H^T_{\text{nu}_i}(\omega_k)H_{\text{nu}_i}(\omega_k)\right)}, \quad k = 1, 2, \ldots, N. \tag{17}$$

The amplitude correlations of FRFs are taken care of by Cross Signature Scale Factor (CSF):[22]

$$CSF(\omega_k) = \frac{2\left|H^T_{\text{exp}_i}(\omega_k)H_{\text{nu}_i}(\omega_k)\right|}{\left(H^T_{\text{exp}_i}(\omega_k)H_{\text{exp}_i}(\omega_k)\right) + \left(H^T_{\text{nu}_i}(\omega_k)H_{\text{nu}_i}(\omega_k)\right)}, \quad k = 1, 2, \ldots, N. \tag{18}$$

First, an isotropic beam is investigated numerically to see if the damping parameters can be conveniently determined. The 'experimental' FRFs in this simulated study are also determined using the same finite element programming. Subsequently, a real experiment is conducted on a Pultruded FRP beam, both in cantilever and under free boundary conditions. For the updating process, the initial finite element model computes the FRFs using the undamped frequencies, modal vectors, and initially assumed modal damping factors. Analytical and experimental FRFs are correlated as explained earlier to form the objective functions. A first order sensitivity matrix is computed for the selected parameters by a finite difference approximation of variables. Finally, the inverse sensitivity method is used to update the stiffness parameters, first using the modal information, followed by an estimation of modal damping coefficients using the FRFs. A Bayesian approach is used to include the variance of the response data. The entire procedure is explained through a flow chart in Fig. 1.

3. NUMERICALLY SIMULATED EXAMPLE

To check the stability and efficiency of the algorithm described above, first a numerically simulated example involving a rectangular isotropic beam of dimensions 500 mm × 40 mm and having thickness of 10 mm is considered and is shown in Fig. 2. A three-noded quadratic beam element (B32)[25] is used

Table 1. Numerically simulated 'experimental' frequencies and assumed modal damping factors.

Mode	Frequency (Hz)	Modal damping factor (%)
1	24.93	5.0E-2
2	99.28	1.3E-2
3	155.90	1.1E-2
4	435.05	1.25E-2
5	528.57	1.50E-2
6	604.20	0.8E-2

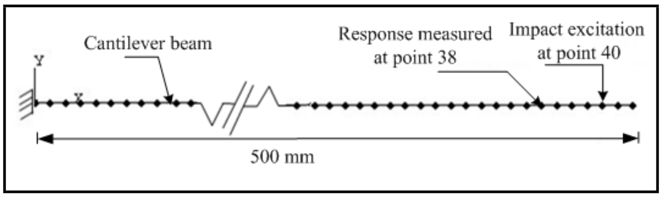

Figure 2. Numerical model of the cantilever beam.

for the finite element modelling of the isotropic beam.[25] The present investigation deals with the average stiffness properties and global average damping parameters. A 40-mesh division along the length was found to be sufficient for convergence of eigenproperties. The actual existing Young's modulus E and in-plane Poission's ratio ν are taken to be 30 GPa and 0.3, respectively. The mass density is assumed as 2012 kgm^{-3}. With the above set of data, the simulated 'experimental' modal properties are computed and presented in Table 1, along with the assumed modal damping factors.

As explained earlier, the determination of material constants from the modal data using the inverse sensitivity method is taken up first. It has been observed that changing the modal damping coefficients to have a different set of 'experimental' modal data has very little effect on the accuracy of the estimation of these stiffness parameters, and thus is not reported here. The updated values of the elastic material constants were used for further updating of the damping coefficients, which requires the simulated 'experimental' FRF data.

It is readily observed that the estimated values of the damping parameters a_0 and a_1 differ depending upon the modes considered. The results are shown in Table 2 for a few selected arbitrary combinations of modes using Eq. (9).[26] The corresponding values of ω_i and ξ_i are taken from Table 1. The first three sets show the variations of the two estimated damping parameters due to the incorporation of up to the first five modes.

While implementing the inverse FRF-based updating algorithm, these values of a_0 and a_1 are chosen as initial values to see if all trials converge to a unique set of parameters. To check the robustness of this FRF-based inverse algorithm, two additional arbitrary sets of values of a_0 and a_1 are also chosen (Trial_4 and Trial_5) that do not immediately correspond to any combination of modes and may not have any physical significance.

Figure 3 shows the monotonic convergence curves for both the parameters, the final values of which are $a_0 = 14.95$ rad/s and $a_1 = 31.60$E-6 s/rad, respectively. The updated mass proportional damping coefficient converged to a value that is quite higher, while the stiffness proportional damping coefficient converged to a somewhat lower value.

A typical set of regenerated FRF curves with different mode combinations are shown in Fig. 4. It clearly shows that the most accurate global representation of damping parameters de-

Table 2. Initial values of damping parameters for numerically simulated example.

	Mode considered for average values of ω_1 and ξ_1	Mode considered for average values of ω_2 and ξ_2	a_0	a_1
Trial_1	1	2	2.48	9.55E-6
Trial_2	1, 2	5	3.74	4.33E-5
Trial_3	2	3	2.00	5.87E-5
Trial_4	—	—	40	5.0E-6
Trial_5	—	—	50	1.0E-6

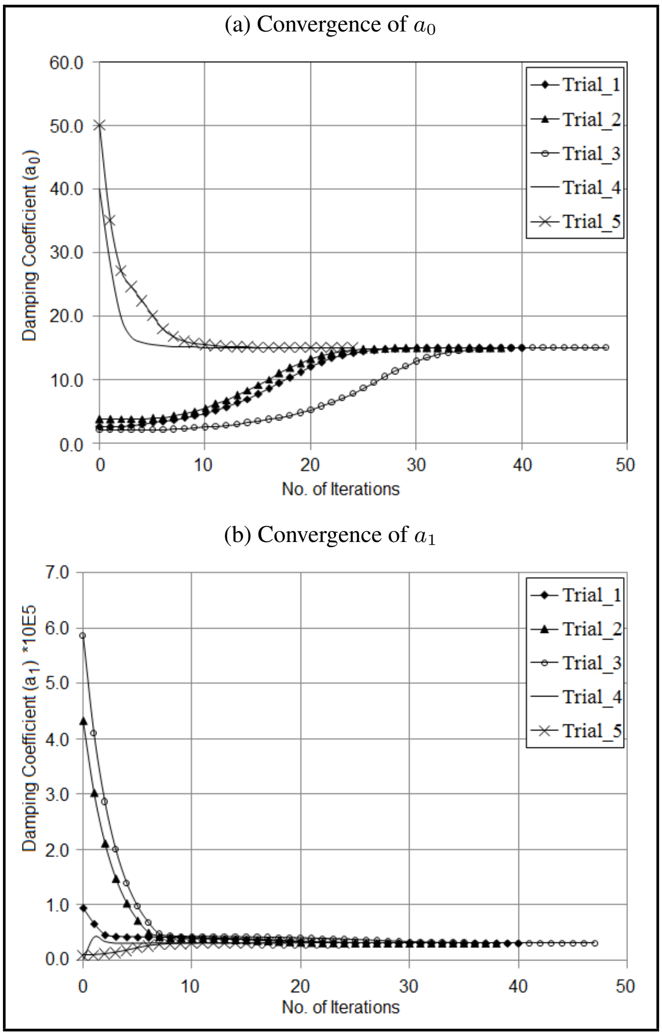

Figure 3. Convergence curves for damping coefficients.

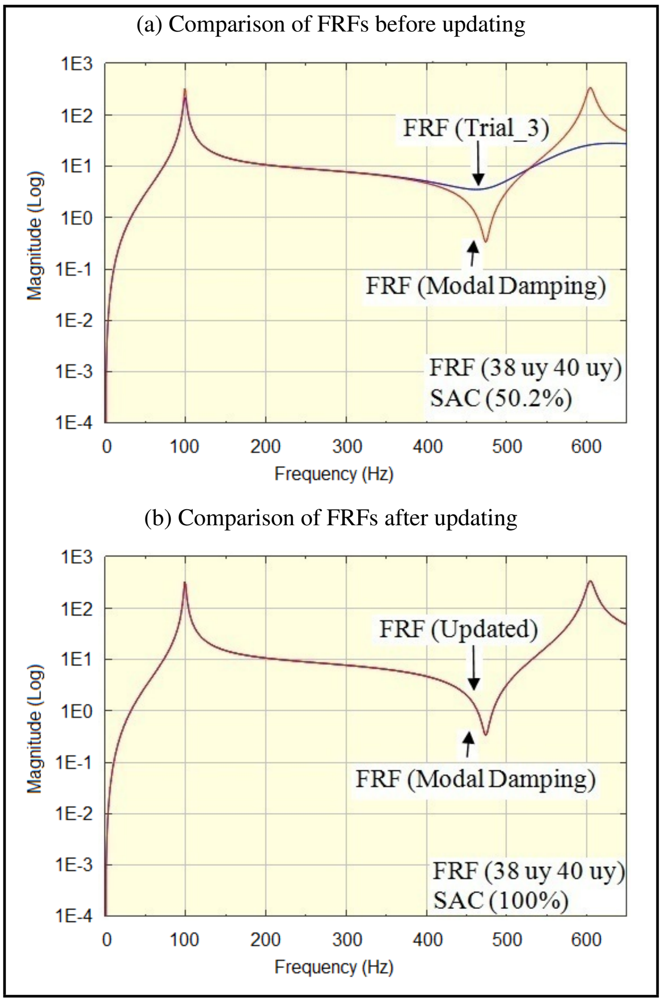

Figure 4. Comparison of FRFs computed using modal damping to those computed using trial values and updated values of damping parameters.

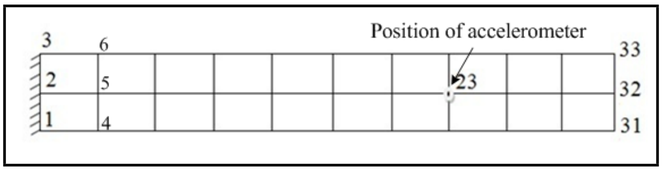

Figure 5. Measurement grid points of the FRP cantilever beam.

pends upon the participation of modes. If that matches with the selected modes, then only the SAC value indicating better correlation between the observation and model will approach unity. This is difficult to predict in practice, and several trials with various combinations of modes are necessary before settling with the most appropriate solution.

4. EXPERIMENTAL INVESTIGATION

Equipped with the knowledge gained from the numerically simulated example, a rectangular FRP composite beam of the same size is fabricated using the pultrusion process with Woven Roving (WR) glass fibres and an epoxy matrix. The exact final average thickness of the beam comes to be 10.12 mm. The mass density was measured to be exactly 2012 kgm^{-3}. First, the modal testing was carried out with a fixed boundary at one end of the beam, the other end being free. An impact hammer fitted with a force transducer (B&K, number 8206-002) was used for exciting the beam at different predefined locations, and the resulting responses were picked up by an accelerometer (IEPE DeltaTron 4507) at a particular node. Both the signals were Fourier transformed in a B&K spectrum analyser, and the FRFs were obtained utilising the PULSE-LabShop software.[27] The frequencies, modes shapes, and modal damping factors were extracted from the measured FRFs using the post-processing software MEScope.[28] Figure 5 shows the position of the accelerometer (point 23) and also the nodes where forces were imparted through the impact hammer in turn (33 nodal points altogether). Figure 6 shows the experimental setup for the modal testing. Very heavy steel billets are used to ensure proper fixity after using a properly bolted connection at the cantilever end. Accelerometers were placed near the supports to check whether near zero support mobility is achieved during testing.

The finite element modelling of the beam was done with shell element (S8R),[25] implementing an equivalent single layer

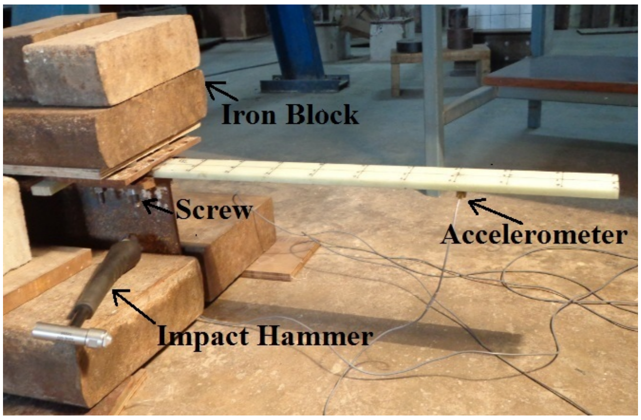

Figure 6. Experimental modal testing of the FRP cantilever beam.

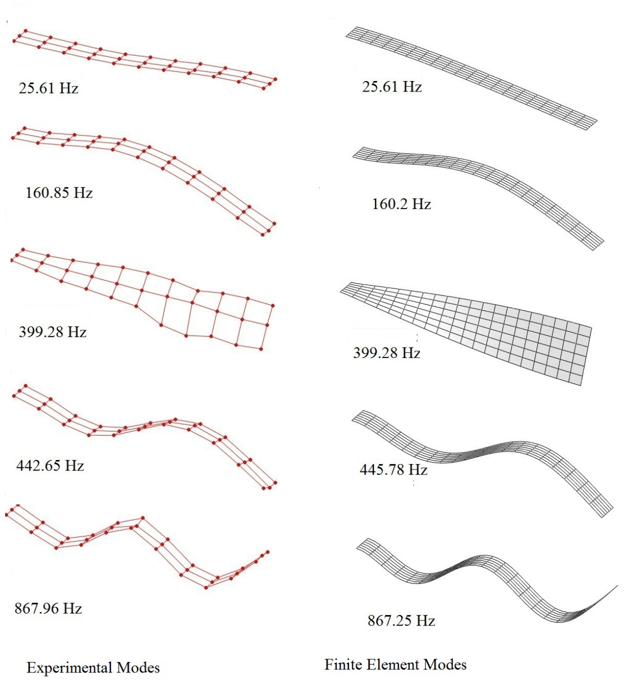

Figure 7. Experimentally and numerically obtained mode shapes for the FRP cantilever beam.

theory for layered composites.[29] The parameters selected for updating are the in-plane stiffness parameters of the beam, out-of-plane shear modulus, and the damping constants. First, the material constants are updated, followed by the estimation of damping coefficients. The initial values to start the iterative model updating process are selected from standard handbooks and manufacturer's data. Figure 7 shows the comparison between properly correlated experimental and numerical mode shapes.

Frequencies obtained using updated elastic material parameters, along with the experimentally measured frequencies, are shown in Table 3. The experimentally obtained modal damping factors are also shown.

The final MAC values between the experimental and updated mode shapes indicate an excellent correlation. To have better insight into the global updating process, the correlation quantities CSAC and CSF were also computed, and excellent correlations were achieved, except near some anti-resonant points.

Table 3. Updated and experimentally observed natural frequencies and damping factors of the FRP cantilever beam.

Mode No.	Updated Freq. (Hz)	Exp. Freq. (Hz)	Modal Damping Factors (%)
1	25.63	25.61	15.56
2	160.06	160.85	2.84
3	399.28	399.28	2.43
4	445.54	442.65	1.47
5	865.86	867.96	1.26

Table 4. Experimentally obtained and updated material parameters.

Parameters	Experimentally obtained elastic parameters (GPa)	Updated and finally used elastic parameters (GPa) for damping matrix updating
E_x	33.05	31.66
E_y	31.80	31.80
G_{xy}	5.73	6.30
G_{xz}	—	5.37
G_{yz}	—	5.37

Table 5. Initial values of damping coefficients from experimentally obtained modal damping factors of the FRP cantilever beam.

	Mode considered for average values of ω_1 and ξ_1	Mode considered for average values of ω_2 and ξ_2	a_0	a_1
Trial_1	1	2	7.93	4.71E-5
Trial_2	1, 2	5	17.07	6.42E-6
Trial_3	2	3	7.22	8.24E-5
Trial_4	2	4	8.78	2.19E-5
Trial_5	—	—	60	1.00E-4
Trial_6	—	—	20	2.00E-6

Next, static characterisation tests were carried out using coupons that were prepared and tested quasi-statically as per ASTM standard (No.D3039/D3039M),[30] and the results are presented in Table 4.

The experimentally obtained Poisson's ratio is 0.15. For the updating of the damping parameters, the initial values are selected again from Eq. (9), in the same way as they were selected in the numerically simulated example. A few such selected sets of damping coefficients are shown in Table 5, along with two arbitrary values to test the robustness of the algorithm from distant points in this practical example.

The FRFs using different trial values of damping parameters are shown in Fig. 8, and it is clear that they still differ from the experimentally observed values. The regenerated responses using the updated damping parameters, however, match almost exactly with the experimentally obtained FRFs, as shown in Fig. 9. The SAC value also approaches 1, indicating very good global correlations.

Figure 10 shows comparisons between the experimental FRFs and the numerically regenerated FRFs that use the experimentally obtained modal damping factors. The convergence curves of the damping parameters from various initial values are shown in Fig. 11, and are found to be monotonic in all cases. The last updated parameters are found to be $a_0 = 42.25$ rad/s and $a_1 = 1.10\text{E-}5$ s/rad, respectively, for this FRP beam, as shown in the Fig. 11, considering five modes altogether. The apparent improvement in global response prediction can be attributed to the incorporation of a number of modes, rather than using only a few selected modes (Eq. (9)).

To test the authenticity of the methodology developed, some more FRFs are compared that were not used in the updating process, and the correlations are found to be excellent. This was observed at most of the anti-resonant points, as well

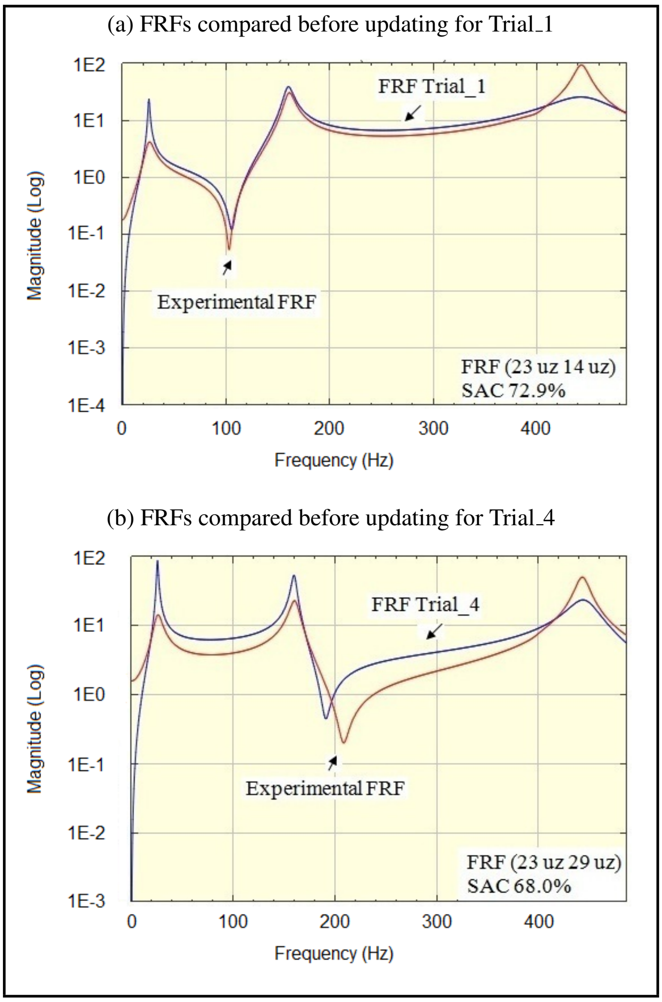

Figure 8. Typical comparison of experimental and trial FRFs at two selected points using different values of viscous damping coefficients.

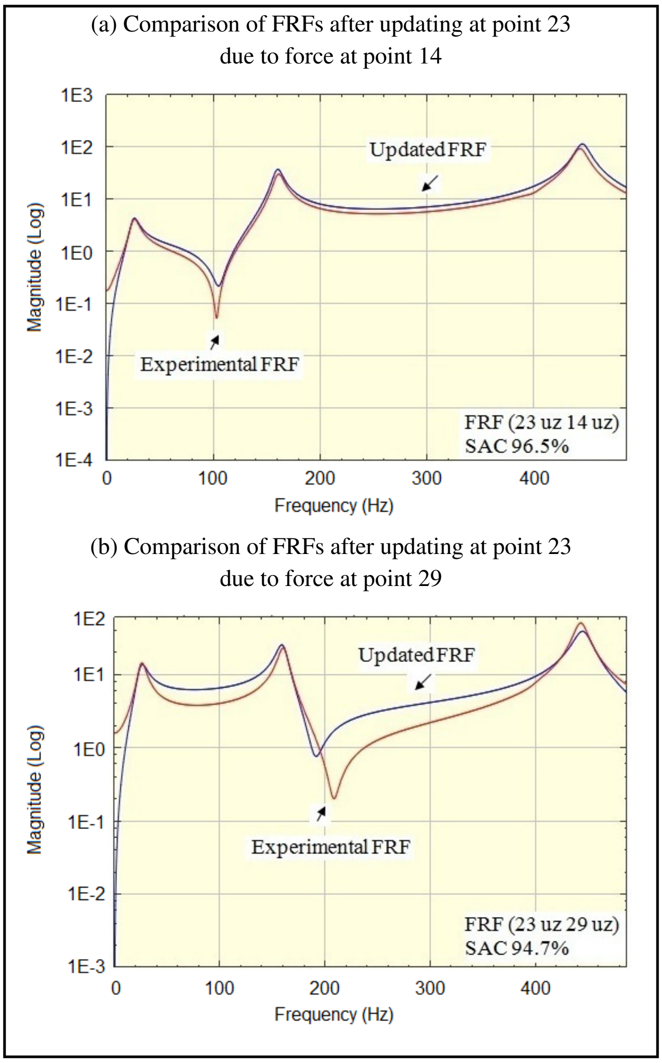

Figure 9. Typical comparison of experimental and updated FRFs at two selected points.

(as shown in Fig. 12). Even, the modes beyond the frequency ranges considered also showed improved correlations (as shown in Fig. 13).

The experimental investigation was then extended to cater to the free boundary conditions, as well, and a two-step finite element model updating procedure was performed. The free boundary conditions were achieved by hanging the beam from soft rubber threads of sufficient length so that the frequency of oscillation was much lower as compared to the fundamental frequency of the free-free beam. The last measured width and length of the beam were found to be 40 mm and 501 mm, respectively, whereas the average thickness was measured to be 10.12 mm. The schematic diagram showing the measurement points, as well as a photograph of modal testing under free boundary conditions, are shown in Fig. 14.

First the material properties were updated, followed by updating the viscous damping parameters from the FRF data using the sensitivity-based model updating algorithm.

The updated in-plane Young's moduli (E_x and E_y) were found to be 31.85 GPa and 30.86 GPa, respectively. The in-plane shear modulus (G_{xy}) was updated to a value of 6.31 GPa, and the out-of-plane shear modulus (G_{xz} and G_{yz}) were updated to 4.77 GPa and 5.56 GPa, respectively. The Poisson's ratio was measured to be 0.15. The experimentally obtained first four frequencies were 165.87 Hz, 453.39 Hz, 800.44 Hz, and 886.53 Hz, and the modal damping coefficients were measured to be 2.59%, 1.30%, 2.52%, and 1.40%, respectively. The experimental mode shapes are compared in Fig. 15 to the finite element mode shapes, indicating very good correlations.

A typical set of FRF curves before and after updating are also shown in Fig. 16, indicating good correlations in terms of improved SAC values. The updated damping parameters are found to be 49.3 rad/s and 5.09E-6 s/rad, which reproduces the modal damping almost exactly.

5. CONCLUSIONS

A finite element model updating algorithm using measured frequency response functions has been implemented to estimate proportional damping parameters of a fibre-reinforced plastic beam with different boundary conditions over a selected frequency range of interest. It has been observed that the material constants need to be updated a-priori before estimating the damping parameters. The number of frequencies to be included is case-specific, and for this example it gives very good accuracy with only a few modes, with which even the out-of-range frequency responses were regenerated with acceptable accuracy. At present, the methodology assumes equivalent viscous damping for all combined effects, such as boundary friction, etc.

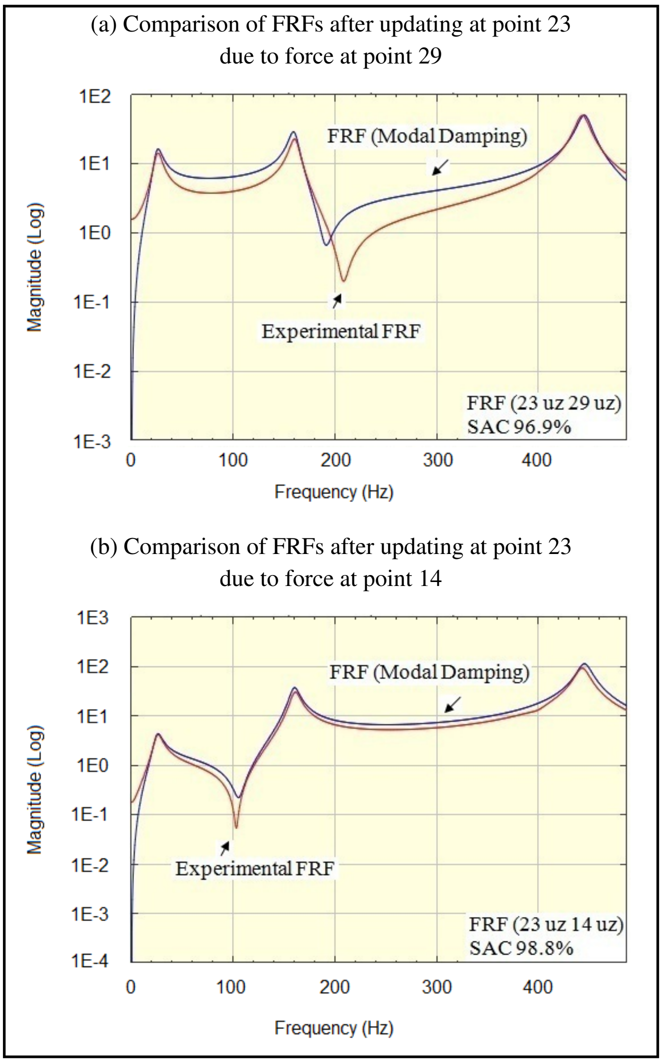

Figure 10. Typical comparison of experimental and numerically regenerated (using the modal damping factors) FRFs.

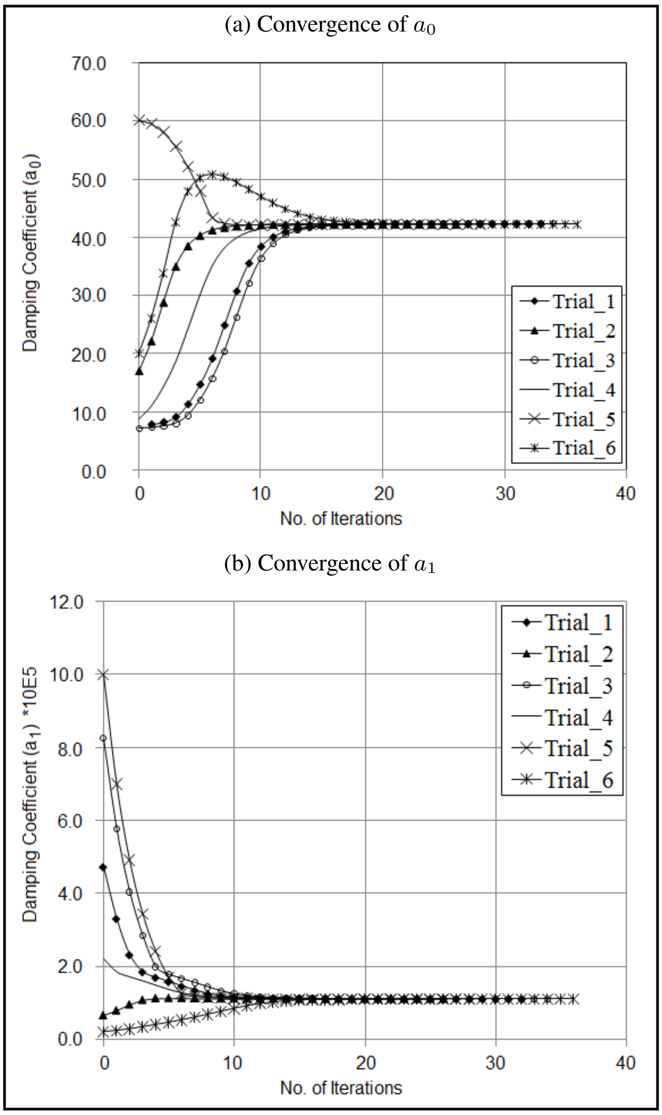

Figure 11. Convergence Curve for damping parameters of the FRP cantilever beam.

REFERENCES

1. Dowell, E. H. and Schwartz, H. B. Forced response of a cantilever beam with a dry friction damper attached, Part-1: Theory, *Journal of Sound and Vibration*, **91** (2), 255–267, (1983). http://dx.doi.org/10.1016/0022-460x(83)90901-x.

2. Tang, D. M. and Dowell, E. H. Damping in beams and plates due to slipping the support boundaries, part 2: Numerical and experimental study, *Journal of Sound and Vibration*, **108** (3), 509–522, (1986). http://dx.doi.org/http://dx.doi.org/10.1016/s0022-460x(86)80044-x.

3. Filipiak, J., Solarz, L., and Zubko, K. Analysis of damping effect on beam vibration, *Molecular and Quantum Acoustics*, **27**, 79–88, (2006).

4. Rayleigh, L. Theory of sound (Two Volumes), Dover Publications, (1877).

5. Zhuang, Li and Crocker, M. J. A review on vibration damping in sandwich composite structures, *International Journal of Acoustics and Vibration*, **10** (4), 159–169, (2005).

6. Gelman, L., Jenkin, P., and Petrunin, I. Vibro-acoustical damping diagnostics: Complex frequency response function versus its magnitude, *International Journal of Acoustics and Vibration*, **11** (3), 120–124, (2006).

7. Akrout, A., Hammami, L., Chafik, K., Ben Tahar, M., and Haddar, M. Vibroacoustic damping simulation of two laminated glass panels coupled to viscothermal fluid layer, *International Journal of Acoustics and Vibration*, **15** (2), 79–90, (2010).

8. Assaf, S. Finite element vibration analysis of damped composite sandwich beams, *International Journal of Acoustics and Vibration*, **16** (4), 163–172, (2011).

9. Mottershead, J. E. and Friswell, M. I. Model updating in structural dynamics: A survey, *Journal of Sound and Vibration*, **167** (2), 347–375, (1993). http://dx.doi.org/10.1006/jsvi.1993.1340.

10. Reix, C., Tombini, C., Gerard, A., and Dascotte, E. Updating the damping matrix using frequency response data, *Proc. 14th International Modal Analysis Conference*, (1996).

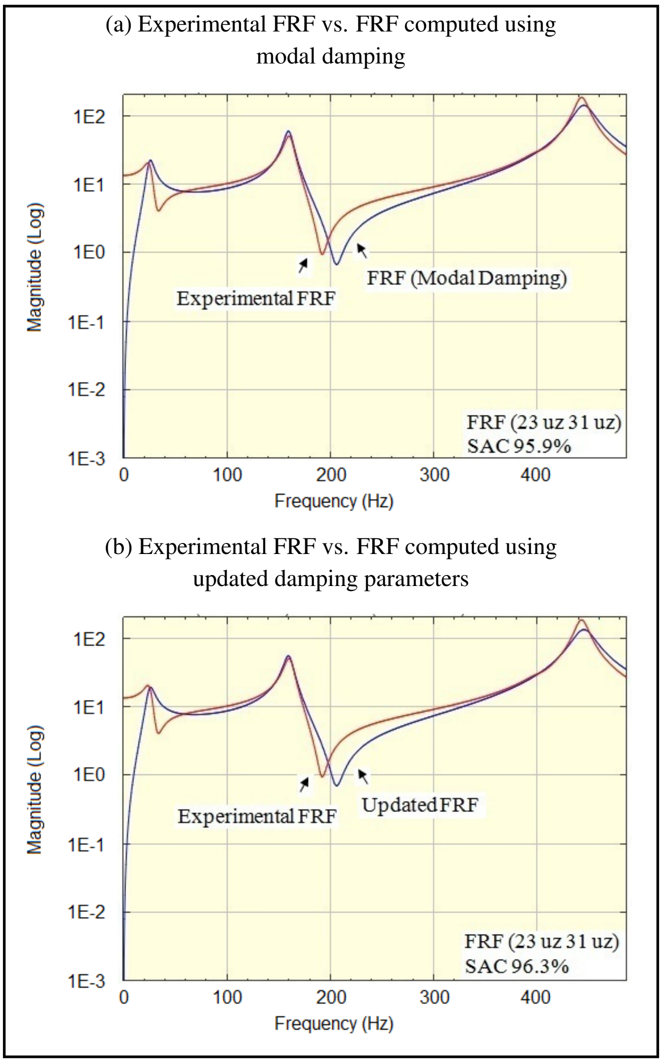

Figure 12. Typical comparison of experimental FRFs to those computed using modal damping and using updated damping parameters.

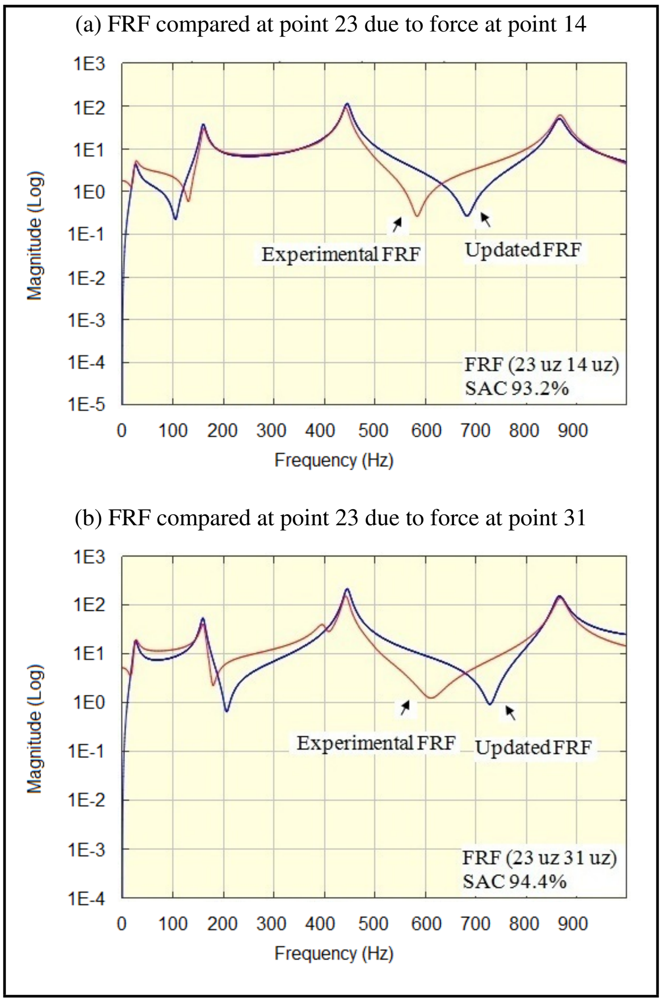

Figure 13. Typical comparison of experimental FRFs to updated FRFs at different points at higher frequency ranges.

[11] Caughey, T. K. Classical normal modes in damped linear dynamic systems, *Journal of Applied Mechanics*, **32** (3), 583–588, (1960). http://dx.doi.org/10.1115/1.3643949.

[12] Woodhouse, J. Linear damping models for structural vibration, *Journal of Sound and Vibration*, **215** (3), 547–569, (1998). http://dx.doi.org/10.1006/jsvi.1998.1709.

[13] Adhikari, S. Damping modelling using generalized proportional damping, *Journal of Sound and Vibration*, **293** (1–2), 156–170, (2006). http://dx.doi.org/10.1016/j.jsv.2005.09.034.

[14] Adhikari, S. and Phani, A. S. Experimental identification of generalized proportional viscous damping matrix, *Journal of Vibration and Acoustics*, **131** (1), (2009). http://dx.doi.org/10.1115/1.2980400.

[15] Minas, C. and Inman, D. J. Identification of a nonproportional damping matrix from incomplete modal information, *Journal of Vibration and Acoustics*, **113** (2), 219–224, (1991). http://dx.doi.org/10.1115/1.2930172.

[16] Lancaster, P. and Prells, U. Inverse problems for damped vibrating systems, *Journal of Sound and Vibration*, **283** (3–5), 891–914, (2005). http://dx.doi.org/10.1016/j.jsv.2004.05.003.

[17] Pilkey, D. F. Computation of a damping matrix for finite element model updating, PhD Thesis, Virginia Polytechnic Institute and State University, (1998).

[18] Friswell, M. I., Inman, D. J., and Pilkey, D. F. The direct updating of damping and stiffness matrices, *AIAA Journal*, **36**, 491–493, (1998). http://dx.doi.org/10.2514/3.13851.

[19] Chen, S. Y., Ju, M. S., and Tsuei, Y. G. Estimation of mass, stiffness and damping matrices form frequency response functions, *Journal of Vibration and Acoustics*, **118** (1), 78–82, (1996). http://dx.doi.org/10.1115/1.2889638.

[20] Fritzen, C. P. Identification of mass, damping, and stiffness matrices of mechanical systems, *Journal of Vibration, Acoustics Stress and Reliability in Design*, **108** (1), 9–16, (1986). http://dx.doi.org/10.1115/1.3269310.

[21] Imregun, M., Visser, W. J., and Ewins, D. J. Finite element model updating using frequency response function data: I. Theory and initial investigation, *Mechanical Systems and Signal Processing*, **9** (2), 187–202, (1995). http://dx.doi.org/10.1006/mssp.1995.0015.

[22] FEMtools, Dynamic Design Solutions, Version 3.6.1.

[23] Allemang, R. J. The modal assurance criterion — Twenty years of use and abuse, *Sound and Vibration*, **37** (8), 14–20, (2003).

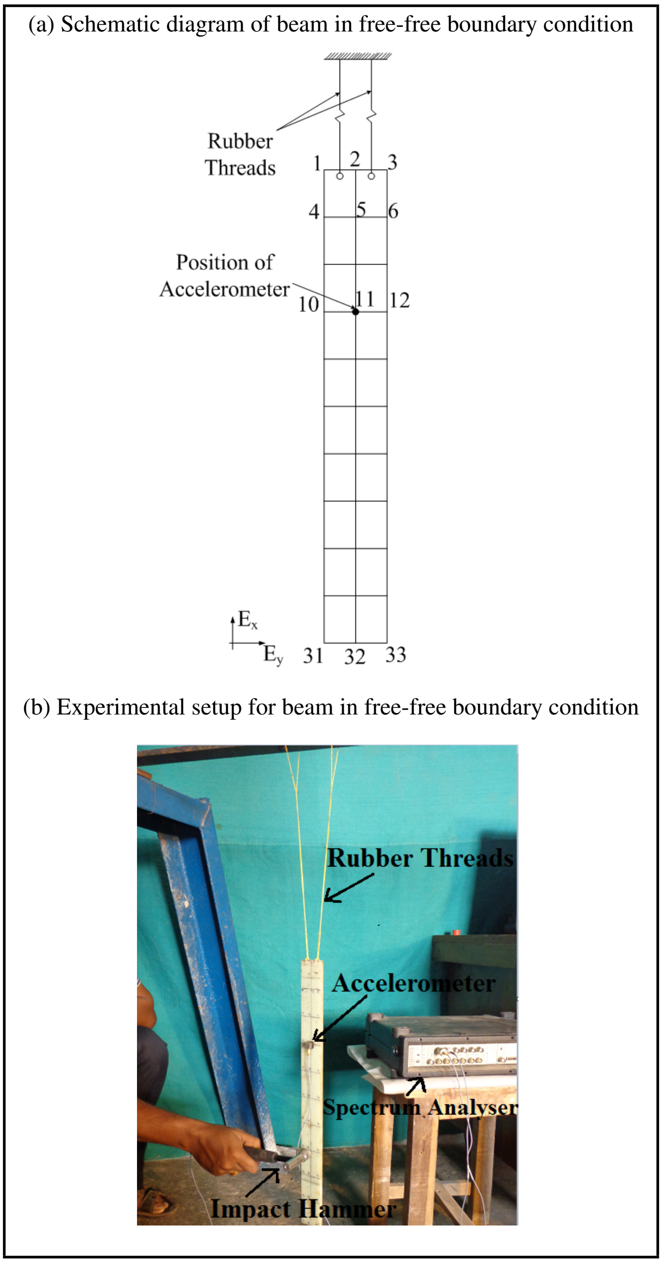

Figure 14. Experimental setup for the FRP beam with free-free boundary conditions.

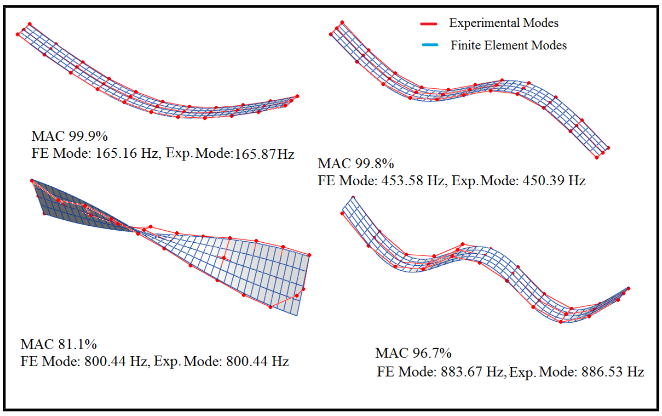

Figure 15. Comparison of experimental and finite element modes for free-free FRP beam.

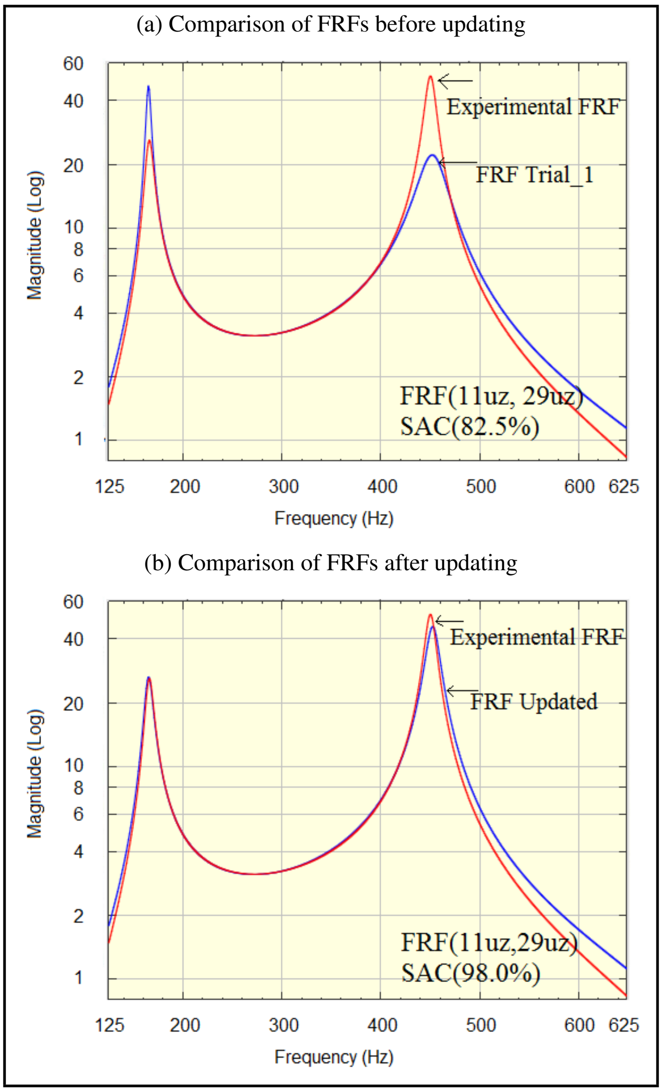

Figure 16. Typical comparison of experimental FRFs with FRFs before and after updating of damping parameters.

[24] Ewins, D. J. Modal Testing: Theory, Practice and Application, Research Studies Press Ltd., London, (2000), 442.

[25] ABAQUS, User's Manual for Version 6.10.

[26] Bathe, K. J. *Finite Element Procedures*, Prentice Hall of India, New Delhi, (2010), 796–798.

[27] PULSE LabShop, Software Package, Bruel & Kjaer, Ver. 13.1.0.246, (2008).

[28] VES ME, Vibrant Technology Inc., Ver. 4.0.0.96, (2007).

[29] Daniel, M. I. and Ishai, O. *Engineering Mechanics of Composite Materials*, Oxford University Press, (2009).

[30] Standard Test Method for Tensile Properties of Polymer Matrix Composite Materials, ASTM Standard D3039/D3039M-2008, (2008). http://dx.doi.org/10.1520/d3039_d3039m.

An Experimental Study on Gear Diagnosis by Using Acoustic Emission Technique

Şaban Ulus and Selçuk Erkaya

Erciyes University, Engineering Faculty, Mechatronic Engineering Department, 38039, Kayseri, Turkey

(Received 24 June 2014; accepted 1 January 2015)

Acoustic Emission (AE) is one of the condition monitoring and diagnosing techniques of rotating machine elements such as gears, bearings, etc. So far, many studies about fault diagnosis on gearboxes have been implemented for vibration monitoring. In addition, a great deal of research on spur gears has been done for understanding the possible gear faults by considering their acoustic characteristics. In this study, possible faults in gears were analysed by the AE technique. A single-stage gearbox system comprising both helical and spur gears was used to identify the existence of possible gear faults, such as pitting and cracking at the tooth root. Noise signal in time-domain is converted to frequency-domain by using Fast Fourier Transform (FFT). In the experimental stage, artificial faults were implemented, and some mathematical parameters such as Root Mean Square error (RMS), Crest Factor (CF), and maximum value of noise level were considered to identify the fault occurrence at the meshing gear. The results show that the AE technique is very effective in diagnosing the defects in a gear system by a contactless measurement. Also, compared to the other diagnostic approaches, it is clear that the gear defects can be determined at an earlier stage by the AE technique.

NOMENCLATURE

AE	Acoustic emission
FFT	Fast Fourier transform
RMS	Root mean square
CF	Crest factor
FCM	Fault condition monitoring
EI	Energy Index
f_{R1}	Rotation frequency of 300 rpm
f_{R2}	Rotation frequency of 500 rpm
f_{R3}	Rotation frequency of 700 rpm
dB	Decibel
SPL	Sound pressure level
BPF	Band pass filter
$P(t)$	Instantaneous sound pressure
T	Time interval averaging
x_{peak}	Maximum peak value of the signal
P_{RMS}	Root mean square value of the sound pressure level
CF0	Crest factor for no loaded condition
CF1	Crest factor for 1 Nm loaded condition
CF3	Crest factor for 3 Nm loaded condition
RMS0	Root mean square value for no loaded condition
RMS1	Root mean square value for 1 Nm loaded condition
RMS3	Root mean square value for 3 Nm loaded condition

1. INTRODUCTION

In the industry today, in order to meet consumer needs, continuity of the production and safety of the processes are of crucial importance. Continuous Fault Condition Monitoring (FCM) can reduce downtime and the total cost of products. In spite of the fact that the initial capital investment cost is high for setting the FCM system, monitoring the health of the structures has a great importance, and FCM requirements in the industry are increasing day by day. Providing a method of early detection of structural, mechanical, or electrical problems allows operators to predict where faults occurred and suggest an approximate time that the system will break down. Unexpected machine failure causes both hitches of the production schedule and increases in cost with financial loss. For this reason, Predictive Maintenance methods are very important. One of them is the Acoustic Emission (AE) technique. It requires a contactless measurement, which is an advantage for mechanical systems and their parts. Any abnormalities or defects in the machinery or equipment must be detected and analysed at an early stage to avoid major problems. Therefore, FCM of rotating machinery, such as at gears and bearings, has a crucial role in the industry, as it keeps the system in a healthy condition for maximum productivity, while detecting and diagnosing faults at an early stage. As a result, it is possible to prevent serious problems, damages, and more cost.[1]

It is difficult to diagnose possible gear faults such as micro-cracks and pitting because of their minimal effect on the system, and these kinds of faults can lead to a rapid destruction of the teeth in meshing gears. Micro-cracks and pitting in gear teeth can be a catastrophic problem resulting in tooth breakage while the system is running. Nowadays, fault diagnosis techniques for rotating machinery, such as vibration monitoring and temperature detection analysis, need a measurement technique with contact. Although vibration monitoring techniques are quite common for detecting and diagnosing faulty conditions of rotating machinery, the AE technique provides early detection of faults.[2]

In the last two decades, a new method for early fault diagnosis, the AE technique, has been researched and gained increasing attention. AE is defined as a matter that results in the generation of structure- or fluid-borne waves due to the rapid release of energy from localised sources within or on the surface of a material. The application of the AE technique is well documented in recent research, and investigators have observed some advantages over classical monitoring techniques. In gearboxes, some investigators have studied the application of AE technology for diagnostic and prognostic purposes.[3,4] Other investigators analysed AE in detecting bending fatigue on spur gears, and noted that AE was more sensitive to crack propagation than vibration and stiffness measurements, and AE was also found to be more sensitive to surface damage than other fault condition monitoring techniques.[5] Husin, et al.[1] investigated the online fault condition monitoring techniques and noted that AE was a complimentary tool for proactive maintenance. Loutas, et al.[6] employed some experimental research on fault diagnosis of gearboxes by using the AE technique. They generated some artificial defects on gears and obtained satisfactory results from AE measurements. Tan and Mba[7,8] investigated the relations between the surface roughness, contact resistance, and AE levels of spur gears under partial elastohydrodynamic lubrication. These observations showed that rotation speed was more efficient than loading conditions on AE levels. They emphasized the surface roughness, rotation speed, and oil temperature for AE measurements. Energy levels of the acquired signal in the analysed time-domain and the Energy Index (EI) for statistical measurements were noted in Al-Balushi and Samanta's work.[9] They also studied one helicopter gearbox by using the AE technique, and comparisons between AE and vibration measurements were implemented. They indicated that AE was more sensitive on early fault diagnosis than the vibration method. In their work, spur gears were used, and relations between oil film thickness, temperature, and AE activity were analysed. It was shown that AE activity was affected by surface asperity contacts more than loading condition.[10]

Belsak and Flasker[11] investigated the crack at the tooth root of the gear, which was a common fault for gearboxes, and they used time- and frequency-domain for damaged and defect-free conditions on crack propagation. The same group[12] investigated the crack size and sideband occurrence by comparing defect-free conditions by using short time frequency spectrum analysis. Fault diagnosis on a single-stage gearbox test rig with only spur gears, similar to vehicle gearboxes, was studied by using FFT and RMS for obtaining the fault characteristics of the gear.[5] It was proved that the early fault detection on crack propagation was possible by AE. Combet, et al.[13] studied two different waveform methods to obtain local and instantaneous averages of the signals. Local faults were recognized, and they found a diagnosing method dependent on the angle at a special frequency range. Raja Hamzah and Mba[14] noted that AE results for spur gears were more sensitive than those for helical gears. Surface roughness and contact length was also important for the acoustic characteristics of gears. Baydar and Ball[15] used an instantenous power spectrum instead of time-frequency distribution for helical gears, and they noted that this method had an advantage not only for fixed loading conditions, but also for variable loading conditions. The same research group[16] investigated the AE and vibration techniques on a cracked gear tooth, a broken gear tooth, and local cracks by using Wigner-Ville distribution, and they obtained results indicating that AE has some advantages on early fault diagnosis. Some diagnosing techniques[17–19] were implemented by using statistical measurements for helicopter gearbox transmission systems, and these methods were found to be reliable, but some of the experiments were not repeated.

In spite of the common use of vibration monitoring method in rotating machinery, up to now, classical vibration monitoring analysis techniques have not been enough for detecting incipient failures such as pitting, micro-cracks, and surface wear in gears. Machine conditions and faults such as gear failures, unbalance, shaft missallignment, and bearing defects can be monitored by using acoustic emission signals at machines' operating conditions. These signals can be used not only for growing failures, but also for incipient failures of the rotating machineries, to reduce or eleminate catastrophic damages. In this study, the AE technique was used to analyse and evaluate the gear defects on both spur and helical gears. This study was employed as an experimental research and is organized as follows: Section 2 shows the materials and methods used in this experimental study. Results obtained from the test system by using the AE technique are outlined in Section 3. And Section 4 gives a conclusion about the experimental study on the gear fault condition monitoring.

2. MATERIALS AND METHODS

In order to observe and analyse AE in gears, a gearbox test rig was designed. Experiments were performed on a single-stage gearbox test rig; that is, as a vehicles' transmission system. A 3 KW electric motor was used for both spur and helical gears. A three-phase frequency inverter, Delta VFD-E, was used for the case of different working speeds. A pinion gear has 51 teeth and the driven gear has 70 teeth. The pinion gear has $f_{R1} = 5$ Hz, $f_{R2} = 8.3$ Hz, and $f_{R3} = 11.67$ Hz rotation frequencies for 300 rpm, 500 rpm, and 700 rpm rotation speeds, respectively. Also, the meshing frequencies for both pinion and driven gears are 255 Hz, 425 Hz, and 595 Hz for 300 rpm, 500 rpm, and 700 rpm rotation speeds, respectively. In the experimental measurements, AE data was recorded after the following processes: (i) the gearbox system was run for about 2 hours to satisfy a working condition stability of the system, and (ii) an acoustic emission sensor was located to collect the signal for data processing.

A tool for acoustic measuring, a Bruel-Kjaer (B&K) portable and multi-channel pulse 3560-B-X05 analyser and 4189-A021 microphone with a pre-amplifier, were used to obtain and analyse the results. An analysis programme was able to evaluate the time- and frequency-domain analysis of the obtained signals from the gearbox test rig. The analyser is able to give necessary information about AE signals by measuring Sound Pressure Level (SPL), which is a logarithmic measure of the effective sound pressure of a sound relative to a reference value. It is measured in decibels (dB) above a standard reference level. The commonly used "zero" reference sound pressure in air is 20 μPa.[20] Sound pressure produces a signal in the microphone of the sound level meter, and the output of the signal is sent to the frequency analyser to get the character of the noise. For all that, before all of the measurements, the test environment and compatibility of the devices were checked.

Table 1. Specification of spur and helical gears.

SPUR GEAR SPECIFICATION		
Parameters	Pinion	Driven
No. of Teeth	51	70
Module	3	3
Shaft Angle	90°	90°
Addendum	3 mm	3 mm
Dedendum	3.5 mm	3.5 mm
Pitch Circle Diameter	153 mm	210 mm
Face Width	25.1 mm	25.1 mm

HELICAL GEAR SPECIFICATION		
Parameters	Pinion	Driven
No. of Teeth	51	70
Module	3 mm	3 mm
Shaft Angle	90°	90°
Addendum	3 mm	3 mm
Dedendum	3.5 mm	3.5 mm
Pitch Circle Diameter	162.819 mm	223.477 mm
Face Width	25.1 mm	25.1 mm
Direction	Right	Left
Pressure Angle	20°	20°
Helix Angle	20°	20°

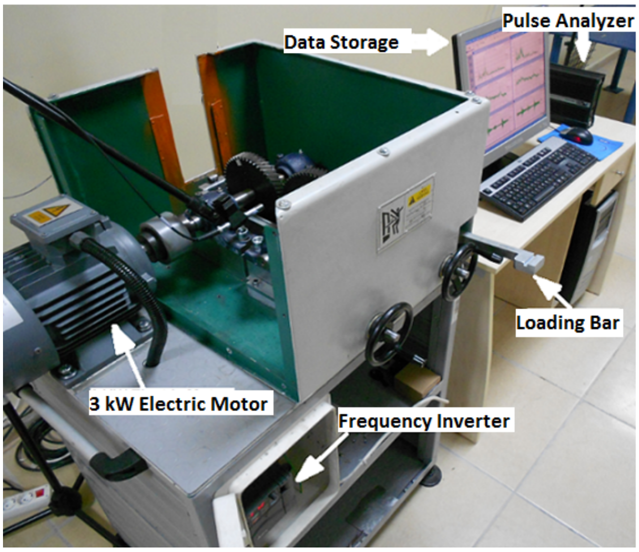

Figure 2. Gearbox Test System.

The AE signal was amplified and filtered using 20/40/60 dB, AE PREAMP/100–1200 KHz with a band pass filter (BPF). The PAC AE5A amplifier is a high performance AE system that amplifies and filters received AE signals from the preamplifier. A block diagram of the measuring system is given in Fig. 1.

Both spur and helical gears have a module of 3 mm. Distances for the shaft center of spur gears and the shaft center of helical gears are 181.5 mm and 193.15 mm, respectively. Detailed information for the gears are given in Table 1. A sliding mechanism was added to the system for setting the different distances between the shaft centers. A loading disc was attached to end of the driven gear shaft to load and break the gear system. The test rig used to measure acoustic signals is shown in Fig. 2.

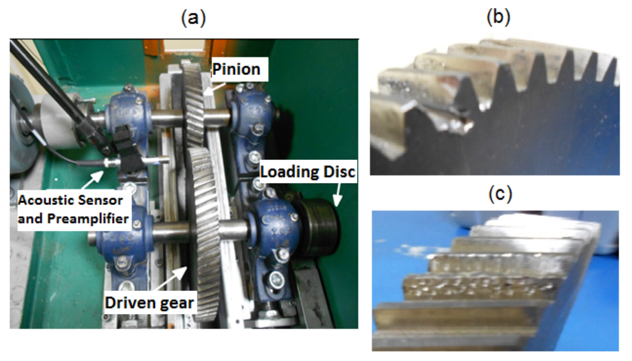

Figure 3. (a) Gearbox test system with AE sensor; (b) Cracked tooth root; (c) Pitting fault.

2.1. Acoustic Emission Technology

Acoustic emission is defined as the generation of transient elastic waves by the rapid release of energy within or on the surface of a material. According to Kaiser,[21] crystalline solids could propagate sound under a mechanical load. Kaiser used high frequency sensors and electrical amplifiers to hear sounds in a wide range of materials under loading conditions. AE sensors are one of the most important tools for obtaining acoustic sound, and they are usually made of piezocrystalls. AE sensors detect mechanical movements or stress waves, and convert them into an electrical signal.

The main advantage of AE is its high sensitivity. The AE method is the most sensitive monitoring technique for early fault detection in rotating machine elements, especially in today's industry. AE sensors can detect sound beyond the human hearing frequency range, between 100 kHz to 1 MHz. AE detection may not be enough for fault condition monitoring itself. The important thing with the application of the AE technique is the attenuation of the signal, and the AE sensor has to be close to source of the noise generation. Therefore, in this study, the AE sensor was placed close to the source of the noise generation; that is, at a 15 cm distance from the left side of the meshing point, without any contact with the gears (Fig. 3).

Signals obtained from the AE sensor are transferred to a B&K multi-channel pulse analyser and data acquisiton system, passing through the pre-amplifier, which has a range 40 to 60 dB.

The traditional techniques for damage detection are based on some statistical parameters of the vibration or acoustic energy. For defect-free conditions of gears, Stewart[22] indicated that the regular meshing component of the signal is dominated by the mesh frequency and its harmonics. It is also observed that the sidebands about the meshing components at the rotational frequency of the gear.

Signal processing techniques (such as time and frequency analysis) and some statistical-mathematical parameters (such as RMS, CF, and average fault) were used to evaluate the faulty conditions of a material. Sound pressure generally can be expressed as the effective sound pressure for a given period of time. The effective value of sound pressure is the RMS value of the instantaneous sound pressure taken at a point over a pe-

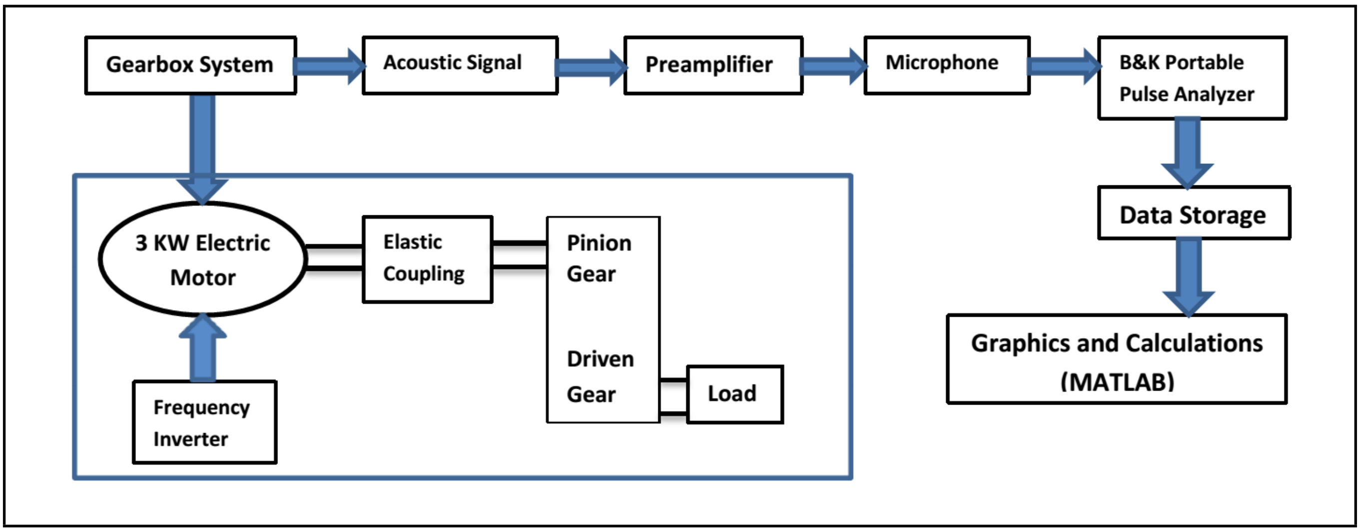

Figure 1. Block diagram of experimental measurement.

riod of time, as

$$P_{\text{RMS}} = \sqrt{\frac{1}{T}\int_0^T P^2(t)\,dt}; \qquad (1)$$

where $P(t)$ is instantaneous sound pressure, and T is the average time interval.[20] The CF is defined as the maximum peak value of the sound pressure signal x, over a period of time (T) divided by the RMS value of sound pressure, and is expressed by

$$\text{CF} = \frac{x_{\text{peak}}}{P_{\text{RMS}}}; \qquad (2)$$

where P_{RMS} is the RMS value of the sound pressure, and x_{peak} is the maximum peak value of the signal. CF values are usable to understand the presence of a small amount of maximum local defects over a signal.

3. RESULTS

In this study, gear faults were investigated by the AE technique. Some artificial faults were formed on gears for experimental investigations. The SPL of the AE signals were measured at 300 rpm, 500 rpm, and 700 rpm shaft rotation speeds, and both helical and spur gear faults were outlined in a frequency spectrum under different loading conditions. Dry friction conditions were considered for all measurements. By considering the used running speeds, it was seen that the meshing frequency and its harmonics/sidebands were dominant between 0 and 1200 Hz. For this reason, the frequency range of the signal in all measurements is arranged as 0 Hz–1200 Hz. In order to eleminate the environmental noise effects, an isolated condition from other noise sources, such as room and motor noise, was implemented for the test system.

As seen in Fig. 4, AE peaks were due to the cracked tooth root that appeared in the meshing harmonics of the gear, and sidebands were also observed near the maximum fault frequency; that is, 765 Hz gives the third harmonic of the gear.

As shown in Fig. 4, at 300 rpm, the crest factor for the no-loaded condition (CF0) was 22.07, 1 Nm for the loaded condition (CF1) was 21.02, and 3 Nm for the loaded condition (CF3) was 20.97. When the gears are in an undamaged state,

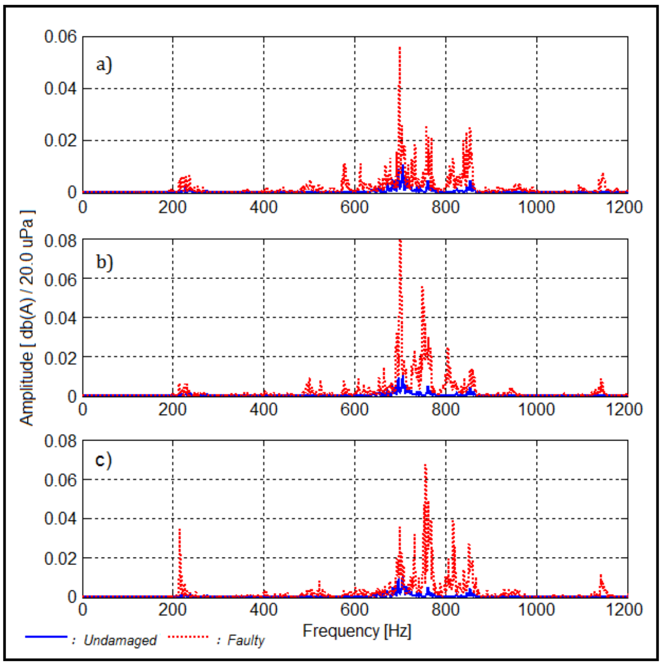

Figure 4. Cracked tooth root fault for helical gear at 300 rpm rotation speed under (a) no loaded condition, (b) 1 Nm loaded condition, and (c) 3 Nm loaded condition.

the crest factor values were relatively lower than those of gears in a faulty state because of the short peaks of the undamaged state of the gear. As seen in the results, very high CF values resulted from high peaks. The root mean square for the no-loaded condition (RMS0) was 0.043 Pa, the root mean square for 1 Nm for the loaded condition (RMS1) was 0.0067 Pa, the root mean square for 3 Nm for the loaded condition (RMS3) was 0.0069 Pa, and those RMS values show the efficient value of faults. It can be clearly seen that there is an increase of RMS values by loading condition.

Results for 500 rpm rotation speed are shown in Fig. 5. The obtained SPL of the gear was higher than that of 300 rpm running speed's results. Sidebands observed near the meshing harmonics related to gear tooth cracks were observed at 700 Hz. In this running speed, CF0, CF1, and CF3 were obtained as 21.98, 20.36 and 23.77, respectively. Also, RMS0, RMS1,

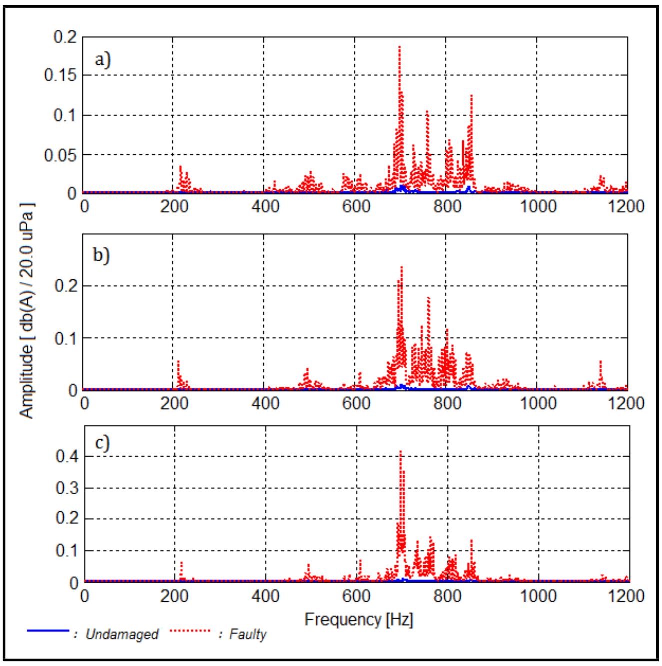

Figure 5. Cracked tooth root fault for helical gear at 500 rpm rotation speed under (a) no loaded condition, (b) 1 Nm loaded condition, and (c) 3 Nm loaded condition.

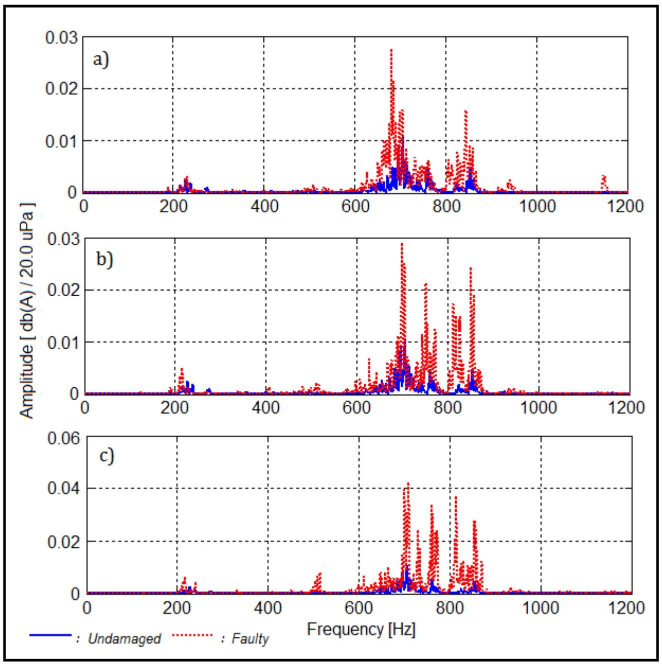

Figure 7. Pitting fault for helical gear at 300 rpm rotation speed under (a) no loaded condition, (b) 1 Nm loaded condition, and (c) 3 Nm loaded condition.

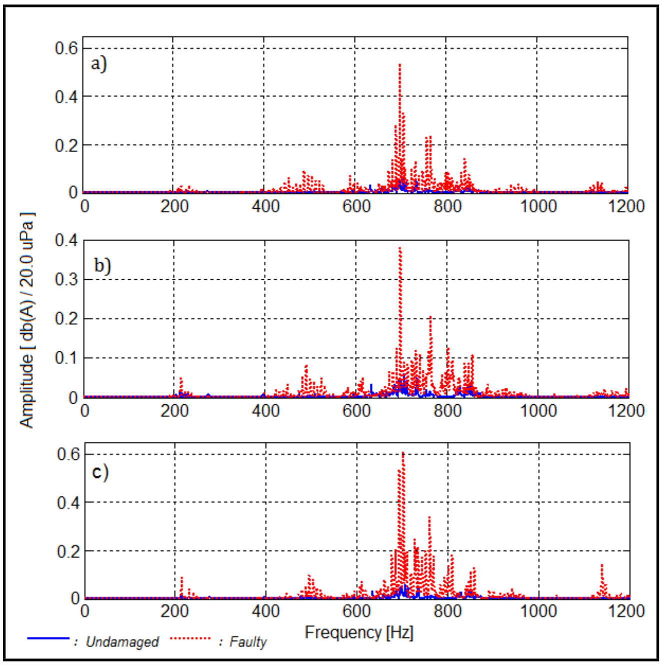

Figure 6. Cracked tooth root fault for helical gear at 700 rpm rotation speed under (a) no loaded condition, (b) 1 Nm loaded condition, and (c) 3 Nm loaded condition.

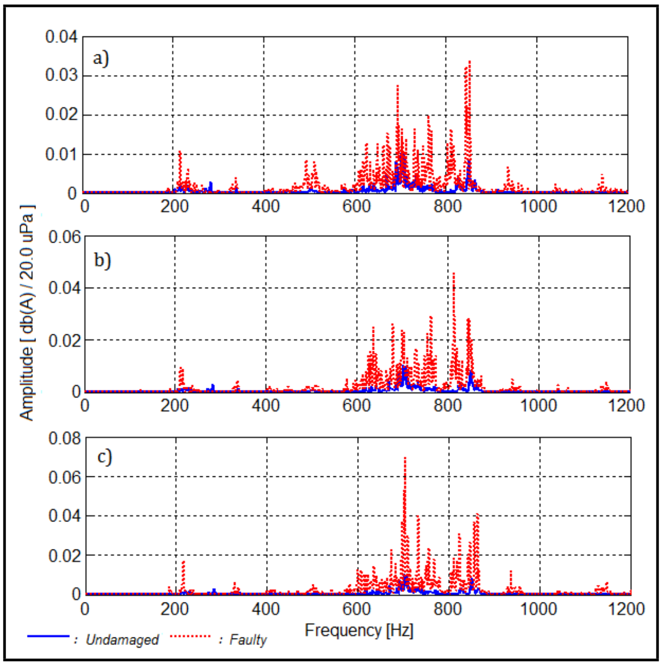

Figure 8. Pitting fault for helical gear at 500 rpm rotation speed under (a) no loaded condition, (b) 1 Nm loaded condition, and (c) 3 Nm loaded condition.

and RMS3 were 0.0147, 0.0222, and 0.0267 Pa, respectively. These RMS values show the efficient value of sound pressure in the graph, and also those RMS values are increased due to increasing loading condition.

Figure 6 gives the results of a 700 rpm rotation speed. As outlined in this figure, SPL of the gear at 700 rpm was higher than that of 300 and 500 rpm. The maximum value of SPL for 700 rpm rotation speed was observed at 700 Hz. At 700 rpm, CF0, CF1, and CF3 were 24.4, 23.39, and 22.3, respectively. Also, RMS0, RMS1, and RMS3 were obtained 0.0319, 0.0249, and 0.0463 Pa, respectively.

For the case of pitting fault in the helical gear, the results at a speed of 300 rpm are given in Figs. 7–9. AE peaks for both cracked tooth roots and pitting faults were seen between 700 Hz and 850 Hz. However, pitting fault on the tooth surface has lower sound pressure levels than that of cracked tooth root. Statistical results for the crest factor were also given as 20.25, 19.86, and 18.8 for CF0, CF1, and CF3, respectively. RMS values were calculated as 0.0026, 0.0028, and 0.0048 Pa for no load, and loaded with 1 Nm and 3 Nm, respectively.

For 500 rpm running speed, calculated values of pitting on the helical gear tooth surface are outlined in Fig. 8 as CF0 = 18.7, CF1 = 20.07, CF3 = 21.1, and RMS0 = 0.0036 Pa,

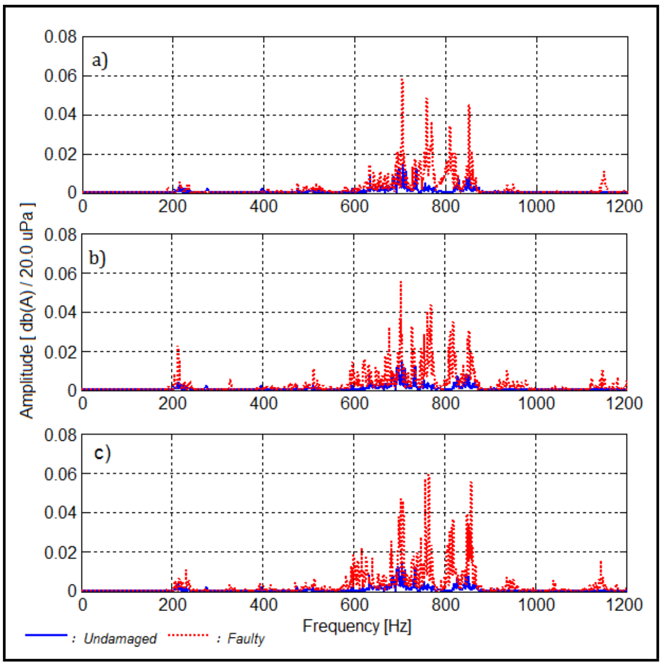

Figure 9. Pitting fault for helical gear at 700 rpm rotation speed under (a) no loaded condition, (b) 1 Nm loaded condition, and (c) 3 Nm loaded condition.

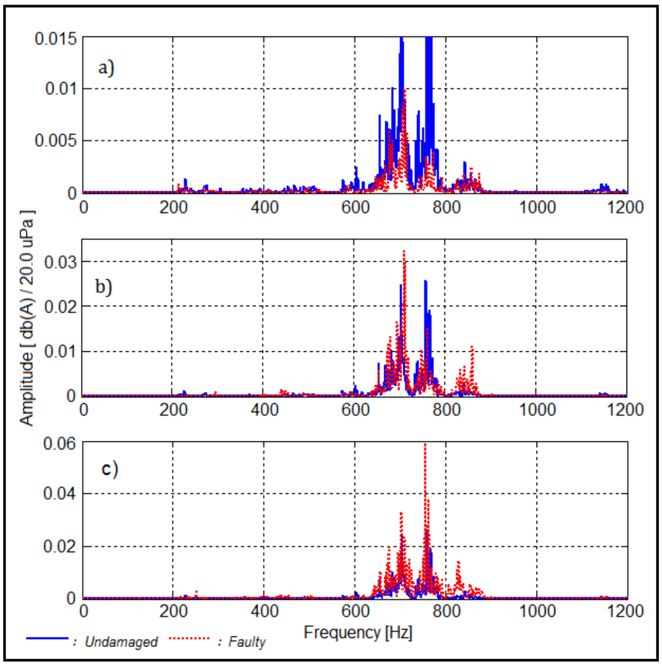

Figure 10. Cracked tooth root fault for spur gear at 300 rpm rotation speed under (a) no loaded condition, (b) 1 Nm loaded condition, and (c) 3 Nm loaded condition.

RMS1 = 0.0045 Pa, and RMS3 = 0.0056 Pa.

In Fig. 9, at a running speed of 700 rpm, due to pitting on the helical gear tooth surface, results were calculated as CF0 = 17.8, CF1 = 18.317, and CF3 = 18.14, and RMS0 = 0.0039 Pa, RMS1 = 0.0061 Pa, and RMS3 = 0.0071 Pa. By evaluating the results in Figs. 7–9, an increase was observed at RMS values of SPL for pitting faults due to increasing loading condition and rotational speed of the shaft. CF values are also high as in the previous results. For easy evaluations, these statistical results of CF and RMS values for a helical gear with a cracked tooth root and pitting faults are outlined in Table 2.

SPL for spur gears originated from cracked tooth roots and pitting faults are presented in Figs. 10–15. Measurement results at a running speed of 300 rpm with and without loaded conditions are depicted in Fig. 10. AE peaks at the loaded condition are observed more clearly than those at no-loaded condition. A measurement of 765 Hz indicates the third harmonic of the gear at 300 rpm, and this result is based on the gear fault itself, such as clearance on the gear shaft. Sidebands near harmonic frequencies indicate faults such as a crack tooth, a broken tooth, etc. CF and RMS values for a running speed of 300 rpm are shown in Fig. 10 as CF0 = 13.49, CF1 = 22.23, CF3 = 23.59, and RMS0 = 0.00051 Pa, RMS1 = 0.0025 Pa, and RMS3 = 0.0039 Pa. It is clear that the loading conditions increase the RMS values.

Figure 11 indicates that the spectrum has similar character with previous result at 500 rpm. The calculated values for CF and RMS can be given as CF0 = 19.9, CF1 = 20.5, CF3 = 19.92, and RMS0 = 0.0037 Pa, RMS1 = 0.0069 Pa, RMS3 = 0.0068 Pa. In Fig. 12, SPL of the cracked tooth root at 700 rpm are presented. The mathematical results are outlined as 22.98, 20.74 and 18.8 for CF0, CF1, and CF3, respectively. Similarly, RMS values are given as 0.0033, 0.0049, and 0.0064 Pa for no load, loaded with 1 Nm and 3 Nm conditions, respectively.

Figures 13–15 specify the results which originated from the pitting fault on a spur gear's tooth surface. SPL for a pitting fault on the spur gear is not so evident for 300 rpm. According to the figure, the obtained statistical results are given as CF0 = 18.81, CF1 = 18.9, and CF3 = 20.27, and RMS0 = 0.0023 Pa, RMS1 = 0.0014 Pa, and RMS3 = 0.0015 Pa. Figure 14 presents the results at a shaft running speed of 500 rpm. These results are more evident than those found at 300 rpm. The calculated parameters for CF and RMS are read as CF0 = 20.58, CF1 = 19.47, CF3 = 17.9, and RMS0 = 0.0051 Pa, RMS1 = 0.0018 Pa, and RMS3 = 0.0030 Pa. The results at a speed of 700 rpm, as seen in Fig. 15, show that two peaks

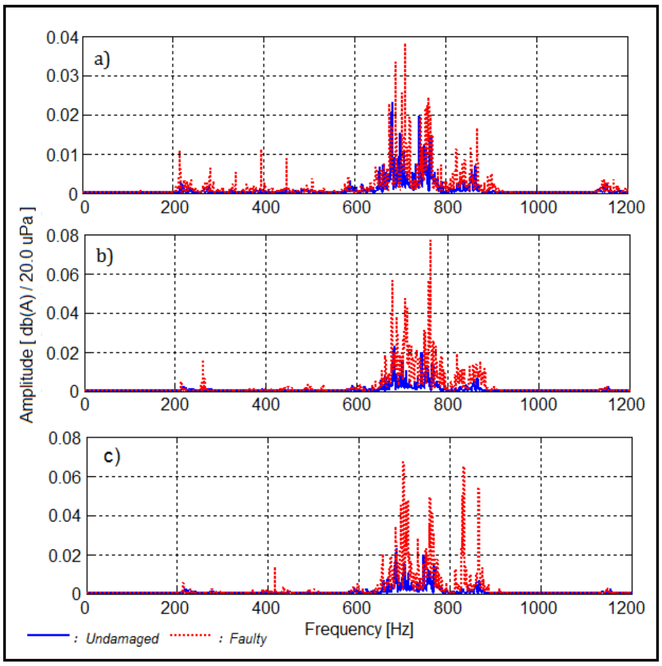

Figure 11. Cracked tooth root fault for spur gear at 500 rpm rotation speed under (a) no loaded condition, (b) 1 Nm loaded condition, and (c) 3 Nm loaded condition.

Table 2. RMS and CF results of helical gears.

	HELICAL GEAR RESULTS for CRACKED TOOTH ROOT FAULT			HELICAL GEAR RESULTS for PITTING FAULT		
	300 rpm	500 rpm	700 rpm	300 rpm	500 rpm	700 rpm
RMS0	0.043	0.0147	0.0319	0.0026	0.0036	0.0039
RMS1	0.0067	0.0222	0.0249	0.0028	0.0045	0.0061
RMS3	0.0069	0.0267	0.0463	0.0048	0.0056	0.0071
CF0	22.07	21.98	24.4	20.25	18.7	17.8
CF1	21.02	20.36	23.39	19.86	20.07	18.317
CF3	20.97	23.77	22.3	18.8	21.1	18.14

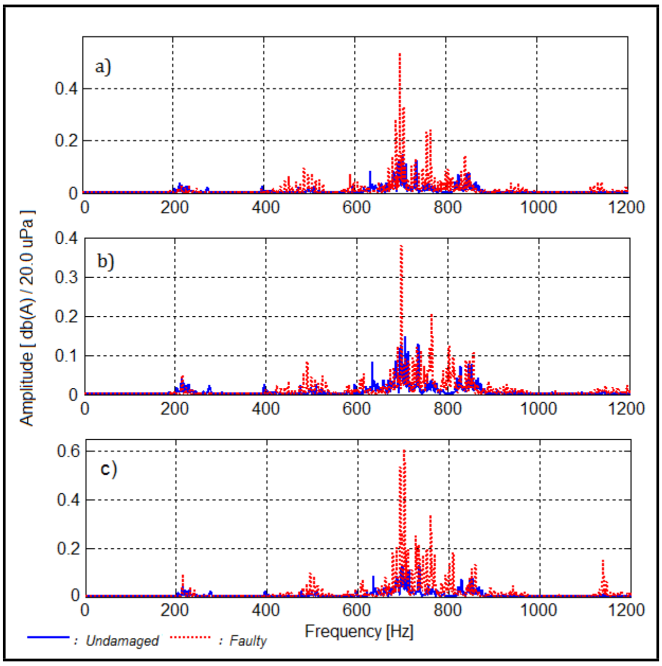

Figure 12. Cracked tooth root fault for spur gear at 700 rpm rotation speed under (a) no loaded condition, (b) 1 Nm loaded condition, and (c) 3 Nm loaded condition.

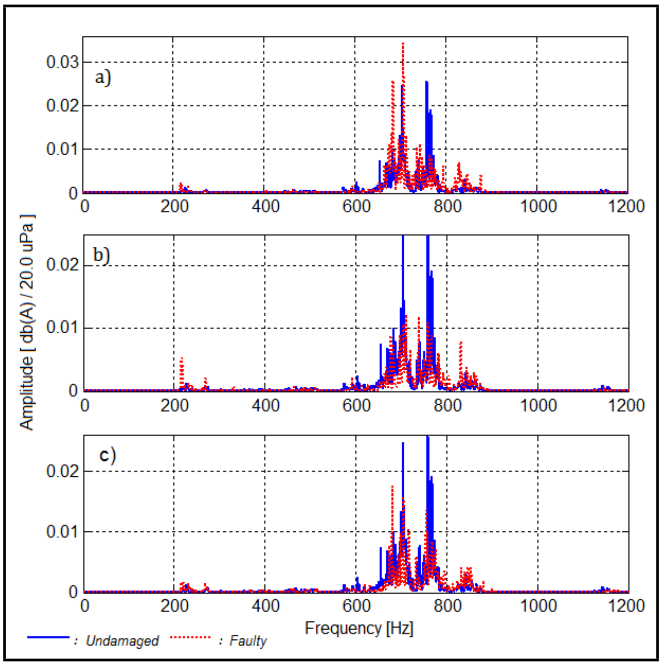

Figure 13. Pitting fault for spur gear at 300 rpm rotation speed under (a) no loaded condition, (b) 1 Nm loaded condition, and (c) 3 Nm loaded condition.

are observed as sidebands of the meshing harmonics, and are evident without any loading. As confirmed from the figure, CF and RMS values are calculated as CF0 $= 27.93$, CF1 $= 22.6$, CF3 $= 20.8$, and RMS0 $= 0.0275$ Pa, RMS1 $= 0.0019$ Pa, and RMS3 $= 0.0039$ Pa. CF values indicate the peak level of the fault signal. A load at the gear wheel plate increases RMS values. For easy evaluations, the statistical results of CF and RMS values for a spur gear with a cracked tooth root and pitting faults are outlined in Table 3.

When analysing the results, it can be seen that CF and RMS values are related to damage severity in the gear unit. All CF values indicate the damage with regard to its high value, as discussed in work by Tan and Mba.[8] RMS values show the efficient value of the signal between undamaged and faulty conditions. From the results at the given operating time, it can be seen that the greater the applied running speed, the greater the AE RMS value. Higher running speeds and loading conditions affect the RMS level of the signal increasingly. Besides all these measurements, the maximum and average values of the signals are increased. In addition, the measurements were carried out after the assembly of different gear types with different faults in the experimental test rig. Measurements were repeated five times for every gear type and condition. As seen from Fig. 10 — that is, a cracked tooth root fault for a spur gear at a rotation speed of 300 rpm — the dominant effect arises from the undamaged condition of spur gear. This problem is probably due primarily to sensitivity losses of assembly conditions, such as gear meshing characteristics, looseness, imperfect alignments of the shaft, etc.[8,10,16] By comparison with the RMS results, CF values have an irregular change in case of loading and running speed changes of the system. As shown in Eq. (2), the reason for this irregularity can arise from the highest AE peak taken into account in the signal relative to RMS.[23,24] In detecting and diagnosing fault signals, RMS results have been more indicative than CF values.

4. CONCLUSION

In this study, AE results obtained from the gearbox test system were analysed under different running speeds and loading conditions for both spur and helical gears. AE data was taken in time domain and converted to frequency domain by using FFT in order to clearly understand the occurrence of the fault location and its source.

Measurements were implemented by using an acoustic sensor near the meshing points of the gears without any contact to the test system. The artificially created gear damages, such as pitting and cracks at the tooth roots, were apparent in the AE graphs. At the meshing frequencies, AE peaks indicate the normal condition of the gear. AE peaks observed near the meshing harmonics, which are called sidebands, indicate the gear

Table 3. RMS and CF results of spur gears.

	SPUR GEAR RESULTS for CRACKED TOOTH ROOT FAULT			SPUR GEAR RESULTS for PITTING FAULT		
	300 rpm	500 rpm	700 rpm	300 rpm	500 rpm	700 rpm
RMS0	0.00051	0.0037	0.0033	0.0023	0.0051	0.0275
RMS1	0.0025	0.0069	0.0049	0.0014	0.0018	0.0019
RMS3	0.0039	0.0068	0.0064	0.0015	0.0030	0.0039
CF0	13.49	19.9	22.98	18.81	20.58	27.93
CF1	22.23	20.5	20.74	18.9	19.47	22.59
CF3	23.59	19.92	18.8	20.27	17.9	20.8

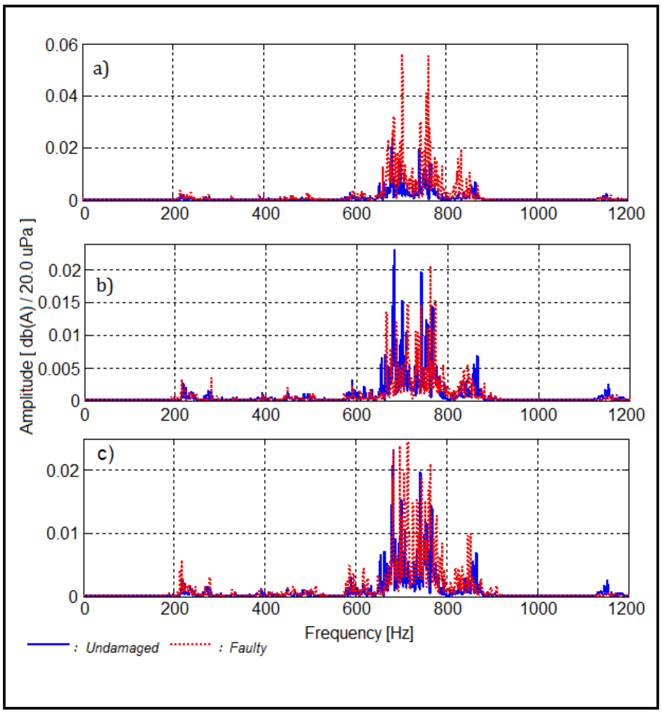

Figure 14. Pitting fault for spur gear at 500 rpm rotation speed under (a) no loaded condition, (b) 1 Nm loaded condition, and (c) 3 Nm loaded condition.

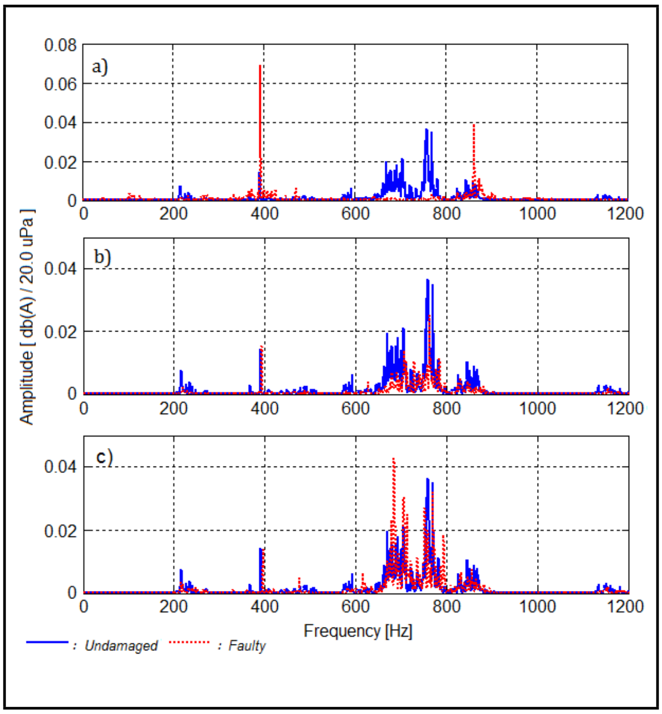

Figure 15. Pitting fault for spur gear at 700 rpm rotation speed under (a) no loaded condition, (b) 1 Nm loaded condition, and (c) 3 Nm loaded condition.

tooth damage, such as cracks and pitting faults. One of the significant observations was the direct relation between AE level and loading conditions. From the statistical values, RMS of the SPL for both helical and spur gears is more consistent and sensitive. Increasing loading and running speed conditions for both gear types caused a change in RMS levels. Also, CF was measured at more than 6, and indicated the damage with its high value in all cases. CF shows the damage severity in comparison with the changing RMS value of the signal. The RMS value of the sound signal changed with the loading conditions at the given frequency range. The loading condition affected the SPL of the gear, and AE peaks were observed at a higher sound level. For this reason, the increasing peak level/RMS ratio indicates a bigger CF value, which shows the severity of the local fault. Corresponding to the running speed of the gear, in general cases, an increasing speed increases the SPL of the signal. Gear defects, loading, and running speed increasingly affect the maximum and average values of the signal. All these statistical measurements confirm the existence of a fault in the gear system by comparing their reference value. Considering the gear types used in the measurements, it can be concluded that sound levels at helical gear meshing points are clearer, and maximum and average values of the fault signal are more apparent than that of spur gears.

ACKNOWLEDGEMENTS

This study is a part of the research project FBA-12-4111. The authors wish to express their thanks for financial support provided by the Scientific Research Projects Coordination Unit of Erciyes University, in carrying out this study.

REFERENCES

[1] Husin, S., Mba, D., and Raja Hamzah, R. I. Viability of application of the acoustic emission (AE) technology for the process and management of maintenance in industries: defect detection, on-line condition monitoring, diagnostic and prognostic tool, *Proceedings of the International Multi Conference of Engineers and Computer Scientists*, **3**, 978–988, (2010).

[2] Singh, A., Houser, D. R., and Vijayakar, S. Detecting gear tooth breakage using acoustic emission: a feasibility and sensor placement study, *Journal of Mechanical Design*, **21**, 587–593, (1999). http://dx.doi.org/10.1115/1.2829503.

[3] Eftekharnejad, B. and Mba, D. Seeded fault detection on helical gears with acoustic emission, *Applied Acoustics*, **70**, 547–555, (2009). http://dx.doi.org/10.1016/j.apacoust.2008.07.006.

[4] Mba, D., Cooke, A., Roby, D., and Hewitt, G. Detection of shaft-seal rubbing in large-scale power generation turbines with acoustic emissions; case study, *Proceedings of Instution of Mechanical Engineers, Part A: Journal of Power and Energy*, **218** (2), 71–81, (2004). http://dx.doi.org/10.1243/095765004773644076.

[5] Metwalley, S. M., Hammad, N., and Abouel-Seoud, S. A. Vehicle gearbox fault diagnosis using noise measurements, *International Journal of Energy and Environment*, **2** (2), 357–366, (2011).

[6] Loutas, T. H., Kalaitzoglou, J., Sotiriades, G., Kayias, E., and Kostopoulos, V. Diagnosis of artificial gear defects on single stage gearbox using acoustic emission, *Advanced Material Research*, **13–14**, 415–420, (2006). http://dx.doi.org/10.4028/www.scientific.net/amr.13-14.415.

[7] Tan, C. K. and Mba, D. Correlation between acoustic emission activity and asperity contact during meshing of spur gears under partial elastohydrodynamic lubrication, *Tribology Letters*, **20** (1), (2005). http://dx.doi.org/10.1007/s11249-005-7793-1.

[8] Tan, C. K. and Mba, D. Limitation of acoustic emission for identifying seeded defects in gearboxes, *Journal of Nondestructive Evaluation*, **24** (1), (2005). http://dx.doi.org/10.1007/s10921-005-6657-9.

[9] Al-Balushi, K. R. and Samanta, B. Gear fault diagnosis using energy-based features of acoustic emission signals, *Proceedings of the Institution of Mechanical Engineers, Part I: Journal of Systems and Control Engineering*, 216–249, (2002). http://dx.doi.org/10.1243/095965102320005418.

[10] Tan, C. K. and Mba, D. Identification of acoustic emission source during a comparative study on diagnosis of a spur gearbox, *Tribology International*, **38**, 469–480, (2005). http://dx.doi.org/10.1016/j.triboint.2004.10.007.

[11] Belsak, A. and Flasker, J. Method for detecting fatigue cracks in gears, *Theoretical and Applied Fracture Mechanics*, **46**, 105–113, (2006). http://dx.doi.org/10.1016/j.tafmec.2006.07.002.

[12] Belsak, A. and Flasker, J. Detecting cracks in the tooth root of the gears, *Engineering Failure Analysis*, **14**, 1466–1475, (2007). http://dx.doi.org/10.1016/j.engfailanal.2007.01.013.

[13] Combet, F., Gelman, L., and La Payne, G. Novel detection of local tooth damage in gears by the wavelet bicoherence, *Mechanical Systems and Signal Processing*, **26**, 218–228, (2012). http://dx.doi.org/10.1016/j.ymssp.2011.07.002.

[14] Raja Hamzah, R. I. and Mba, D. The influence of operating condition on acoustic emission (AE) generation during meshing of helical and spur gear, *Tribology International*, **42**, 3–14, (2009). http://dx.doi.org/10.1016/j.triboint.2008.06.003.

[15] Baydar, N. and Ball, A. Detection of gear deterioration under varying load conditions by using the instantaneous power spectrum, *Mechanical Systems and Signal Processing*, **14** (6), 907–921, (2000). http://dx.doi.org/10.1006/mssp.1999.1281.

[16] Baydar, N. and Ball, A. A comparative study of acoustic emission and vibration signals in detection of gear failures using Wigner Ville distribution, *Mechanical Systems and Signal Processing*, **15** (6), 1091–1107, (2001). http://dx.doi.org/10.1006/mssp.2000.1338.

[17] Dempsey, P. J. A comparison of vibration and oil debris gear damage detection methods applied to pitting damage, NASA/TM-2000-210371, NASA Glenn Research Center, (2000).

[18] Decker, H. J. Crack detection for aerospace quality spur gears, NASA/TM-2002-211492, NASA Glenn Research Center, (2002).

[19] Blunt, D. M. and Keller, J. A. Detection of fatigue crack in a UH-60A planet gear carrier using vibration analysis, *Mechanical Systems and Signal Processing*, **20**, 2095–2111, (2006). http://dx.doi.org/10.1016/j.ymssp.2006.05.010.

[20] Guangzhong, C. Acoustical measurement and fan fault diagnosis system based on LabVIEW, *Practical Applications and Solutions Using LabVIEW Software*, Folea S., Ed., InTech, (2011), **11**, 229–252.

[21] Miller, R. K. and Intire, P. *Nondestructive Testing Handbook, Vol. 5: Acoustic Emission Testing*, American Society for Nondestructive Testing, (1987), 2nd edition.

[22] Stewart, R. M. Some useful analysis techniques for gearbox diagnostics, Technical Report MHM/R/10/77, Institute of Sound and Vibration Research, University of Southampton, (1977).

[23] Dron J. P., Bolaers, F., and Rasolofondraibe, I. Improvement of the sensitivity of the scalar indicators (crest factor, kurtosis) using a de-noising method by spectral subtraction: application to the detection of defects in ball bearings, *Journal of Sound and Vibration*, **270**, 61–73, (2004). http://dx.doi.org/10.1016/s0022-460x(03)00483-8.

[24] Tandon, N. A comparison of some vibration parameters for the condition monitoring of rolling element bearings, *Measurement*, **12**, 285–289, (1994). http://dx.doi.org/10.1016/0263-2241(94)90033-7.

High Damping Characteristics of an Elastomer Particle Damper

Marcelo Bustamante, Samir N. Y. Gerges and Erasmo F. Vergara

Federal University of Santa Catarina, Department of Mechanical Engineering, Laboratory of Vibration and Acoustics, Campus Universitario, P.B. 476, Trindade, Florianopolis, SC, CEP 88040-900, Brazil

Jorge P. Arenas

Institute of Acoustics, University Austral of Chile, PO Box 567, Valdivia, Chile

(Received 16 September 2014; accepted 14 December 2015)

Research testing has led to the development of an Elastomer Particle Damper (EPD), which can add considerable damping to a structure by directing the vibration to a set of interacting elastomer particles through a rigid connection. This vibration treatment presents highly nonlinear behavior that is strongly dependent on both the vibration amplitude and frequency. Curves of damping loss factor (DLF) of an EPD system with vertical motion as a function of frequency and acceleration are reported herein. The results show that the elastomer particle damper has two distinct damping regions. The first region is related to the fluidization state of the particles, as described in the literature, obtained when the damper is subjected to vertical acceleration close to 1 g and frequencies below 50 Hz. The second region presents high values of DLF to acceleration values lower than 1 g, and the frequency range is dependent upon the stiffness of the particles. A high degree of effectiveness is achieved when the working frequency of the elastomer particle dampers is tuned to a natural frequency of a plate and when they are strategically located at points having large displacement. The performance of EPDs was compared with that of a commercial constrained layer damping installed in an aircraft floor panel. The EPDs achieved an acceleration level attenuation in the aircraft floor panel similar to that of the commercial constrained layer damping system.

1. INTRODUCTION

Traditional damping treatments use viscoelastic materials to convert strain energy into heat energy through the relative internal motion between molecules. Energy dissipation can be provided to a vibrating structure by a constrained damping layer in which a viscoelastic material is sandwiched between the structure to be damped and a stiff metal layer. Then, bending of the composite produces shear and the mechanical energy is dissipated in the middle layer as heat. These materials have been used quite successfully to address problems of noise and vibration control.[1] However, the temperature sensitivity in polymer-damping processes is a major disadvantage.[2] Another drawback is that the damper properties are strongly dependent on frequency and strain.

As an alternative, the use of particle dampers (PDs) can be an interesting solution. PDs are stiff enclosures containing a large number of either elastic or viscoelastic particles (e.g. sand, ball bearings, and elastomer balls) as shown in Fig. 1. Damping performance of PDs is usually not strongly temperature dependent and thus they can be used in harsh environments. Several studies have been carried out on PDs, mainly with metal spheres, providing modeling and experimental results.[3–7] However, in this study, elastomer particles were used because the interaction between them is quieter, which is an important aspect in noise and vibration control.

PDs can be added to a structure in two ways: 1) by attaching an enclosure to an exterior surface or 2) by partially filling manufactured or pre-existing voids inside the structure with particles.

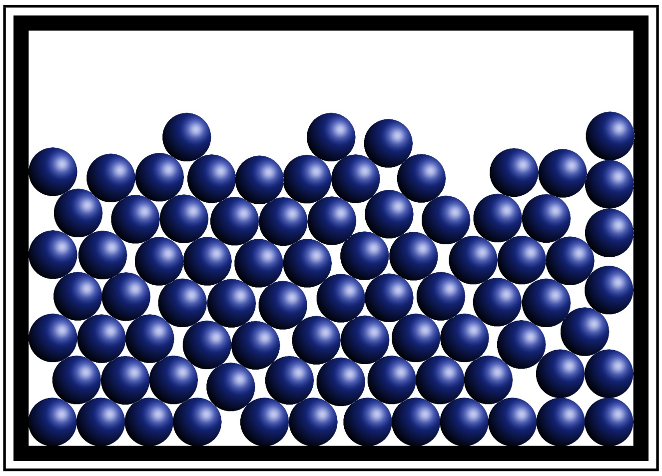

Figure 1. Schematic diagram of a particle damper.

The operating principle of PDs is based on energy dissipation through multiple inelastic collisions, interparticle friction, and friction between the particles and the walls of the container. The resulting system is highly nonlinear. Its damping capacity is greatly dependent on the level of acceleration which the container undergoes. There are a significant number of parameters affecting the damper performance. These include particle size, shape, number and density, the size and shape of the enclosure, and the properties that affect the particle-particle and particle-enclosure interactions, such as the coefficients of friction and restitution.[3]

PDs show different dynamic behaviors when the vibration level changes. When the vibration amplitudes are very low, the system is said to be in a "condensed state", where the particles are in contact with each other and moving together. When the amplitudes of vibration are high, it is said that the system is in a "fluidization state" where the particles move individually as fluid particles.[8] During the transition between the two regimes, in some regions the particles are fluidized and in others they are still condensed. The presence of these two regimes and the transition from one to another is also dependent on the coefficient of restitution and the number of particles involved. Other authors have also considered the presence of a "gaseous state" of the particles as they adopt a chaotic and uncorrelated motion.[9]

The mass ratio between the particle damper and the primary system is also an important parameter to take into account. The size of a damping system with particle dampers is increased with an increasing in this mass ratio.[10] Even with a low mass ratio, the particle dampers can be very effective in the attenuation of vibrations.[11]

In addition, particle size significantly affects the energy dissipation of the damper.[12,13] A particle damper with very small particles dissipates energy mostly by friction. However, as the particle size increases the energy will be mainly dissipated through inelastic collisions. Furthermore, the efficiency of the damper is highly dependent on the coefficient of friction of the particles and not so much on the coefficient of restitution.[14] In the first part of this article, the fluidization state of an EPD inserted in the free end of a beam fixed at its opposite end forming a single-degree-of-freedom (SDOF) system was investigated. Frequency Response Function (FRF) curves are obtained experimentally for different levels of excitation.

Subsequently, the study was expanded at frequencies of the EPD system using the Power Input Method (PIM). Using this method it was possible to raise the damping loss factor curves as a function of the acceleration and frequency experienced by the damper. The EPDs studied were applied for controlling a vibration mode of a steel plate and the vibration level of an aircraft floor plate.

Two types of elastomer particles were used and the curves for the stress versus percent elongation for these materials are shown in Fig. 2. These elastomers are referred to herein as elastomers A and B. Elastomer B is stiffer than elastomer A. The geometries of the elastomer particles are shown in Fig. 3. These geometries are very irregular and two different geometries of elastomer B were tested.

The gap formed by the free space between the container and the particles is an important parameter in relation to the damper efficiency. Results from several studies regarding the optimal gap have been published.[10,11,15–19] However, for simplicity, PDs with roofless containers were considered in this study. Thus, no particle collisions occurred in the upper wall when the damper was subjected to accelerations greater than 1 g in the vertical direction.

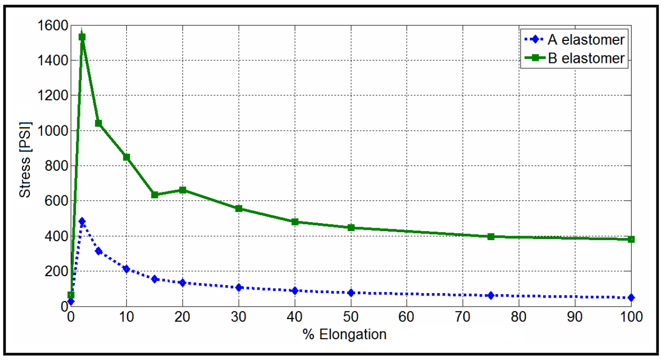

Figure 2. Curves for the stress versus percentage elongation of the elastomers used in the Elastomer Particle Damper (data provided by the manufacturer).

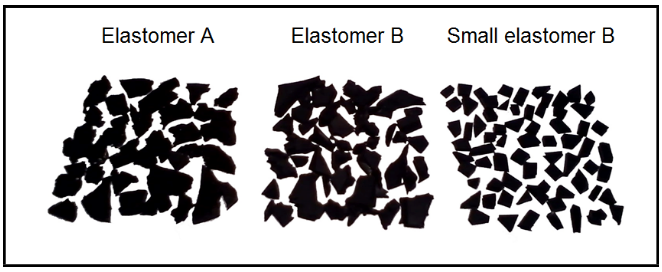

Figure 3. Geometry of elastomer particles used in the Elastomer Particle Damper.

2. EXPERIMENTAL SET-UP MEASUREMENT SYSTEM

2.1. Inertance Curves of Beam-EPD SDOF System

The experimental set-up shown in Fig. 4 was implemented for measuring the inertance in a SDOF cantilever beam system where the PD was located at the free end. The aluminum beam has a length of 280 mm, a width of 38 mm, and thickness of 3 mm. The container was made of an acrylic rectangular box of inner dimensions 100 mm in length, 100 mm in width, and 50 mm in depth. The container was filled with 0.08 kg of elastomer A particles up to a height of 21.3 mm. A vibration exciter was used to apply a force at the center of the beam. The applied force was measured using a force sensor inserted between the shaker and the beam. An accelerometer was located at the free end to measure the inertance FRF at this point relative to the force applied to the center of the beam. The vertical motion at the free end can be considered as an SDOF for the first mode shape of the beam and relatively high levels of acceleration are achieved.

A decrease in the length of the beam increased the natural frequency of the SDOF system. To achieve higher frequencies, it is necessary to clamp the two beam ends and place the particle damper at the center.

At its first natural frequency, the SDOF system was excited with a swept sine signal in order to obtain smoother curves and thus more precise damping loss factor calculations. A frequency bandwidth of 20 Hz, with the center frequency close to the natural frequency of each SDOF system, was used. A set of inertance curves alternating the acceleration of the box from -30 dB to +10 dB (reference 1 g) was obtained.

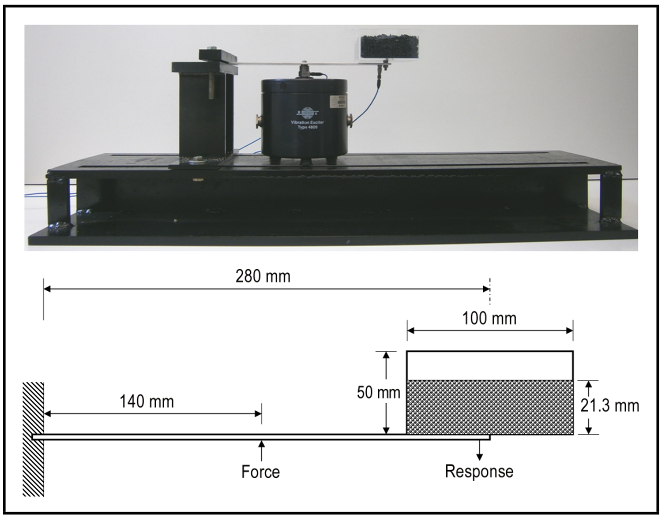

Figure 4. SDOF measurement system used to obtain the inertance FRF of the elastomer particle damper.

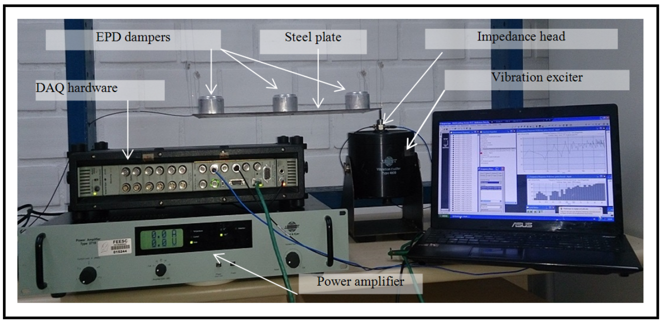

Figure 5. Measurement system used to obtain inertance curves of the steel plate with and without EPDs.

2.2. Inertance Curves of a Steel Plate with and without EPDs

The measurement system used to carry out the inertance measurements for a steel plate with and without EPDs is shown in Fig. 5. The steel plate, with dimensions L_x= 41.2 cm, $L_y = 21.02$ cm, and $L_z = 0.21$ cm, and mass of 1.357 kg was discretized into 60 equally-spaced elements. The plate was hung from a metal structure using nylon cables. In this way, the plate was positioned horizontally and with free boundary conditions. A vibration exciter connected to a power amplifier was placed in the vertical direction at the right corner of the plate. A data acquisition system is controlled by software installed on a notebook. An impedance head was placed between the vibration exciter and the plate. An accelerometer was placed alternately at each of the sixty plate elements.

Three cylindrical EPDs were each attached to the plate with a total mass of 0.044 kg. Therefore, the mass ratio (the ratio between the mass of the EPD and the mass of the primary system) was $0.044 \times 3/1.357 = 0.097$. The inertance measurement of the plate without dampers was carried out with only one acceleration input level of -30 dB, considering a linear system. In the case of the steel plate with dampers, the system is nonlinear, and the system was excited with different acceleration levels at inputs from -42 dB to +7 dB (reference 1 g).

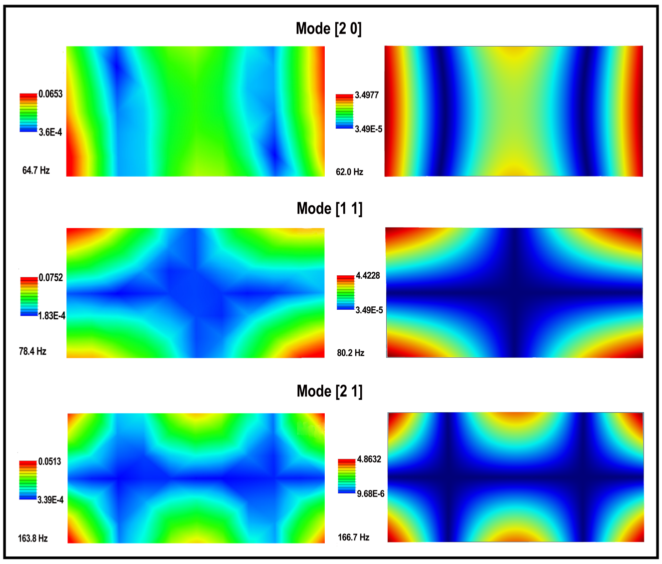

Figure 6. Experimental and simulated modal shapes of three first modes of a steel plate with dimensions $L_x = 41.2$ cm, $L_y = 21.02$ cm, and $L_z = 0.21$ cm. Left: Experimental results. Right: Finite Element Analysis results.

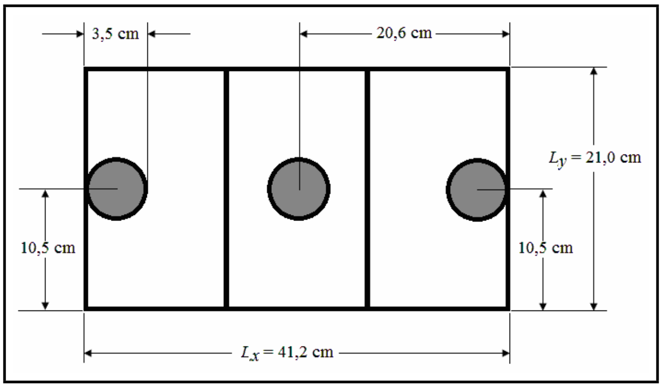

Figure 7. Nodal lines of the first mode and proper placement of dampers for damping the first mode of vibration.

2.3. Defining the Quantity and Position of EPDs Needed for the First Mode of Vibration

In order to determine the modal shapes of the steel plate and to define the EPD position, measurements and numerical simulations using a Finite Element (FE) approach were performed. The finite element modeling was performed using COMSOL Multyphysics 4.3. A plate geometry with dimensions $41.2 \times 21.02 \times 0.21$ cm^3 and free boundary conditions was defined. The plate was assumed isotropic with a Youngs modulus $E = 210$ GPa, density $\rho = 7860$ kg/m^3, and Poissons ratio $\nu = 0.33$. A fine mesh of shell elements and COMSOL eigenfrequency solver were used in order to perform this modal analysis.

The three first mode shapes are shown in Fig. 6. The blue lines are nodal lines, and red areas indicate the maximum displacement. The mode shape of the first mode of the plate with free boundary conditions, defined as mode [2 0], presents two nodal lines and three areas of displacement. Therefore, it is desirable to place at least one EPD inside each of these areas (see Fig. 7).

Figure 8. Steel plate with free boundary conditions. The vibration exciter was located at a corner of the plate and the accelerometer at the elements of the uniformly discretized plate. Left: Plate without dampers. Right: Plate with 3 EPDs. Dimensions are shown in Fig. 7.

Figure 8 shows a closer view of the uniformly discretized horizontal steel plate with and without EPDs. The vibration exciter appears in the lower right corner and the accelerometer is positioned at the opposite corner.

2.4. Measurement Techniques Used

2.4.1. Half-power bandwidth method

Half-power bandwidth method was used to measure the damping loss factor of the beam-EPD system and the vibration mode [2 0] of the steel plate with EPDs. This widely employed method uses an FRF of the structure, such as the inertance curve, and calculates the damping loss factor η using the equation:

$$\eta = \Delta\omega/\omega_0; \tag{1}$$

where $\Delta\omega$ is the bandwidth defined by the frequencies corresponding to the half-power point (-3 dB from peak value) and ω_0 is the resonance frequency of the SDOF system. According to Blake,[20] the damping of the system is defined with good approximation for η values lesser than 0.2.

In the plate, the driver point and response point were established within the areas of greater displacement of the vibration mode $[2\ 0]$. The driver point was located at an element situated on a corner, and the response point was located at an element at the center of the opposite side.

2.4.2. Power input method

Another method available to quantify the damping of a structure is the power input method (PIM).[21,22] This method uses the following equation to determine the damping loss factor:

$$\eta = \frac{\mathrm{Re}\{Y_{ii}(\omega)\}}{\sum_{j=1}^{N} m_j\omega|Y_{ij}(\omega)|^2}; \tag{2}$$

where Y_{ii} is the point-driven mobility, Y_{ij} is the transference mobility between the input point i and the response point j, and m_j is the mass of each of the N elements of the discretized structure. For the application of the method the system must satisfy three key assumptions:[23] (1) the replacement of strain energy with kinetic energy, (2) linearity of the system, i.e. the mobility is independent of amplitude, and (3) the structure can be suitably discretized so that the kinetic energy can adequately be determined with a modest number of observation points, each accurately representing the velocity of a discretized mass.

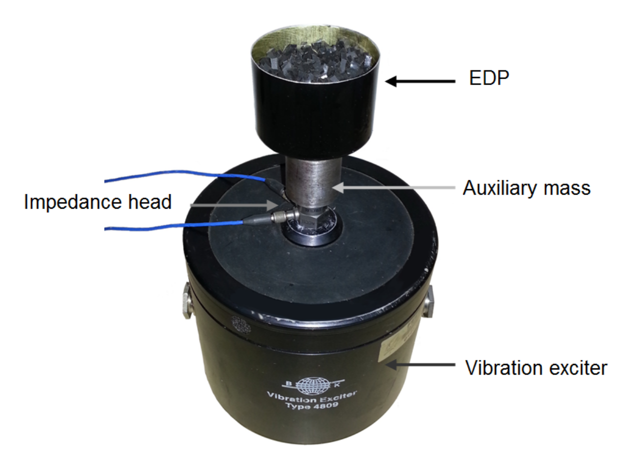

Figure 9. Experimental set-up used to measure the damping loss factor of an EPD as a function of acceleration and frequency.

As shown in Fig. 9, the EPD container was considered as a stiff mass, and it was connected directly to the vibration exciter. An impedance head was placed between the vibrator exciter and the EPD container. Thus, only the point-driven mobility curve Y was necessary to measure. In this situation, Eq. (2) is written as

$$\eta = \frac{\mathrm{Re}\{Y(\omega)\}}{M\omega|Y(\omega)|^2}; \tag{3}$$

where M is the mass of the EPD container plus the particle mass.

This method has a significant advantage over other forms of damping loss factor measurement because it does not require the presence of a primary structure (as in the case of the beam-EPD system) and because measurements can be carried out at any acceleration level and frequency as desired.[18] However, this relationship is approximate since the kinetic energy of particles is not considered.

PIM was also used applying Eq. (2) to obtain the damping loss factor for the steel plate with three EPDs considering the 60 elements of the uniformly discretized plate.

2.4.3. Spatial-average response

A commonly used measure of the plate surface vibration is the space-average value of the time-average squared vibration velocity defined by:[24]

$$\langle \bar{v}^2 \rangle = \frac{1}{S}\int_S \bar{v}^2 dS; \tag{4}$$

where the upper bar denotes time-average and $\langle\rangle$ denotes space-average. S extends over the total vibrating surface of the plate, v is the point velocity, and $\langle \bar{v}^2 \rangle$ is known as the spatial-averaged mean-square velocity.

Similarly, the spatial-averaged mean-square mobility can be defined as

$$\langle \bar{Y}^2 \rangle = \frac{1}{S}\int_S \bar{Y}^2 dS; \tag{5}$$

where Y is the mobility function defined as $Y(\omega) = v(\omega)/F(\omega)$.

If a plate is discretized into N elements, then Eq. (5) is

$$\langle \bar{Y}^2 \rangle = \frac{1}{S} \sum_{j=1}^{N} \bar{Y}_{ij}^2 \Delta S_j; \tag{6}$$

where i is the drive point where the force is applied. If the N elements have the same dimensions and considering that $\bar{Y}^2 = Y_{rms}^2$, then the spatial-averaged mean-square inertance (or simply called spatial-averaged mobility) is given by:

$$\langle \bar{Y}^2 \rangle = \frac{1}{N} \sum_{j=1}^{N} (Y_{rms}^2)_{ij}. \tag{7}$$

The mobility curves were obtained exciting the system with a swept sine signal from 20 Hz to 2 kHz.

2.5. Aircraft Floor Panel with EPDs

In order to test the actual performance of the EPDs, the attenuation of the spatial-averaged response of an aircraft floor panel with 60 uniformly distributed EPDs on its surface and with a commercial constrained damping layer were compared. The aircraft panel is made of a honeycomb aluminum core and two epoxy/glass skin layers. The dimensions of the panel were 1.47 m$\times$$0.61$ m. The thickness and mass of the panel were 10.5 mm and 2.79 kg, respectively. Each cylindrical EPD had a total mass of 0.0306 kg. Therefore, the mass ratio was $0.0306 \times 60/2.79 = 0.66$. The mass of the damping layer was 1.917 kg and thus the mass ratio was 0.69. The vibration treatments applied to the aircraft floor panel are shown in Fig. 10. Figure 11 shows the measurement system employed for this purpose. The vibration exciter was located at the bottom of the floor base, in the vertical direction, at two different points. The system was exited with white noise, and the response was measured at 8 randomly located points on the floor panel surface. Finally, the spatial-averaged response of the 8 points was calculated. A single acceleration-level curve was obtained allowing easy comparison of the performance of the two vibration control treatments applied to the floor panel.

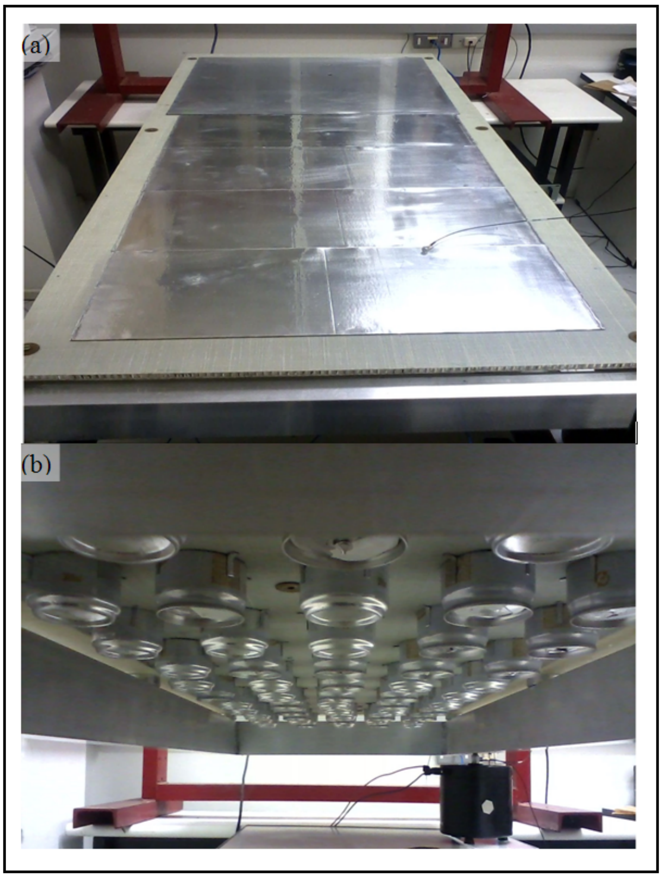

Figure 10. (a) Aircraft floor panel with a constrained layer damping system. (b) Aircraft floor panel with 60 elastomer particle dampers attached to the bottom and evenly spaced under the panel.

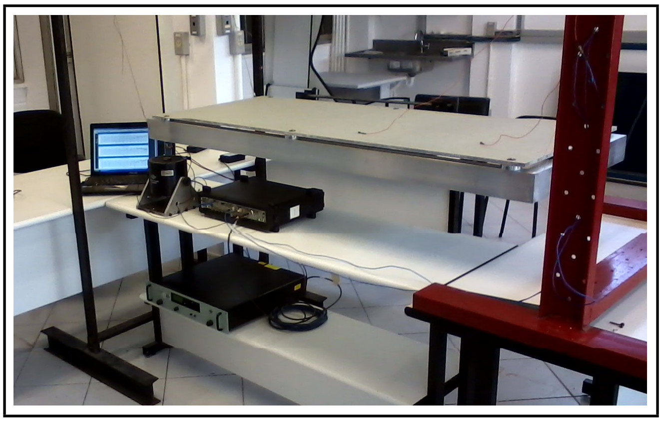

Figure 11. Mounting and measurement system used for testing the aircraft floor panel.

3. RESULTS AND DISCUSSION

3.1. Beam-EPD SDOF System

3.1.1. Fluidization state

Recent research studies reported by the authors have led to the development of a type of particle damper consisting of elastomer particles of irregular geometry held within a container.[10] Based on the work of Liu et al., this EPD was inserted into the SDOF experimental system shown in Fig. 4, and the FRF curves were obtained for different levels of excitation.[3] White noise with a bandwidth of 50 Hz centered at 25 Hz was used as the excitation signal, and the results are shown in Fig. 12(a). A set of inertance FRF curves were obtained alternating the input power from -30 dB to +10 dB for an EPD with 0.08 kg of elastomer particles.

As noted above, this system is highly nonlinear. When the excitation level is low (-30 dB), the curves show a peak at a lower frequency compared with the corresponding curve for the empty box due to increased mass. As the level of excitation increases, the curves become wider and have a lower peak value which indicates an increase in the damping. Initially, the curves are smooth and later show fluctuations, which are due to the stick-slip friction mechanism, as explained by Papalou and Masri.[4] As the level of excitation significantly increases, the frequency of the peak value on the FRF curve begins to shift toward that of the peak value on the curve for the empty box. This is because once the particles start to spend more time in the air, the effective mass decreases and there is a point at which the curve reaches the lowest peak value. This point was defined by the authors as the fluidization point of the particle

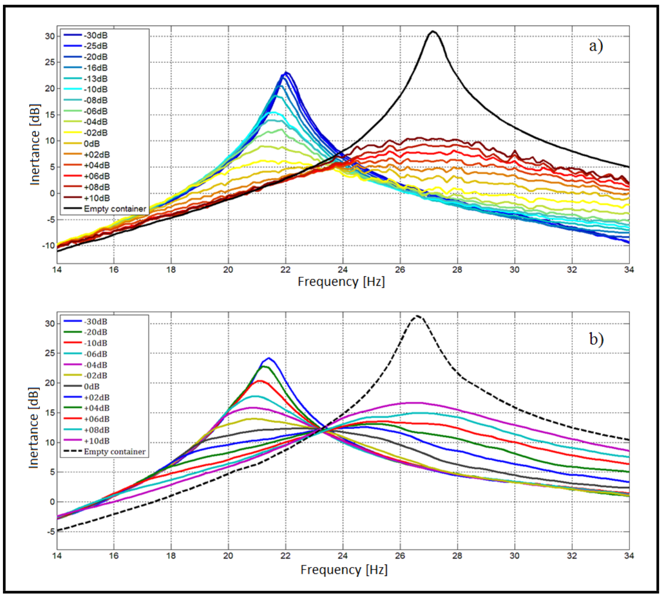

Figure 12. Inertance FRF curves for an elastomer particle damper in a SDOF system as a function of the power input level applied to the center of the beam. (a) System excited with white noise. (b) System excited with a swept sine signal.

damper.[25] At this point, the attenuation of the peak value and damping achieved is the maximum possible for this damper. The frequency of the fluidization point is between the natural frequency of the system with the empty box and that for the box with particles. Note that the fluidization point is achieved when the EPD is subjected to vibration with acceleration close to 1 g, that is, the acceleration needed to overcome gravity. Under this condition, the particles adopt the behavior of a moving fluid with random shape, and a high degree of damping is achieved through friction as well as the inelastic collision between the particles and the walls.

However, due to the high degree of irregularity associated with the FRF curves obtained for the EPD, which are shown in Fig. 12(a), it was difficult to accurately determine the center frequency and half-power band. This problem was solved by exciting the system with a swept sine signal, and smooth FRF curves were obtained. Fig. 12(b) shows an example of the FRF curves obtained with this type of signal. This is consistent with previously published results which indicated that the harmonic and random excitation will each cause the damper to behave in a different manner.[4] Thus, the response of such dampers is also dependent on the type of excitation.

Figures 13 and 14 show the 3D plots of the inertance as a function of the acceleration and frequency of the SDOF system for the box without particles and the box containing 0.08 kg of elastomer particles, respectively. These figures facilitate an understanding of the fluidization phenomenon, which was explained above by comparing the response of the systems with and without particles. When particles are absent, the system is practically linear for the entire acceleration range studied. When the particles are placed in the box, greater attenuation by damping is achieved when the system is excited with a power input close to 0 dB. Above this value, the frequency of the inertance peak values increases, tending toward the value corresponding to the empty box (27 Hz).

The results obtained in this previous study are encouraging. However, they were obtained for natural frequencies of the SDOF system between 20 and 30 Hz. Thus, the dissipative behavior of the elastomer particle damper in a wider frequency range needs to be determined so that the applicability of this damper to noise and vibration problems can be established. Since this damping system is dependent on the acceleration to which it is subjected, this variable also needs to be studied. Thus, experimental curves for the damping as a function of the acceleration and frequency of an elastomer particle damper with 0.04 kg of particles were obtained and are reported herein.

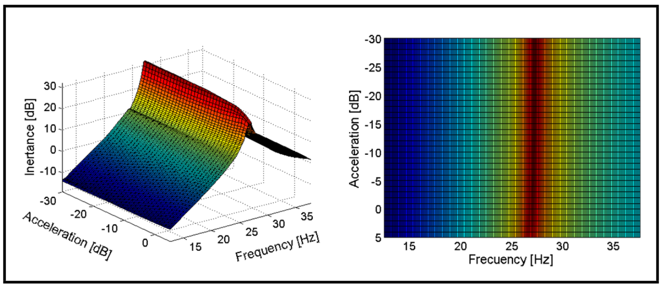

Figure 13. 3D plot of the inertance of the SDOF system with the box without particles as a function of the power input and frequency.

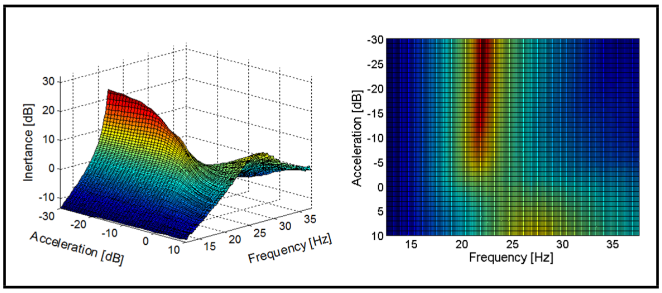

Figure 14. 3D plot of the inertance of the SDOF system with the box containing 0.08 kg of elastomer particles as a function of the power input and frequency.

3.1.2. Damping loss factor as a function of acceleration and frequency of EPD system

The damping loss factor of an EPD with 0.04 kg of elastomer particles was measured as a function of acceleration and frequency. The PIM was used considering Eq. (3). The results are shown in Figs. 15 to 18, each showing a 3D plot with two views. The left-hand image gives an isometric view and in the right-hand the graph is viewed from above (top view), showing the damping loss factor in the acceleration-frequency plane.

A damping region is present at low frequencies, starting at 20 Hz, with acceleration value close to 0 dB, namely around 1 g of acceleration, which is associated with the fluidization phenomenon observed in earlier studies. In addition to the damping region where fluidization occurred, it was found that this EPD presents another region of damping at an acceleration level lower than 0 dB (reference 1 g). This is a positive feature because the EPD may also be used in structures subjected to relatively small acceleration levels.

Figure 15 shows the damping loss factor of the EPD system with 0.04 kg of elastomer A particles. We observed the region of highest damping between 30 and 40 Hz. This region overlaps with the fluidization region.

Figure 16 shows the damping loss factor for the EPD sys-

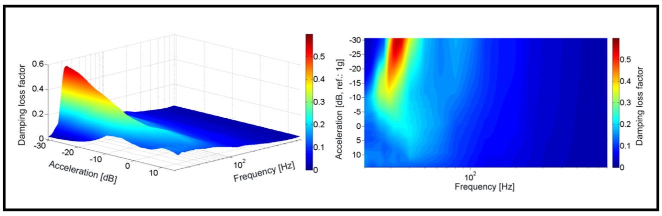

Figure 15. 3D plots for the damping loss factor of an EPD system with 0.04 kg of elastomer A particles as a function of acceleration and frequency.

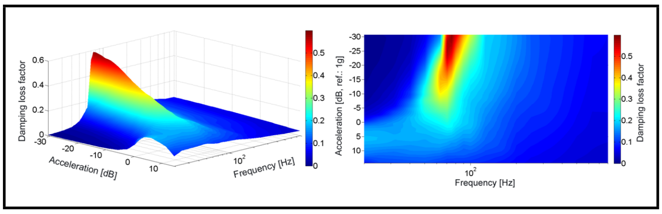

Figure 16. 3D plots for the damping loss factor of an EPD system with 0.04 kg of elastomer B particles as a function of acceleration and frequency.

tem with 0.04 kg of elastomer B particles. For this EPD, there is an increase in the frequency range of the maximum damping region to values between 60 and 90 Hz. This is probably because elastomer B is stiffer than elastomer A. The region of fluidization is observed with greater clarity at low frequencies due to less overlapping with the other damping region.

Figure 17 shows the damping loss factor of the EPD system with 0.04 kg of small elastomer B particles. Since these particles are made of the same material as those related to the data in Fig. 16 but are of smaller size, they have a higher stiffness; therefore, the region of highest damping is shifted to frequencies in the range of 80 to 120 Hz. This figure also clearly shows the fluidization region at around 1 g of acceleration.

Figure 18 shows the damping loss factor of the EPD system with a 0.04 kg rigid steel mass glued to the container (with no particles in the container). The damping obtained was not significant showing that in the previous cases damping was achieved due to the presence of the particles inside the box.

3.2. Steel Plate with EPDs

In order to control the vibration mode [2 0] of the steel plate, three EPDs were applied. The working frequency of the EPDs was tuned to the natural frequency $f_{2,0}$ of the steel plate. The EPDs were strategically located as explained in Section 2.3.

These results are presented in two sections. Section 3.2.1 reports the measurements obtained with the half-power bandwidth method in order to analyze the attenuation achieved at the natural frequency $f_{2,0}$ by applying different levels of acceleration at the input. Section 3.2.2 reports the results obtained in the frequency band between 20 Hz and 2 kHz for the spatial-

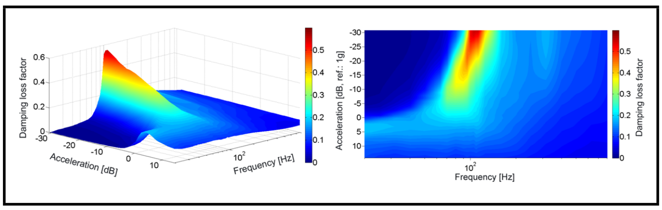

Figure 17. 3D plots for the damping loss factor of an EPD system with 0.04 kg of small elastomer B particles as a function of acceleration and frequency.

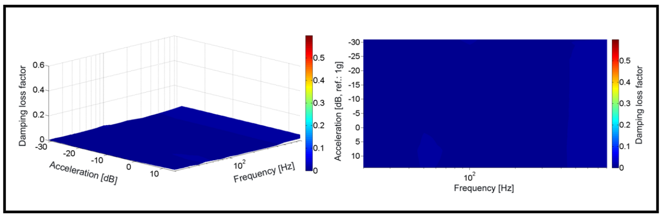

Figure 18. 3D plots for the damping loss factor of an EPD system with 0.04 kg of rigid mass (no particles in the container) as a function of acceleration and frequency.

averaged mobility and the damping loss factor of the steel plate with and without EPDs using the PIM method.

3.2.1. Attenuation and damping at natural frequency $f_{2,0}$ of the steel plate

Figure 19 shows the inertance curves centered at the natural frequency of the plate with and without dampers. The black curve corresponds to the plate without dampers and the other curves correspond to the plate with three EPDs, with different acceleration levels applied at the input. A large attenuation of the peak value is observed for each curve. It can be observed that, as expected, the lower the applied acceleration, the greater the damping peak value for the attenuation of the plate. This behavior is in contrast to that of the case when the EPD is not tuned to the natural frequency of the system, as is the case for the curves shown in Fig. 12. In this case, the curves exhibit greater attenuation when the EPD is subjected to accelerations close to 1 g and less attenuation when the acceleration decreases. In this situation, the damping region associated with the fluidization state of the particles prevails.

Figure 19b shows the same curves as that in Fig. 19a but in a 3D plot using data interpolation. The inertance curves are shown as a function of the frequency and acceleration experienced by the EPD. The color bar shows the inertance values (in dB) associated with each color on the graph. The peak value of the inertance curve for the plate without dampers at natural frequency $f_{2,0}$ was 52.7 dB. The greatest attenuation of the acceleration level was 31 dB, obtained with the lowest level of acceleration at the damper of -42 dB.

The damping loss factor for each of the curves in Fig. 19a, obtained for the plate with three EPDs and without EPDs, was calculated using the half-power bandwidth method. The results are shown in Fig. 20. Given that the steel plate without dampers shows linear behavior, which means that the FRF curves do not vary with the amplitude of excitation, only one inertance measurement was taken and the calculated damping loss factor η was 0.0032. The damping loss factor of the plate with dampers was much higher for all levels of acceleration applied. The maximum value was 0.2, obtained with the lowest level of input acceleration of -42 dB, in agreement with the attenuation results. The minimum value for η was 0.07, which was obtained with an input acceleration level of -0.8 dB.

3.2.2. Attenuation and damping in the frequency range of 20 Hz to 2 kHz

Mobility curves in the frequency range of 20 Hz to 2 kHz were obtained for each of the 60 evenly spaced elements on the steel plate with and without the EPD. These curves were used

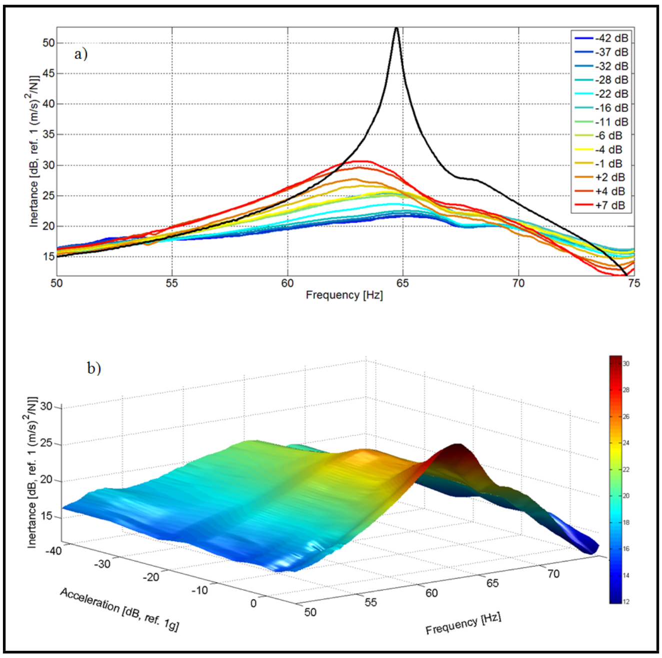

Figure 19. Inertance curves of the steel plate with three EPDs with different acceleration levels. (a) Inertance curves as a function of frequency. The black curve corresponds to the plate without EPDs. (b) The inertance curves presented in a) shown as a function of frequency and acceleration.

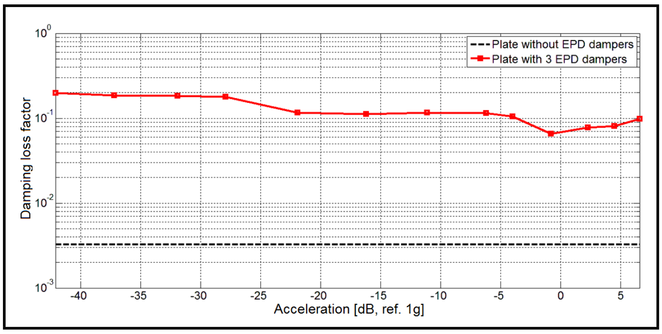

Figure 20. Damping loss factor of the steel plate with and without EPDs obtained with the half-power bandwidth method at natural frequency $f_{2,0}$.

to obtain the curves for the spatial-averaged mobility (shown in Fig. 21) and for the damping loss factor using the PIM method (shown in Fig. 22).

The peak corresponding to the natural frequency $f_{2,0}$ = 64 Hz of the steel plate without dampers was almost eliminated by the use of the EPDs as can be observed in Fig. 21. The peak attenuation value was close to 24 dB. Above this natural frequency $f_{2,0}$, the EPDs still provide damping for the plate. At frequencies between 70 Hz and 2 kHz, it was observed that some peaks were greatly attenuated ($>$ 15 dB), others were slightly attenuated (around 5 dB) and some were not attenuated. At the natural frequency $f_{1,1}$ = 78 Hz the attenuation was small, and the peak value at the natural frequency $f_{2,1}$ = 164 Hz was not attenuated. This is because in both cases, the dampers were located along the nodal lines of each mode where the displacement is zero; therefore, the vibration is not effectively transmitted to the dampers. The nodal lines can be seen in Fig. 6. Figure 22 shows the damping loss factor for the steel plate with three EPDs, obtained through the PIM method in the frequency range of 20 Hz to 2 kHz. A high damping peak centered at 60 Hz, which defines the

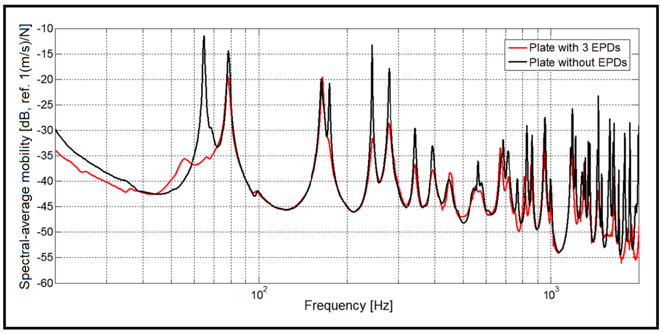

Figure 21. Spatial-averaged mobility curves of steel plate with and without EPDs.

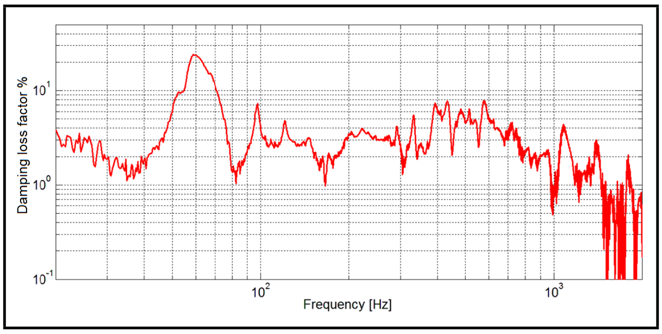

Figure 22. Damping loss factor of a steel plate with three EPDs obtained through the Power Input Method (PIM).

damper working frequency, is clearly observed. Furthermore, the dampers provided damping of over 2% across almost the entire frequency band analyzed, decreasing only above 700 Hz, approximately. This damping curve is consistent with the attenuation obtained for the plate shown in Fig. 21, where the peak near 60 Hz was strongly attenuated and most other peaks were attenuated by the damping added to the plate.

3.3. Aircraft Floor Panel with EPDs

Figure 23 shows the spatial-averaged acceleration level of the aircraft floor panel without damping treatment. This curve is taken as a reference to calculate the vibration attenuation of the floor panel with a damping layer treatment.

Figure 24 shows the vibration attenuation of the spatial-averaged response of the aircraft floor panel with two types of vibration control treatments: a constrained damping layer and the 60 EPDs. It can be verified that the two treatments show similar performance, although higher attenuation is provided by the constrained layer at high frequencies (above 600 Hz) and higher attenuation is provided by the EPDs at mid-range frequencies (60 to 300 Hz).

4. CONCLUSIONS

An initial study on the dynamic behavior of a SDOF cantilever beam system with an EPD on the free end was carried out. A fluidization state was observed, as described in the literature. For the vertical displacement of the EPD, this state appears when the acceleration is close to 1 g and the particles adopt a motion similar to that of a fluid. The vibration energy dissipation mechanism is due to the friction and inelastic collisions between the particles themselves and between the

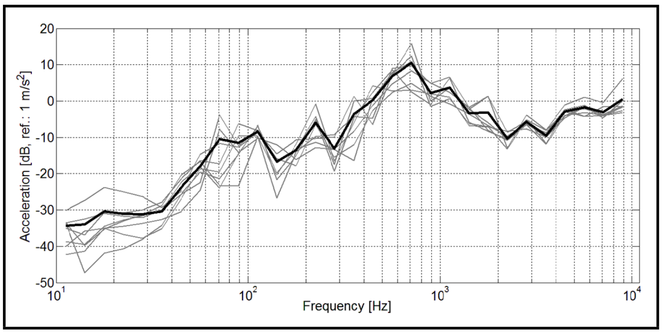

Figure 23. Acceleration level of the aircraft floor panel with stiff connection. Gray curves: acceleration level measured at each of eight randomly located points on the panel. Black curve: spatial-averaged acceleration level.

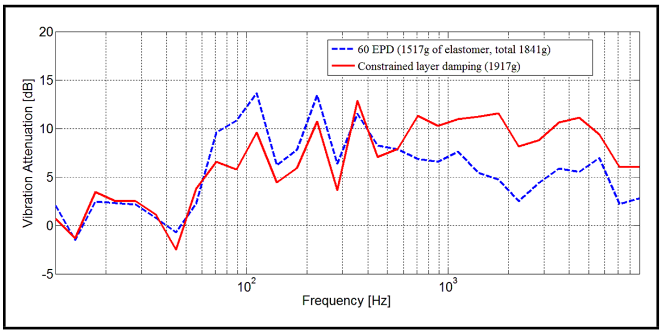

Figure 24. Attenuation of the spatial-averaged response of the aircraft floor panel with two damping vibration control techniques: 60 EPDs and a commercial constrained damping layer.

particles and the walls of the container. The inertance peak value decreases as the acceleration increases down to a minimum value before increasing again. When the minimum peak value on the curve is reached, the maximum possible damping is achieved by the system. Thus, it was appropriate to define the fluidization point of an EPD as the point at which this minimum inertance peak value occurs.

The study on the damping loss factor as a function of acceleration at a fixed frequency was expanded, and it was observed that the fluidization process is maintained for a few decades of frequency. In addition, another region where the particle dampers provided a high degree of damping was noticed. In this study, it was found that the frequency range was dependent upon the particle stiffness. Greater particle stiffness is associated with a higher center frequency of the band damping of the EPD.

These results open up a broader field of application, where the acceleration in the vertical direction of the particle damper is not limited to being close to 1 g, but may be lower. However, this indicates the need to model the damping frequency as a function of parameters such as the stiffness, mass, and the coefficient of restitution of the particles. Discrete element models have been comprehensively applied to particle dampers and might represent a good alternative for modelling.[12,13,26–30]

The effectiveness of EPDs is greatly improved when the working frequency is tuned to a vibration mode of a plate and when the dampers are strategically located at points at which high displacement occurs. In particular, the three EPDs in this study, tuned to the vibration mode [2 0] of a steel plate, were applied. The result was that the peak of the spatial-averaged mobility curve corresponding to this vibration mode was attenuated by 24 dB and was almost eliminated. Above the working frequency of the EPD (70 Hz to 2 kHz), the damper continues adding damping to the plate, achieving a damping loss factor of between 1 and 8%. In this frequency range, the added damping achieves an attenuation peak of up to 15 dB.

The performance of the EPDs was compared with that of a commercial constrained damping layer installed in an aircraft floor panel. The EPDs achieved an attenuation of the acceleration level on the aircraft floor panel similar to that of the commercial damping layer, with a somewhat better performance at mid-range frequencies and slightly poorer performance at high frequencies. These results are quite encouraging considering that elastomer particle dampers offer advantages such as easy construction, independence of temperature, and durability.

The work described in this article has been concerned with vertical excitation of the particle damper. Although the results presented here have demonstrated the effectiveness of the damper, further work should also address the effects on the damper performance of both the direction of excitation and the shape of the damper body.

ACKNOWLEDGEMENTS

The authors wish to acknowledge the representatives of ITT Enidine Inc. for partially funding this research project and to CNPq-Brazil for funding Ph.D. students and research staff.

REFERENCES

1 Xu, Z.-D., Zhu, J.-T., and Wang, D.-X. Analysis and optimisation of wind-induced vibration control for high-rise chimney structures. *Int. J. Acoust. Vib.* **19**, 42–51, (2014).

2 Wetton, R. E. Design and measurement of polymeric materials for vibration absorption and control, *Appl. Acoust.*, **11** (2), 77–97, (1978). http://dx.doi.org/10.1016/0003-682X(78)90010-5

3 Liu, W., Tomlinson, G. R., and Rongong, J. A. The dynamic characterization of disk geometry particle dampers, *J. Sound Vib.*, **280**, 849861, (2005). http://dx.doi.org/10.1016/j.jsv.2003.12.047

4 Papalou, A. and Masri, S. F. Response of impact dampers with granular materials under random excitation, *Earthquake Eng. Struct. Dyn.*, **25**, 253267, (1996). http://dx.doi.org/10.1002/(sici)1096-9845(199603)25:3<253::aid-eqe553>3.3.co;2-w

5 Yang, M. Y. *Development of master design curves for particle impact dampers*, PhD diss., Dept. of Mechanical and Nuclear Engineering, The Pennsylvania State University, USA, (2003).

6 Friend, R. D. and Kinra, V. K. Particle Impact Damping, *J. Sound Vib.*, **233** (1), 93118, (2000). http://dx.doi.org/10.1006/jsvi.1999.2795

7 Darabi, B. and Rongong, J. A. Polymeric particle dampers under steady-state vertical vibrations, *J. Sound Vib.*, **331**, 33043316, (2012). http://dx.doi.org/10.1016/j.jsv.2012.03.005

[8] Duran, J. *Sand, powders, and grains: An introduction to the physics of granular materials*, Springer-Verlag, New York, (2000). http://dx.doi.org/10.1007/978-1-4612-0499-2

[9] Saluea, C., Pschel, T., and Esipov, S. E. Dissipative properties of vibrated granular materials, *Phys. Rev. E.*, **59** (4), 44224425, (1999). http://dx.doi.org/10.1103/PhysRevE.59.4422

[10] Araki, Y., Yuhki, Y., Yokomichi, I., and Jinnouchi, Y. Impact Damper with Granular Materials: 3rd Report, Indicial Response, *B. JSME*, **28** (240), 12111217, (1985). http://dx.doi.org/10.1299/jsme1958.28.1211

[11] Papalou, A. and Masri, S. F. An experimental investigation of particle dampers under harmonic excitation, *J. Vib. Control*, **4** (4), 361379, (1998). http://dx.doi.org/10.1177/107754639800400402

[12] Chen, T., Mao, K., Huang, X., and Wang, M. Y. Dissipation mechanisms of nonobstructive particle damping using discrete element method, *Proc. SPIE*, **4331**, 294301, (2001). http://dx.doi.org/10.1117/12.432713

[13] Saeki, M. Impact damping with granular materials in a horizontally vibrating system, *J. Sound Vib.*, **251** (1), 153161, (2002). http://dx.doi.org/10.1006/jsvi.2001.3985

[14] Bai, X.-M., Shah, B., Keer, L. M., Wang, Q. J., and Snurr, R. Q. Particle dynamics simulations of a piston-based particle damper, *Powder Technol.*, **189** (1), 115125, (2009). http://dx.doi.org/10.1016/j.powtec.2008.06.016

[15] Bapat, C. N. and Sankar, S. Single unit impact damper in free and forced vibration, *J. Sound Vib.*, **99** (1), 8594, (1985). http://dx.doi.org/10.1016/0022-460X(85)90446-8

[16] Duncan, M. R., Wassgren, C. R., and Krousgrill, C. M. The damping performance of a single particle impact damper, *J. Sound Vib.*, **286**, 123144, (2005). http://dx.doi.org/10.1016/j.jsv.2004.09.028

[17] Cempel, C. and Lotz, G. Efficiency of vibrational energy dissipation by moving shot, *J. Struct. Eng.*, **119** (9), 26422652, (1993). http://dx.doi.org/10.1061/(ASCE)0733-9445(1993)119:9(2642)

[18] Yang, M. Y., Lesieutre, G. A., Hambric, S. A., and Koopmann, G. H. Development of a design curve for particle impact dampers, *Noise Control Eng.*, **53**, 513, (2005). http://dx.doi.org/10.3397/1.2839240

[19] Bannerman, M., Kollmer, J., and Sack, A. Movers and shakers: Granular damping in microgravity, *Phys. Rev. E.*, **84**, 011301, (2011). http://dx.doi.org/10.1103/PhysRevE.84.011301

[20] Blake, R. E. Ch. 2: Basic vibration theory, *Harris' Shock and Vibration Handbook*, Allan G. Piersol and Thomas L. Paez Eds., McGraw-Hill, New York, (2010), 6th ed.

[21] Carfagni, M. and Pierini, M. Determining the loss factor by the power input method (PIM), Part 1: Numerical investigation, *J. Vib. Acoust. ASME*, **121**, 417421, (1999). http://dx.doi.org/10.1115/1.2893996

[22] Carfagni, M. and Pierini, M. Determining the loss factor by the power input method (PIM), Part 2: Experimental investigation with impact hammer excitation, *J. Vib. Acoust. ASME*, **121**, 422428, (1999). http://dx.doi.org/10.1115/1.2893997

[23] Torvik, P. J. Ch. 35: Material and slip damping, *Harris' Shock and Vibration Handbook*, Allan G. Piersol and Thomas L. Paez Eds., McGraw-Hill, New York, (2010), 6th ed.

[24] Fahy, F. J. and Gardonio, P. *Sound and structural vibration—Radiation, transmission and response*, Academic Press, Oxford, (2007), 2nd ed. http://dx.doi.org/10.3397/1.2741307

[25] Bustamante, M., Gerges, S. N. Y., Cordioli, J., Martin, O., Weisbeck, J., and Ott, M. Experimental study on some parameters that affect the performance of an elastomer particle damper, *Proc. ASA*, Montreal, Canada, (2013). http://dx.doi.org/10.1121/1.4801066

[26] Lu, Z., Masri, S. F., and Lu, X. Parametric studies of the performance of particle dampers under harmonic excitation, *Struct. Control Hlth.*, **18**, 7998, (2011). http://dx.doi.org/10.1002/stc.359

[27] Snchez, M., Rosenthal, G., and Pugnaloni, L. A. Universal response of optimal granular damping devices, *J. Sound Vib.*, **331**, 43894394. (2012). http://dx.doi.org/10.1016/j.jsv.2012.05.001

[28] Lu, Z., Lu, X., and Masri, S. F. Studies of the performance of particle dampers under dynamic loads, *J. Sound Vib.*, **329**, 54155433, (2010). http://dx.doi.org/10.1016/j.jsv.2010.06.027

[29] Lu, Z., Lu, X., Lu, W., and Masri, S. F. Experimental studies of the effects of buffered particle dampers attached to a multi-degree-of freedom system under dynamic loads, *J. Sound Vib.*, **331**, 20072022 (2012). http://dx.doi.org/10.1016/j.jsv.2011.12.022

[30] Lu, Z., Lu, X., Lu, W., and Masri, S. F. Shaking table test of the effects of multi-unit particle dampers attached to an MDOF system under earthquake excitation, *Earthq Eng. Struct. D.*, **41**, 9871000, (2012). http://dx.doi.org/10.1002/eqe.1170

About the Authors

Ruqiang Mou received his BS from Sichuan University, Chengdu, China, in 2013, and he will receive his MS from Sichuan University in 2016 in mechanical and electronic engineering.

Li Hou received his MS from Chongqing University, Chongqing, China, in 1992 and his PhD from Sichuan University in 2000. He is currently a professor and PhD supervisor at Sichuan University. His research interests cover mechanical transmission, intelligent control and embedded systems, and CAD/CAPP/CAM/PMD.

Zhijun Sun received his MS from Xihua University, Chengdu, China, in 2012, and he will receive a PhD from Sichuan University in 2015. He is now studying mechatronics at Sichuan University. His research interests focus on mechanical transmission.

Yongqiao Wei received his BS from Sichuan University, Chengdu, China, in 2012, and he will receive his MS in Mechanical design and theory from Sichuan University in 2015. He is currently a student in mechanical design and theory at Sichuan University.

Bo Li received his BS from Sichuan University, Chengdu, China, in 2012, and he will receive his MS in mechanical design and theory from Sichuan University in 2015. He is currently a student in mechanical design and theory at Sichuan University..

Zhi-cheng Qiu is a professor at South China University of Technology (SCUT). He received his bachelors degree in mechanical design and manufacturing and his masters degree in fluid power transmission and control from Harbin Institute of Technology, Harbin, in 1995 and 1997, respectively. In 2000, he received his engineering PhD in mechatronic engineering from Shenyang Institute of Automation, Chinese Academy of Sciences. Afterwards, he did postdoctoral research in control theory and control engineering at Beijing Institute of Control Engineering, Beijing. He has been employed by South China University of Technology since 2003 and is engaged in teaching and scientific research work. He was named associate professor in 2004 and professor in 2009, and he was authorized as a doctoral supervisor in 2010. His current research field is active vibration control of flexible structures and flexible robots control.

Fan-kong Meng received his bachelors degree in mechanical design manufacturing and automation from Shandong University of Technology, Zibo, China, in 2010, and he received his masters degree in mechatronic engineering from South China University of Technology, Guangzhou, in 2013. He is now working for the FAW Car Company, Changchun, China.

Jian-da Han is a professor at Shenyang Institute of Automation, Chinese Academy of Sciences. He received his bachelors degree from Xian Jiaotong University in 1990. He received his PhD in mechatronics from Harbin Institute of Technology, Harbin, China, in 1998. He has been employed by State Key Laboratory of Robotics, Shenyang Institute of Automation, Chinese Academy of Sciences, Shenyang, China. His research interests include sensor-based robot control, flexible manipulators, intelligent mobile robots, and multirobot coordination and cooperation. He is also the Principal Investigator of several 863 projects in China. He was authorized as a doctoral supervisor in 2002.

Jin-guo Liu is a professor at Shenyang Institute of Automation, Chinese Academy of Sciences. He received his bachelors and masters degrees in mechanical engineering and automation from the University of Science and Technology Liaoning, in 2000 and 2003, respectively. In 2007, he received his engineering PhD in pattern recognition an intelligent system from Shenyang Institute of Automation, Chinese Academy of Sciences. He was named professor in 2010 and was authorized as a doctoral supervisor in 2012. His research interests include space robots, robotmechanism, etc.

Dariusz Bismor obtained his masters degree in electronics at the Silesian University of Technology in 1995 and his PhD degree in control sciences at the same university in 1999. His professional activities are related to signal processing in application to active noise control. His areas of expertise also include discrete control systems, adaptive control, and system identification. He has experience in teaching adaptive control, operating systems, and object-oriented programming. Currently, he is an associate professor at the Institute of Automatic Control, Silesian University of Technology. In 2010, he published a book titled "Programming for Control Systems" (in Polish) for which he received the Polish Ministry of Science and Higher Education award. He is a member of the IIAV, the Polish Acoustical Society (PTA), the European Acoustical Association (EAA) and the IEEE. He is also a ham (amateur) radio operator.

About the Authors

Zbigniew Ogonowski graduated from Silesian University of Technology, Gliwice, Poland, in 1978. He received his PhD from SUT in 1986. Currently, he is a lecturer at the Institute of Automatic Control of SUT. His areas of expertise are computer controlled systems, discrete control algorithms, adaptive control, system identification, and optimization. His experiences concern application of (adaptive) predictive controllers in the industry, as well as the industrial self-tuning control and multilayered control systems. His special interest is focused on application of modern control theory to active noise and vibration control. Dr. Ogonowski is the coauthor of the unique method of passive and active acoustical observations of orogen tension in mines, which provides the base for decision-making procedures as a part of the safety system. He also worked on application of adaptive control in fully active suspension of car body as well as the adaptive control of unstable electro-magnetic bearing systems. He also focuses on magnetoreological dumpers in semi-active systems. His recent works have been devoted to modeling and modern control of semi-active vibration systems applied in vehicles. He also works on the upper control layer systems that manage safety of the car-driving process by using adaptive algorithms cooperating with lower-layered direct control of suspension systems.

Krzysztof Czyz obtained his PhD in automatic control with honors in 2006 at the Silesian University of Technology, Gliwice, Poland. He is an assistant professor at the Institute of Automatic Control at Silesian University of Technology. His areas of expertise include adaptive control, digital signal processing, embedded systems, and programmable logic. Additionally, he has a wide background in the practical application of signal processing and control algorithms.

Ali Valipour is currently an assistant professor of mechanical engineering at Shahid Chamran University of Ahvaz (SCU). Ali received his BS from Azad University of Ahwaz in 2005 and his MS (2009) and PhD (2015) in mechanical engineering from Iran University of Science and Technology (IUST). His research activities include acoustics, finite element simulation, offshore structures, nondestructive testing, and noise measurement.

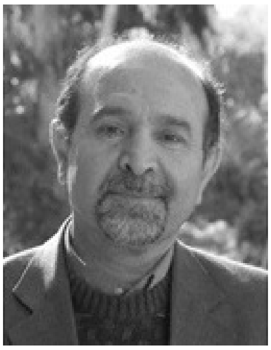

Mohammad Riahi is currently a professor of mechanical engineering at Iran University of Science and Technology (IUST). He has served as department chair and associate dean for research. Mohammad received his BS (1981) and MS (1986) in mechanics from Illinois, USA and PhD in manufacturing from Iowa, USA (1991). Dr. Riahis research activities include Nondestructive Testing (NDT), acoustics and AE, and measurements and condition monitoring in industrial maintenance.

Nowrouz M. Nouri is currently a professor of mechanical engineering at Iran University of Science and Technology (IUST). He was educated in mechanical engineering and graduated from the University of Zahedaan with an emphasis in fluid mechanics. He later continued his graduate studies in Ecole Ploy Technique in France where he received his PhD working on vortex phenomenon (1993). Dr. Nouri has completed many industrial and scientific projects and has served as department chair and associate dean at Iran University of Science and Technology (IUST).

Hamid Reza Gharavian is currently an engineer in applied hydrodynamics at the Marine Systems Research Institution. Hamid Reza received his BS from Ferdowsi University of Mashhad in 2011 and his MS in 2014 in mechanical engineering from Iran University of Science and Technology. His research activities include acoustics, mechatronics, and control systems.

Roger Serra received his MS degree in 1996 and his PhD degree in 1999 in mechanical engineering from Franche-Comt University in Besanon, France. Since 1999, he has been a professor at INSA Centre Val de Loire (INSA CVL), Blois, France and member of the Rheology and Mechanical Laboratory (LMR) at Franois Rabelais University, Tours, France. He has 18 international journal publications as main authors, and 55 national and international conferences. His research interests include mechanical vibration analysis and structural dynamics, experimental modal identification, structure health monitoring, machining vibrations, cutting tool wear monitoring, signal processing, vibratory fatigue, and characterization mechanics. He is a reviewer for many international journals, editor associate of two special issue and member of the IJMFMP editorial review board.

Wafaa Rmili was born in Casablanca, Morocco, in 1978. She received her MS in Science and Materials Engineering from the National Polytechnic Institute of Toulouse (INPT), France, in 2003, and her PhD in Mechanical Engineering and Manufacturing from Polytech'Tours (Ecole Polytechnique de l'Université de Tours), France, in 2007. Her main research interest is vibratory analysis cutting tool wear monitoring.

Sun Zhijun is a doctoral student of mechanical engineering at Sichuan University, Chengdu, China. He has researched the theory of engagement, gear modeling, the meshing analysis and vibration analysis of the gear, especially the CATT gear though the theoretical derivation, finite element analysis, and meshing experiment. Meantime, he has an invention patent about the processing device of the CATT gear. He is currently working on the project which is supported by National Natural Science Foundation of China. He will do more studies on the vibration analysis of the gear and its processing device in the future. His research interests include the gear transmission technology and vibration analysis of the planetary gear train processing device.

About the Authors

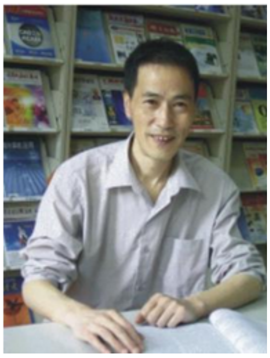

Hou Li is a professor of new-type transmission technology at Sichuan University, Chengdu, China. He received his PhD mechanical engineering from Chongqing University, Chongqing, China. His research interests include the mechanical transmission and CAD/CAPP/ CAM.

Chang Qinglin received his BS degree from Sichuan University, Chengdu, China, in 2012 and he will receive a PhD degree from Sichuan University in 2017 in mechatronic engineering in Sichuan University. His research interests are the gearing theory and the gear dynamics.

Wei Yongqiao received his BS degree from Sichuan University, Chengdu, China, in 2012 and will receive his MS degree from Sichuan University in 2015 in mechanical design and theory. He is currently a student in mechanical design and theory of Sichuan University.

Li Wei is a teaching assistant of the College of Mechanical Engineering in Xihua University, Chengdu, China. He received his masters degree in mechanical engineering at Xihua University, Chengdu, China. His direction of research focuses on PDM, mechatronics, and robotics.

V.H. Saran is currently an associate professor in the Department of Mechanical & Industrial Engineering at Indian Institute of Technology Roorkee, Roorkee, India. His areas of specialization are vehicle dynamics and human response to vibrations.

Vikas Kumar is pursuing his PhD from the Department of Mechanical & Industrial Engineering, Indian Institute of Technology Roorkee, Roorkee, India. He received his Bachelor of Technology (mechanical engineering) from Kurukshetra University, Kurukshetra, Haryana, India, in 2006 and his Master of Technology (machine design) from National Institute of Technology, Kurukshetra, Haryana, India in 2011. He obtained All India Rank-917 in the GATE-2008. His research interest is focused on the human response to whole body vibration, mechanical vibration etc.

Diego Francisco Ledezma-Ramirez graduated with a degree in mechanical and electrical engineering from Universidad Autnoma de Nuevo Len, Mxico, in 2003, and completed hsi PhD at the Institute of Sound and Vibration Research, University of Southampton, United Kingdom from 2004 to 2008, obtaining his degree in 2009 in the field of shock isolation using semiactive stiffness control. Currently, he is an associate professor at Universidad Autonoma de Nuevo Leon, teaching structural dynamics at undergraduate and postgraduate levels on aeronautical engineering and automotive engineering. His current research activities focus on shock and vibration isolation using nonlinear stiffness and damping.

Neil S. Ferguson originally joined the Institute of Sound and Vibration Research (ISVR) in 1980 to work with Bob White on the fundamental problem of rolling noise, considering the wheel-rail interaction, on a PhD project sponsored by British Rail. When this was completed, a two year period was spent at Swansea University working with Brian Clarkson on the dynamic response of satellites to the launch noise and vibration environment using a method for high frequencies (Statistical Energy Analysis (SEA)). After moving into aerospace structural dynamics, he returned to the ISVR in 1986 as the British Aerospace lecturer, with a particular focus on acoustic fatigue, incorporating both numerical predictions for the behavior of carbon-fiber-reinforced composites and nonlinear structural dynamics. As lecturer since 1997 and then senior lecturer, his research interests have widened to consider the noise and vibration (vibroacoustics) of practical engineering structures in widely diverse areas such as transport (trains, cars, ships, satellite structures), buildings, and even domestic appliances! The analysis and approaches tend to be analytical and mathematical, typically considering a wave propagation approach in order to gain insight and understanding of the underlying physics. His present research includes considering variability and uncertainty in structural dynamics, vibration control for shock, nonlinear dynamics, and applications of wave motion for structural control and response predictions.

Michael Brennan graduated from the Open University in 1987 while he was serving in the Royal Navy. He received an MS in sound and vibration studies (1992) and a PhD in the active control of vibration (1995), both from the University of Southampton, United Kingdom. He has been a research professor in the Department of Mechanical Engineering, UNESP, Brazil since 2010. Prior to this, he was professor of engineering dynamics and Chairman of the Dynamics Research Group in the Institute of Sound and Vibration Research (ISVR) at the University of Southampton (1995-2010). He is a past president of the European Association of Structural Dynamics (2005-2008), and a past Associate Editor of the Transactions of the ASME Journal of Vibration and Acoustics (2007-2013). He is currently a guest professor at Harbin Engineering University in China and visiting professor at the ISVR, University of Southampton. He has a wide range of research interests, encompassing vibration, acoustics, vibroacoustics, and rotor dynamics.

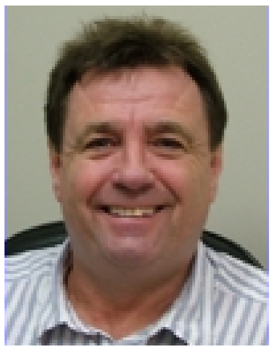

About the Authors

Seyyed Mohammad Hasheminejad received a BS in mechanical engineering from California State University, Chico, his masters in mechanical engineering from Santa Clara University, Santa Clara, CA, and his PhD degree in mechanical engineering from University of Colorado, Boulder, USA, in 1992. Since 1993, he has been a full-time faculty member at the Mechanical Engineering Department, Iran University of Science and Technology (IUST), Tehran, Iran. Hasheminejad has conducted several national and industrial research projects in the fields of passive/active noise and vibration control, and structural acoustics. He has so far published over 130 ISI-indexed research papers.

Seyyed Mohammad Parvasi received his BS in mechanical engineering from Isfahan University of Technology, and received his masters in mechanical engineering from Iran University of Science and Technology. He is currently a PhD candidate at University of Houston, TX, USA. His research interests include vibration and acoustics.

Ali Fadavi-Ardakani received his BS in railway engineering from Iran University of Science and Technology. Presently, he is an MS candidate in the mechanical engineering department of Iran University of Science and Technology. His research interests include structural acoustics, vibration and active structural acoustic control (ASAC).

Dr. Sushanta Chakraborty is an associate professor in the Department of Civil Engineering, Indian Institute of Technology Kharagpur, India. His research interest is in finite element model updating of fibre, reinforced plastics structures, vibration of floors, etc.

Mr. Subhajit Mondal is an institute research scholar in the Department of Civil Engineering, Indian Institute of Technology Kharagpur, India. He is currently pursuing his PhD in the department, and his area of research is related to the combined numerical and experimental investigation on damping of fibre reinforced plastics structures.

Şaban Ulus graduated from the Mechanical Engineering Department at Erciyes University in 2011. He received his MS degree from the same university in 2013. He is a PhD candidate at Eryiyes University and works as a research assistant in the Mechatronic Engineering Department. His field of interest and research areas are computer aided design, mechanism and machine theory, noise and mechanical vibration, and mechatronic systems.

Selçuk Erkaya graduated from the Mechanical Engineering Department at Erciyes University in 2001. He received his MS and PhD degrees from the same university. He currently works in the Mechatronics Engineering Department at Erciyes University. His research areas are mechanism and machine theory, noise and mechanical vibrations, neural networks and optimization, mechatronics, and robust design of mechanical systems.

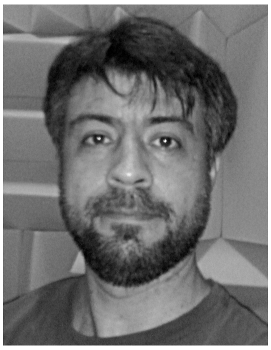

Marcelo Bustamante obtained his BS in acoustical engineering from the Austral University of Chile in 2005. In 2009, he obtained his MS in mechanical engineering, and in 2014, a PhD in mechanical engineering, both in the area of vibration and acoustics from the Federal University of Santa Catarina (UFSC), Brazil. His main research areas have been the attenuation of vibrations using damping and isolation passive techniques applied to aircraft floor and car oil panels and the development of elastomer particle dampers.

About the Authors

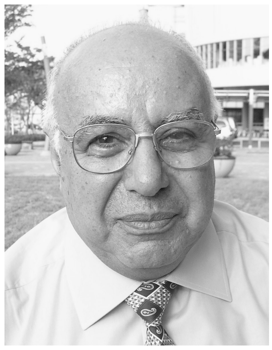

Samir Gerges was born in Egypt in 1941, and he obtained his BS in Mechanical/Aeronautical Engineering from Cairo University in 1964 and his MS in 1970. He obtained his PhD from ISVR, Southampton University, UK in 1974. Later, he was a post-doctoral research fellow from 1974 to 1978 at ISVR, Southampton University and Sussex University in the UK. He has been a professor of noise and vibration since 1978 at the Federal University of Santa Catarina (UFSC), Brazil, teaching acoustics, noise control, and signal processing for undergraduate and graduate students. His current interests include industrial and construction noise, hearing protectors, experimental and numerical vibro-acoustics analysis for industrial and vehicle applications and general room acoustics. He was the founder of the Industrial Noise Lab (LARI) at UFSC and founder member of the Brazilian Acoustical Society (SOBRAC) in 1983. He was President of SOBRAC from 19941997 and again from 20002002. He is a member of the IIAV Board of Directors and has been an IIAV Fellow member since 1999 and ASA Fellow. Dr. Gerges is also a member of the editorial board of the Journal of Building Acoustics, Journal of Noise Control Engineering, and the International Journal of Acoustics and Vibration. He was President of ICA from 2007 to 2010. He has coordinated several technical research projects on NVH and sound quality for FORD, GM, EMBRAER, and FIAT, among others. He has more than 320 papers published in journals and congresses.

Erasmo Vergara obtained his BS in acoustical engineering from the Austral University of Chile in 1995. Later, he obtained his MS in 1999 and PhD in 2003, both in acoustics and vibration from the Mechanical Engineering Department of the Federal University of Santa Catarina (UFSC), Brazil. He developed post-doctoral research from 2003 to 2007 in the Vibration and Acoustics Laboratory (LVA) at UFSC, working on hearing protection and impulsive noise as well as aeronautical and vehicular noise. He taught in the Acoustics Engineering program at the Federal University of Santa Maria (UFSM), Brazil, from 2007 to 2012. Since 2012, he has been a professor in the Mechanical Engineering Department at UFSC, where he teaches acoustics, psychoacoustics, environmental noise, and building acoustics at the graduate and undergraduate levels. His research interests are building noise control, product sound quality, and experimental and numerical simulation of noise pollution. He is a member of the Brazilian Acoustical Society (SOBRAC) and German Society of Acoustics (DEGA). Dr. Vergara has published several papers in international congresses and scientific journals.

Jorge P. Arenas received his BS in acoustical engineering in 1988 and his MS in physics in 1996 both from Austral University of Chile. In 2001, he obtained his PhD in mechanical engineering from Auburn University in the USA. Dr. Arenas was one of the recipients of the 2000 Harry Merriwether Fellowship at Auburn University. He also gained professional experience at the Institute of Acoustics in Madrid, Spain, and at the University of Southampton in the UK. Currently, he is the Director of the Institute of Acoustics. He has also been a visiting lecturer in several universities of Spain and Latin America. In addition, he has been actively co-operating as a consultant with industry, and he has published several technical articles in international congresses and journals. Dr. Arenas has been a member of the International Institute of Acoustics and Vibration (IIAV) since 1995 and of the Acoustical Society of America (ASA) since 1993. In ASA, he has served as a member of the Technical Committee on Noise in several occasions. He is a member of the editorial board of three journals, including the International Journal of Acoustics and Vibration. He has been a member of the scientific, organizing, and international advisory committee of several international congresses including ICSV, Internoise, and FIA (Iberoamerican Federation of Acoustics). He has served as a member of the Board of Directors of IIAV, Vice President for Communications of IIAV, and he is currently President Elect of IIAV.

Machining Dynamics: Frequency Response to Improved Productivity

By: Tony L. Schmitz and K. Scott Smith
Publisher: Springer Science + Business Media
2009, Hardcover, 303 pages with CD of numeric examples in MATLAB
ISBN 978-0-387-09644-5
Price: US $179

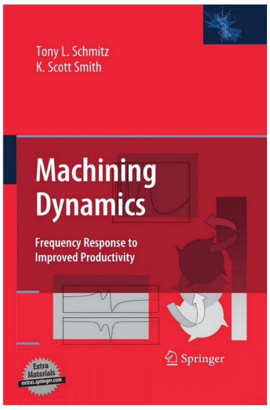

Schmitz and Smith demonstrate the importance of modal dynamics theory in machining performance in their book based on graduate courses they offer in mechanical vibrations and manufacturing.

The book includes seven chapters—each one featuring an epigraph of Einstein's sayings. The most interesting appears in Chapter 3: "Make everything as simple as possible, but not simpler" ("Turning Dynamics"). Indeed, their book illustrates how difficult it is to simplify the power of physico-mathematical simulation for the manufacturing processes because of the complexity of real phenomena.

The first chapter is the introduction. In Chapter 2 "Modal Analysis", the authors introduce the readers to the elements of the theory of 1-DOF and 2-DOF mechanical systems. In Chapters 3–7 (which are named "Turning Dynamics", "Milling Dynamics", "Surface Location Error in Milling", "Special Topics in Milling", and "Tool Point Dynamics Prediction"), the authors demonstrate the applications of analysis, both in the frequency and time domains, to the real problems of machining dynamics. One of them—the chatter caused by the relative movement of the work piece and cutting tool—notably affects such typical machining processes as turning, milling, drilling, and grinding. Generally, the vibration is one of the main limiting factors for high-speed machining. The associated noise issue may also be important.

The authors consider both forced and self-generated vibration. Their approach is to show how the vibration effect can be understood and alleviated with the help of analytical and numeric simulations. Even though the authors made their calculations as simple and straightforward as possible, the book does not seem to be easy for reading. Some equations look quite cumbersome just because of their notable size. It looks like unimportant routine mathematics could be omitted in most cases with no challenge to the final equations obtained. Certainly, the multiple brief conclusions ("In a nutshell") made to summarize and specify the methods and effects are helpful. The students, however, should do their homework studies (in particular, using the MATLAB examples on the CD) to better understand the methods and results under study.

Some of the discussion seems to be unnecessarily lengthy, and the book could be improved by splitting it into two main parts: one for manufacturing engineers (with mostly verbal models and recommendations) and a separate one for design engineers (with analytical and numeric models and results). Both groups could benefit from the first part, while vibration specialists could get a more advanced knowledge from studying the second part. The other well-known Einstein quotation is recommended for the second part: "Intellectuals solve problems, geniuses prevent them".

While the book is for important for machining dynamics, such changes might be incorporated into the next edition to make the book more popular with future engineers and scientists.

Roman Vinokur
ResMed Motor Technologies, Chatsworth, CA, USA.

IIAV 2016 Elections

President-Elect (2016–2018)

Eleonora Carletti

Eleonora Carletti obtained her M.Sc. degree in physics in 1979 and served as a lecturer in applied physics at the University of Ferrara for several years. She joined the Italian National Research Council of Italy in 1984. Currently she is the head of the Acoustics and Vibration Department at the Institute of Agricultural and Earth-Moving Machinery (IMAMOTER) and is a contract professor at the University of Modena - Engineering Department, within the University M.A. degree program in "Oleodinamics". Her area of expertise is the noise and vibration control of complex sources and her recent activity mainly concerns product sound quality applied to machinery. She is a member of the Expert Noise Group at the European Commission (DG GROWTH) and a member of the Scientific Advisory Board of the Acoustics Research Institute of the Austrian Academy of Sciences in Vienna. She has been a member of the Presidency Committee of the Acoustical Society of Italy (AIA) from 2002 to 2013 and a member of the Director Board of the Acoustical Society of Italy from 2014 to the present. She has been an active member of the International Institute of Acoustic and Vibration (IIAV) for many years, serving IIAV in the position of Vice President for Professional Relations from 2008 to 2012 and in the position of Director from 2000 to 2004, from 2006 to 2010 and from 2013 to the present. She served as one of General Chairs of the 22nd International Congress of Sound and Vibration (ICSV22) held in Florence, Italy, in July 2015.

Vice-President for Professional Relations (2016–2020)

Marek Pawelczyk

Marek Pawelczyk obtained his M.Sc. in 1995, Ph.D. in 1999, D.Sc. (habilitation) in 2005, and attained the scientific title of professor in 2014. He is currently a full titular professor at the Silesian University of Technology, and holds the positions of vice-director of the Institute of Automatic Control, and head of the Measurements and Control Systems Division. He is an author of three books on active control, about 150 journal and proceedings papers, and five patent applications. He has been a frequent reviewer for several international journals, book publishers, international conferences, and Ph.D. theses in several countries. He cooperates closely with industrial companies. He is a co-investigator of several research projects including: ultrasonic monitoring of petroleum fractions; safety monitoring in mines; active personal hearing protections systems; active noise control in industrial halls; active control of machinery; noise reduction in large-scale HVAC systems; active noise control in headrests; and semi-active control of vehicle suspension. He has received many prizes from domestic and international organizations. He has been involved in the IIAV for many years. Since 2008 he has been the Managing Editor of the International Journal of Acoustics and Vibration. In 2007-2011 he served as the IIAV Vice-President for Communications, and in 2012-2014 President of the IIAV. He was the General Chair of the 16th ICSV held in Krakow, Poland, in 2009.

Directors (2016–2018)

Luis Bento Coelho

Luis Bento-Coelho graduated in electrical engineering from the Instituto Superior Técnico, in Lisbon, Portugal, and received M.Sc. and Ph.D. degrees from the Institute of Sound and Vibration Research (ISVR), University of Southampton, UK. He is currently emeritus professor at Instituto Superior Técnico (IST), Lisbon University, where he is Head of the Acoustics and Noise Control Group. Luis Bento-Coelho is a fellow of the International Institute of Acoustics and Vibration (IIAV), Doctor Honoris Causa of the University of Pitesti, Romania, a chartered acoustical engineer of the Portuguese Council of Engineers, and President of the General Assembly of the Portuguese Acoustical Society. He was a member of the EU Noise Policy Working Group on the Assessment of Exposure to Noise, member of the European Green Capital City Award Expert Panel (European Commission), and is a member of the European Expert Panel on Noise (European Environmental Agency). He was chair of the 12th International Congress on Sound and Vibration (ICSV12), held in Lisbon in 2005 and has served as both President and Vice-President of IIAV. He has more than 200 publications in acoustics in major journals and conference proceedings. His current research interests focus on modeling sound emission and propagation in rooms and in urban environments.

John Davy

Dr John Davy has been an acoustics researcher for 42 years, mainly in the area of building acoustics. He currently has offices at CSIRO and at RMIT University in Melbourne, Australia. For the past six years he has been a regular visitor to the University of Canterbury in Christchurch, New Zealand. He is the chair of the Australian Government's Independent Scientific Committee on Wind Turbines. He chairs one committee and is a member of another committee of the National Association of Testing Authorities, Australia. John has been a member of the Scientific Committee for 16 ICSV conferences, attended four ICSV conferences and co-authored a paper at another ICSV conference. He was the Technical Programme Co-chair for the Inter-noise 2014 conference which was held in Melbourne, Australia. John served as a member of two European COST Actions on acoustics topics between 2009 and 2014. He is the author of 120 scientific papers.

Ricardo E. Musafir

Ricardo E. Musafir obtained his BS in civil engineering (1978), and his MS (1984) as well as his DS (1990) in mechanical engineering (acoustics). He is an associate professor in both the (graduate) Department of Mechanical Engineering, and in the Department of Water Resources and Environmental Sciences, (School of Engineering), at the Federal University of Rio de Janeiro, Brazil. He has served as editor for general acoustics for the Journal of Sound and Vibration since 2009. His research areas of interest include aeroacoustics, sound source modeling, and environmental acoustics. He has been involved in noise legislation, having helped make the noise ordinances for the city and for the state of Rio de Janeiro. He is a member of the Brazilian Standards Committee on Acoustics. He has published 15 papers in major scientific journals and 75 in conference proceedings. Ricardo E. Musafir has been an IIAV member since 2000, having attended and presented papers in most of the ICSV congresses since then. He was General Chair of ICSV18, which took place in Rio de Janeiro in 2011, and served as member of the IIAV Board of Directors for the period 2010-2014.

Georges Kouroussis

Georges Kouroussis was awarded a master's degree in mechanical engineering from the Faculty of Engineering of Mons in France June 2002. He was also awarded a PhD in applied sciences from the FPMs on the vibratory nuisance of ground vibrations in May 2009. He works presently as senior lecturer/associate professor in the Department of Theoretical Mechanics, Dynamics and Vibrations of the University of Mons. He takes part in the Theoretical Mechanics and Dynamics Labs, exercises and courses. Georges Kouroussis was appointed Associate Editor of "Shock and Vibration" in 2015. He also serves on the editorial boards of the "International Journal of Rail Transportation", "Urban Rail Transit" and "Transport".

James Talbot

James Talbot graduated from Cambridge University with a BA and MEng degree in Mechanical Engineering, having been a sponsored student of Westland Aerostructures. He went on to spend two years with the engineering consultancy, Atkins, before returning to Cambridge to complete his PhD on the vibration isolation of buildings. This was followed by his post-doctoral research within the EU project CONVURT on the control of noise and vibration from underground railways. After working on the CONVURT project, Dr Talbot returned to Atkins where he spent a further nine years working primarily in the fields of vibration engineering and structural integrity. His experience covers experimental work, and theoretical analysis and design, from across a wide range of industries. Dr Talbot returned to Cambridge University in 2013 as a lecturer in the Structures Group of the Civil Engineering Division. He was elected an official fellow of Peterhouse (College), where he is director of studies for first-year undergraduates in engineering. He is a chartered engineer and a fellow of the Institution of Mechanical Engineers, and a member of the Institute of Acoustics (UK) and the International Institute of Acoustics and Vibration (IIAV.)

Obituary Notice of Franz Ziegler

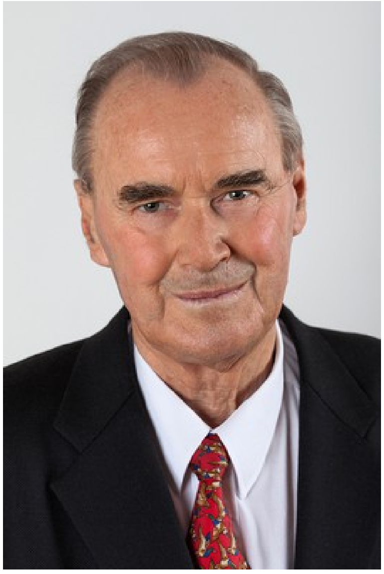

It is with great sadness that we have to announce the death of Franz Ziegler, Professor Emeritus of Rational Mechanics at the TU Vienna, and the President of the International Institute of Acoustics and Vibration (IIAV) in 2006-2008, who passed away on January 4, 2016. He was named as an Honorary Fellow of IIAV.

Franz Ziegler joined the Faculty of Civil Engineering of the Vienna University of Technology (TU Vienna) in 1972, where he taught and conducted research for over 34 years, serving as the Head of the Institute of Rational Mechanics. While Franz "retired" to emeritus status in 2006, he remained active in research, and editorial activities until his death.

Franz Ziegler was highly recognized internationally. He was an exceptionally innovative researcher in various fields of theoretical and applied mechanics, such as wave propagation, deterministic and random vibrations of elastic and inelastic structures, thermal stresses, fluid-structure interaction, dynamic plasticity, structural control, and numerical and experimental methods in structural dynamics. The results and findings of his research are recorded in about 300 papers published in peer reviewed journals, books, and conference proceedings. He was the author of the comprehensive textbook "Mechanics of Solids and Fluids", published in several editions in German, English, and Russian. As a Member of the Editorial Board of various prominent scientific journals, particularly as an Editor of Acta Mechanica, Franz dedicatedly served the scientific community.

The contributions of Franz Ziegler were recognized through many awards, including the Peter Kapitza medal of the Russian Academy of Natural Sciences, and the EUROMECH Solid Mechanics Prize. He was awarded as Honorary Doctor of the Polytechnical State University of St. Petersburg, Russia. He was elected Full Member of the Austrian Academy of Science, elected Member Abroad of the Russian Academy of Natural Sciences, and elected Member Abroad of the Russian Academy of Sciences. He served as Secretary General of the International Union of Theoretical and Applied Mechanics (IUTAM), President and Deputy President of the International Association of Applied Mathematics and Mechanics (GAMM), President of the International Institute of Acoustics and Vibration (IIAV), and Chairman of the Board of the Austrian Association of Earthquake Engineering and Structural Dynamics (OGE).

The funeral service was held in the church and burial in the cemetery of the town of Gattendorf, Province of Burgenland, Austria, on January 23, 2016.

Franz Ziegler will be sorely missed.